

Demonstration and Evaluation of a Nanocrystal-Nanowire Solar Cell

David Andrew Jacques

Submitted in accordance with the requirements for the degree of

Doctor of Philosophy

As part of the integrated MSc/PhD in Low Carbon Technologies

The University of Leeds

Energy Research Institute

School of Chemical and Process Engineering

Doctoral Training Centre in Low Carbon Technologies

October, 2015

The candidate confirms that the work submitted is his own, except where work which has formed part of jointly authored publications has been included. The contribution of the candidate and the other authors to this work has been explicitly indicated below. The candidate confirms that appropriate credit has been given within the thesis where reference has been made to the work of others.

Chapter 4 includes the following work;

Bush, R., Jacques, D. A., Scott, K., & Barrett, J. (2014). The carbon payback of micro-generation: An integrated hybrid input–output approach. *Applied Energy*, *119*, 85-98.

The work detailed within this paper was all the candidate's own with the exception of the following; Ruth Bush who considered the aspects pertaining to micro-wind generation and John Barrett and Kate Scott who considered uncertainty and future emissions.

Chapter 5 includes the following work;

Jacques, D. A., Gooding, J., Giesekam, J. J., Tomlin, A. S., & Crook, R. (2014). Methodology for the assessment of PV capacity over a city region using low-resolution LiDAR data and application to the City of Leeds (UK). *Applied Energy*, *124*, 28-34.

The work detailed within this paper was all the candidate's own with programming help from Dr Rolf Crook and guidance from all of the authors.

Chapter 6 includes the following work;

Jacques, D. A., Guan, D., Geng, Y., Xue, B., & Wang, X. (2013). Inter-provincial clean development mechanism in China: A case study of the solar PV sector. *Energy Policy*, *57*, 454-461.

The work detailed within this paper was all the candidate's own with guidance from all of the authors.

This copy has been supplied on the understanding that it is copyright material and that no quotation from the thesis may be published without proper acknowledgement. The right of David A. Jacques to be identified as author of this work has been asserted by him in accordance with the Copyright, Designs and Patents Act 1988.

Acknowledgements

To colleagues, friends, family and Laura. Thank you for putting up with me.

Abstract

Climate change is likely to have a major impact on future civilisation. To combat the worst effects of this, progress in renewable energy is necessary. With a plentiful resource, solar photovoltaics is one such renewable technology that holds promise. However, the incumbent photovoltaic technology currently suffers from high costs, a carbon intensive manufacturing process and a limited potential for efficiency improvement.

The aims of this research was to address these three issues through the fabrication of a novel solar cell architecture and identification of further areas that have the potential to improve device performance. This architecture utilises nanomaterials and therefore reduces material use and allows for less energy intensive fabrication processes while also allowing for a higher theoretical efficiency limit than that of silicon.

Upon proof-of concept and despite efforts to improve cell efficiency, the output was still exceedingly low (External quantum efficiency circa 0.3 %). It was also deemed impractical to perform a life cycle analysis on such a prototypal device. However, analysis of a standard silicon device resulted in carbon intensities greater than 100 g/kWh CO₂e, reaffirming the need to replace silicon. Through development of both a solar resource assessment methodology and a policy mechanism, avenues for carbon reduction were identified and quantified. For example, a reduction in the carbon intensity of the Chinese national grid could save over 500,000 tonnes CO₂e in UK Feed-in tariff installations alone. Upon maturing of the demonstrated device, all chapters can be combined to maximise electrical output, minimise cost and reduce the levels of carbon intensity.

Table of contents

1	Introduction	1
1.1	Current Solar Cells and the Need for Further Research	1
1.2	The Third Generation and the Use of Nanotechnology in Photovoltaics	2
1.3	Current Nano-Photovoltaic Devices.....	6
1.4	The Proposed Device	9
1.5	Aims and Objectives.....	12
1.5.1	Outline of thesis	13
2	Device Fabrication and Characterisation	15
2.1	Introduction	15
2.2	Fabrication Characterisation Techniques	15
2.2.1	X-ray Diffraction	15
2.2.2	Transmission Electron Microscopy	17
2.2.3	Scanning Electron Microscopy	18
2.2.4	Energy Dispersive X-ray Spectroscopy	18
2.2.5	Atomic Force Microscopy	19
2.2.6	Optical Spectroscopy	19
2.2.7	Four-Point Probe.....	20
2.3	Fabrication of the Primitive Device.....	20
2.3.1	Polishing.....	21
2.3.2	Oxidation.....	26
2.3.3	Nanowire Deposition	30
2.4	The Primitive Cell	34
2.4.1	Current-Voltage Characterisation.....	35
2.4.2	Photoresponse	37
2.4.3	Electropolishing.....	39
2.5	Decoration.....	41

2.5.1	Nanocrystal selection.....	41
2.6	Conclusion.....	51
3	Device Optimisation Through Geometry and Configuration	53
3.1	Introduction	53
3.2	Silver Loading.....	54
3.2.1	Results.....	54
3.3	Nanocrystal Loading.....	57
3.3.1	Results.....	57
3.4	Solvent Use	61
3.4.1	Results.....	62
3.5	Silver Nanowire Size.....	64
3.5.1	Results.....	64
3.6	Filamentary Nanomesh.....	67
3.6.1	Results.....	68
3.7	Deposition Order.....	70
3.7.1	Results.....	70
3.8	Nanowire and Nanocrystal Mixing.....	73
3.8.1	Results.....	73
3.9	Pre-Fabrication Mixing.....	81
3.9.1	Results.....	81
3.10	Ageing	83
3.10.1	Results.....	84
3.11	Conclusion.....	92
4	Device Optimisation by Nanocrystal Modification	94
4.1	Introduction	94
4.2	Application to Solar Cells	99
4.3	Results.....	101
4.3.1	Mercaptopropionic Acid	101

4.3.2	Inorganic Metal Sulphide Shell	106
4.3.3	Acidic Ligand Removal	108
4.3.4	Octylamine	111
4.3.5	Pyridine	114
4.3.6	Core-Shell Nanocrystals	117
4.3.7	Acid Treatment	120
4.4	Conclusion.....	122
5	Life Cycle Analysis	124
5.1	Introduction	124
5.2	Application of LCA to the Demonstrated Device	128
5.3	Application of LCA to Silicon Photovoltaics	130
5.3.1	Material Composition	130
5.3.2	Operational Lifetime	131
5.3.3	Results	131
5.3.4	Application to Policy	133
5.3.5	Carbon intensity of solar PV.....	138
5.3.6	Carbon payback time	139
5.4	Conclusion.....	140
6	Methodology for the Assessment of PV Capacity Over a City Region Using Low-Resolution LiDAR Data	142
6.1	Introduction	142
6.2	Background	143
6.3	Methodology.....	143
6.3.1	Small Buildings	144
6.3.2	Large Buildings	146
6.4	Application to the City Region of Leeds.....	147
6.4.1	Roof Profile Assessment	148
6.4.2	Validation	151

6.5	Combination with Life Cycle Analysis	153
6.6	Conclusion.....	155
7	Inter-Provincial Clean Development Mechanism	157
7.1	Introduction	157
7.2	Background on China	157
7.3	An Overview of the Clean Development Mechanism.....	159
7.4	The Establishment of an Inter-Provincial Clean Development Mechanism in China 162	
7.5	IP-CDM Implementation Procedure	165
7.6	Tackling the Flaws	166
7.7	Potential Impact of the IP-CDM.....	167
7.8	A Case Study of Solar Photovoltaics.....	168
7.8.1	The mutual benefits of solar PV and the inter-provincial CDM.....	170
7.8.2	Combination with Life Cycle Analysis	172
7.9	Conclusion.....	173
8	Conclusion.....	175
8.1	Summary	175
8.2	Future Work.....	179
9	References	181

List of Figures

Figure 1.1: Illustration of component parts of a NC-SB solar cell.....	7
Figure 1.2: Illustration of component parts of a depleted-heterojunction solar cell.....	7
Figure 1.3: Illustration of component parts of a QDSSC.....	8
Figure 1.4: Schematic diagram of the nanocrystal-decorated AgNW-TiO ₂ Schottky barrier solar cell. Image not to scale. Credit for image: Rolf Crook.....	10
Figure 1.5: Cross-sectional diagram of the activated device.....	10
Figure 1.6: Band diagram of the nanocrystal-decorated AgNW-TiO ₂ Schottky barrier solar cell. Charge separation can occur through visible photon absorption in the NCs or UV photon absorption in the TiO ₂	12
Figure 2.1: Schematic diagram of X-ray diffraction.....	16
Figure 2.2: Schematic diagram of transmission electron microscopy (image taken from [89]).	18
Figure 2.3: Mechanism of electropolishing 1) electrolyte 2) cathode 3) sample (anode) 4) deburred particles moving from sample to cathode.....	22
Figure 2.4: SEM images of a titanium chip before (a) and after electropolishing (b).....	24
Figure 2.5: Surface roughness measurements of a chip at each stage of processing.....	25
Figure 2.6: SEM (a) and EDX (b) image of an electropolished sample exhibiting salt artefacts.	25
Figure 2.7: SEM view of titanium chip before (a) and after (b) thermal oxidation.....	27
Figure 2.8: EDX spectroscopy of the top (a) and side (b) of a thermally oxidised chip.....	28
Figure 2.9: A typical XRD spectra for a sample post-thermal oxidation.....	29
Figure 2.10: Evidence of stress induced on titanium as a result of thermal oxidation.....	29
Figure 2.11: SEM (a) and TEM (b) images of typical Ag nanomeshes. Credit for microscopy: Priten Khagram.....	32
Figure 2.12: AFM map of a sample surface before (a and b) and after (c and d) AgNW deposition.....	32
Figure 2.13: SEM image of a nanomesh that has been deposited through a spin-casting technique. Credit for microscopy: Niamh Ryall and Norah Algarou.....	34
Figure 2.14: Photographs of the PCB used for device characterisation (a) and a primitive cell attached to a PCB ready for characterisation (b).....	35
Figure 2.15: Typical IV curves for fabricated primitive devices. Solid line shows curve that closely follows the diode equation. Dashed line shows a more typical curve with larger reverse bias leakage.....	36
Figure 2.16: Equivalent circuit of a solar cell.....	37

Figure 2.17: Process of refining values for the wavelength dependent power output of the light source. Extrapolation is shown in part a) where orange points have been added to include lower wavelengths. Interpolation is shown in part b where resolution has increased from 10 nm to 2 nm.	38
Figure 2.18: Typical EQE (a) and photovoltage (b) curves for a fabricated primitive device.	39
Figure 2.19: IV curve for a non-electropolished device.	40
Figure 2.20: Photocurrent produced by a non-electropolished device.	40
Figure 2.21: Optical characterisation of the selected NCs.	42
Figure 2.22: TEM images of CdSe (a) and CdTe (b). Images courtesy of Priten Khagram.	42
Figure 2.23: SEM images of a decorated cell.	43
Figure 2.24: EDX maps of a CdSe-decorated cell.	44
Figure 2.25: Typical changes in IV curves upon NC decoration. a) illustrates how NC decoration can increase the current density whereas b) illustrates how NC decoration can reduce the current density. c) shows a less common 'ideal' case where the IV curve is unaffected by NC decoration.	45
Figure 2.26: Typical changes in EQE curves upon NC decoration. a) and b) shows an 'ideal' case where the response under UV illumination is unaffected, c) and d) shows a more typical case where UV response is greatly increased. Left hand plots display response over whole range of wavelengths, right hand plots display response under visible illumination only.	46
Figure 2.27: Typical changes in photovoltage curves upon NC decoration. a) and b) shows an 'ideal' case where response under UV light is unaffected, c) and d) shows a more typical case where UV response is greatly increased.	47
Figure 2.28: NA-IQE values for CdSe and CdTe.	48
Figure 2.29: Average EQE performance of selected NCS.	48
Figure 2.30: Average photovoltage performance of selected NCS.	49
Figure 2.31: Average maximum current density after activation by selected NCS.	49
Figure 2.32: Example of a definitive visible response ($> 0\%$ EQE at $> 400\text{ nm}$) (a) and possible visible response (b).	51
Figure 3.1: Typical change in EQE for a cell that was recycled after measurement (a) and successively layered and annealed (b).	55
Figure 3.2: Typical change in photovoltage for a cell that was recycled after measurement (a) and successively layered and annealed (b).	55
Figure 3.3: Maximum current density from IV curve as a function of silver loading.	56
Figure 3.4: Number of short circuits observed for each loading of silver measured.	56
Figure 3.5: SEM images of relatively low (a), medium (b) and high (c) loadings of NCs.	57

Figure 3.6: EDX spectroscopy of film caused by NC overloading. Green is Se response, red is Ti response.....	58
Figure 3.7: Photocurrent (top) and photovoltage (bottom) performance under visible light upon successive depositions of CdSe (left) and CdTe (right) NCs.....	59
Figure 3.8: Photocurrent (top) and photovoltage (bottom) performance under UV light upon successive depositions of CdSe (left) and CdTe (right) NCs.....	60
Figure 3.9: Maximum current density upon successive loadings of CdSe (a) and CdTe (b) NCs.	60
Figure 3.10: Ratio of visible response to UV response for EQE (top) and photovoltage (bottom) upon successive depositions of CdSe (left) and CdTe (right) NCs.	61
Figure 3.11: Primitive cell before (a) and after (b) addition of solvent.	62
Figure 3.12: Change in maximum current density due to solvent deposition.....	63
Figure 3.13: Change in peak EQE (a) and peak photovoltage (b) of a primitive device due to solvent deposition.....	63
Figure 3.14: SEM images of primitive cells formed with short wires (a) and long wires (b).	65
Figure 3.15: Typical IV curves for long and short wires.	65
Figure 3.16: Typical EQE (a) and photovoltage (b) plots for long and short wires.	66
Figure 3.17: EQE (a) and photovoltage (b) plots displaying size of visible peak compared to UV peak for both short-wire and long-wire cells.....	67
Figure 3.18: Illustration of increased surface area coverage due to filamentary structure (wires drawn to scale).....	68
Figure 3.19: SEM image of filamentary nanomesh.....	68
Figure 3.20: Typical IV curves for cells utilising a filamentary nanomesh compared with a normal nanomesh.....	69
Figure 3.21: Typical EQE (a) and Photovoltage (b) curves using a filamentary nanomesh compared with a normal nanomesh.....	69
Figure 3.22: EQE (a) and photovoltage (b) plots displaying size of visible peak compared to UV peak for both normal nanomeshes and filamentary nanomeshes.	70
Figure 3.23: SEM images of cells with NWs deposited first (a) and NCs deposited first (b)..	71
Figure 3.24: Average photovoltage response under visible and UV light (a) and the ratio of response under visible light to response under UV light (b).	71
Figure 3.25: Average EQE response under visible and UV light (a) and the ratio of response under visible light to response under UV light (b).	72
Figure 3.26: Average maximum current density produced through IV characterisation.	73
Figure 3.27: TEM and SEM images of a 1:1 quantity mix of AgNW and CdSe NCs after 24 hours. Credit for photography: Priten Khagram.	74

Figure 3.28: TEM images of NC adsorption on to a NW surface. Credit for photography: Priten Khagram.	75
Figure 3.29: Emission (top) and absorption (bottom) spectra of NC/NW mixes. Right hand side shows silver subtracted from the results of the 0 hour and 24 hour mix.	76
Figure 3.30: Maximum current density as a function of NC density.	77
Figure 3.31: EQE performance of devices with a range of NC to NW ratios.	77
Figure 3.32: Photovoltage performance of devices with a range of NC to NW ratios.	78
Figure 3.33: Ratio of response under visible light to response under UV light for both EQE (a) and photovoltage (b).	78
Figure 3.34: Comparison of typical photovoltages produced through both deposition types.	79
Figure 3.35: Comparison of typical EQEs produced through both deposition types.	80
Figure 3.36: Difference in maximum current density between pre-deposition mixing and a typical activated cell.	80
Figure 3.37: Typical IV curve for a cell after pre-fabrication mixture deposition.	81
Figure 3.38: Illustration of the EQE as a function of wavelength of a working (a) and not-working (b) cell after pre-fabrication mixture deposition.	82
Figure 3.39: Illustration of the photovoltage as a function of wavelength of a working (a) and not-working (b) cell after pre-fabrication mixture deposition.	82
Figure 3.40: SEM images of cells fabricated using a pre-fabrication mixture of AgNW and CdSe NCs.	83
Figure 3.41: EQE under UV light of a typical primitive (a) and activated (b) cell.	84
Figure 3.42: Photovoltage under UV light of a typical primitive (a) and activated (b) cell.	85
Figure 3.43: Photovoltage of an activated device for every day of measurement. Days less than the 25th day are solid black, the 25th day is orange and days after the 25th are dashed black.	85
Figure 3.44: Photocurrent and photovoltage of a typical activated cell under visible light.	86
Figure 3.45: Maximum current density produced under generation of IV curves for a typical primitive (a) and activated (b) cell.	86
Figure 3.46: Series resistance of a typical primitive (a) and activated (b) cell.	87
Figure 3.47: Leakage resistance of a typical primitive (a) and activated (b) cell.	87
Figure 3.48: Position of peak UV EQE (top) and photovoltage (bottom) for primitive (left) and activated (right) cells.	88
Figure 3.49: Wavelength of initial EQE (a) and photovoltage (b) response.	89
Figure 3.50: SEM and EDX of a typical primitive device after two months.	89

Figure 3.51: SEM (a) and carbon EDX mapping (b) of a typical activated device after two months.	90
Figure 3.52: SEM and multi-element EDX mapping of a typical activated device after two months.	91
Figure 4.1: A nanocrystal encapsulated by ligands.	94
Figure 4.2: Molecular structure of the native ligands of the NCs used in this structure.	96
Figure 4.3: A nanocrystal comprising of a core encapsulated by a shell.	97
Figure 4.4: Band gap structures formed in core-shell NCs.	98
Figure 4.5: Molecular structure of mercaptopropionic acid.	102
Figure 4.6: Absorption and emission spectra before and after ligand exchange with MPA, CdTe (a) and CdS (b).	102
Figure 4.7: IV curves of cells before and after activation by MPA-capped CdTe (a) and CdS (b).	103
Figure 4.8: EQE plots of cells activated by MPA-capped CdS (a and b) and CdTe (c and d).	104
Figure 4.9: Photovoltage plots of cells activated by MPA-capped CdS (a and b) and CdTe (c and d).	104
Figure 4.10: IQE plot of a typical MPA-capped and native ligand-capped CdTe-activated cell.	106
Figure 4.11: IV curves for CdTe (a) and CdS (b) before and after metal sulphide shell treatment.	107
Figure 4.12: EQE plots for CdS (a and b) and CdTe (c and d) activated cells before and after metal sulphide shell treatment.	107
Figure 4.13: Photovoltage plots for CdS (a and b) and CdTe (c and d) activated cells before and after metal sulphide shell treatment.	108
Figure 4.14: IV curves for CdTe-activated cells that have undergone acidic ligand stripping both pre-deposition (a) and post deposition (b).	109
Figure 4.15: EQE plots for Post-deposition treatment (a and b) and pre-deposition treatment (c and d) of CdTe-activated cells.	110
Figure 4.16: Photovoltage plots for Post-deposition treatment (a and b) and pre-deposition treatment (c and d) of CdTe-activated cells.	111
Figure 4.17: Molecular structure of octylamine.	112
Figure 4.18: Absorption and emission spectra before and after ligand exchange with octylamine.	112
Figure 4.19: IV characteristics of a typical cell when primitive, activated by octylamine-capped CdTe and after annealing.	113
Figure 4.20: EQE (a and b) and photovoltage (c and d) plots of cells activated by octylamine-capped NCs.	113

Figure 4.21: EQE (a) and photovoltage (b) plots of a typical octylamine-capped NC-activated cell after annealing.....	114
Figure 4.22: Molecular structure of pyridine.	115
Figure 4.23: Absorption and emission spectra before and after ligand exchange with pyridine.	115
Figure 4.24: IV characteristics of a typical cell when primitive, when activated by pyridine-capped CdTe and after annealing.	116
Figure 4.25: EQE (a and b) and photovoltage (c and d) plots of a typical cell when primitive, activated by pyridine-capped CdTe and after annealing.	116
Figure 4.26: Absorption and emission spectra of CuInS ₂ NCs with and without a ZnS shell.	117
Figure 4.27: Example of a noisy photocurrent response when utilising CuInS ₂ NCs that had a ZnS shell.	118
Figure 4.28: EQE plots for core-only (a and b) and ZnS-shell (c and d) CuInS ₂ -activated cells.	118
Figure 4.29: Photovoltage plots for core-only (a and b) and ZnS-shell (c and d) CuInS ₂ -activated cells.....	119
Figure 4.30: Comparison of the average effectiveness of ligand exchange techniques.	120
Figure 4.31: IV characteristics of a typical primitive cell before acid treatment, after acid treatment and after decoration with CdTe.	121
Figure 4.32: EQE (a and b) and photovoltage (c and d) plots of a typical acid-treated cell before and after CdTe NC deposition.	122
Figure 5.1: Methodological framework of lifecycle analysis.....	126
Figure 5.2: Material composition by mass of the considered solar PV single crystalline panel.	131
Figure 5.3: Emission results from single silicon solar PV installation (3kWp) comparing process-based and hybrid-based results.	132
Figure 5.4: Considered scenarios for rate of scheme uptake.....	136
Figure 5.5: Considered scenarios for rate of decrease of grid carbon intensity.....	136
Figure 5.6: Quantity of carbon dioxide saved under each scenario. Horizontal line indicated DECC's prediction.....	137
Figure 5.7: Carbon intensity of solar PV for different levels of levels of average annual irradiance.	138
Figure 5.8: Carbon payback time under different levels of annual irradiance and grid decarbonisation scenarios.	140
Figure 6.1: Illustration of roof profile catalogue when viewed from above. Depiction of a complex profile is an example.	144

- Figure 6.2: Sets of typical LiDAR points to illustrate each of the roof profile classes: a) gabled, b) hipped, c) flat, and d) complex. Points are viewed along the major axis. Grey lines provide a guide to the profile. Grey circles identify LiDAR points that are dismissed. 145
- Figure 6.3: Boundary of the City of Leeds used in this assessment. Geometrically-corrected aerial photograph overlaid with small and large buildings filled in black and white respectively. Credit for photography: UKMap © The GeoInformation Group 2006; OS MasterMap [Shape geospatial data] EDINA Digimap Ordnance Survey Service 2013. 148
- Figure 6.4: Area weighted histograms of roof segments for a) pitch of small buildings, b) pitch of large buildings, c) pitch of all buildings, d) orientation of small buildings, e) orientation of large buildings, and f) orientation of all buildings. Roof pitches are plotted as angles relative to the horizontal. Orientations are plotted as angles relative to north in a clockwise direction. The arrow in figure a) indicates the effect of assuming all flat roofs are given an artificial incline of 15°. 149
- Figure 6.5: Plots of specific annual yield and cumulative annual output as a function of fraction of total area for a) small buildings, b) large buildings, and c) all buildings. The most optimally angled roof segments are considered first. 151
- Figure 6.6: Comparison of the small building algorithm output, the TIN algorithm output, and the large building algorithm output, for examples of respectively small building hipped, gabled, and flat roof profiles. Credit for photography: UKMap © The GeoInformation Group 2006; OS MasterMap. 153
- Figure 6.7: Difference in the potential CO₂e savings for PV installation over the region of the City of Leeds. 154

List of Tables

Table 2.1: EQE Success rate of activated cells.	50
Table 2.2: Photovoltage success rate of activated cells.	50
Table 3.1: List of NC materials and the solvents that they are suspended in.....	62
Table 3.2: Properties of wires used in the study.	64
Table 4.1: Native ligands of the NCs used in this study.	95
Table 5.1: Aggregated LCA results (gCO ₂ e/kWh) from electricity generation technologies [211].	125
Table 5.2: Expected electricity generation for different annual irradiance values.	135
Table 5.3: Description of grid decarbonisation scenarios used.	137
Table 6.1: Comparison between classification from algorithm and validation from aerial photography. The units are number of buildings.	152
Table 7.1: Carbon intensity reduction targets of each province [312].	164
Table 7.2: Solar resource map of China [329].	169

Nomenclature List

AFM	Atomic force microscopy
AgNWs	Silver nanowires
CDM	Clean development mechanism
CER	Certified emission reduction
DECC	Department of Energy and Climate Change
DSSC	Dye sensitized solar cell
EDX	Energy dispersive X-ray spectroscopy
EPBT	Energy payback time
EQE	External quantum efficiency
FiTs	Feed-in tariffs
FOM	Haacke figure of merit
FRET	Förster resonance energy transfer
FSR	Feasibility study report
GDP	Gross domestic product
GHG	Greenhouse gas
HCSC	Hot carrier solar cell
IBSC	Intermediate band solar cell
IEA	International Energy Agency
IPCC	International Panel on Climate Change
IP-CDM	Inter-provincial clean development mechanism
IR	Infrared
IV	Current-voltage
LCA	Life cycle analysis
LiDAR	Light detection and ranging
MEG	Multiple exciton generation
MFA	Ministry of Foreign Affairs
MOST	Ministry of Science and Technology
MPA	Mercaptopropionic acid
NA	Nanocrystal area
NC	Nanocrystal

NC-SB	Nanocrystal Schottky barrier
NDRC	National Development and Reform Council
NL	Native ligand
NPC	National People's Congress
PCB	Printed circuit board
PDD	Project design document
PDRC	Provincial Development and Reform Commission
PLS	Photoluminescence emission spectroscopy
PV	Photovoltaics
QD	Quantum dot
QDSSC	Quantum dot sensitized solar cell
SA	Silver area
SBH	Schottky barrier height
SEM	Scanning electron microscopy
SILAR	Successive ionic layer adsorption and reaction
TCE	Transparent conducting electrode
TEM	Transmission electron microscopy
TGA	Thermogravimetric analysis
UV-Vis	UV-Visible absorption spectroscopy
XRD	X-ray diffraction

1 Introduction

Climate change is already happening and collective, decisive action is needed if the worst impacts that it could bring are to be avoided. Scientific consensus tells us that by 2050, global greenhouse gas (GHG) emissions must be reduced by at least 40 per cent from 2010 levels [1]. The UK government has gone even further by producing the 2008 Climate Change Act which set a legally binding target to reduce greenhouse gas emissions by 80 % by 2050 compared with 1990 emissions. It is clear that climate change is a major problem facing the whole world and one that needs to be tackled with urgency.

The electricity generation sector contributes to 33 % of the UK's total GHG of emissions [2]. This percentage can be reduced through the use of renewable energy. The EU has set a union-wide target for renewable energy to account for 20 % of the total energy mix by 2020. The UK Department of Energy and Climate Change (DECC) have set out to achieve this union wide target by setting a U.K. renewable energy target of 15 % renewable energy by 2020. According to the latest statistics provided by DECC [3], this has already been achieved with renewable energy technologies accounting for 19 % of the current UK energy mix. However, as will be discussed, these targets may not be sufficient. It should also be remembered that the UK is a net importer of electricity with 5.7 % of electricity being imported [3] and therefore the penetration of renewable energy sources in other national grid mixes will also be of importance. Ultimately any anthropogenic climate change is to be avoided and to achieve this, a truly sustainable energy supply is necessary.

The fact that current worldwide power consumption is a tiny fraction of the 122,000 TW of energy incident on Earth from the sun [4], indicates the important role that solar power could have in achieving a low carbon future. In the UK, solar photovoltaics (PV) only currently accounts for 3 % of the electricity that is generated by renewable energy but is growing significantly. From 2013 to 2014, PV capacity doubled and was the largest contributor to the increase in renewable energy use in 2014. PV capacity now stands at 5.4 GW. The main cause of this increase is the Renewables Obligation, with the Feed-in Tariff system also making an impact [3]. The UK government has acknowledged that there is significant potential for further deployment of solar PV and has estimated a deployment of between 7 and 20 GW by 2020 equating to 6 – 18 TWh of electricity generation [5].

1.1 Current Solar Cells and the Need for Further Research

Currently silicon solar cells make up 93 % of solar PV installations [6]. Silicon PV is a relatively mature technology. However, despite its maturity, its wholesale price is still struggling to reach grid parity in most countries [7]. Silicon wafer processing (typically

through Czochralski / Siemens processes) is an energy intensive process. This high use of energy results in a high cost when compared to fossil fuels and a high level of embodied emission when compared to some alternative solar cell designs [8, 9]. Further to this, silicon solar cells are limited by the Shockley-Queisser limit [10]. Indeed, single junction solar cells are approaching their theoretical efficiency limits and thus further work utilising the same materials will only yield limited results [11, 12]. The latest Status report from the EU JRC has identified the need for novel design concepts utilising alternative materials and the necessity for improvements in module and cell manufacturing [13].

These remaining issues with silicon based PV technologies have directed research aims towards looking at structures that while maximising efficiency, minimise material use and levels of embodied carbon. There have been a number of approaches to reduce cost and emissions through reducing the amount of silicon required with second generation, thin film solar cells but these to date have seen limited application [14]. That is because despite the promise of reduced financial pay-back and energy pay-back times through a reduced material usage and cheaper substrates, commercial efficiencies have remained comparatively low [15]. Second generation PV technologies have been slow to scale up with module efficiencies being significantly lower than lab-determined cell efficiencies [15]. These issues have been attributed to poor material reproducibility and uniformity over large areas [16, 17].

1.2 The Third Generation and the Use of Nanotechnology in Photovoltaics

To combat these cost and scalability hurdles, new developments in nanotechnology, materials and physical sciences are being utilised to develop what is regarded as the third generation of solar PV [18]. The objective for third generation PV is to exceed the theoretical efficiency limit that dictates first generation devices while maintaining the low production cost of second generation devices.

Current third generation concepts include tandem cells [19], dye-sensitised cells [20], hot carrier cells [21], the use of fluorescent collectors [22], organic cells [23] and the use of nanotechnology [24].

Nanotechnology is predicted to have a major role in third generation solar cells. Due to the unique properties of nanocrystals various applications are possible. One such application of nanotechnology is through quantum size confinement. Due to the small length scales involved, the energy levels of nanocrystals can become discrete and the size of the effective band gap will now be a function of both the size and size distribution of the used

nanocrystals [25]. This therefore indicates that by selecting the particle size, the optical and electrical properties of the material are tuneable.

A quantum dot (QD) is defined as nanometre sized three-dimensional semiconducting structures which confine electrons and holes in dimensions smaller than their corresponding De Broglie wavelength. A result of which is the quantisation of energy levels. A nanocrystal (NC) is a broader term that refers to a crystal that has some of its dimensions in the order of nanometres but not necessarily small enough to lead to quantum size confinement and not necessarily a semiconductor. The NCs that are used in solar photovoltaics however are typically QDs and both terms (QD and NC) are typically found to be used interchangeably in literature. For the sake of consistency, NC will be the preferred term in this work.

Other concepts for incorporating nanotechnology in to PV design include downshifting. Downshifting is designed upon the principle of generating lower energy photons from higher energy photons. There can be two purposes behind doing so. The first purpose is that through the production of more than one low energy photon from one high energy photon increases the number of photons reaching the photoactive layer [26]. The second reason is to shift the photons towards a region where the cell external quantum efficiency (EQE) is high [27]. For downshifting to occur, the NC needs to have a band structure that contains one or more intermediate levels. This will allow electrons that are excited into high-energy states to relax into these intermediate states and therefore produce a photon of lower energy than the one that caused excitation [28]. It should be remembered however that since the electronic properties of the semiconducting material haven't changed, the open circuit voltage and the fill factor will also remain unchanged [4]. For downshifting to be a sensible engineering decision, the absorption band of the nanocrystals has to be large enough to cover the region where the EQE is low and the emission band has to cover the region where the EQE is at its best.

Upshifting is another potential application of nanotechnology in PV. It follows the same theoretical lines as downshifting but works in reverse. Upshifting converts low energy photons in to high energy photons. For most PV technologies this would involve converting infrared (IR) photons to photons in the near-IR or visible part of the spectrum [28]. Naturally, energy must be conserved and therefore upshifting is necessarily a multiphoton process [29]. In its most simplistic model, two photons are absorbed sequentially by initial excitation of a ground state electron to an intermediate state followed by excitation to a further excited state. Relaxation of this electron to the ground state will yield a single higher energy photon that can be utilised by the active layer of the solar cell. There are in fact several other upshifting mechanisms that have been discussed in literature. These include an energy transfer upconversion mechanism and a cooperative sensitisation mechanism [30].

An alternative to upshifting are intermediate band solar cells (IBSC). These work by introducing a band of certain width within the band gap and therefore allow an exciton to be made through a two-step process. First the electron is excited to the intermediate band and is then excited further to the original conduction band. Of all potential NC applications to date, IBSCs have shown the most promise [28]. A NC IBSC device would operate through the embedding of nanocrystals into the matrix of original bulk semiconductor crystal. At a relatively high packing density, a collection of overlapping mini-bands are formed that lead to an effective intermediate band structure which will improve the closed circuit current without any decrease of the open circuit voltage [31]. It must be ensured however that the intermediate band is electrically isolated from the external contacts so that no current is extracted from it and instead, all current is taken from the conduction band [32].

As well as reducing energy losses due to thermal relaxation of optically excited carriers, the introduction of an intermediate band increases a cell's response to the solar spectrum and in this way can be seen as quasi-analogous to the multijunction solar cell [33]. While the realisation of IBSCs has been proposed through the utilisation of impurity doping [34] and dilute semiconductor alloys [35], it is nanocrystal IBSCs that seem to be receiving the most attention (e.g. [36-38]) and it is through the use of NCs that the intermediate band concept was initially demonstrated [39]. A remaining issue of NC-IBSCs is that the intermediate band remains quite shallow relative to the optimal positioning at approximately a third of the band gap [40]. While intermediate bands have been demonstrated, it is still very much a research topic with conversion efficiencies being beneath 1%. Reasons for this poor performance include small carrier lifetime associated with the junction technology, lattice mismatching due to defects and a high resistance [33]. It has been calculated that the theoretical conversion efficiency for IBSCs is 65.1% under AM1.5 conditions [41]. These values are comparable to the limits calculated for an optimised triple-junction solar cell (67%) [42].

When electron excitation occurs in solar cells, the electrons are often excited to higher energetic states than the bottom of the conduction band. The electrons then undergo thermalisation through the release of phonons (producing heat). This thermalisation process is known as one of the main loss mechanisms in solar cells and if these electrons can be captured before the thermalisation process, a higher open circuit voltage will be obtained [4]. Hot carrier solar cells (HCSC) are cells that aim to achieve this goal and it has been calculated that this could lead to an increase in the theoretical maximum efficiency limit to 55% for AM0 irradiation [43]. The initial thermalisation process is fast (around 1 ps) and therefore the capturing of these 'hot' electrons is non-trivial [44]. A potential way of achieving this is through the use of nanocrystals. Due to the widening of the distance

between energy states in NCs, the relaxation rate of the carriers is slowed down with respect to bulk material. This slowing of relaxation time can be attributed to a ‘phonon bottleneck’ which occurs when the spacing between the electronic levels is much greater than the highest phonon frequency of the lattice. When this occurs, hot-carrier relaxation can only happen through the slower multiphonon emission [45]. This slowing of relaxation time therefore increasing the time available to extract the carriers while they are still at an increased energy state and the utilisation of NCs in this manner have been shown to slow relaxation time by up to 1000 times [44].

Alternatively to hot electron extraction, it has been postulated that a single photon absorption by a NC semiconductor could result in the generation of more than one electron-hole pair. This is referred to as multiple exciton generation (MEG) and naturally, can only occur if the incident photon has at least double the energy of the semiconducting band gap [28]. By utilising more of the incident photon’s energy, losses are reduced and the theoretical efficiency limit is increased. As opposed to an increase in the open circuit voltage as with HCSC, there would be an increase in the number of charge carriers and therefore the closed circuit current would be increased. This increase in maximum theoretical efficiency has been calculated to be a raise from around 31% to around 45% with the optimal band gap shifting from 1.45 to 0.95 eV [28].

For MEG to occur, an electron with energy greater than twice the conduction band collides with an electron in the valence band. This reduces the energy of the high energy electron to that of a conduction band, a result of which is the second electron to be promoted to the conduction band by gaining the energy lost by the first electron [46]. This is the reverse of Auger recombination and is a more efficient process in NCs over bulk materials as when energy levels are discrete, coulomb interactions are enhanced and rules concerning the conservation of momentum are relaxed [47]. MEG realisation in solar cells has recently been achieved but overall device efficiency remains low [48].

Surface plasmons are oscillations of charge density which at certain energies can resonate resulting in an increased light scattering into the substrate, reduced reflectance and therefore increased light path length [49, 50]. Surface plasmon resonance is an effect associated with metal nanostructures, the intensity and frequency of which are dictated by the shape, size and type of material used [51, 52].

Surface plasmon resonance is one way in which nanotechnology is also being considered for use when considering a replacement for ITO as a transparent conducting electrode (TCE). ITO is the most commonly used TCE and is utilised both in solar PV and in flat panel displays. However, due to high demand and a relative scarcity, indium prices have increased

and there is a concern over supply shortage [53]. Alternatives to ITO are therefore being researched. These include single walled carbon nanotubes, graphene and metal nanowires. However, the carbon containing TCEs hold large sheet resistances due to high junction resistances between the tubes [54].

Nanotechnology can be further utilised through the use of using silver nanowires (AgNWs) as TCEs. AgNWs are a promising, flexible TCE material typically used with organic and thin film solar cells [55-57]. AgNWs are being developed to offer a cheap alternative to indium tin and can be produced using soft solution synthesis methods with an average length of tens of microns [58]. Various deposition methods can produce TCEs with sheet resistances of $\sim 10 \Omega/\square$ and light transmission over the visible spectrum of $\sim 90\%$ [54, 59-61]. Further to the high light transmission properties, AgNWs also benefit from localised surface plasmon resonances [49, 50].

1.3 Current Nano-Photovoltaic Devices

Most existing solar cells that utilise NCs as the active light absorbing component can be broadly classified as either NC Schottky barrier (NC-SB) solar cells, depleted NC heterojunction solar cells, or QD sensitized solar cells (QDSSC). Other NC-incorporating solar cells include extremely thin absorber cells [62], hybrid NC-organic heterojunction cells [63] and radial NW p-n junction cells [64].

The Schottky and depleted-heterojunction devices incorporate NCs as a polycrystalline colloidal thin film [65]. Light is absorbed throughout the thin film, which behaves as a semiconducting medium transporting both electrons and holes. In the Schottky device, as shown in Figure 1.1, the metal-to-semiconductor work function results in an internal electric field in the thin film to drive charge separation. Schottky junction solar cells hold the advantage in that they are simple and therefore relatively low cost [66]. Furthermore, SB solar cells do not require a window semiconductor layer. Such window layers, while necessary in forming a P-N junction, create complexities when attempting to minimise recombination and promote generation of excitons near the depletion region.

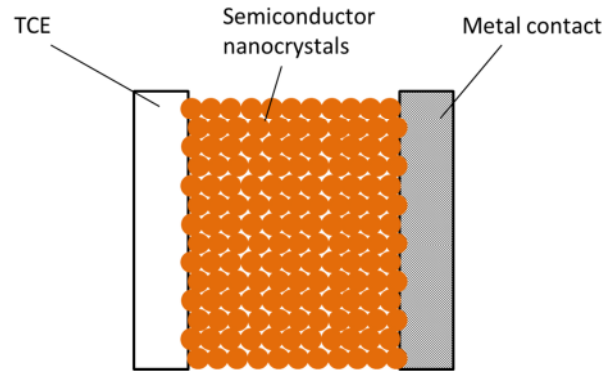


Figure 1.1: Illustration of component parts of a NC-SB solar cell.

Disadvantages of typical NC-SB solar cells include the fact that minority carriers have to travel the entire film before reaching their destination electrode therefore increasing the possibility of recombination. Secondly, V_{oc} can often be limited by Fermi-level pinning due to defects at the metal-semiconductor interface [67]. One way to counteract this is through the use of NCs with a large Bohr radius which enhances electronic coupling between NCs thus diminishing the effect of surface traps on NCs and therefore improving charge transport properties [68].

A depleted-heterojunction solar cell, as illustrated in Figure 1.2, typically consists of an electron transporting layer such as TiO_2 and a thin film of semiconducting NCs. The interface between these two materials forms a type II heterojunction thus creating an internal electric field. Most depleted heterojunction NC solar cell research has been focused on chalcogenide NCs [67]. These cells hold advantages over NC-SB cells in that they typically have a larger V_{oc} due to better carrier separation at the NC film/transporter material interface and back electron transfer is suppressed due to the built-in field of the depletion region [67].

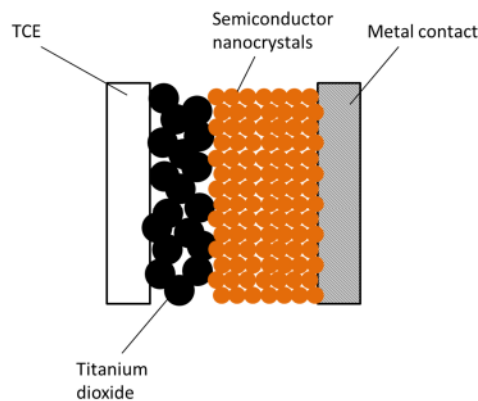


Figure 1.2: Illustration of component parts of a depleted-heterojunction solar cell.

Most research in NC solar cells has been concentrated on QDSSCs [67], an example of which is shown in Figure 1.3. In quantum dot sensitized solar cells, NCs directly replace the organic dye in the established dye-sensitized solar cell (DSSC), where electrons are injected from the NC donor into an electron transporter which is usually TiO_2 . The electrons are replenished from a hole transporter material which can be organic, inorganic, or liquid [69]. Compared with DSSCs, the performances of QDSSC devices are still low. These low performances are often attributed to issues with NC surface states or back electron transfer at the solid-liquid interface [70], anodic corrosion is also an issue [71].

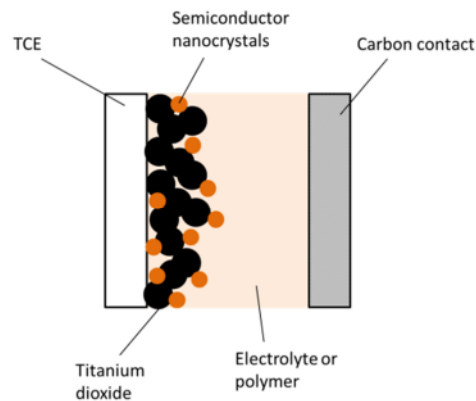


Figure 1.3: Illustration of component parts of a QDSSC.

This work will focus on the ability to sensitise a TiO_2 based cell with nanocrystals. However, as opposed to the typical QDSSC, charge separation will be achieved through a Schottky barrier. Compared to the relatively complex design of QDSSCs, SB cells hold the potential of providing a simple, robust, low cost and low carbon architecture that can be enhanced through nanotechnology.

Currently all NC-SB solar cells follow a similar design where a colloidal NC film is deposited on to an ITO substrate, metal contacts are then evaporated on to the back of the device, the interface between NCs and metal contacts thus forming a Schottky barrier.

Various NC materials have successfully been utilised to form a NC-SB solar cell. Early successes were frequently found through using lead chalcogenides with the aim of utilising incident infrared solar energy [72]. As the technology improved, power conversion efficiencies grew from 1.3% [73] to 2 % [74, 75] and is now at a record high for the material of 3.6 % [76]. These structures were also shown to be capable of achieving exceptionally large short-circuit photocurrents [75]. Through experimentation of different lead

chalcogenides tuned by size to have similar band gaps it has been found that PbS NC cells show a larger V_{oc} while PbSe NC cells generate a larger I_{sc} [75].

Other NC materials used include Si and CdTe where power conversion efficiencies are 0.02 % and 5 % respectively [77, 78]. It has also been noted that the CdTe NC-SB cell has an IQE approaching unity [78] whereas the poor performance of the Si NC-SB cell has been attributed to the indirect band gap nature of Si NCs and a poor leakage resistance due to a high quantity of trap states [77].

As stated, all of the discussed NC-SB devices use the same cell architecture and have ITO as the TCE with an evaporated back metal contact typically made of aluminium. McFarland and Tang proposed a novel SB cell design where light absorption and charge separation occurs through different materials. Typically the photoactive layer, as well as absorbing photons, has the role of forming a SB with the metal through which charge separation is achieved. In this proposal, the SB is formed by an ultrathin metal-semiconductor junction, organic photoreceptors are then deposited on top. Photoexcited electrons travel ballistically through the metal and over the Schottky barrier thus producing photocurrent [79]. The semiconductor is therefore only present for the purpose of majority charge transport and separation. Typical values for this device are V_{oc} of 600–800 mV and I_{sc} of 10–18 $\mu\text{A cm}^{-2}$ under 100 mW cm^{-2} illumination of visible light. The internal quantum efficiency was found to be 10 %. Despite claiming a remarkably high chance of ballistic travel due to the long ballistic path length of low energy electrons, an IQE of 10 % still leaves room for improvement.

As well as being used in PV applications, this architectural setup can also be utilised as a water splitter, creating hydrogen [80]. The fabricated devices have the advantages of being rugged, resistant to UV degradation, and cost effective [81]. Further benefits include that the band gap and semiconductor thickness constraints that are typically imposed on SB devices are removed. Also, several different photoactive materials could be utilised simultaneously for more efficient conversion.

1.4 The Proposed Device

This work proposes a modified version of the device discussed whereupon as opposed to the deposition of a photoactive dye, inorganic NCs are used. Furthermore, AgNWs can be used to replace the thin metal layer to function simultaneously as the TCE and metal for SB formation.

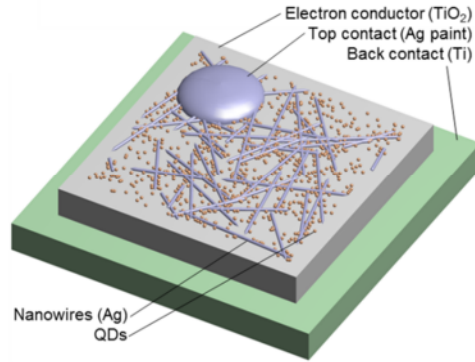


Figure 1.4: Schematic diagram of the nanocrystal-decorated AgNW-TiO₂ Schottky barrier solar cell. Image not to scale. Credit for image: Rolf Crook.

To fabricate this nanocrystal-decorated AgNW-TiO₂ Schottky barrier solar cell, as illustrated in Figure 1.4, a titanium chip is mechanically and electrically polished before being annealed in air to form a top oxide layer. Silver nanowires are drop-cast or sprayed on top of the oxide layer and annealed to form an Ag nanomesh, referred to here as a primitive cell which can only absorb UV light. The base titanium is connected to an external electrical contact and a second electrical contact is connected to the nanomesh with conductive silver paint. NCs then decorate the unactivated (primitive) device through drop-casting NCs in suspension and the solvent evaporated away. This forms an activated cell that is active under both UV and visible light.

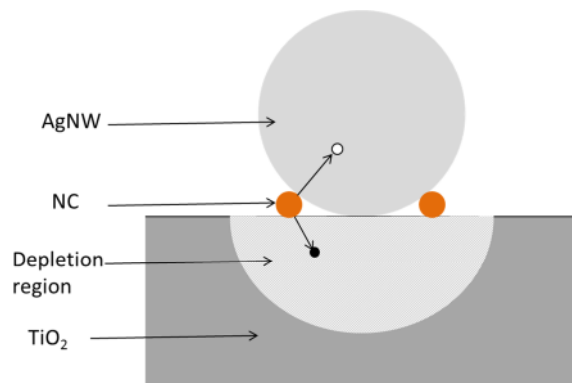


Figure 1.5: Cross-sectional diagram of the activated device.

As illustrated in Figure 1.5, the activated device operates over three interfaces. A large SB is formed between the metallic nanomesh and the TiO₂ film, with the depletion region extending laterally in the film underneath the NCs. This SB provides an internal electric field to drive electrons from the NCs to the back contact and prevents a short circuit between

the TiO₂ and Ag nanomesh. Each active NC is in contact with both a nanowire and the TiO₂ film. Charge is generated through two mechanisms.

Under all energies of light that are greater than the band gap of the selected NC material, the NC can absorb a photon upon which excitation occurs. The excited electron is injected in to the TiO₂ in an established fast mechanism [44, 82] and the hole travels in to the Ag nanomesh. Ballistic transport of electrons from the NC through the AgNW and into the TiO₂ can also occur [83].

At wavelengths less than 390 nm, the TiO₂ will also absorb incident photons that haven't been absorbed by nanocrystals or reflected by the nanomesh and the cell will operate in the same manner as a typical Schottky barrier solar cell. If the photons are absorbed in the depletion region, then the electric field will accelerate the electrons and holes in different directions (drift). If the photons are absorbed deeper in the TiO₂, beyond the depletion region, then the carriers will diffuse until they reach the depletion region or a contact (diffusion).

Carrier movement is illustrated in Figure 1.6. As charge generation, charge separation and transport are carried out by different components, it becomes possible to work on the individual components with a large number of technical options available to optimise and thus improve the performance of the whole device. As V_{oc} is limited by the potential barrier between TiO₂ and Ag, the optimal NC material will exhibit p-type behaviour with a band gap slightly larger than the barrier height to maximise the energy range of absorbed photons. TiO₂ has been extensively studied as a bulk host for NCs due to its high density of states allowing electrons from NCs such as CdSe to flow in to the conduction band of the bulk semiconductor[84].

This architecture ensures that there is no necessity to percolate charge carriers through a network of NCs as all NCs are to be in direct contact with the electrode thereby reducing interfacial issues that are observed in other NC solar cells [24, 68]. Further advantages include that due to the reduced role of the NCs in SB formation, defects within the NCs don't reduce V_{oc} .

The cell proposed by McFarland cell is limited by the maximum theoretical output efficiency limit of a conventional cell whereas with the potential added benefits of nanotechnology, this maximum efficiency limit is increased. Furthermore, it has been a challenge to obtain a dye with close to ideal absorption properties, the use of NCs enables the opportunity to tune the effective band gap of the solar cell [85].

To the author's knowledge, AgNWs have never previously been used as the metal contact in a Schottky barrier solar cell. As well as the advantages of AgNWs as a TCE, the AgNW

mesh enhances the possibility for unabsorbed UV photons to enter the bulk semiconductor and therefore despite the reduced importance of the exciton generating ability of the TiO_2 , a photocurrent can be produced due to both semiconducting materials. The typically used aluminium metal contacts have been found to degrade rapidly in the presence of NCs. However, a deep-work function metal like silver suffers no such rapid catastrophe in air.

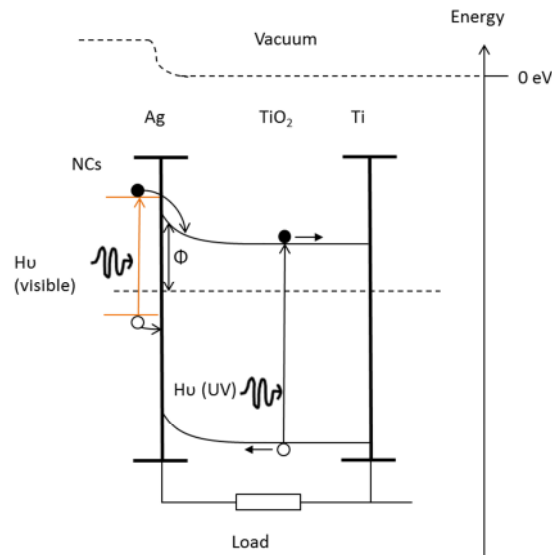


Figure 1.6: Band diagram of the nanocrystal-decorated AgNW- TiO_2 Schottky barrier solar cell. Charge separation can occur through visible photon absorption in the NCs or UV photon absorption in the TiO_2 .

1.5 Aims and Objectives

The overarching aim of this study is to develop potential methods to address the current issues of silicon PV. This is achieved primarily through the fabrication, characterisation and optimisation of the novel third generation solar PV cell architecture that has been introduced in this chapter but also through consideration of associated methods of increasing the electrical output and reducing the levels of embodied carbon.

This aim will be achieved through completion of the following objectives:

- Fabrication of an unactivated, primitive cell and complete characterisation of its constituents and performance as a complete device.
- Activation of the primitive cell through NC decoration and characterisation.
- Optimisation of architecture through considerations of loading and structure.
- Improvement in cell performance through manipulation of NC ligands.

- Conductance of a life cycle analysis (LCA).
- Appreciation of more realistic carbon savings values as determined by LCA through the conductance of a novel large scale solar resource assessment methodology.
- Use of said methodology in determination of optimum locations for solar PV installation.
- Development of a policy mechanism proposal to reduce the quantity of carbon embodied in a PV installation.

1.5.1 Outline of thesis

Chapter 2 presents the proposed cell architecture and explains the methods used for fabrication. This includes polishing and oxidation of the titanium and deposition of AgNWs. The motivation is given for each material and technique selected with reference to previous studies. Upon standardisation of the fabrication technique, activation of the primitive solar cell design with inorganic NCs is performed. This activation enables the cell to absorb visible light. Characterisation methods are also introduced.

Chapter 3 recognises the low efficiencies of the cells produced in Chapter 2 and involves efforts to optimise the activated solar cell design through consideration of device geometry and configuration. Photoresponse and IV characteristics are used to compare optimisation techniques and quantum efficiencies are determined.

Chapter 4 attempts to address the same issues as those recognised in Chapter 3. Efforts are made to increase device performance through NC modification.

Chapter 5 involves the performance of a life cycle analysis (LCA) of solar PV. Recognition is made to the fact that due to a lack of data, LCA is difficult to be performed on novel nano-activated solar cells and silicon is therefore used as a case study to enable methodological development and to quantify the carbon dioxide equivalent embodied in a typical solar PV installation.

Chapter 6 introduces a methodology to assess the PV capacity of a region. Through combination of the results of Chapter 5 with the developed solar resource assessment model, an appreciation of the embodied carbon and potential carbon savings of widespread solar PV can be achieved.

Chapter 7 identifies China as a critical market for PV as well as a leading contributor to anthropogenic GHG emissions. A policy mechanism to expedite the implementation of renewable energy generating systems is proposed. The mitigation potential of the policy is then assessed through the work developed in the previous chapters.

Chapter 8 concludes by summarising the work and providing suggestions for further work.

2 Device Fabrication and Characterisation

2.1 Introduction

This thesis aims to explore potential avenues to decrease the carbon intensity and cost of solar PV while allowing for opportunities for improvements in efficiency. The primary method of accomplishing this goal is in developing an alternative, novel solar cell that allows for comparison with current PV technologies. This cell utilises nanotechnology to reduce the quantities of embodied carbon and allows the potential to overcome the theoretical efficiency limits of the incumbent silicon technology. In this chapter, characterisation techniques used in this work are detailed before fabrication of the device is discussed. Finally, proof of concept is demonstrated.

2.2 Fabrication Characterisation Techniques

Multiple techniques will be utilised for characterisation during cell fabrication and measurement of cell performance. To ensure accurate and knowledgeable progression, each fabrication step must be fully characterised. Working with nanoscale materials adds complexity to this task as it can often be non-trivial to assess materials that often come in small quantities and are undetectable to the human eye. Fabrication characterisation techniques include: X-ray diffraction, scanning electron microscopy, energy dispersive X-ray spectroscopy, tunnelling electron microscopy, UV-Visible absorption spectroscopy, photoluminescence spectroscopy, atomic force microscopy and four-point probe measurements. Upon fabrication of a cell, its performance will be measured through photocurrent, photovoltage and current-voltage (IV) characterisation all of which will be measured via electrical contacts. When photovoltage is referred to, this is always at open-circuit unless otherwise stated.

2.2.1 X-ray Diffraction

X-ray diffraction (XRD) is used to determine the structure of crystals. A crystal has a periodic lattice structure with a repeating unit cell. This unit cell can either be a single atom or atoms in a fixed arrangement. The distance between the planes of crystals can be represented in three dimensions with three unit lengths and three angles. These parameters can be determined by XRD. X-ray diffraction utilises the principle of constructive interference of waves as demonstrated by Figure 2.1.

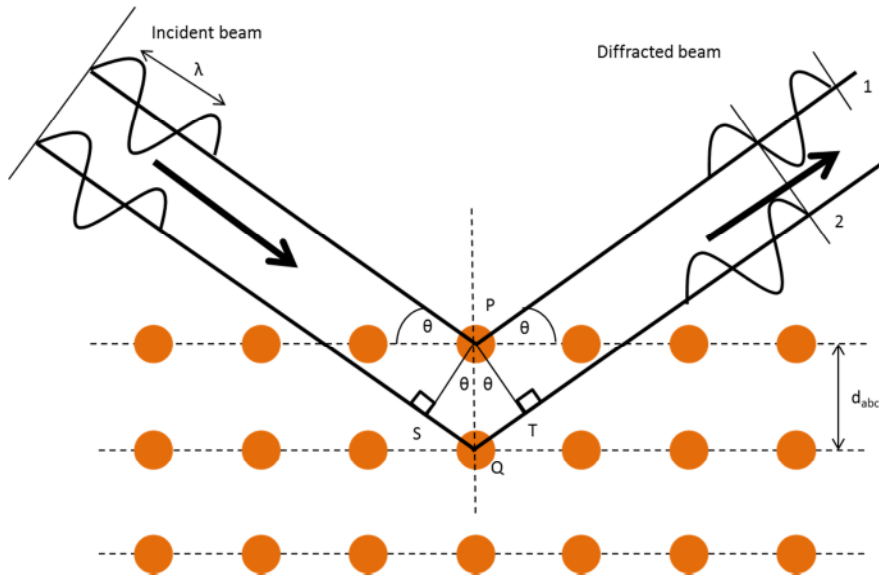


Figure 2.1: Schematic diagram of X-ray diffraction.

An incident X-ray beam will be diffracted from the planes of the crystal at different depths. These diffracted beams will then constructively interfere if the path difference, $SQ + QT$, is an integer number of wavelengths i.e. when:

$$SQ + QT = n\lambda \quad (2.1)$$

And from the trigonometry of the setup, it can be seen that:

$$SQ = QT = d_{abc} \sin \theta \quad (2.2)$$

Therefore, the condition for constructive interference is when:

$$n\lambda = 2d_{abc} \sin \theta \quad (2.3)$$

This is known as Bragg's law and through this relationship, compounds in an unknown sample can be identified through the use of libraries of diffraction data. X-rays are used as opposed to any other waveform as their wavelength is typically of the same order of magnitude as the spacing between the planes of the crystal and therefore diffraction will be emphasised.

Overall, analysis of the XRD diffraction pattern can achieve quantification of each present phase, the crystallinity of a sample, the crystal structures and their lattice parameters, crystallite size and strain. It is quick and non-destructive but, by its nature, can only study crystal structures. Furthermore, due the limited penetration depth of the X-rays, XRD is only able to study the surface of materials.

XRD is particularly suited to NC measurement as the Scherrer equation can be applied to the obtained spectra [86]. The Scherrer equation relates nanocrystallite size to the broadening of

a peak in a diffraction pattern. It must be remembered however that as other factors can contribute to the width of a diffraction peak, this equation only provides a lower bound for crystallite size [87].

2.2.2 Transmission Electron Microscopy

Transmission electron microscopy (TEM) is used for imaging thin specimens of material and under typical operation, it performs under the same basic principles as an optical microscope. However, through use of high energy electrons as opposed to photons, TEM can achieve a much higher resolution (due to the decreased De Broglie wavelength of electrons at higher energies) and this therefore makes the technique well suited to nano-characterisation. The lighter areas of the image produced will represent the places where a greater number of electrons were able to pass through the sample and darker areas will represent the denser areas of the object. The image can therefore provide information on the structure, texture, shape and size of the sample. Figure 2.2 illustrates how a TEM works. TEM has a typical maximum resolution of the order of angstroms.

Difficulties with using TEM include the fact that it is relatively time intensive and as it requires transmission of electrons through the sample, only thin samples may be used. Typical critical thickness is in the order of tens of nanometres [88]. This therefore makes TEM applicable for nanoparticle (e.g. CdSe NC or AgNW) characterisation such as determining size and shape. Due to the thickness of the bulk titanium, whole cell characterisation cannot be performed through TEM analysis. TEM is typically non-destructive but care should be taken to ensure that the high energies used aren't heating or sintering the sample [88].

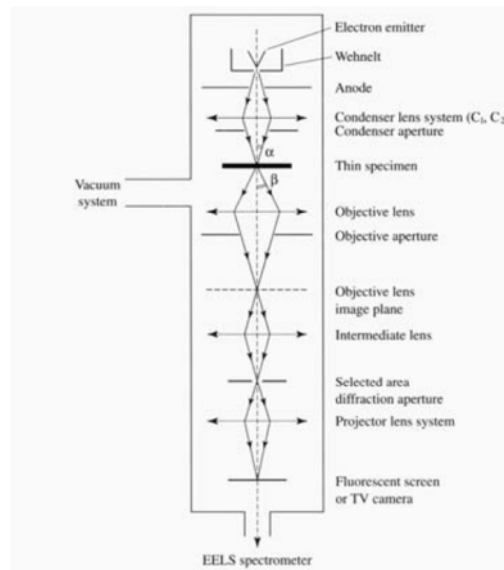


Figure 2.2: Schematic diagram of transmission electron microscopy (image taken from [89]).

2.2.3 Scanning Electron Microscopy

Scanning electron microscopy (SEM), like TEM, utilises high energy electrons to achieve an improved resolution over optical microscopy. Most commonly, secondary electrons are used for detection. These are emitted electrons that arise upon the relaxation of an atom that has been excited by the incident electron beam. Emitted secondary electrons are only detectable if originated from near the surface of a sample and due to this, SEM is utilised only for surface characterisation. Due to this fact SEM is more suited to whole-cell characterisation. However, as lower energy electrons are used, the resolution is typically an order of magnitude worse than TEM. Like TEM, SEM is non-destructive but time-intensive.

2.2.4 Energy Dispersive X-ray Spectroscopy

Energy-dispersive X-ray spectroscopy (EDX or EDS) can be performed using TEM and SEM. EDX can achieve elemental analysis by examining emitted X-rays of atoms, the wavelengths of which are unique to each element. The high energy incident electron beam can stimulate an inner electron, ejecting it from the atom and an outer electron can fill the hole that this has caused. The energy difference between the outer and inner shells can be conserved through the release of an X-ray. The energy and quantity of these X-rays can be measured by an energy-dispersive spectrometer and from this information, the elemental composition can be measured. EDX can however be affected by overlapping peaks from different elements and also inhomogeneous, rough samples may not give a fair representation due to certain X-rays not being able to escape the sample and reach the

spectrometer. Due to characterisation of atomic properties, EDX is particularly well suited to nano-characterisation and through combination with SEM/TEM can be performed on samples invisible to the human eye. EDX is relatively simple and has an advantage in that it is quantifiable but artefacts must be considered carefully [88].

2.2.5 Atomic Force Microscopy

Atomic force microscopy (AFM) operates through the use of a sharp probe attached to a cantilever, as the probe moves over the surface, forces between the sample and the tip lead to the cantilever deflecting as determined by Hooke's law. A laser beam focussed on the cantilever will detect any change in position and height of each point can be recorded as the tip progresses across a sample. The forces interacting between the tip and the surface include Van der Waals forces and electrostatic forces. AFM has a potential angstrom resolution and holds the advantage over electron microscopy in that it provides three dimensional surface profiles as opposed to a two dimensional projection, charging – the collection of incident electrons within the sample – is also not an issue for AFM. AFM however suffers from having a low scanning area size and slow scanning speeds. Care must be taken when analysing images obtained through AFM as artefacts arising from things such as probe size, vibrations and surface contamination need to be considered. Due to its ability to measure a sample over three dimensions, one of the main uses of AFM is the ability to measure the roughness of a sample at a high resolution.

2.2.6 Optical Spectroscopy

While not having the resolution necessary to visualise nanoscale materials, optical spectroscopy is still useful in semiconductor characterisation. Two main methods are discussed here, UV-Visible absorption spectroscopy and photoluminescence emission spectroscopy.

UV-Visible absorption spectroscopy (UV-Vis), as is evident in the name utilises wavelengths of light ranging from UV to visible, this range of wavelengths is particularly suited to PV research as the desirable semiconductors for PV applications should have band gaps in this region of the spectrum. To generate absorption spectra, radiation is generated by a source and passed through a filter and monochromator to emit a single desired wavelength. For each wavelength, the intensity of light is measured after it is passed through a sample and the absorption by the sample is determined. When the wavelength of incident light is of energies greater than the band gap of the semiconductor, absorption should increase significantly and through this, the wavelength that this starts to occur can be identified and the band gap of the semiconductor determined. Care must be taken when determining the

absorption spectra of a sample that particles suspended in a solvent don't settle during measurement. This can be achieved through applying constant agitation or stirring. Absorption spectroscopy is a quick, non-destructive method that should give clear indication of a band gap of a material. It should be remembered however that scattering is more common in nanomaterials and it is often difficult to tell the difference between scattering and absorbance.

Photoluminescence emission spectroscopy (PLS) is another contactless, non-destructive method that utilises photons to probe the electronic structure of materials. A suspension of a substance is illuminated with light of a high frequency, a detector then sweeps wavelengths to identify which wavelengths the sample is emitting at as a result of the illumination. For semiconducting materials, most of the emission will be due to recombination of an excited electron with the hole created due to its excitation. Practically, this technique is very similar to UV-Vis and therefore can be used to corroborate the results found with that technique. It also has the same benefits and drawbacks.

2.2.7 Four-Point Probe

The 4-point probe is used to measure sheet resistances of thin films such as the Ag nanomesh. This consists of four spring probes equally spaced in a row. A current is applied between the outer two probes, while the voltage between the inner two probes is measured. The sheet resistance of a thin film (where the thickness is much less than the probe spacing) is given by dividing the voltage measured by the current applied and then multiplying by a geometric correction factor. This correction factor takes in to account the finite size of the sample. Care must be taken when applying the probes to the sample, contact is necessary but excessive force is likely to damage the mesh. If a mesh is relatively sparse, it should be ensured that the probes are indeed in contact with an AgNW. When measuring a non-uniform nanomesh, multiple measurements should be taken and averaged.

2.3 Fabrication of the Primitive Device

To fabricate the primitive device, commercially pure titanium of a thickness of 3 mm is purchased and cut in to 10 mm by 10 mm chips. To create a primitive cell from the chip for testing before nanocrystal decoration, it must undergo the following preparation steps:

1. Polishing
2. Oxidation
3. AgNW deposition

Each step will be discussed in turn before illustrating the typical output of a primitive device. NC decoration so that the device becomes activated and is responsive when illuminated with visible light will then be examined.

2.3.1 Polishing

To ensure even and homogenous oxidation of the titanium that will be used in the solar cell, it must be polished to as smooth a finish as possible. Polishing methods include mechanical polishing, chemical polishing and electropolishing. However, it has been found that due to certain properties of titanium (existence of a reaction layer, high chemical activity, and low thermal conductivity), electropolishing is the only method that achieves a satisfactory finishing [90].

As well as achieving a bright and clean appearance, electropolishing can provide a microscopically smooth surface. Other benefits of electropolishing include deburring, size control and the fact that the finished product should be free of residual contamination. The surface will also retain the true grain structure and properties of the bulk metal [91]. It has been found that through effective electropolishing, the average surface roughness could be reduced to values of around $0.03 \mu\text{m}$ with SEM imaging show an even and completely featureless surface [90].

Electropolishing typically works through immersing the metallic sample in an electrolyte solution that has to be temperature controlled through means of a water bath or other apparatus. The sample serves as the anode and is connected to the positive terminal of a DC power supply. The cathode, which is attached to the negative terminal, is also immersed in the electrolyte. When the DC supply is turned on, a current will pass from the anode and the surface of the metal is oxidized and dissolved in the electrolyte. The material will then travel to the cathode where a reduction reaction occurs. This process is illustrated in Figure 2.3. After polishing, the samples should be washed in alcohol and then air dried [90].

Naturally, for the surface to smoothen, the more protruding parts must dissolve faster than the recesses. This process is defined as deburring and occurs due to an increased current density on the corners (burrs). This increased current density occurs as during electropolishing, a film covers the surface of the metal sample. This film is thickest over depressions and thinnest over projections and therefore the resistance caused by the film is smallest at the projections resulting in the greatest rate of metallic dissolution.

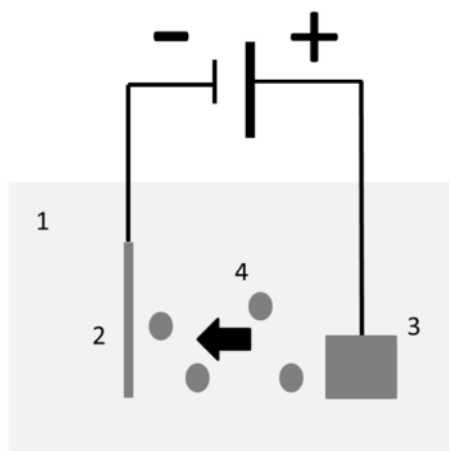


Figure 2.3: Mechanism of electropolishing 1) electrolyte 2) cathode 3) sample (anode) 4) deburred particles moving from sample to cathode.

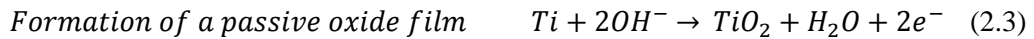
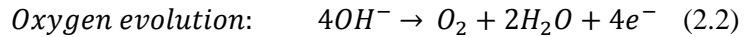
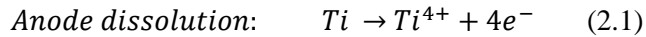
Electropolishing will only provide the required results if the correct electrolyte is selected and the correct electrolytic conditions are used [91]. Other important factors include temperature (some solutions must be cooled to temperatures lower than 273 K to obtain well-finished surfaces [92]), the specific gravity of the electrolyte, acidic concentration and metals content. For example, if the electrolyte contains excessive water then an oxide film can form on the sample [93, 94] or if the electrolyte flow rate is too high then anisotropic etching will take place, creating a rough surface tracing the profile of crystallites within the bulk of the sample [95]. Other common problems encountered during electropolishing include inconsistency over large or complex surfaces, the formation of undesired compounds on the sample surface and the influence of sample crystal morphology and composition influencing performance [96].

The electrolytes are most often concentrated acid solutions with a high viscosity. Example acids include perchloric, hydrofluoric and sulphuric acid. However, there have recently been a number of reports describing effective electropolishing using less hazardous alcoholic electrolytes at accessible temperatures and anode potentials. One such report is by Tajima et al. [90] who used an electrolyte containing ethanol, isopropanol, aluminium chloride and zinc chloride with temperatures kept down to 30 °C. Other methods include using an electrolyte of sulphuric acid in ethanol [94] and using a NaCl ethylene glycol electrolyte solution [97].

Electropolishing of titanium has also been achieved by Poullou et al. using potentials from 45 to 70 V at temperatures from 30 to 40 °C. It was also observed that outside this range,

films that were probably composed of titanium chloride were formed on the anode hindering further electropolishing [96]. It was also found that a small area cathode could be used to reduce self-heating through the limitation of electrolyte current.

It has been postulated that during electropolishing of titanium, three reactions are occurring at the anode [91]:



This oxide film is the layer that forms more thinly over protrusions thus promoting deburring. It typically has a thickness of a few nanometres and develops easily and rapidly on the titanium surface [98]. Further to the oxide film, a viscous layer thought to be titanium chloride also forms. If this viscous layer remains on the anode, it will cause an impedance to the electropolishing process and result in poorly finished surfaces. Generally, electrolyte agitation is therefore required to remove the bubbles and viscous layer from the surface and to refresh the passive oxide film. This agitation is most often provided through the use of stirring bars, vibration or ultrasound [90].

2.3.1.1 Results

The overall method selected for use was chosen so as to utilise a safe electrolyte and obtainable conditions. All procedures were selected so as to achieve as high a reproducibility as possible. However this still remained an issue with samples looking visibly different from each other.

First, the sample are mounted on to sample holders using a thermoplastic bonding material and then mechanically polished using grinding machines, first to a 6 micron finish before being cleaned and polished down to a 3 micron finish. Care is taken to clean the sample thoroughly between steps so as not to carry abrasives over from a coarse stage of grinding to a finer one [99]. The sample holders are then heated to enable removal of the samples. The samples are then ultrasonicated for ten minutes in acetone to remove any of the remaining thermoplastic material.

As per Poullou et al. and Tajima et al. [90, 96], the electrolyte solution is made up from a mixture of ethanol and isopropanol. Zinc chloride and aluminium chloride are then dissolved carefully in to the mixture. To ensure a sufficient amount of polishing time without reaching the higher currents that occur when the electrolyte temperatures are high, the electrolyte is cooled through placement in a water bath and the water bath cooled using an immersion

cooler for 20 minutes. A power supply is connected and set at a constant voltage of 50 V and maximum current of 1 A. The power supply is then turned on for 20 minutes and the sample electropolished. After 20 minutes, the power supply is turned off, any remaining ice in the water bath is removed and the apparatus is left alone for 5 minutes to equilibrate the water bath temperature back to room temperature before the next sample is prepared for electropolishing.

Upon removal from the electrolyte, each sample is washed in water to dissolve any salts, acetone is then used to remove organic particles and grease deposited by manual handling and finally, the sample is washed with propanol to remove any residues left by acetone treatment. Cleaning is performed through ultrasonication for 10 minutes for each solvent. Only one sample is cleaned at a time to prevent samples from scratching each other.

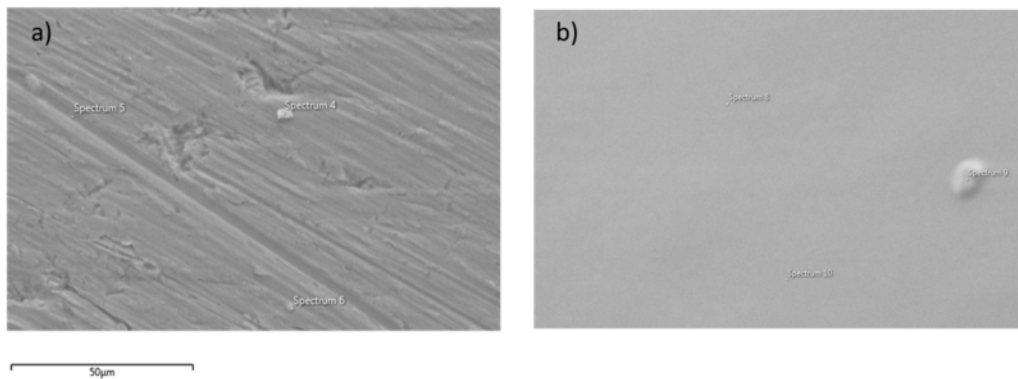


Figure 2.4: SEM images of a titanium chip before (a) and after electropolishing (b).

Figure 2.4 shows visual evidence of the effect of electropolishing. The left image (before electropolishing) shows grooves and dents within the sample. The sample is also displaying a directionality which if left may influence the positioning of any deposited nanowires. After electropolishing (right), the sample is much smoother with just one blemish and no visible directionality.

Surface roughness is most commonly measured using the roughness parameter R_a . This measures the arithmetic average of the absolute values of deviation from the mean height. R_a can be measured using AFM. When performing measurements, care should be taken to ensure that a large enough area is measured so that artefacts don't influence the value.

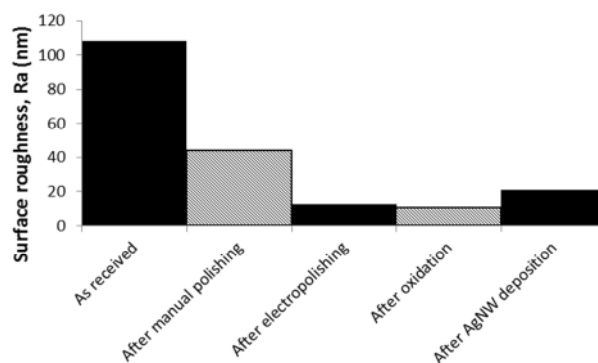


Figure 2.5: Surface roughness measurements of a chip at each stage of processing.

Figure 2.5 shows how the R_a value of a sample changes through each stage in processing. It can be seen that a combination of manual polishing and electropolishing decreases the surface roughness by a factor of 8 and that the roughness remains pretty constant after oxidation. AgNW deposition on to the electropolished surface increases the roughness as would be expected. If the electropolishing step is omitted and only the manual polishing performed, the surface roughness of the oxidised surface is found to be 4 times greater than if electropolishing was performed. This holds significance as smoother TiO_2 surfaces have been found to have a dramatically increased photosensitivity, especially in the short wavelength range [100].

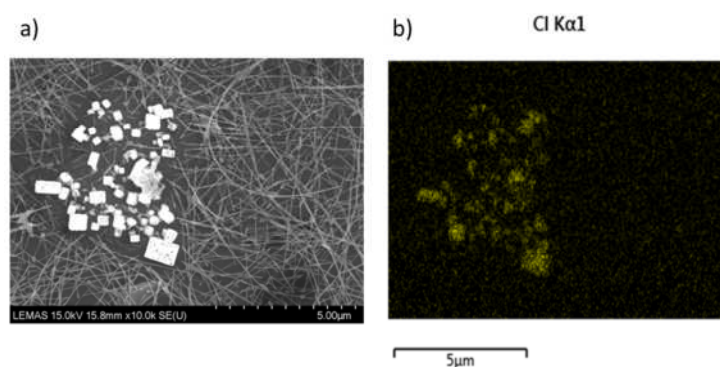


Figure 2.6: SEM (a) and EDX (b) image of an electropolished sample exhibiting salt artefacts.

Upon SEM imaging of electropolished devices it was found that some samples exhibited large crystals (Figure 2.6). EDX spectroscopy of these crystal-containing areas showed large counts of chlorine atoms. This therefore suggests that traces of zinc chloride and aluminium chloride were not being effectively removed from the samples. It was found that initial washing of the chip with a polar solvent such as DI water before acetone and propanol washing effectively removed any such salt depositions.

2.3.2 Oxidation

The process of thermal oxidation of titanium to produce TiO_2 is one that has been extensively studied [81, 101, 102], it is relatively simple [103] and is a well understood area. However, there are variations in the reported thickness of the oxide layer produced with seemingly no correlation with temperature and time [81, 100, 104-108]. Hossein-Babaei et al. found that thermal oxidation of a titanium chip at $700\text{ }^\circ\text{C}$ in air resulted in a 1 micron thick layer of rutile on the top surface of the chip. This was deemed to be the optimum temperature with oxide layers grown below $600\text{ }^\circ\text{C}$ resulting in a mixture of rutile and anatase and oxide layers grown at temperatures above $800\text{ }^\circ\text{C}$ being able to be easily laminated from the titanium substrate. A temperature of $700\text{ }^\circ\text{C}$ left a structurally rugged and mechanically stable layer [81]. It has also been found that high temperatures ($> 900\text{ }^\circ\text{C}$) create the formation of a polycrystalline TiO_2 layer with random orientation [102]. Other thermal oxidation studies included $700\text{ }^\circ\text{C}$ for 1 hour leaving a polycrystalline rutile of 5.6 micron thickness [101], $650\text{ }^\circ\text{C}$ for 14 hours resulting in a 1 micron thick layer of rutile, a micron layer of rutile being formed at $600\text{ }^\circ\text{C}$ for 30 minutes and 35 micron thick layer of rutile being formed at $850\text{ }^\circ\text{C}$ for 4 hours [106].

A mix of rutile and anatase can form under thermal oxidation at temperatures up to $500\text{ }^\circ\text{C}$ [109]. However, at temperatures greater than this, thermal oxidation is found to result in the rutile crystal structure which is attributed to an acceleration of the phase transformation of anatase to rutile due to the formation of a large quantity of oxygen vacancies in the oxide film [103].

As well as thermal oxidation, another common route to achieve a titanium dioxide film is chemical anodisation [110, 111]. Chemical anodisation is the process of increasing the natural oxide layer through the application of a direct current through an electrolytic solution and using the sample as the anode. The current releases oxygen at the anode surface thus allowing the reaction of oxygen with metal ions that have migrated through the oxide layer to further form titanium oxide [112].

Analogous to the temperature in thermal oxidation, the thickness of the oxide layer is a function of the applied voltage [113] with an empirically derived rate of growth found to be 2 nm/V [114]. Despite this opportunity for fine thickness control, chemical anodisation has the drawbacks of added experimental complexity and the potential formation of impurities within the TiO_2 .

As thermal oxidation has been shown to result crack free films [109], doesn't rely on the use of harsh chemicals and is relatively simple, it has been selected as the best method for creating the Ti/TiO_2 bulk of the proposed device.

2.3.2.1 Results

To ensure a continuously rutile structure and strong adherence to the Ti substrate under favourable lab conditions, a temperature of 700 °C for 30 minutes was selected for oxidation of the titanium substrates. Immediately after electropolishing, samples were oxidised to prevent any impact from native oxide layer formation. The oven was heated to temperature with the samples in the oven, upon reaching 700 °C, 30 minutes were timed, after which the oven was switched off and the door opened to allow the samples to cool. Upon oxidation, the results are visible through observation of the light interference phenomena [113] with the colour of the layers ranging from gold to purple.

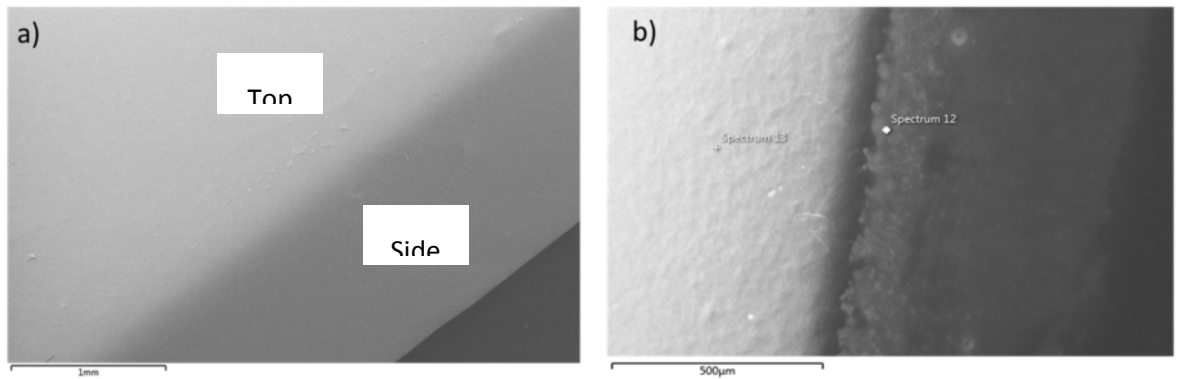


Figure 2.7: SEM view of titanium chip before (a) and after (b) thermal oxidation.

Figure 2.7 shows the change in appearance of the sample when viewed under an SEM, Figure 2.8 shows EDX spectroscopy of both the top and side of a sample showing that the continuous film on the top of the chip is indeed TiO_2 and that at lower depths, the chemical composition is approaching pure titanium.

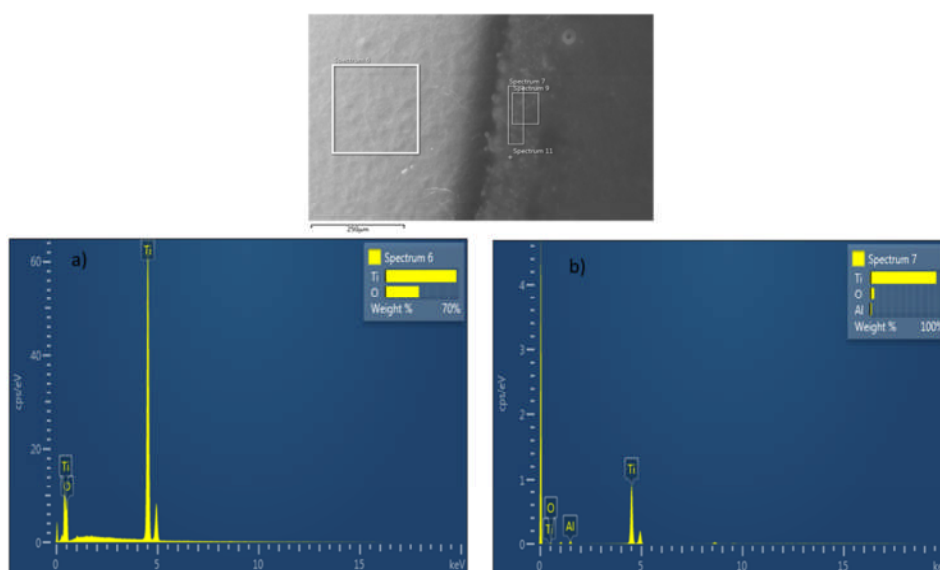


Figure 2.8: EDX spectroscopy of the top (a) and side (b) of a thermally oxidised chip.

Due to the multiple stoichiometries of titanium oxide available, measuring the thickness of the oxide layer formed is difficult. It has been shown that, especially above 450 °C, TiO₂ forms a solid solution with the Ti substrate resulting in a diffuse boundary [115] and this is exemplified in Figure 2.7. It can however be estimated that the thickness of oxide layer ranges from 50 to 250 microns which is significantly thicker than the value quoted in literature [81]. Some of the disparity in these results may be attributed to a variation of measurement technique used and the subjective determination of the boundary of the TiO₂ stoichiometry.

On top of SEM and EDX, XRD analysis was also performed on the samples after thermal oxidation. A typical XRD spectrum is illustrated in Figure 2.9 and compared to reference data for rutile and titanium. Owing to the thinness of the oxide layer formed, the largest peaks directly correlate to the titanium base which is still at a penetrable depth for the X-rays used. However, there are peaks apparent at 54.5 ° and 27.5 ° that in no way correlate with titanium and instead directly correlate with the rutile reference therefore confirming its presence. The XRD spectra produced also closely correlate with those observed in literature [102, 109] for thermal oxidation performed under similar conditions.

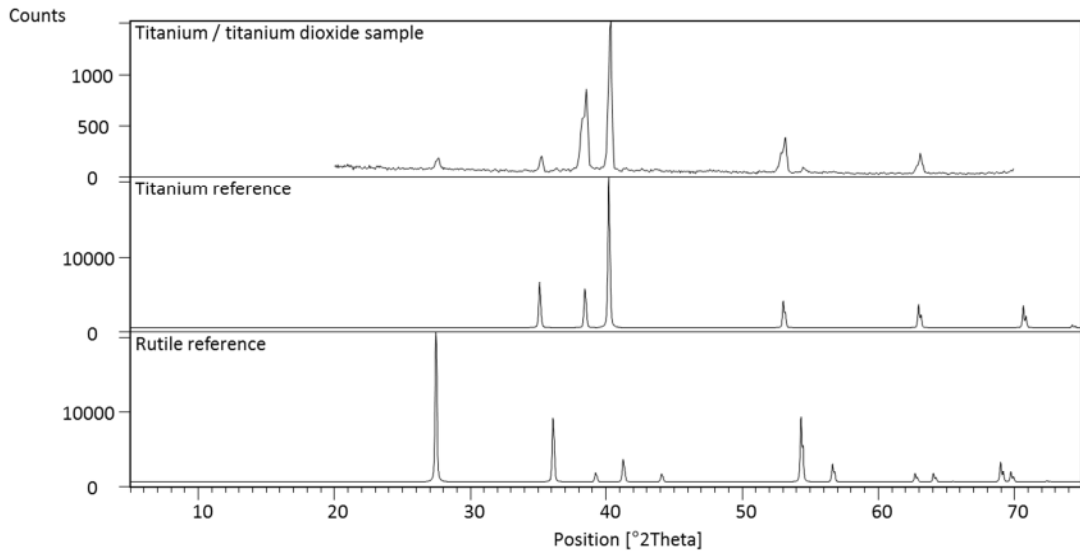


Figure 2.9: A typical XRD spectra for a sample post-thermal oxidation.

Further evidence of the thermal formation of an oxide layer is evident in the twin peak that becomes apparent in the titanium response at 53° as illustrated in Figure 2.10. This isn't observed in untreated titanium and is brought about due to stress induced from the oxidation process. This stress alters the particle spacing and therefore alters the coherency of the X-ray's observed.

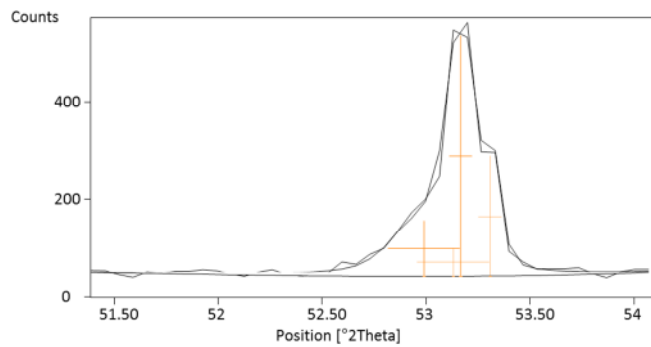


Figure 2.10: Evidence of stress induced on titanium as a result of thermal oxidation.

Upon obtaining XRD spectra, a Scherrer calculation can be performed [86]. For the spectra displayed in Figure 2.9, a crystallite size of 24 nm is determined. This agrees well for values found in literature for similar oxidising conditions [81, 116].

2.3.3 Nanowire Deposition

As a TCE, ITO is expensive, and requires high temperature processing [117]. Indium also suffers from a supply risk [54, 118]. In fact, the price of Indium has soared since 2011 and is expected to also increase sharply in the future [119]. Furthermore, it is a very brittle material and fails catastrophically after around 150 bend cycles [119].

Nanostructured transparent conducting electrodes are flexible [119] and can be spray-cast therefore allowing scaling up to large area deposition [120]. Carbon nanotubes have been extensively studied [121-123]. Other materials suitable include polymers [124] and graphene [125]. However, these have still failed to reach the high values of the Haacke figure of merit (FOM) [126] that can be obtained in ITO. To achieve the standards of ITO, where it is straightforward to obtain sheet resistances in the order of $10 \Omega/\square$ while having a transmittance $> 90 \%$ [127], the FOM must reach around 3.49×10^{-2} . However, the best results for graphene and carbon nanotubes are of the order of 2.82×10^{-5} [128] and 1.97×10^{-3} [129] respectively. For carbon nanotube networks, these low values are attributed to high contact resistance between the tubes and some of the tubes possessing semiconducting properties therefore contributing to optical absorption but not to electrical conductivity [117].

Recently silver nanowires have come under much interest [117, 119, 127] with values of 3.49×10^{-2} for the FOM already being obtained [127]. AgNWs can be formed under low-temperature processing and form a nanomesh with low sheet resistances of around $10 \Omega/\square$ and light transmission over the visible spectrum of around 90% [54, 59-61]. Furthermore, AgNWs hold interesting plasmonic properties which can be utilised to increase light scattering within the cell therefore increasing the light path length and increasing the chance of a photon being absorbed [49, 50]. Indeed, it has been reported that due to this increased light path length, solar cells incorporating AgNWs as the TCE as opposed to an ITO standard can increase the efficiency of a cell by 10% [130]. Other studies have found similar improvements of efficiency attributed to plasmon resonance [131, 132]. AgNW nanomeshes are also found to have a better FOM than thin (25 – 50 nm) silver films. This is intuitive as one would expect the optical transmittance to be greatly reduced for thin films.

These Ag nanomeshes are also extremely electromechanically robust with no change in properties when flexed over 1000 cycles [127] and while the proposed device is not flexible, architectural adjustments could be made that would enable the device mechanism to operate over a flexible substrate. For the proposed device, the nanomesh will form the Schottky barrier with the TiO_2 as silver has a suitable work function to create a desirable Schottky barrier height (SBH). Negatives associated with use of AgNWs as a TCE include that costs are still currently a factor, this is expected to come down as demand increases to industrial

levels [127] and a low adhesion of the network on to the substrate [133], this may be able to be improved through chemical treatment [127].

When deposited correctly, the films are extremely uniform with transmittance varying spatially by less than 2 % [127]. It has been reported by Langley et al. that the properties of the Ag nanomesh are independent of the deposition method [133]. Spray-casting has been found to be a robust approach to produce uniform, large-size films [134, 135]. There are however issues with creating a high density network with this method [120].

Thermal annealing has been found to be critical, reducing the sheet resistance by over a factor of 100 [133]. This is attributed primarily to the local sintering of nanowire junctions which decreases the junction resistance. However, the temperatures used in this treatment may also remove any organic precursors or ligands used in AgNW synthesis. Naturally, there is an optimum temperature and if this is surpassed, the nanowires will start to change shape eventually resulting in spheroidization therefore losing the physical continuity of the nanomesh and therefore removing its electrical conductivity. This thermal annealing has been found to have no effect on the optical properties of the nanomesh [133].

The optimum loading to achieve a peak in the electro-optical properties of the Ag nanomesh was found by Langley et al. to be 100 mg/m^2 . This was found to give a total transmission of 82.9 % and a sheet resistance of $9.5 \Omega/\square$ [133]. De et al. with nanowires of a different aspect ratio, found this value to be 47 mg/m^2 [127].

2.3.3.1 Results

Figure 2.11 shows electron microscopy images of typical nanomeshes formed. It is apparent that the meshes are continuous and randomly orientated. The TEM image shows that the wires are smooth and of the correct diameter. The SEM image was used to calculate the percentage coverage of the nanomesh which was typically found to be around 35 %.

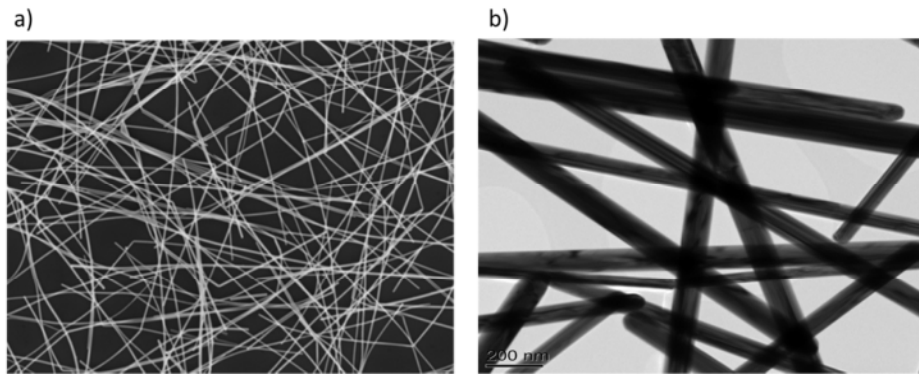


Figure 2.11: SEM (a) and TEM (b) images of typical Ag nanomeshes. Credit for microscopy: Priten Khagram.

Achievement of AgNW deposition is further exemplified in Figure 2.12 which shows a typical AFM scan of the surface of device before and after NW deposition. The peak illustrated in the bottom of the figure was found to be just over 100 nm which when accounting for tip radius, agrees well with the manufacturer stated diameter of 90 nm. These AFM images also prove that there is a level of adhesion to the TiO_2 surface with the nanowires able to withstand any pressure exerted upon them by the AFM tip. However as acknowledged above, the adhesion is still only weak with the whole mesh being able to be wiped clean very easily by force applied by the finger. As discussed previously and displayed in Figure 2.5, the surface roughness increases upon AgNW deposition, as expected.

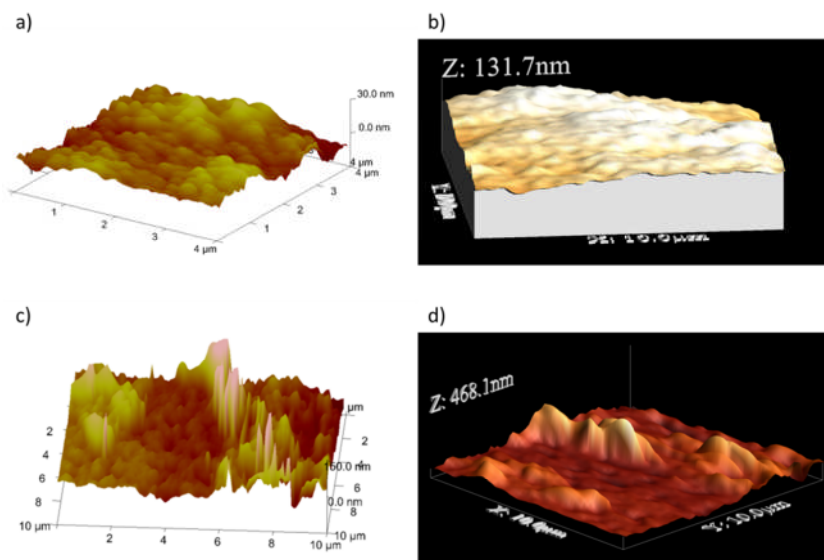


Figure 2.12: AFM map of a sample surface before (a and b) and after (c and d) AgNW deposition.

Transmittance values can't be obtained for the Ag nanomesh once deposited on to the TiO₂ surface. However, sheet resistance values for the nanomesh when deposited on TiO₂ and when deposited on a glass substrate are extremely similar and it can therefore be assumed that the optical transparency will be similar. When measured on a glass substrate, transparency values in the order of 90% are obtained which when combined with sheet resistances in the order of 20 Ω/\square produce a FOM of 1.74×10^{-2} which is the same order of magnitude as the FOM of ITO.

Contrary to literature discussed above, different deposition techniques were found to produce different results. It is of the believe of the author that Langley et al. possibly only compared continuous meshes as opposed to the effectiveness of each deposition technique in creating a continuous mesh. Deposition techniques include: drop-casting, spin-casting, doctor blading, dip coating, layer by layer and spray-casting. In this work, three different deposition techniques were studied: drop-casting, spray-casting and spin-casting.

Drop-casting involves the deposition of very small volumes of suspensions on to a surface with a pipette. The solvent is left to evaporate leaving only the desired material on the substrate. Drop-casting is a very simple technique with very low waste. It does however have its limitations when scaling up to larger surface areas. Uniformity is also an issue with ring like structures caused by the solvent droplet often being visible. This can be managed through the selection of an appropriate solvent that evaporates within a suitable time. Spin-casting involves dropping the suspension on to a spinning substrate, this is thought to increase uniformity over drop-casting and the thickness of the deposited film can be controlled through varying parameters such as angular velocity and solution viscosity [136]. This is however a relatively wasteful technique. Spray-casting involves the deposition of suspension through use of a spray gun, typically used in painting applications. Through this, the film morphology can be controlled by the air pressure within the gun, the distance between nozzle and substrate, and the gun-tip geometry. Spray-casting is suitable for large area coverage and can be independent to the substrate topology.

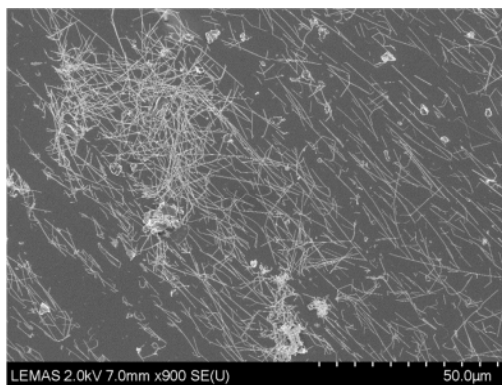


Figure 2.13: SEM image of a nanomesh that has been deposited through a spin-casting technique. Credit for microscopy: Niamh Ryall and Norah Algarou.

Figure 2.13 illustrates a typical SEM image of a spin-cast sample. Directionality can be seen in the image. This combined with areas containing no nanowires suggests that this will not be a completely electrically continuous surface. Furthermore, it can be seen that many of the wires are shorter than the stated length of 30 microns suggesting that this deposition technique damages the wires. Drop-casting and spray-casting produced indistinguishable results under micron magnification, with nanomeshes being produced as illustrated in Figure 2.11. However, on a millimetre scale, spray deposition is more uniform. It was found however that the spray gun utilised for the spray-casting method was prone to blocking. Spray-casting was also a more wasteful process with many wires being lost. It was for these reasons that drop-casting was selected as the AgNW deposition method.

In a standard deposition, a total of 20 μL of 2.5 mg/ml AgNW dispersion in ethanol was deposited in three drops. The samples were then heated to 160 $^{\circ}\text{C}$ for 20 minutes. Similarly to the oxidation process, the 20 minutes was timed from when the oven reached the correct temperature and the oven door was opened upon completion of the process. The samples were then left to cool before having each edge wiped with an acetone soaked cloth to form a border that prevents any short circuits with the base titanium.

2.4 The Primitive Cell

The combination of the procedures discussed forms the primitive cell. The Ti/TiO₂/AgNW device is now able to be utilised to produce electricity under illumination by UV light. To perform electrical measurements on the device, the titanium base is attached to a printed circuit board (PCB) with conductive silver paint and this forms the bottom contact. The top contact is made by attaching a thin wire strand to the Ag nanomesh with conductive paint and soldering the other end of the wire strand to another section of the PCB. Wires can then be attached to both the top and bottom contacts, the PCB attached by screws to an optical

breadboard and the IV characteristics and wavelength-dependent photoresponse measured. An example of the PCB design can be seen in Figure 2.14.

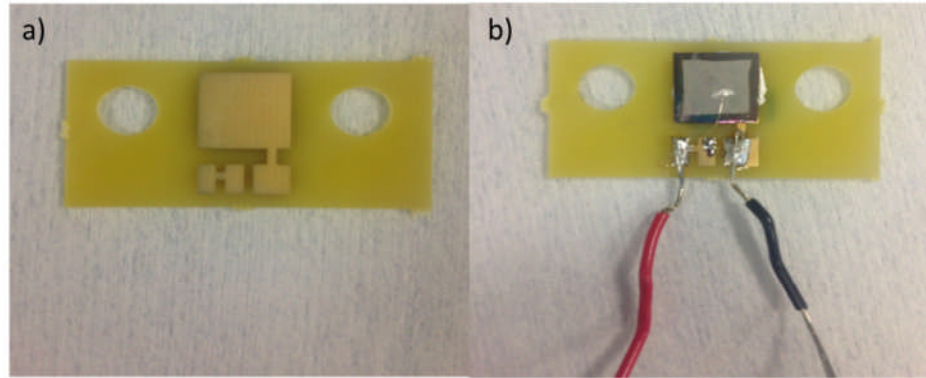


Figure 2.14: Photographs of the PCB used for device characterisation (a) and a primitive cell attached to a PCB ready for characterisation (b).

2.4.1 Current-Voltage Characterisation

Due to the Schottky barrier formed, under an applied voltage, the current that passes through the cell follows the diode equation (2.4) [137]:

$$I = I_0 \left[e^{\frac{q(V-IR_S)}{nkT}} - 1 \right] + \frac{V-IR_S}{R_L} \quad (2.4)$$

Where R_S is the series resistance, R_L the leakage resistance, n the ideality factor and I_0 is the saturation current which is derived through equation (2.5):

$$I_0 = AA^*T^2 e^{-\frac{\phi q}{kT}} \quad (2.5)$$

Where A is the contact area, A^* the Richardson constant, ϕ the barrier height and all other variables have their usual meanings.

Recording the current as a function of voltage to generate IV curves is therefore a quick non-destructive method to assess whether a Schottky barrier has successfully formed between the TiO_2 and Ag nanomesh. When generating IV curves, care should be taken so as not to apply such a high voltage that the cell is damaged. Figure 2.15 shows typical IV curves obtained for fabricated primitive cells. Under forward bias the curve has exponential form confirming that a Schottky junction has been created at the Ag/ TiO_2 interface and an ohmic contact at the TiO_2/Ti interface. An IV curve with diodic features is a good indicator of a successful primitive device.

Many of the cells fabricated exhibited a similar IV curve as the one depicted by the dashed line, exhibiting a large reverse bias current. This can be attributed as a tunnelling feature [138]. Tunnelling will affect both the reverse and forward bias characteristics. When in reverse bias, a size-dependent exponential reverse bias current is produced, as discussed by Smit et al. [138]. Forward bias tunnelling results in the undesired effects of a decreased leakage resistance.

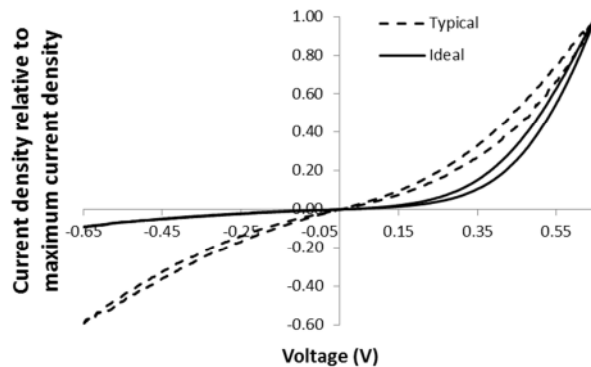


Figure 2.15: Typical IV curves for fabricated primitive devices. Solid line shows curve that closely follows the diode equation. Dashed line shows a more typical curve with larger reverse bias leakage.

The magnitude of the current density produced can be used to ascertain the effectiveness of the continuity of the nanomesh. When no nanomesh is present, the only SB formed is between the top contact and the TiO_2 , this produces a maximum current density less than $1 \mu\text{A}/\text{cm}^2$. When an incomplete mesh is present such as that illustrated in Figure 2.13, it is only the SB formed by the parts of the mesh that are in physical contact with the top contact that can be measured, this produces a maximum current density in the order of tens of $\mu\text{A}/\text{cm}^2$. When the whole mesh is entirely continuous, such as that illustrated in Figure 2.11, all of the silver that is in contact with TiO_2 contributes to the detectable SB and a maximum current density in the order of hundreds of $\mu\text{A}/\text{cm}^2$, is produced. A Short circuit will create an ohmic contact producing a linear curve with the maximum current dictated only by whatever resistor is applied to protect the circuit, in this case, 100Ω .

The electrical characteristics of each cell produced were extremely variable and impossible to control experimentally. One possible reason for the observed invariability is defects in the TiO_2 layer. It was found by Marri and Ossicini that these defects can drastically influence the Schottky barrier height therefore changing the conditions for the propagating electrons. These defect levels can reduce the Schottky barrier height to less than 20 % of the theoretical value [139].

IV curves can also give information on the leakage and series resistance, variables that are illustrated in the equivalent circuit as shown in Figure 2.16. The leakage resistance incorporates any alternative routes or mechanisms for electrons other than the desired external circuit. A low leakage resistance indicates an easy path for recombination and therefore a high value is desired. The leakage resistance can be estimated by measuring the gradient of the IV curve at low voltages. The series resistance is caused through contact resistance between metal and semiconductor and also the low conductivity of the bulk semiconductor. A low series resistance is desirable. The series resistance can be measured through measuring the gradient of the IV curve at high voltages. The leakage resistance and series resistance for a typical cell is calculated to be $1.05 \times 10^6 \Omega$ and $4.19 \times 10^4 \Omega$ respectively.

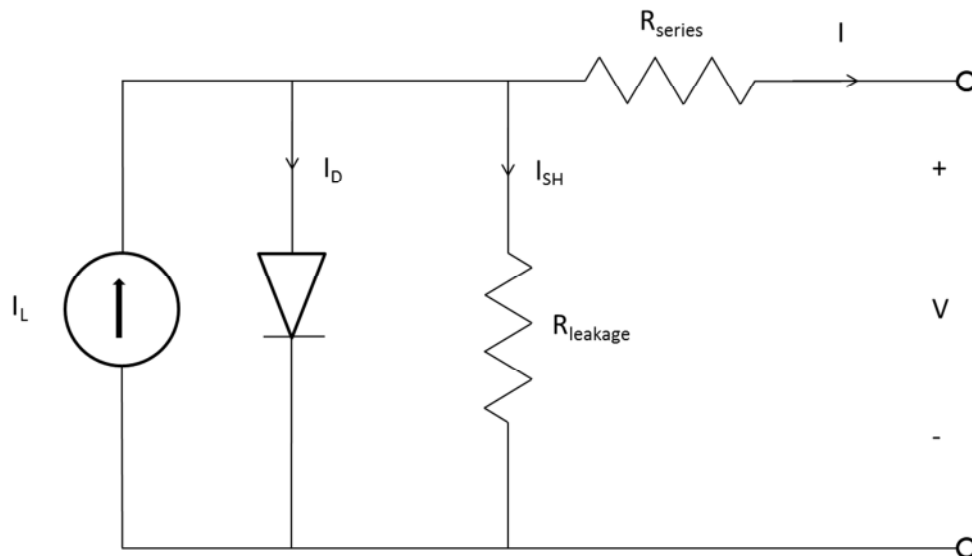


Figure 2.16: Equivalent circuit of a solar cell.

A curve fitting algorithm can be performed using the equivalent circuit diode equation (2.4), incorporating a series and leakage resistance. The algorithm can be used to derive the reverse saturation current and therefore Schottky barrier height of the fabricated devices. The calculated typical SBH of 0.94 eV lies in between theoretical calculations (0.84 eV) [140] and experimental values from literature (1 eV - 1.8 eV) [81, 116].

2.4.2 Photoresponse

As a functioning cell under UV light, the primitive device produces both a current and a voltage that are functions of wavelength. To measure the output of a cell, a programmable light source is used to sweep over a range of wavelengths and the current/voltage is

measured at each wavelength. The full range of the light source used was 800 – 260 nm and every sweep was scanned from higher wavelengths (lower energies) to lower wavelengths (higher energies). This removes any chance of a false reading at any wavelength due to the persistent photoresponse caused by illumination under UV light.

When measuring the photocurrent of a cell, it is useful to determine the quantum efficiency of a device. The external quantum efficiency is the ratio of electrons produced to the number of photons incident on the device. The internal quantum efficiency is the ratio of electrons produced to the number of photons absorbed by the device. As some photons will be reflected or scattered by the semiconducting material, the internal quantum efficiency will always be greater than the external. To determine either, the number of photons incident from the programmable light source must be determined for each wavelength.

A silicon photodiode of known optical responsivity is used to calibrate the device and determine the power output of the light source as a function of wavelength. This was achieved through using a series of tabulated values for the responsivity of the photodiode. These values however did not span the whole range of wavelengths covered by the light source and were also not of a sufficient resolution so as to be combined with the photoresponse data. The data for the power output of the light source was therefore extrapolated to include lower wavelengths and then interpolated from a 10 nm to 2 nm resolution. This process is shown in Figure 2.17.

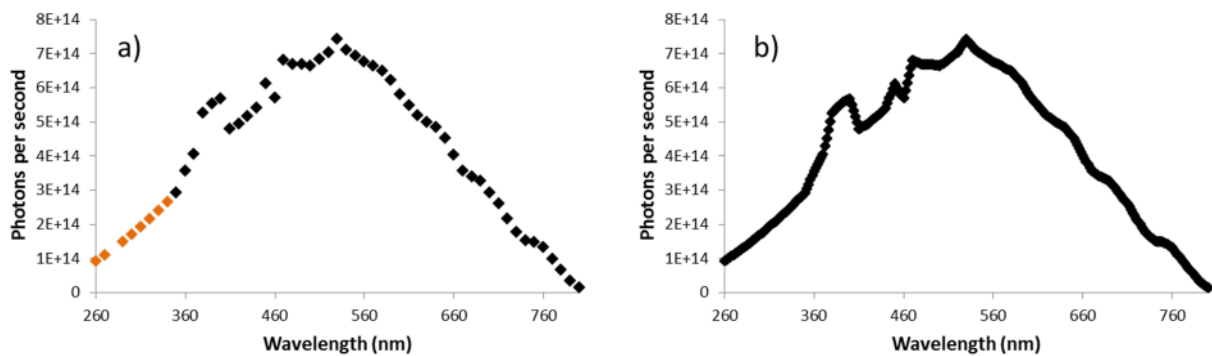


Figure 2.17: Process of refining values for the wavelength dependent power output of the light source. Extrapolation is shown in part a) where orange points have been added to include lower wavelengths. Interpolation is shown in part b where resolution has increased from 10 nm to 2 nm.

The values given in Figure 2.17 are for photons that are incident on the silicon photodiode. These therefore need to be scaled instead to the number of photons that are incident on the cell by dividing by the area of the diode and multiplying by the area of the cell. This poses

the question of what constitutes the cell area. Multiple values can be defined as the cell area. The first of which is the grey area illustrated in Figure 2.14, this is an area of 0.7 cm by 0.7 cm which equates to 0.49 cm^2 and is the area that AgNWs are applied to. However, the active area of the solar cell is only where a SB is formed which is where the AgNWs are in contact with the TiO_2 bulk. As illustrated in Figure 2.11 and discussed previously, the nanomesh covers on average 35 % of the TiO_2 surface. This area is defined as the silver area (SA) and a more appropriate EQE can be used that considers photons incident on the area covered by the nanomesh only. The EQE is adjusted to take this in to account and is defined as the SA-EQE.

Figure 2.18 shows typical EQE and photovoltage plots of a primitive cell. It can be seen from both plots that the device is active only in the UV region and that it starts to become active at around 390 nm which correlates to the band gap of TiO_2 . Also visible on both plots but more apparent on the photovoltage plot is a secondary peak at around 370 nm. This peak can be attributed the previously discussed plasmonic resonance properties of the wires. This wavelength is where silver nanowires observe a maximum in their light scattering properties and correlates well with the findings of Veres et al. [141].

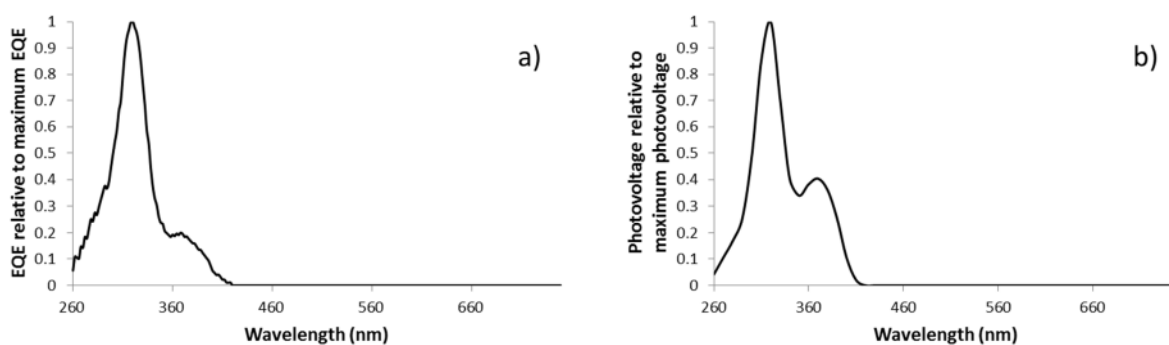


Figure 2.18: Typical EQE (a) and photovoltage (b) curves for a fabricated primitive device.

Theoretically, upon the wavelength of light reaching energies equal to and higher than the band gap of TiO_2 , the EQE should remain constant. However, as illustrated in Figure 2.18, this is not the case with an observed rise in output starting at the band gap of TiO_2 , reaching a peak at 330 nm and then decreasing at wavelengths lower than this. This profile is possibly due to errors associated with the extrapolation shown in Figure 2.17.

2.4.3 Electropolishing

Electropolishing is the most time intensive step of the device fabrication and despite the best efforts to select a method that reduces the chemical risk involved, aluminium chloride and

zinc chloride are still both classed as hazardous materials. It is therefore sensible to assess the necessity of the electropolishing step.

Figure 2.19 illustrates a typical IV curve from a device that hasn't been electropolished. The current densities reached are those close to what may be expected for a short circuit and although the curve exhibits some curvature, therefore indicating some diodic behaviour, it is much more linear than the typical IV curves as shown in Figure 2.15.

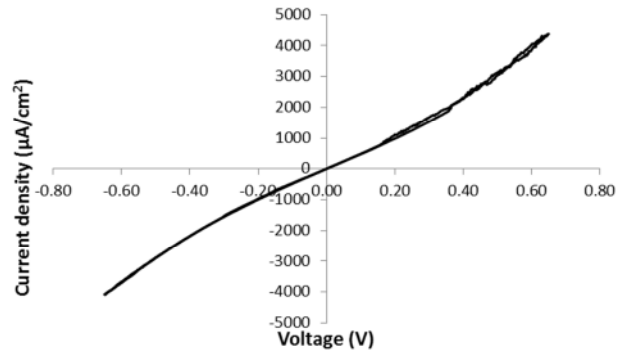


Figure 2.19: IV curve for a non-electropolished device.

Furthermore, as seen in Figure 2.20, there is no true photocurrent produced with any reading simply displaying noise. Furthermore, devices that hadn't been electropolished displayed no photovoltage under any wavelength of illumination. This is most likely due to the rough TiO_2 surface preventing any successful formation of a nanomesh upon AgNW deposition. It is therefore apparent that electropolishing is a necessary step.

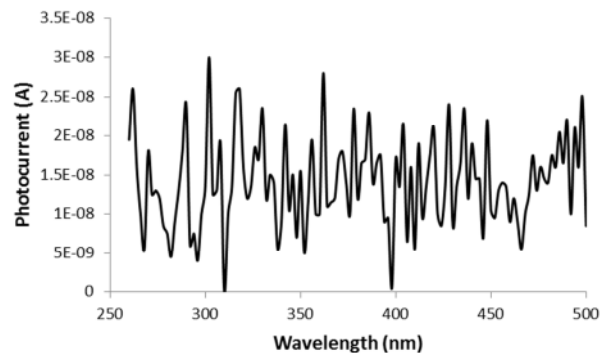


Figure 2.20: Photocurrent produced by a non-electropolished device.

The issue of decorating rough surfaces with nanomaterials has also been addressed by Klem et al. [73] where they achieved success through the utilisation of molecular linkers. This was however seen as a more complex option and thus avoided during demonstration of proof of concept.

2.5 Decoration

Upon fabrication and characterisation of a primitive cell, NC decoration can then take place. Typically, 90 μL of 0.5 mg/ml NC suspension is deposited in ten stages. NC suspensions contain ligands to act as capping agents. These ligands are often electrically insulating and removal will therefore increase cell performance. The most typical method to remove such ligands is through heating to a temperature such that the boiling point is reached so that the ligands either decompose or evaporate away. These temperatures however are typically around 500 $^{\circ}\text{C}$ and are therefore so high that the Ag nanomesh will be destroyed. Therefore no thermal treatment was performed on the deposited NCs. Ligand considerations will be discussed in more detail in Chapter 4.

2.5.1 Nanocrystal selection

Four different NC materials were selected so that they all had a reliable availability and had band gaps that fell within the visible region of the spectrum. These NCs are CdSe, CuInS₂, CdTe and CdS. The manufacturer's stated emission wavelengths of these NCs are 560 nm, 690 nm, 710 nm and 400 nm respectively. CdSe, CdTe and CdS were all sourced from Sigma Aldrich while CuInS₂ NCs were fabricated by the University of Leeds School of Physics and Astronomy [142]. While some of the NCs selected contain Cd which is known as having toxicity issues, one of the main objectives of the study is to demonstrate the functioning of a novel cell architecture and therefore the use of commonly used and greater understood materials will enable simplification in reaching the aim. Alternative NC materials can be further studied if necessary. Furthermore, utilising the material in its nanoform allows a reduction in material usage by a factor of 10 or more [143].

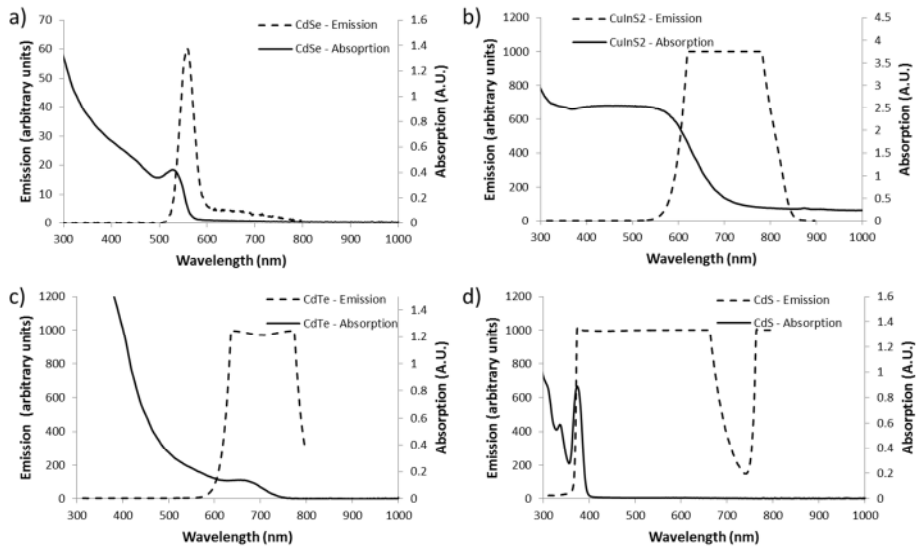


Figure 2.21: Optical characterisation of the selected NCs.

Figure 2.21 shows absorption and emission spectra for these selected NCs. It can be seen that all spectra correlate with the manufactures stated emission. CdSe exhibits very small FWHM values indicative of a very small size distribution. Conversely, CuInS₂ NCs seem to have a large size distribution as suggested by the broad absorption peaks. Many of the emission plots have a plateau where the signal has been too large for the detector. These peaks can therefore not be utilised to measure the FWHM as the maximum is not known.

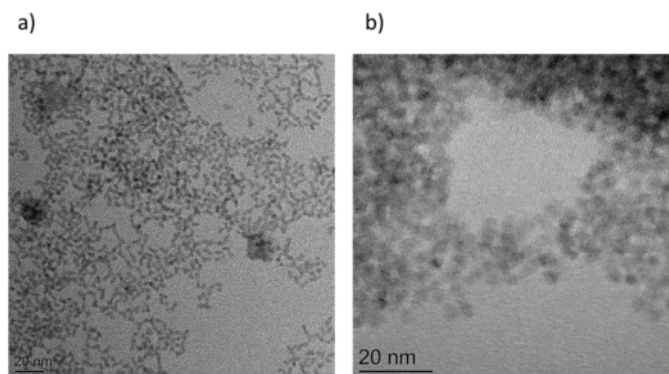


Figure 2.22: TEM images of CdSe (a) and CdTe (b). Images courtesy of Priten Khagram.

Figure 2.22 shows a typical TEM image for CdSe and CdTe. In both instances, particles are shown to be monodisperse, spherical and of a diameter of around 4 nm. After deposition on a primitive cell, the cell is now activated and is able to produce electricity upon illumination

with visible light. Figure 2.23 shows SEM images of a decorated device. The NCs can clearly be seen adsorbed on the Ag nanomesh.

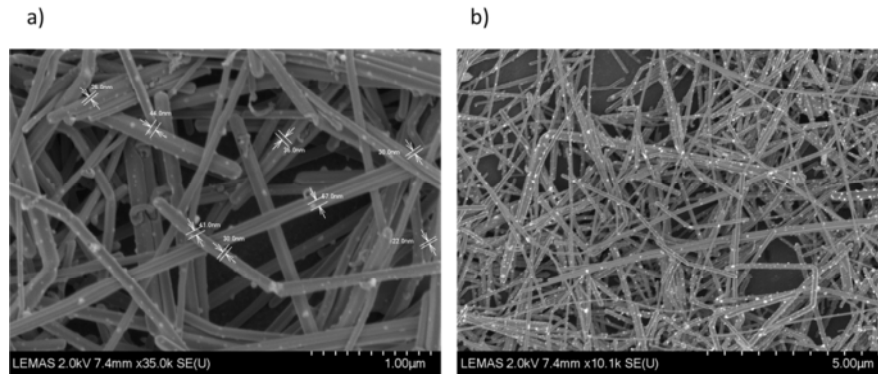


Figure 2.23: SEM images of a decorated cell.

Due to the relative roughness of the TiO_2 surface compared to the surface of AgNWs it is difficult to visually determine the effectiveness of NCs adsorption on the TiO_2 surface and therefore EDX spectroscopy was performed on selected devices. Typical EDX output maps are illustrated in Figure 2.24. The contrast in counts between Ti and Ag can clearly be seen illustrating where the AgNWs are lying on top of the TiO_2 in the image. Care should be taken when analysing CdSe X-ray emission with silver as the $L\alpha$ signal of silver is energetically similar to the $L\alpha$ signal of Cd and this may be why the Cd map has a closer resemblance to the silver map than the Se map. However, even when comparing Ag and Se maps, it can be seen that while there does seem to be a coverage over the whole area there does also seem a preference for the CdSe to adsorb upon the Ag nanomesh over the TiO_2 surface.

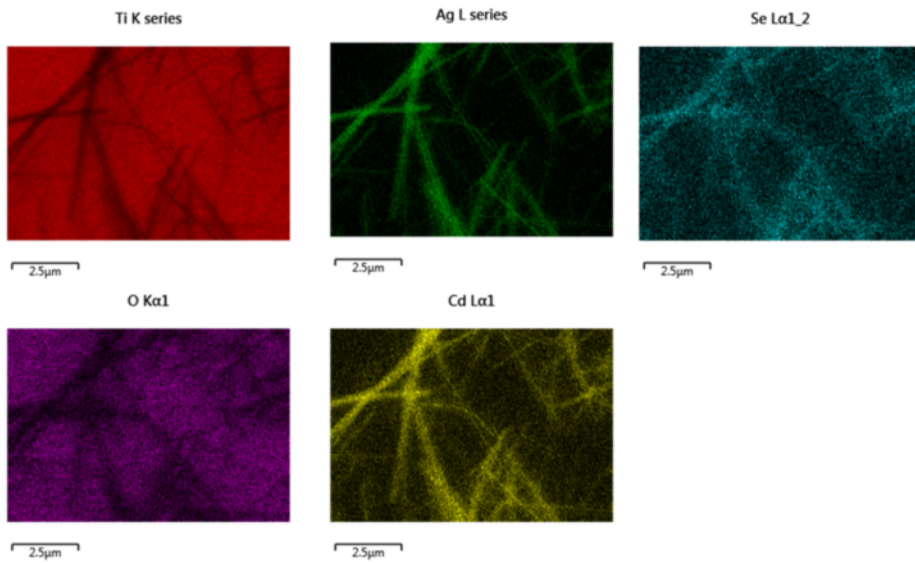


Figure 2.24: EDX maps of a CdSe-decorated cell.

Typical IV curves of NC-decorated cells, before and after NC deposition are illustrated in Figure 2.25. While some IV curves showed very little variance, such as those shown in the bottom plot, it was not uncommon for NC decoration to either improve or degrade the quality of the IV curve. This change in shape showed no trend with a similar amount of decorated cells exhibiting an improvement as those exhibiting a degradation. NC deposition did however tend to increase sheet resistance by about 60% and this is likely due to the solvents used which will be discussed in later chapters.

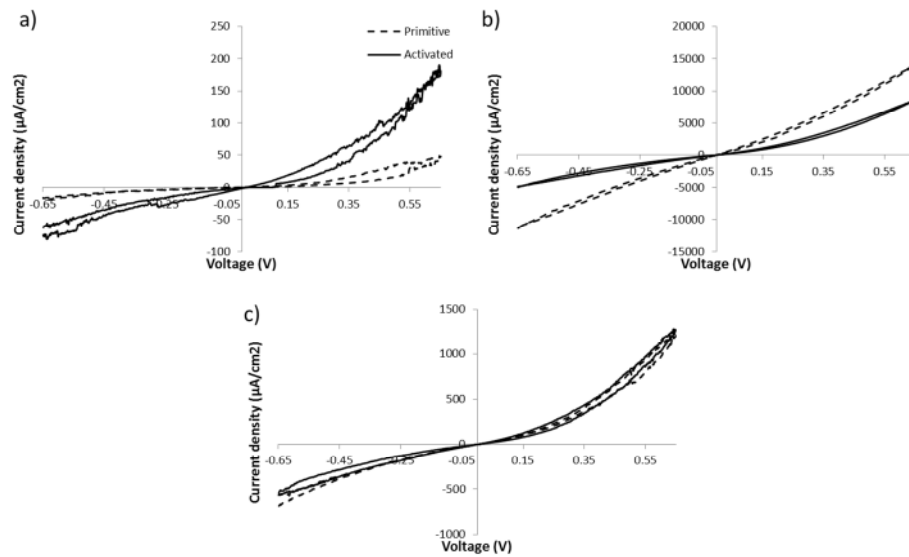


Figure 2.25: Typical changes in IV curves upon NC decoration. a) illustrates how NC decoration can increase the current density whereas b) illustrates how NC decoration can reduce the current density. c) shows a less common 'ideal' case where the IV curve is unaffected by NC decoration.

Figure 2.26 illustrates how the EQE curve will typically change upon activation by NCs, in this case, CdSe. As discussed above, the primitive cell shows no response when illuminated by visible light yet, upon decoration by CdSe, the device does produce a current under visible light. The top image illustrates an 'ideal' case where the UV response which should be solely influenced by the SB formed between the Ag and TiO_2 is unchanged by deposition. However, as illustrated in the bottom image, this was not always the case and more frequently the response of the activated cell under UV light was much greater than that of the primitive cell. These phenomenon occurred most of the time which is somewhat contradictory to the IV curve results discussed above. One would expect that a frequent increase in EQE under UV light would mean that there would be an increase in current density possibly brought about due to rearrangement of the nanomesh through solvent deposition.

Analogous to adjusting the overall EQE to consider the silver area in the primitive device, when evaluating the EQE in the visible region, the coverage of NCs that are active in cell performance should be taken in to account. Assuming that only NCs that are in contact with a silver nanowire and the TiO_2 bulk contribute to electricity production, as shown in Figure 1.5, the active area will be a monolayer of NCs that are in contact with, and run parallel to each silver nanowire. The ratio of the width of an NC either side of a single wire compared to the width of the wire itself is 7.2 %. The 35 % coverage of the Ag nanomesh therefore needs a further 7.2% coverage factor incorporated. This equates to 2.5 % of the entire cell

area and is the area adjustment factor used when considering the EQE contribution of the NCs. This area adjustment factor is defined as the nanocrystal adjusted (NA) area which is used to give the NA-EQE.

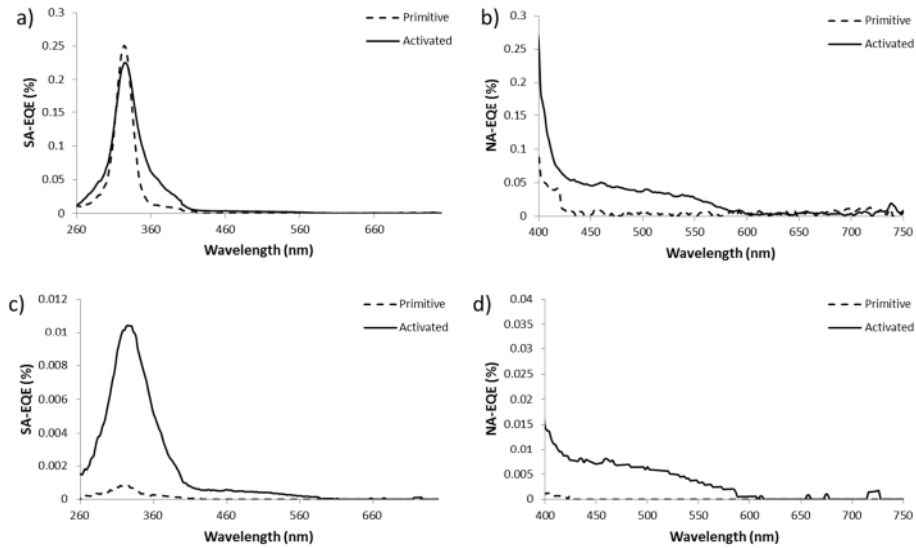


Figure 2.26: Typical changes in EQE curves upon NC decoration. a) and b) shows an ‘ideal’ case where the response under UV illumination is unaffected, c) and d) shows a more typical case where UV response is greatly increased. Left hand plots display response over whole range of wavelengths, right hand plots display response under visible illumination only.

Despite the increase in response under UV light, the new response under visible light can only be attributed to the activation caused by the CdSe NCs. Under both circumstances, the response can be seen to start at roughly 600 nm, this correlates well with absorption spectra shown in Figure 2.21. Furthermore this visible response is seen to occur regardless of how the response under UV light is affected.

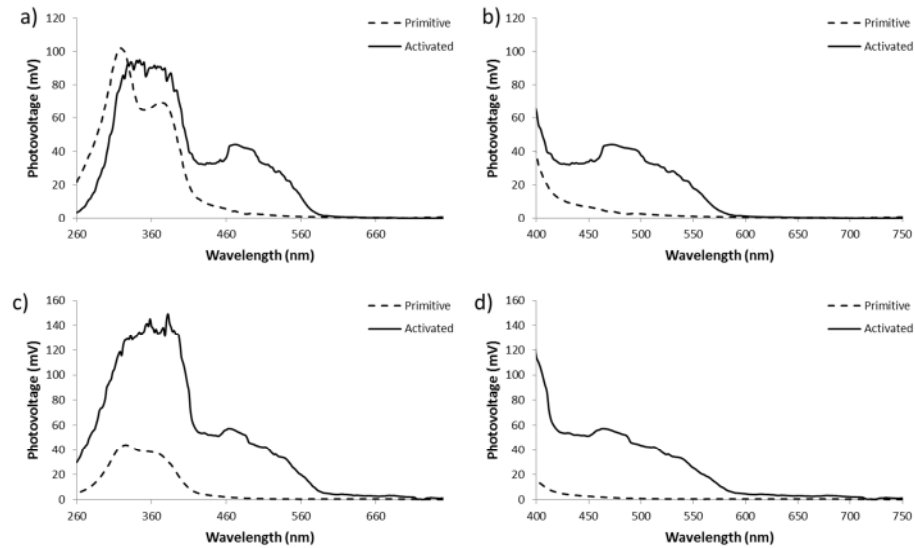


Figure 2.27: Typical changes in photovoltage curves upon NC decoration. a) and b) shows an 'ideal' case where response under UV light is unaffected, c) and d) shows a more typical case where UV response is greatly increased.

Figure 2.27 shows how the photovoltage is changed upon NC activation. The trends displayed here are the same as those for the EQE. Activation causes voltage to be produced by the cell upon illumination with visible light. This response occurs when the energy of incident light is equal to or greater than the band gap of the utilised NC (in this case CdSe). On occasion, the photovoltage in the UV region is unaffected but more typically, the photovoltage is increased.

It should be noted that even when taking in to account the silver area and NC area coverage, the EQE and photovoltages when compared to McFarland and Tang [79] and other NC SB solar cells [74, 75] are extremely low. The maximum values of the EQE for the cells shown as an example in Figure 2.26 approach a tenth of a percent and when illuminated by light of a wavelength of 500 nm, the EQE of the activated devices are of the order of a thousandth of a percent. These values are therefore too small for any practical use.

As stated in Chapter 1, McFarland and Tang obtained an IQE of 10% [79]. To convert the EQE of the NCs in to the IQE, one must consider the number of photons absorbed. This will be the same area of the cell as was considered for the NA-EQE. However, as it is only the photons that are absorbed by the NCs that are to be taken in to account, the absorption cross section of the NCs must be considered as opposed to the physical cross section. The absorption cross section can be determined by multiplying the wavelength dependent absorption coefficients that are determined through absorption spectroscopy in Figure 2.21 by the volume number density of the NCs that can be found in literature [144, 145].

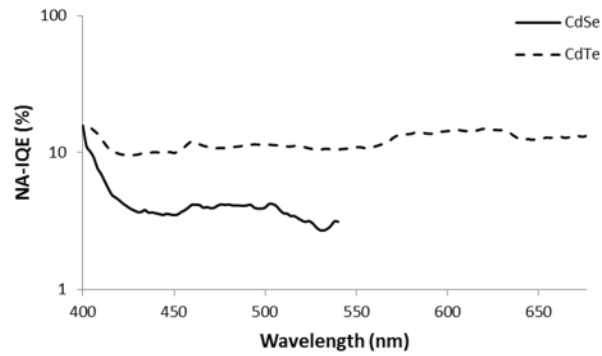


Figure 2.28: NA-IQE values for CdSe and CdTe.

Multiplying the NA-EQE with the ratio of the physical cross section of the NCs to the absorption cross section of the NCs will yield the NA-IQE as shown in Figure 2.28. As the absorption coefficient is necessary to determine the IQE, values can only be displayed for energies equal to or smaller than the band gap of the NC considered.

It can be seen that CdSe has a value of around 5 % under visible illumination. CdTe performs better with a NA-IQE greater than 10 %. This is comparable to McFarland and Tang and suggests that with a low EQE but reasonable IQE, research should be focussed on improving the number of photons absorbed by the device.

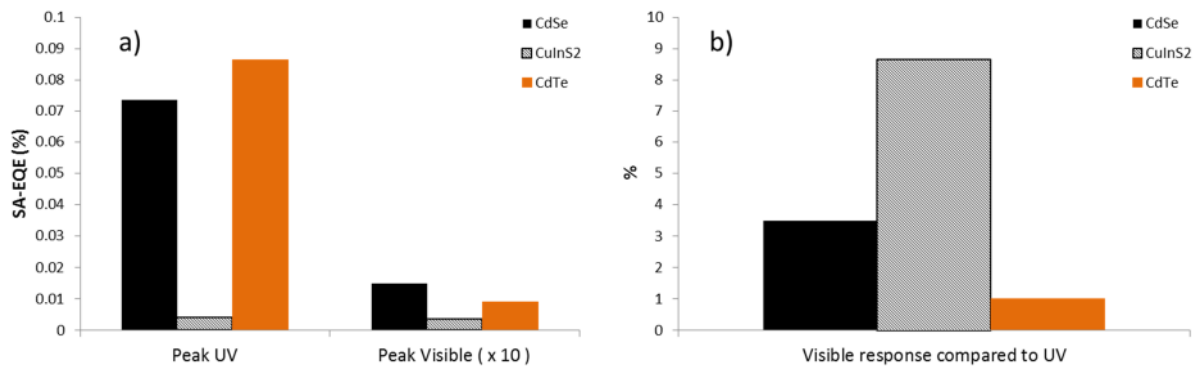


Figure 2.29: Average EQE performance of selected NCS.

For further experimentation, identification of which NC material would be most appropriate was necessary. It was decided that CdS would have limited use as the band gap of the material was too close to the band gap of TiO_2 and may therefore be difficult to ascertain which parts of any EQE or photovoltage plot are to be attributed to either material. The

remaining three materials were then assessed to see which gave the greatest response. To do so, the average peak EQE response under UV light and the average peak response under visible light for each type of material were compared, as shown in Figure 2.29. The peak response under visible light was defined as the response at 500 nm as this is at an energy great enough that all NCs should be excited regardless of any size distribution while maintaining an energy small enough so as to discount any activity from TiO_2 . The ratio of response under visible light to the response under UV light is also shown. It can be seen that while the visible response of CuInS_2 -activated cells is low, it shows a high response ratio therefore enabling easy inspection of the visible part of any EQE plot.

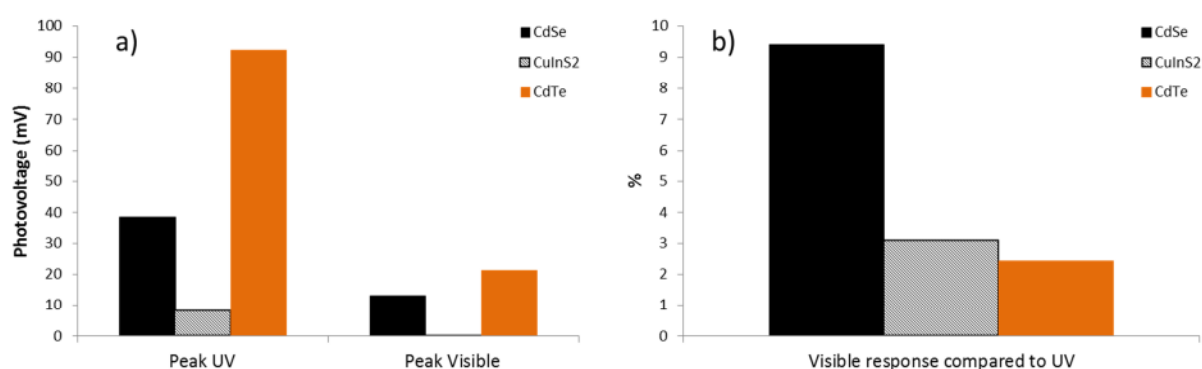


Figure 2.30: Average photovoltage performance of selected NCS.

Figure 2.30 shows the same comparison as before except for photovoltage instead of EQE. It can be seen that conversely to the EQE performance, CuInS_2 displays a relatively poor ratio of visible to UV response. Furthermore the maximum current density of devices activated with CuInS_2 is also very poor, as illustrated in Figure 2.31.

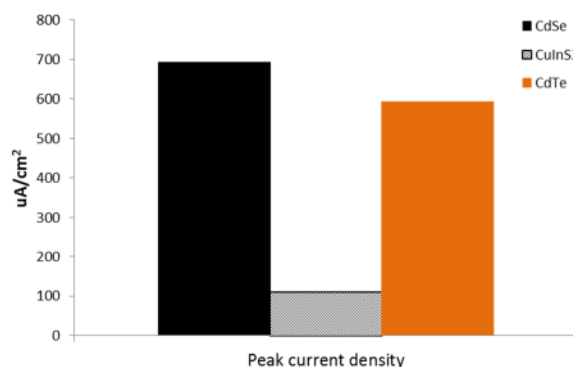


Figure 2.31: Average maximum current density after activation by selected NCS.

The previous three figures however only compare functional devices and the success rate of each type of NC material must be taken under consideration. These are displayed in Tables 2.1 and 2.2.

Table 2.1: EQE Success rate of activated cells.

Material	Devices Displaying Conclusive EQE Response Under Visible Light (%)	Devices Displaying Possible EQE Response Under Visible Light (%)
CdS	0	40
CdSe	63	100
CdTe	75	100
CuInS ₂	11	88

Table 2.2: Photovoltage success rate of activated cells.

Material	Devices Displaying Conclusive Photovoltage Response Under Visible Light (%)	Devices Displaying Possible Photovoltage Response Under Visible Light (%)
CdS	0	0
CdSe	38	38
CdTe	25	63
CuInS ₂	33	33

An example of a cell illustrating a possible response is given in Figure 2.32. Because of the noise contained within the results, it is difficult to ascertain if there is indeed a visible response. Results such as that shown on the right of Figure 2.32 are naturally undesirable and attempts to minimise them should therefore be made. For this reason, CuInS₂ was also discounted and future experimentation, where possible, would revolve around the use of CdSe and CdTe.

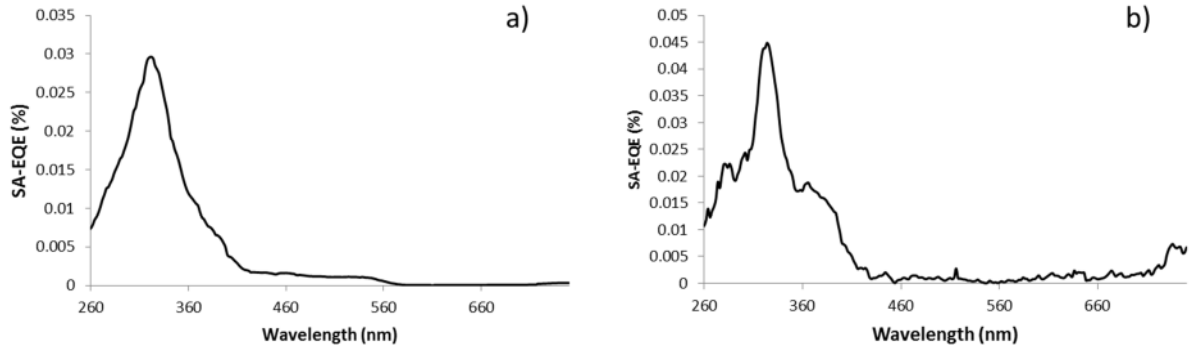


Figure 2.32: Example of a definitive visible response (> 0 % EQE at > 400 nm) (a) and possible visible response (b).

2.6 Conclusion

A solar cell has been proposed to combine NCs and NWs in a novel architecture. The primitive device (active under UV light only) is developed and characterised. Upon standardisation of the fabrication techniques of this device, NCs are deposited to decorate the cell and make it active (under UV and visible light). When illuminated by visible light, photoelectrons generated from within NCs are injected into the TiO_2 while holes transfer in to the Ag nanomesh. Under UV illumination, the TiO_2 will also absorb photons with the device operating as a typical SB solar cell

It was found that electropolishing is vital to the device performance, decreasing the surface roughness by more than a factor of 5. Oxidation causes only a slight increase in surface roughness and results in a layer of nanocrystalline rutile adhered to the titanium substrate. Drop-casting of silver nanowires is found to be the most suitable technique and upon annealing, an electrically continuous nanomesh is formed to act as a transparent conductive electrode. Both the optical and electrical properties of the Ag nanomesh are found to be of a suitable standard. Upon formation of the primitive cell, IV characteristics, photocurrent (EQE) and photovoltage was measured.

Drop-casting is again utilised for NC deposition and the technique is found to successfully activate the primitive cell. Photovoltage and photocurrent responses are now observed under visible light. The IV characteristics show no significant change. SEM imaging and EDX mapping is also used to confirm the presence of NC decoration upon the surface of silver nanowires. Four types of NCs were assessed and two, CdTe and CdSe, were selected for further experimentation.

The main driver behind the development of the new architecture was to produce a cell that through low cost, low energy fabrication processes and the potential for high efficiencies can help in improving the state of solar PV. However, despite successful demonstration of a novel nanocrystal-nanowire SB solar cell architecture, it is acknowledged that both the EQE and photovoltage recorded for the devices are low. Chapters 3 and 4 will consider device optimisation techniques with the aim of increasing electrical output and thus increasing the efficiency and amount of carbon dioxide equivalent saved.

3 Device Optimisation Through Geometry and Configuration

3.1 Introduction

As discussed in Chapter 2, while the EQE of the demonstrated device is still low, the IQE can be comparable to values found in literature and further research is required to confirm areas which could make an improvement to the device.

Loss mechanisms that could be reducing EQE include electron-hole recombination loss mechanisms such as recombination inside the NC or recombination on the NC surface. Back reaction loss mechanisms could also be an issue, this includes back reaction of electron transfer directly into the Ag nanomesh rather than TiO_2 and majority carrier diffusion from TiO_2 to nanowires. Low absorption of light will also cause losses, this could be as a result of limitation due to the size of the NC absorption cross section or through an insufficient active NC density. Internal cell resistance will also cause losses, series resistance may be increased through energy loss from electrons either transferring from NC to TiO_2 or from TiO_2 to contact. Leakage resistance may be reduced through pinholes, short circuits or conductive channels through TiO_2 .

Improvements could therefore be made through reducing these loss mechanisms. This will be achieved by increasing the percentage of photons absorbed by the device through optimisation of NC and nanowire geometry, increasing energy transfer between NCs and making any back reactions less probable. A porous TiO_2 structure would likely improve EQE however, as discussed previously, this rough structure may encounter difficulties when incorporating an Ag nanomesh.

It has already been shown how electropolishing of the TiO_2 , which affects the surface texture, has a critical impact on cell performance and it is likely that other factors that affect structure could have as stark an impact. The quantity of the materials used in the solar cell will also likely have a significant impact on performance. Considerations for the Ag nanomesh and NC must also be made and an optimum value for both the amount of AgNW and the amount of NC material be obtained.

This chapter will begin by considering how variations in the size, shape, density and configuration of materials used influences EQE before also considering how the performance of the device changes with time. The following chapter will consider the use of ligands in NC modification. Ligands are a fundamental component of colloidal NCs and can have a significant impact on NC solar cell performance.

When results from a typical device are shown, the term typical is defined as a device that illustrates the overall trend of the experiment and displays values close to the average. When a response for UV illumination is quoted the wavelength that this refers to is 324 nm, this correlates to the peak response of the primitive device. When a response for visible illumination is quoted, the wavelength that this refers to is 500 nm. This wavelength enables comparison of CdSe and CdTe responses whilst ensuring that no response from TiO₂ is observed.

3.2 Silver Loading

The quantity of AgNW on the surface of the cell will affect performance in a multitude of ways. This will occur in such a manner where there is most likely an optimum value. Too many wires and optical transparency is decreased and the likelihood of a short circuit is increased. Too few and the Ag nanomesh may not be continuous across the entire cell and the available area for NCs to become in contact with both TiO₂ and Ag NW is decreased.

Due to the variability in the electrical characteristics between cells, it is not viable to compare a certain value on one cell with a different value on another cell. To ascertain the optimum loading of silver for the nanomesh, the same cells were used while the quantity of silver was controlled and two techniques were used to overcome the intrinsic variability. The first method of doing this involved depositing the lowest quantity of silver, annealing the silver to the cell and then characterising the cell. This is followed by further deposition of silver and further annealing. This however means that upon the n^{th} loading of silver, the first batch of AgNWs will have been annealed n times which will itself cause inaccuracies. The second method involves the removal of the first loading of AgNWs on to the cell after deposition, annealing and measurement. The removal involves washing the cell in ethanol and wiping with a cleanroom standard dry wipe cloth until current is unable to pass along the surface of the cell. The increased use of solvent and manual handling in this method may however affect the cell substrate through removing oxide or adding roughness to the surface therefore influencing results. There may also be remnants of silver left on the surface.

3.2.1 Results

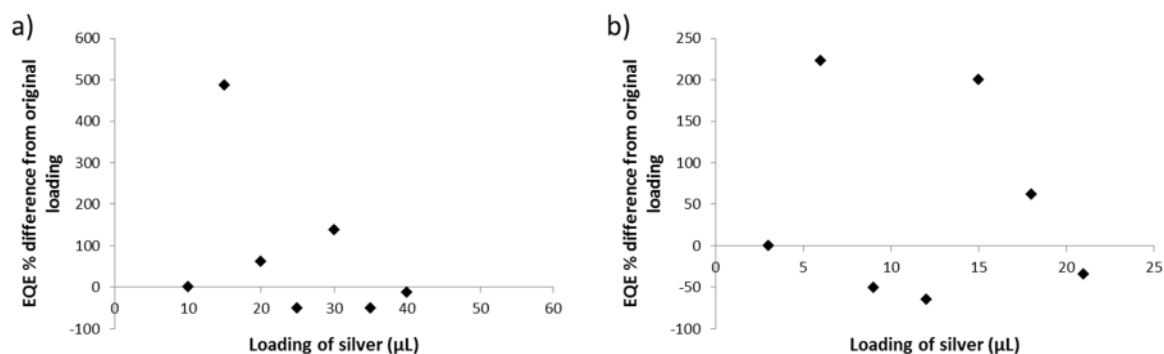


Figure 3.1: Typical change in EQE for a cell that was recycled after measurement (a) and successively layered and annealed (b).

Figure 3.1 shows the typical change in EQE for cells that have had their loading of AgNWs varied. It illustrates how no obvious trend was found with a seemingly random response to quantity of silver. Some cells showed a positive trend with EQE raising as the quantity of silver increased. However, some cells showed the exact opposite with the EQE falling as the quantity of silver increased. Others, such as those in Figure 3.1, showed a varied response. The experimental method chosen seemed to bear no impact upon results.

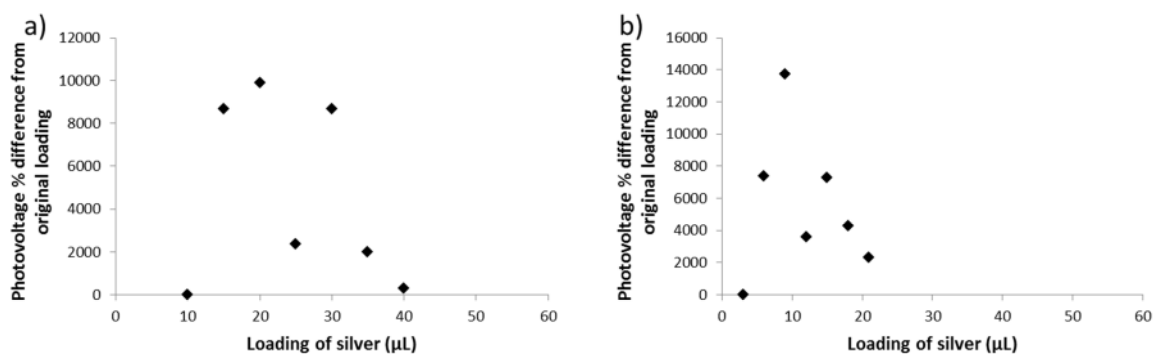


Figure 3.2: Typical change in photovoltage for a cell that was recycled after measurement (a) and successively layered and annealed (b).

The change in peak photovoltage as function of silver loading is displayed in Figure 3.2. For cells that were recycled after each measurement, the voltage improvement always peaked at a loading of around 20 μL of silver. The voltage of the samples that were repeatedly annealed however showed no quantitative trend with a peak occurring after the second annealing, suggesting that these results are too dependent on the unintended effects of the experimental procedure. It was also found that the cells that gave relatively large photovoltages were found less frequently at loadings over 30 μL .

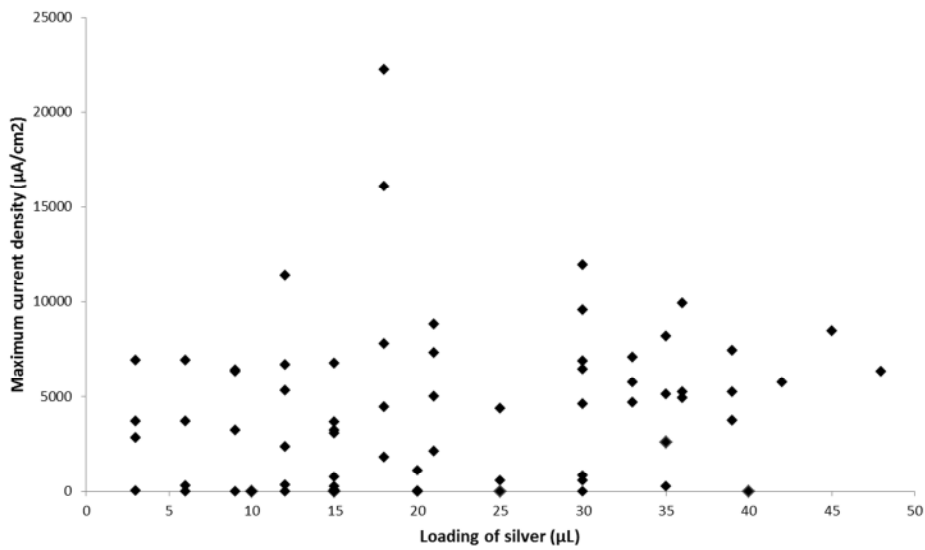


Figure 3.3: Maximum current density from IV curve as a function of silver loading.

Figure 3.3 shows how the maximum current from IV curves changes with respect to the loading of silver. It can be seen that while the two highest values occur at 18 μL , these values seem to be anomalies. Overall, there is no significant trend with high loadings of silver displaying a similar maximum current as those with low loadings.

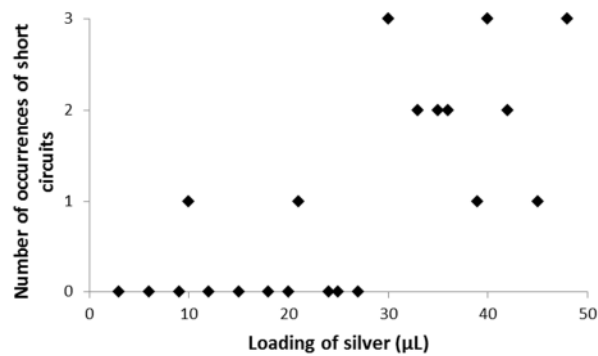


Figure 3.4: Number of short circuits observed for each loading of silver measured.

Despite results not being definitive, 20 μL of AgNW at a concentration of 2.5 mg/ml was chosen to be the standard. This correlates with the results of the photovoltage measurements and while the IV curves suggest that a larger current is beneficial, as shown in Figure 3.4, loadings larger than 20 μL increased the probability of a short circuit which renders the cell useless.

This volume of AgNW deposition equates to 1020 mg/m^2 which is a factor of ten greater than the 100 mg/m^2 value obtained by Langley et al. [133] and 20 times greater than the value of 47 mg/m^2 found by De et al. [127]. It should however be noted that wires of different aspect ratios were used as well as different cell architectures and therefore some variability within the results is to be expected.

3.3 Nanocrystal Loading

Just as with AgNWs, the quantity of NCs on the cell will have an optimum value, there is a simultaneous requirement to have as many NCs as possible achieving both an interface with the TiO_2 and with the Ag but not so many NCs so that non-functional NCs are absorbing photons that would otherwise be absorbed by a functional NC or by the TiO_2 .

3.3.1 Results

Figure 3.5 shows SEM images illustrating how varying the quantity of the NC deposition can affect device performance.

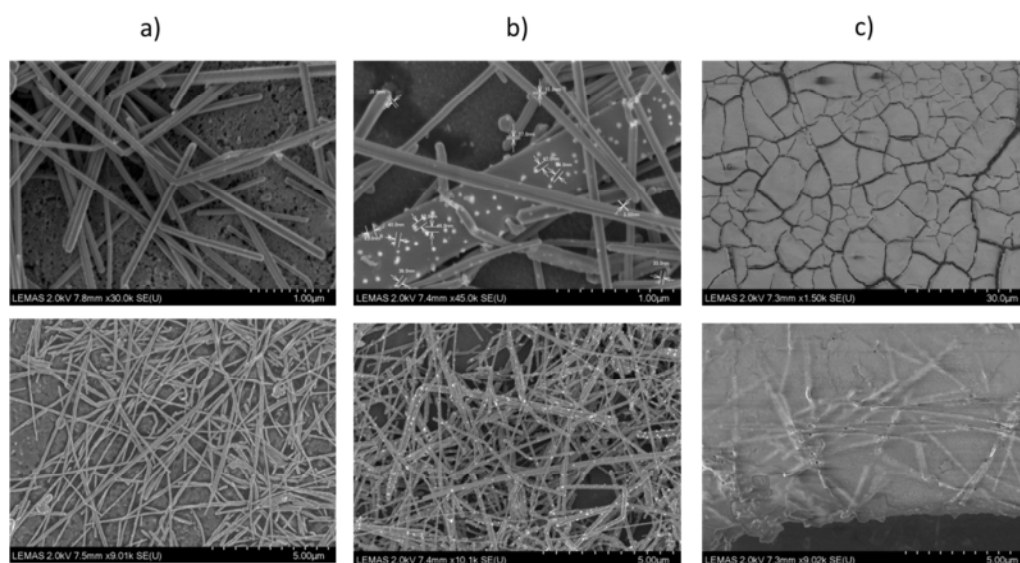


Figure 3.5: SEM images of relatively low (a), medium (b) and high (c) loadings of NCs.

It can be seen that at a certain loading, a film will form consisting of non-functional NCs which will absorb all photons before they have a chance to reach the functional NCs that are in contact with both Ag and TiO_2 . Thus this film will prevent the device from performing as a solar cell. EDX spectroscopy of an example of this film is shown in Figure 3.6. The red response from titanium is clearly seen in the cracks of the film which is dominated from the

response, coloured green, attributed to Se from the CdSe deposition. Cracks are thought to form during solvent evaporation which causes the film to shrink.

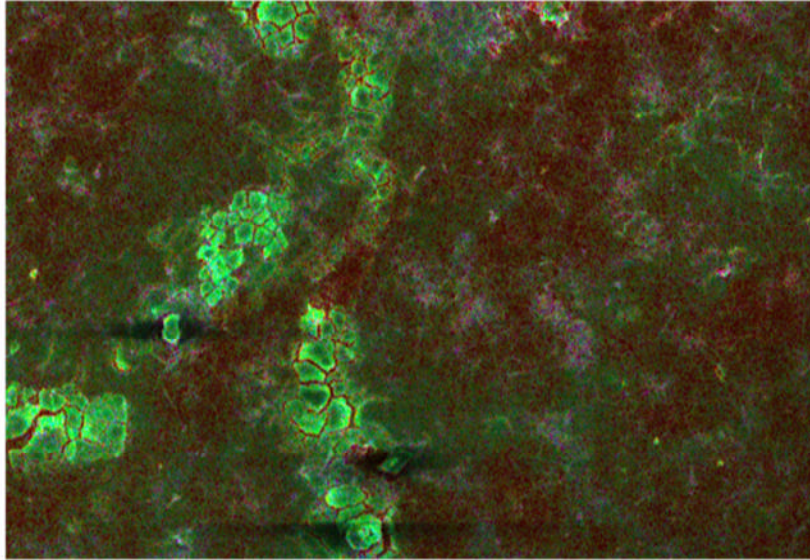


Figure 3.6: EDX spectroscopy of film caused by NC overloading. Green is Se response, red is Ti response.

Unlike when determining the optimum loading of silver, NCs aren't annealed after deposition. There is therefore no need to consider different experimental techniques. NCs can be deposited, measurements can be taken and then further NCs can be deposited without the change in any other properties of the cell. As NC loading increases, the amount of solvent the cell is exposed to is also increased however and as will be discussed later, this will have an effect.

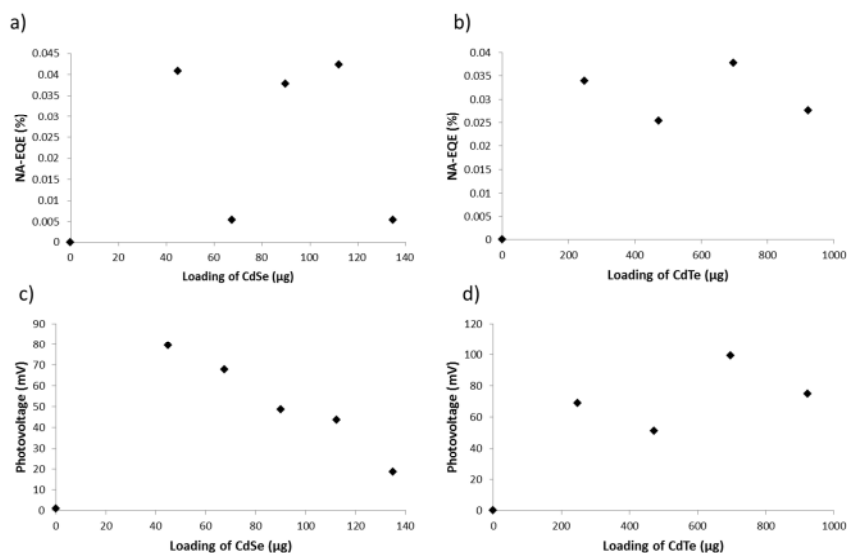


Figure 3.7: Photocurrent (top) and photovoltage (bottom) performance under visible light upon successive depositions of CdSe (left) and CdTe (right) NCs.

Figure 3.7 shows the performance of typical activated solar cells under visible light. It can be seen that the cells become functional upon NC decoration and in the case of CdTe, the loading after activation doesn't seem to have any effect of the photovoltage or photocurrent with both values staying close to constant. After activation, subsequent loading of CdSe NCs is seen to deteriorate the photovoltage. The Current produced shows neither improvement nor degradation upon successive loadings but instead fluctuates up and down.

As well as activating cells, NC deposition also affects the performance of the cell response under UV light. This alteration in response, while not as strong as the change in response under visible light, is still significant. Figure 3.8 illustrates the change in photoresponse of typical cells after NC decoration.

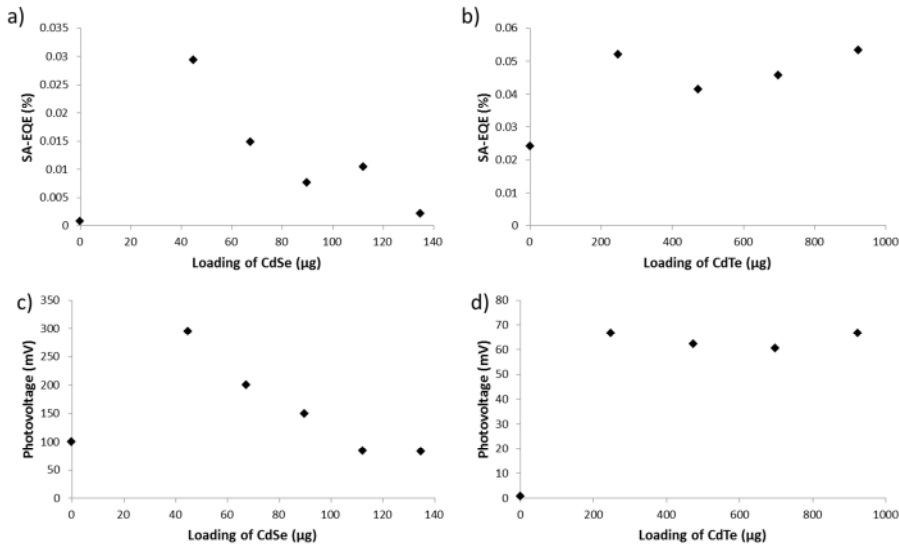


Figure 3.8: Photocurrent (top) and photovoltage (bottom) performance under UV light upon successive depositions of CdSe (left) and CdTe (right) NCs.

It can be seen that NC activation in all circumstances actually improves the UV response. However, further deposition of CdSe NCs shows a steep decline in both EQE and photovoltage. Further CdTe doesn't show this problem with the UV response staying constant after the initial activation. This implies that as well as simply becoming responsive under visible light, NC deposition is changing the fundamental properties of the solar cell. Figure 3.9 supports this evidence illustrating how subsequent NC depositions actually decrease the maximum current density produced for an IV curve.

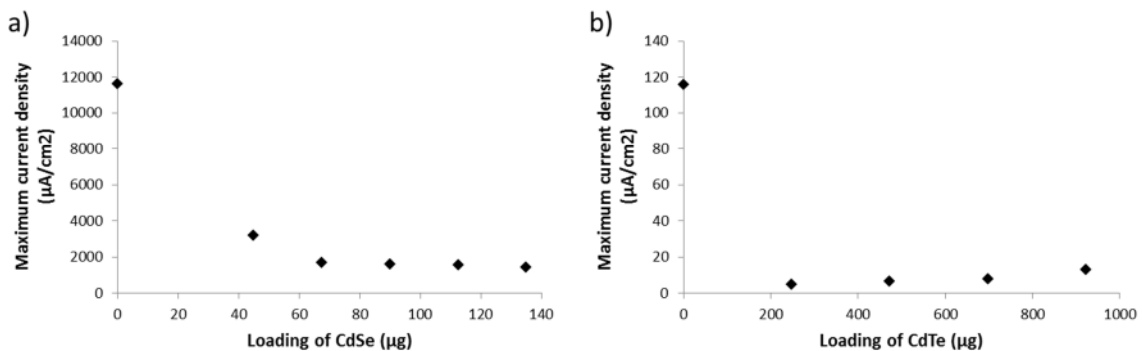


Figure 3.9: Maximum current density upon successive loadings of CdSe (a) and CdTe (b) NCs.

It is therefore apparent that NC deposition has multiple impacts and it is therefore impossible to judge the effectiveness of NC loading on a cell if the SBH and other properties

are being affected through the deposition. A more useful method to measure the effectiveness of the NC loading while taking in to consideration the change in properties is to consider the size of the visible response as a fraction of the maximum UV response (Vis/UV ratio), as illustrated in Figure 3.10. CdTe deposition shows a steady increase as loading increases while the CdSe response seems to stay constant for both EQE and photovoltage. This suggest that, as is expected, increasing the amount of material that absorbs in the visible and reducing the amount of UV light that is incident on the TiO₂ increases the ratio of visible to UV performance, as illustrated with CdTe. However for CdSe, this occurrence may be counteracted by the negative impact of the NC deposition that is suggested in Figure 3.8. The difference in impact of CdTe and CdSe deposition may be due to the different solvents that are used for the two materials and this is what will be considered next.

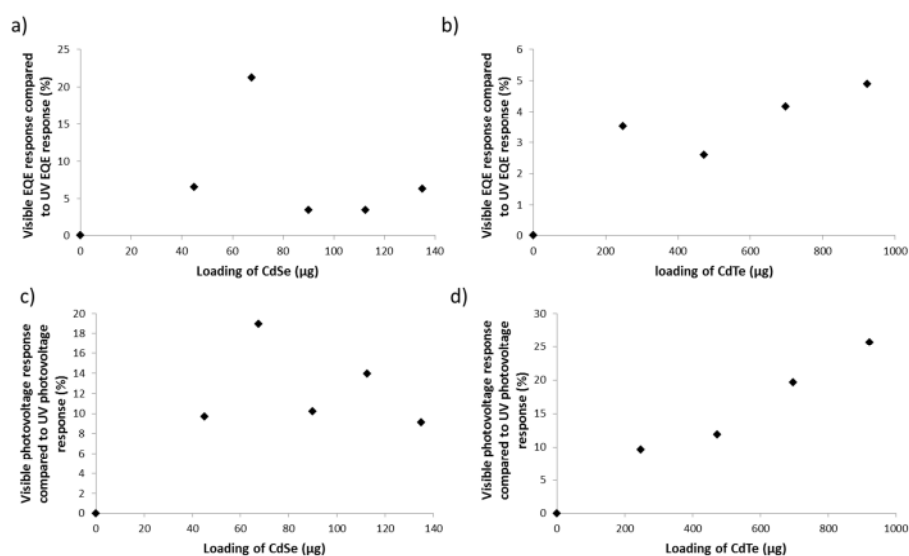


Figure 3.10: Ratio of visible response to UV response for EQE (top) and photovoltage (bottom) upon successive depositions of CdSe (left) and CdTe (right) NCs.

3.4 Solvent Use

As demonstrated in Figures 3.7 and 3.8, the initial addition of solvent has a beneficial effect, it is only subsequent additions of CdSe where degradation occurs. An explanation for this initial improvement is shown in figure 3.11. Dropcast AgNWs are shown on the left and the images on the right display the same primitive cell after further deposition of ethanol. This extra addition of solvent appears to remove any island-like structures and create a more continuous, homogeneous mesh.

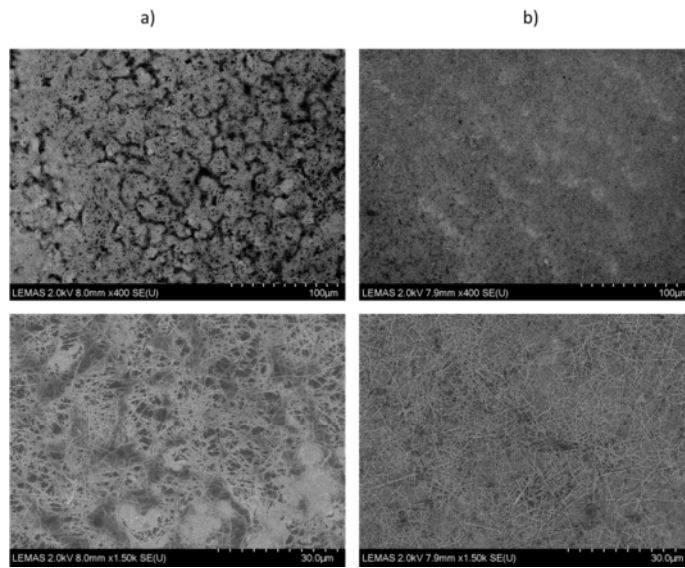


Figure 3.11: Primitive cell before (a) and after (b) addition of solvent.

Each type of NC is provided in its own solvent. It must therefore be ascertained if the solvent used alone has any effect on the functioning of the solar cell before determining what effect the NCs have. Table 3.1 lists the NCs used and the solvents they are suspended in.

Table 3.1: List of NC materials and the solvents that they are suspended in.

Material	Solvent
CdS	Toluene
CdSe	Toluene
CdTe	Water
CuInS ₂	Chloroform

3.4.1 Results

To assess the effect that solvents can have, primitive cells were manufactured and different solvents were deposited in steps with EQE, photovoltage and IV characteristics taken at the end of each step. Figure 3.12 shows the effect that the different solvents can have on the maximum current density produced through IV characterisation.

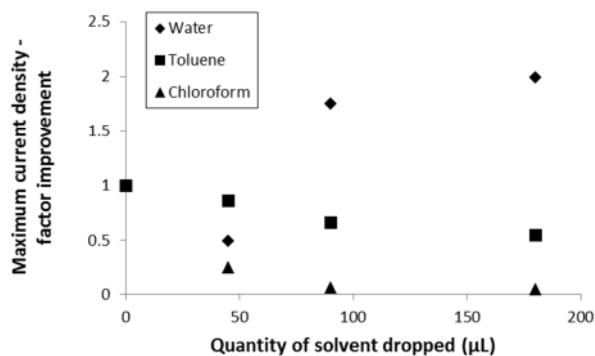


Figure 3.12: Change in maximum current density due to solvent deposition.

It can be seen that Chloroform has a significant detrimental effect on the maximum current density produced with values being decreased by up to a factor of 100. Toluene shows a less severe decrease whereas water has the opposite effect, improving cell performance.

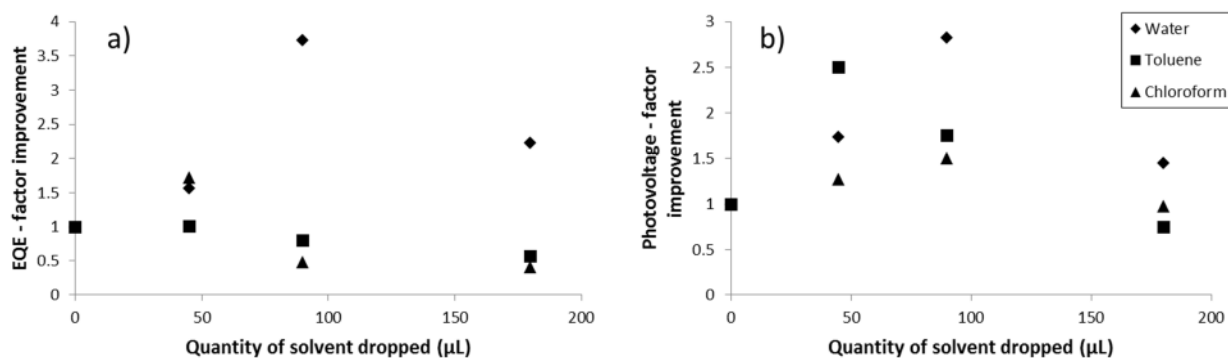


Figure 3.13: Change in peak EQE (a) and peak photovoltage (b) of a primitive device due to solvent deposition.

Figure 3.13 shows how peak EQE and peak photovoltage are affected by solvent deposition. EQE follows a similar progression as the maximum current density with both toluene and chloroform degrading the quality of results whereas water improves the device. Up to the second deposition of solvents, the photovoltage of all cells increases with water showing the greatest increase. The final deposition then shows a decrease in photovoltage for all solvents. This is in fact true for the EQE as well with water starting to have a lower improvement.

If the Ag nanomesh is not well bonded and has poorly sintered junctions due to an insufficient annealing temperature, the solvent used may form a thin layer between AgNWs. The conductivity of the solvent may then have an impact on device performance. In this

circumstance, a highly polar solvent such as water may help reduce junction resistance, as observed.

These results may therefore explain the difference in results between CdSe and CdTe deposition. Toluene, the solvent for CdSe, is shown to have a detrimental impact on device performance so therefore repeated introduction of this solvent with successive CdSe deposition is likely to negatively impact the results whereas the opposite is true for water and CdTe.

3.5 Silver Nanowire Size

Varying the size of the AgNWs used for the nanomesh also has the potential to influence cell performance. Shorter, thinner wires would increase the chance of decorating NCs being in simultaneous contact with both the Ag nanomesh and the TiO₂ surface. Longer wires however increase the chance of creating a fully electronically conductive nanomesh and increase the active area of the cell due to an increased contact area between Ag and TiO₂. Ideally, the AgNWs used would be long and thin. This quality is illustrated through the wire's aspect ratio which is defined as the length of the wire divided by its diameter. A large aspect ratio is therefore desired. However, it is typically found that wires that have a longer length tend to have the higher aspect ratio. To assess the best size of AgNW to be used, the same mass (50 µg) of two different sizes were deposited to form the primitive cell and then decorated with NCs to become activate under visible light. Table 3.2 displays the properties of the AgNWs used.

Table 3.2: Properties of wires used in the study.

AgNW Type	Mean Length	Mean Width	Aspect Ratio	Source
Short	10 µm	60 nm	17	Sigma Aldrich
Long	25 µm	90 nm	28	Blue Nano

3.5.1 Results

Figure 3.14 shows SEM images of typical primitive cells consisting of short or long wires. It can be seen that both types of wires form a fully conductive network and also have a similar amount of surface coverage.

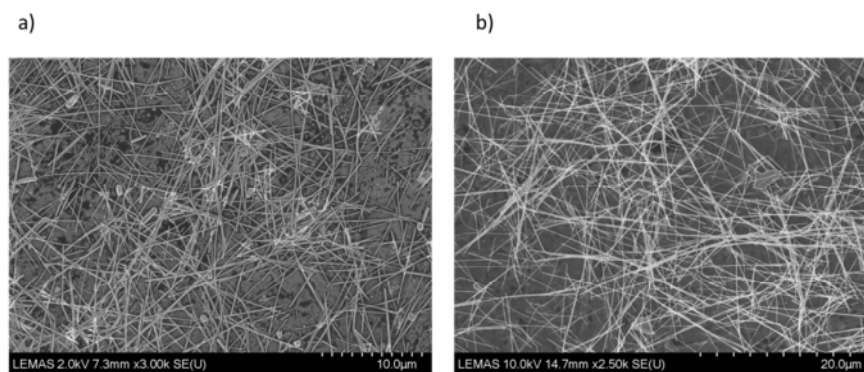


Figure 3.14: SEM images of primitive cells formed with short wires (a) and long wires (b).

The fully conductive mesh is also confirmed by the fact that the IV curves displayed reasonable high values for the maximum current. When no mesh is present, the only Schottky barrier present during measurement is that created through contact between the top measurement contact and the TiO_2 bulk. Due to this small size a maximum current in the order of nA/cm^2 is observed. The average maximum current of cells containing short wires was $3000 \mu\text{A}/\text{cm}^2$ and for long wires, the average value was $860 \mu\text{A}/\text{cm}^2$. Figure 3.15 shows typical IV curves for both types of Ag nanomeshes. It can be seen that the IV curve for short wires exhibits more noise and this can be attributed to the greater amount of AgNW junctions that will be present in the device.

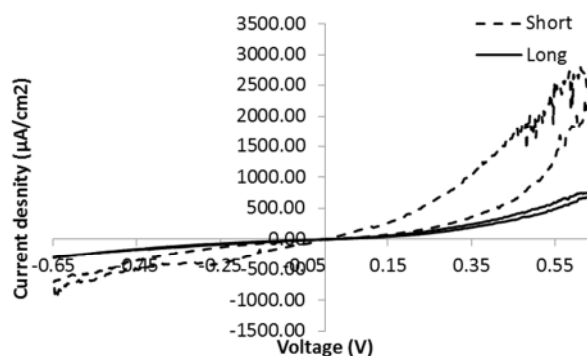


Figure 3.15: Typical IV curves for long and short wires.

Shorter nanowires, perhaps surprisingly, tend to produce a larger photocurrent than longer AgNWs with the average SA-EQE being four times larger for short wires. However, as with the IV curves, the plots exhibit more noise. Unlike previous measurements, the shorter wires displayed a lower photovoltage on average, typically, the shorter wires produced a half as

strong photovoltage when compared to longer wires. Typical photocurrent and photovoltage plots are displayed in Figure 3.16.

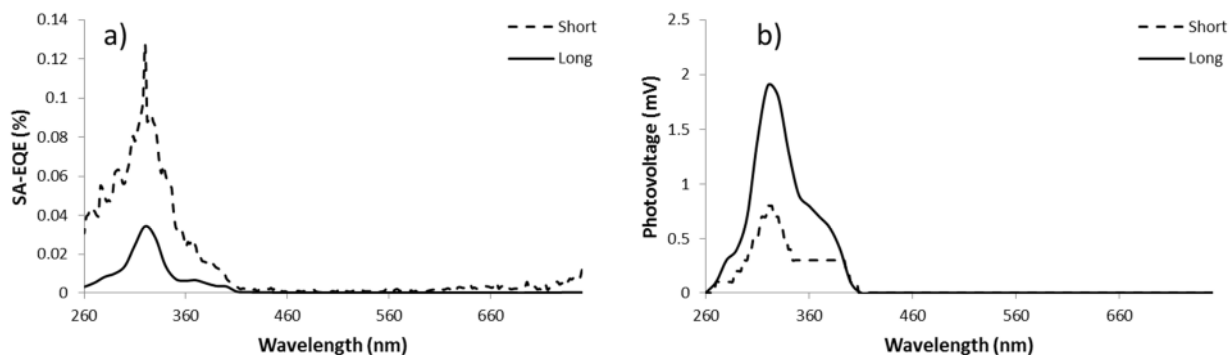


Figure 3.16: Typical EQE (a) and photovoltage (b) plots for long and short wires.

Both primitive cells consisting of short wires and primitive cells consisting of long wires were then activated by CdTe NCs and tested to assess their relative efficiency. As discussed previously, the variation between cells is so great that a comparison of two different cells is not a useful way to determine the effectiveness of the techniques used. The purpose of comparing two different nanomesh structures is to ascertain which one allows for the largest possible response under visible light. The better the nanomesh, the more NCs that are simultaneously in contact with the mesh and TiO_2 . A useful metric to compare cells is therefore again the relative intensities of the visible peak of the individual cell when compared with the peak formed under UV illumination.

Figure 3.17 shows that both short-wire cells and long-wire cells exhibited visible responses even under the lightest loading of NCs ($45 \mu\text{g}$). However, there is very little difference in the relative magnitude of the visible response. For the same loading of NCs, long wire cells had an average photocurrent response under visible light that equates to 1.74 % that of its response under UV light. Short-wire cells have a marginally lower ratio of 0.99%. This trend is reversed under for photovoltage response with short-wire cells having a visible response on average of 7.59% that of the UV response. This value for long-wire cells is 3.78%.

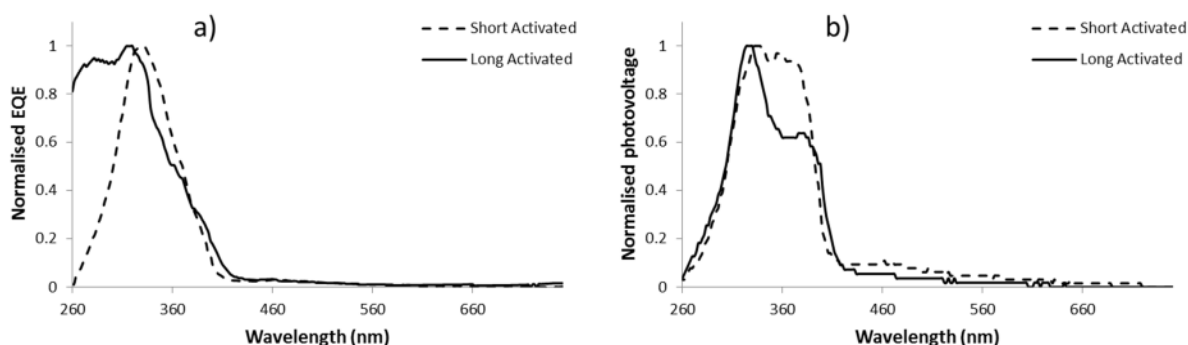


Figure 3.17: EQE (a) and photovoltage (b) plots displaying size of visible peak compared to UV peak for both short-wire and long-wire cells.

Despite showing possibly worse qualities, the long wires had a better guarantee of supply for the remainder of the study and were therefore chosen to be used for all further experiments. Furthermore, upon decoration with CdTe NCs, it was feared that when using short wires, the resulting plots would display significant noise and any visible response that will be produced would be lost within in the noise.

3.6 Filamentary Nanomesh

In the most similar cell design to the demonstrated device, it was noted that the overall efficiency of the device was limited by low coverage of the photo-active layer and the resulting low photon absorption [79]. This holds true for the proposed device and it is therefore desirable to increase photon absorption to optimise the efficiency of the cells produced. One intention of the use of a nanomesh is to create a network of wires that can cover a large area and therefore enable the decorating NCs to be simultaneously in contact with the silver and with the TiO₂. For this purpose, it was proposed that a filamentary structure would achieve this through having the complete mesh structure of the long wires but with the short wires increasing the surface area and therefore increasing the chance of creating the three-way interface of NC-TiO₂, NC-Ag and Ag-TiO₂. Figure 3.18 illustrates the proposed filamentary structure.

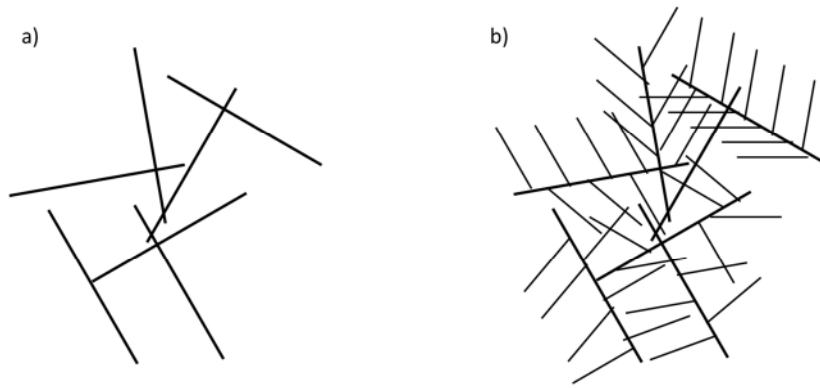


Figure 3.18: Illustration of increased surface area coverage due to filamentary structure (wires drawn to scale).

3.6.1 Results

To create this nanomesh structure, a further 25 μg of short wires were deposited on top of an already annealed 50 μg of long wires. Figure 3.19 shows the result of this process. The filamentary structure is clear on the right of the figure. However, on the left it appears that upon annealing the short wires, a solid mass of silver forms between the long and the short wires therefore potentially negating its use through the loss of transparency.

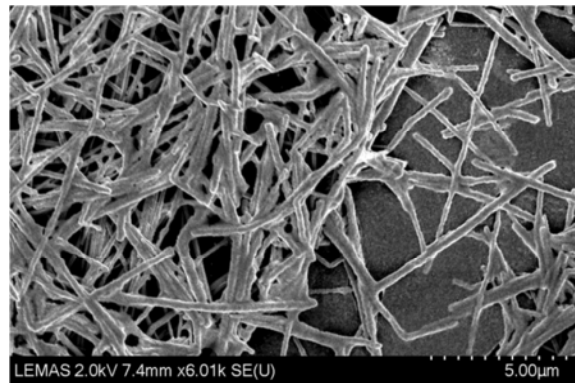


Figure 3.19: SEM image of filamentary nanomesh.

For the primitive device, introducing the short wires as filaments resulted in a slight improvement of the maximum current produced with IV curves and an on average, increase in EQE by a factor of two. The average photovoltage also increases, in this instance, by a factor of 4. These trends are illustrated in Figures 3.20 and 3.21.

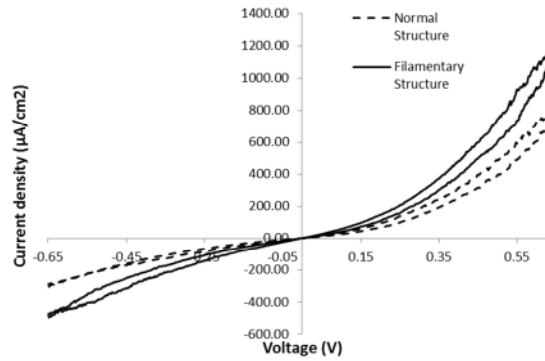


Figure 3.20: Typical IV curves for cells utilizing a filamentary nanomesh compared with a normal nanomesh.

These results are to be expected as there is a greater amount of silver in contact with the TiO_2 . However, the results are more conclusive than the previous study looking at varying the loading of silver. This could be due to the ability of the smaller wires to fall in between the longer wires during deposition and therefore coming in to contact with the TiO_2 surface as opposed to the previous study where a further loading of long wires may simply rest on top of the previously deposited silver and therefore not be in contact with the bulk semiconductor and thus not affecting the Schottky barrier characteristics.

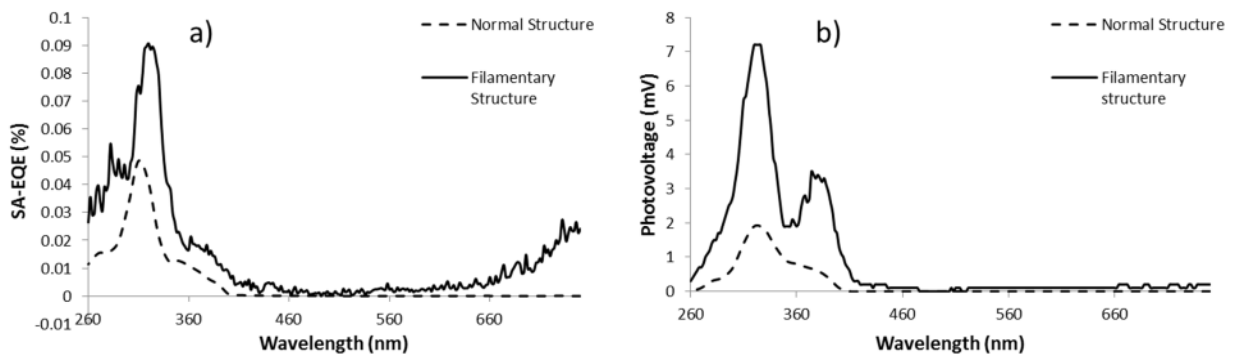


Figure 3.21: Typical EQE (a) and Photovoltage (b) curves using a filamentary nanomesh compared with a normal nanomesh.

Upon decoration, the filamentary structure did exhibit a photoresponse. It can be seen by Figure 3.22 however that this structure showed negligible effect over a normal nanomesh structure. In fact, both the photovoltage and photocurrent perform slightly worse under visible light for the filamentary structure than for the normal nanomesh.

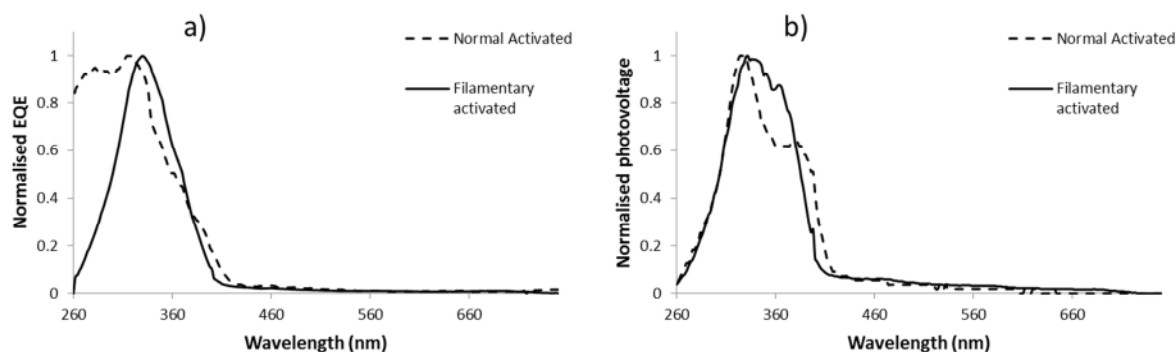


Figure 3.22: EQE (a) and photovoltage (b) plots displaying size of visible peak compared to UV peak for both normal nanomeshes and filamentary nanomeshes.

3.7 Deposition Order

With the intention to create a NC activated SB solar cell, it could be easy to figure that first a SB must be formed through the fabrication of a primitive cell. However, one could argue that to ensure as high a coverage of TiO_2 by NCs as possible, it may be beneficial to deposit the NCs first. This deposition order has the secondary advantage in that it enables annealing of the NCs at temperatures much higher than the Ag nanomesh could withstand therefore allowing the removal of electrically insulating ligands. In this case, CdSe was used, these NCs are capped with hexadecylamine which has a boiling point of 330 °C. NCs were deposited on to a Ti/ TiO_2 substrate and heated to 400 °C to ensure complete removal of ligands. This temperature was necessary to ensure complete ligand removal however there is a possibility that damage to NCs may have occurred due to oxidation. AgNWs were then deposited and annealed at 160 °C to form the nanomesh as usual. These cells were compared to a standard batch of CdSe-decorated cells.

3.7.1 Results

The difference between both types of cells can be clearly seen in SEM images such as those displayed in Figure 3.23. When NCs are deposited after NWs, they can be clearly seen decorating the NWs however if NCs are deposited before the NWs, they cannot be seen on the NWs. It is however impossible to ascertain the NC coverage on the TiO_2 bulk due to the roughness of the TiO_2 surface.

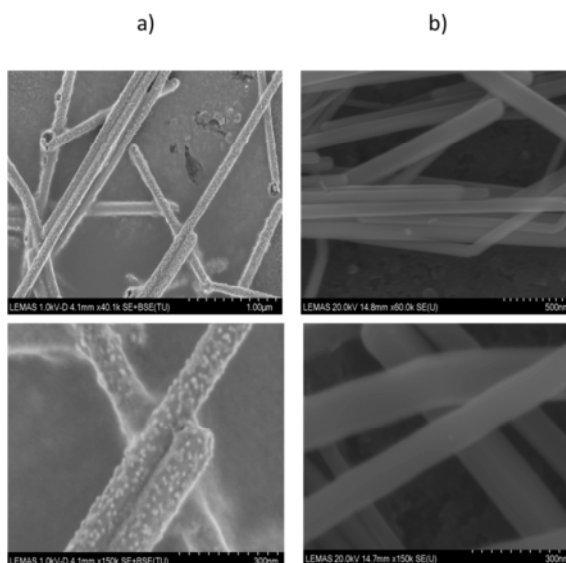


Figure 3.23: SEM images of cells with NWs deposited first (a) and NCs deposited first (b).

Figure 3.24 shows the average peak photovoltage of each type of device under both visible and UV light.

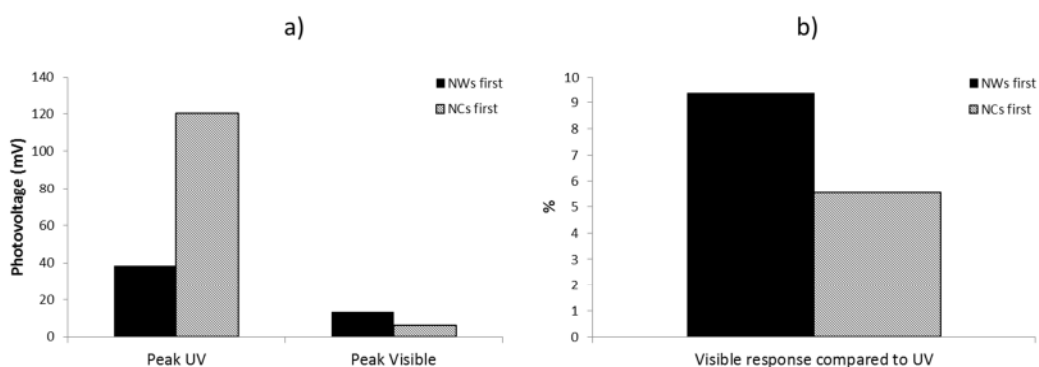


Figure 3.24: Average photovoltage response under visible and UV light (a) and the ratio of response under visible light to response under UV light (b).

It can be seen that cells where the NCs were deposited first perform better under UV light. This implies that more photons are reaching the TiO_2 bulk which may be attributed to the removal of any ligands which may be absorbing photons for cells where the NWs were deposited first. However, under visible light, cells where NWs were deposited first are more active, this is in spite of the presence of electrically insulating ligands and can be attributed to the increased frequency of the three necessary interfaces being formed. Photovoltage is related to Schottky barrier height. If there is no Schottky barrier, then the photovoltage will

go down, as observed. The increased response under visible light of cells where NWs were deposited first is emphasized when comparing the ratio of visible response to UV response.

Figure 3.25 compares the average SA-EQE of both types of cells. Cells where NCs were deposited first and annealed exhibit a greater EQE under both visible and UV light. However, when the ratio is considered, the average response of NW-first cells under visible light is 3.5 % of the UV response. This value for NC-first cells is only 2 %. Therefore, while it is evident that having the nanomesh structure already in place helps in creating an increased photovoltage under visible light, depositing NCs first allows for a greater current to be produced under visible light. This can be attributed to the removal of ligands which allows any charge generated within the NC to travel easier. For the purpose of this study, depositing NWs first is still helpful when looking for a EQE under visible light as any response will be easier to identify due to the greater ratio in response between UV and visible.

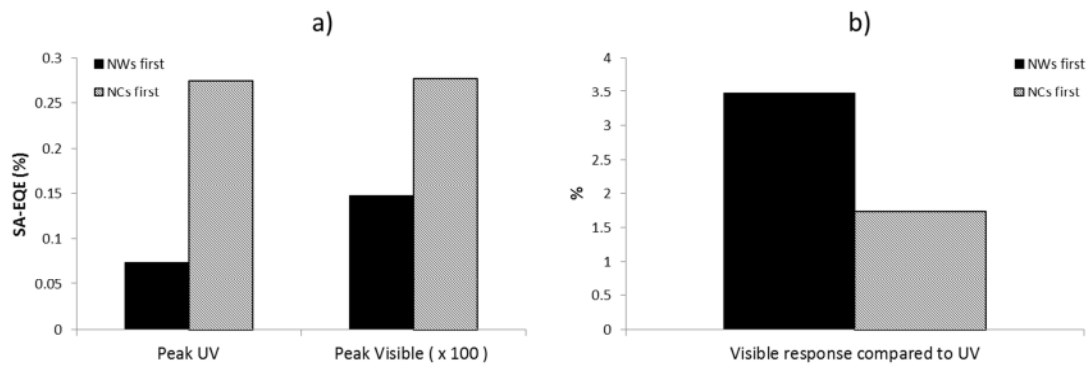


Figure 3.25: Average EQE response under visible and UV light (a) and the ratio of response under visible light to response under UV light (b).

Despite having a higher average photovoltage and photocurrent, cells where NCs were deposited first have a much lower maximum current density under IV characterisation. This is illustrated in Figure 3.26. It was also noted that the IV curves produced for when NCs were deposited first tended to be less ideal and had a greater amount of noise and reverse bias leakage.

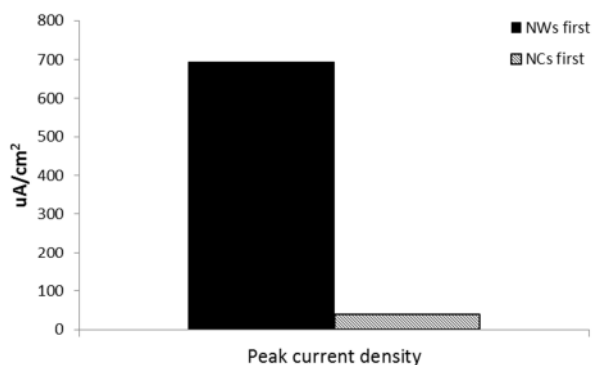


Figure 3.26: Average maximum current density produced through IV characterisation.

These results suggest that there is less of a contact area between the nanomesh and TiO₂ when the NCs are deposited first. The presence of NCs will reduce the interfacial area of the two materials thus increasing the series resistance and reducing the current in IV measurements.

3.8 Nanowire and Nanocrystal Mixing

As opposed to depositing one material before the other, it is also possible to mix the NCs and AgNWs together in solution first and then deposit them simultaneously. This can lead to the advantage of reduced toluene use which, as discussed previously is detrimental to cell performance and enhanced adsorption of the NCs to the surface of the silver. It also creates the opportunity to image the AgNW/NC combination before deposition through TEM. Mixing of NCs with larger nanofibrous material has been successfully trialled by Kochuveedu et al. and the degree of NC adsorption has been found to be tuneable by the amount of time the substances were allowed to mix [146]. This study will therefore consider both the quantity of NC to be included as well as the mixing time.

3.8.1 Results

Figure 3.27 displays images of NCs adsorbed on to the surface of silver nanowires. It can be seen that NCs can cluster around NW junctions and ‘connect’ NWs together. NC coverage is also found to be inconsistent with clusters of NCs being found on some parts of a nanowire and no NCs at all being adsorbed on other areas. It is however impossible to determine if this NC clustering occurred before or after adsorption. A final point to note is the wastage that these images indicate. Many NCs are seen to not be in contact with a NW and therefore unable to contribute to the solar cell performance. Regardless, as there is still available space on the NW surface, despite its wastefulness, an increase in NC loading may improve device performance.

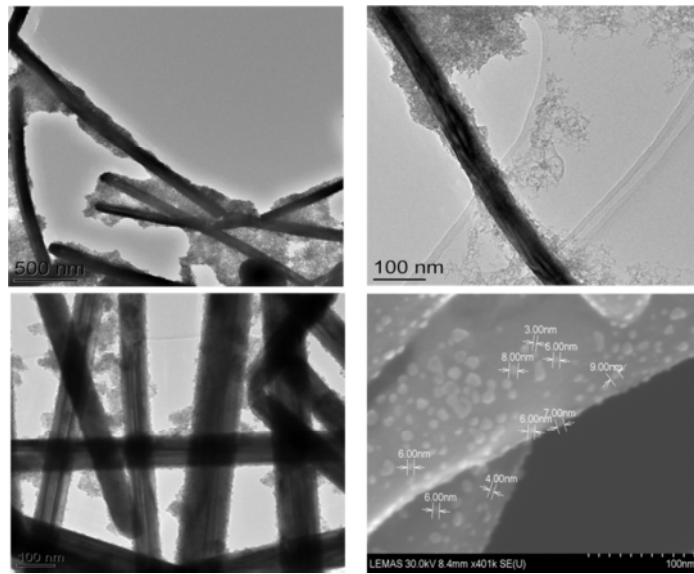


Figure 3.27: TEM and SEM images of a 1:1 quantity mix of AgNW and CdSe NCs after 24 hours. Credit for photography: Priten Khagram.

Figure 3.28 shows high magnification TEM images of NC adsorption on to the NW surface. Upon adsorption, the typically smooth NW surface increases in roughness. It can be seen that even in areas of low NC coverage, there is still agglomeration of NCs. It is possible that this agglomeration is the cause behind incomplete NW coverage with it perhaps being energetically favourable for NCs to adsorb on to an agglomeration cluster over a bare NW surface.

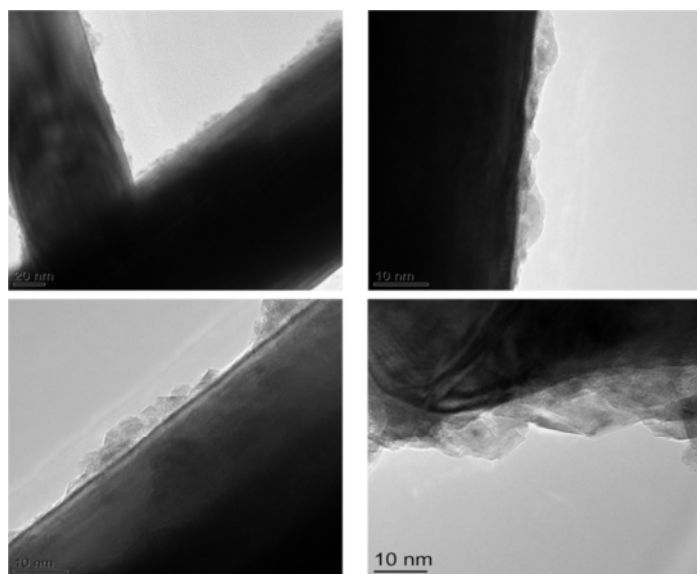


Figure 3.28: TEM images of NC adsorption on to a NW surface. Credit for photography: Priten Khagram.

Figure 3.29 Shows absorption and emission results from two different mix batches. The first batch is upon a brief initial mixing of materials before measurements (0 hours) and the second batch is where the materials have been allowed to mix for 24 hours before optical measurement. Both mixes had a 1:1 weight ratio of NC to NW. It can be seen that both mixes exhibit an emission shoulder at around 475 nm which is also apparent in the AgNW emission spectra. However, both mixes also have a large emission shoulder that extends in to the red. This shoulder can be attributed to neither the CdSe nor AgNW.

Further to this unexplained feature, the emission intensity of the peak found around 575 nm for the batch that has been mixed for 24 hours is considerably larger. While one may expect the introduction of silver to increase quenching of emission due to the possibility of charge separation, the excitation of NCs was caused by UV illumination and thus the increase in intensity can be attributed to plasmonic effects which are observed to be stronger under UV illumination. After mixing for 24 hours, the NCs may have lost labile ligands thus becoming closer and better attached to the NWs hence the plasmonic effects of NWs which causes the light to be more ‘focussed’ in the region around the NWs will have a greater effect. The position of the emission peak is the same for both mixes as it is for the pure CdSe sample indicating that the band gap structure of the semiconductor remains unchanged.

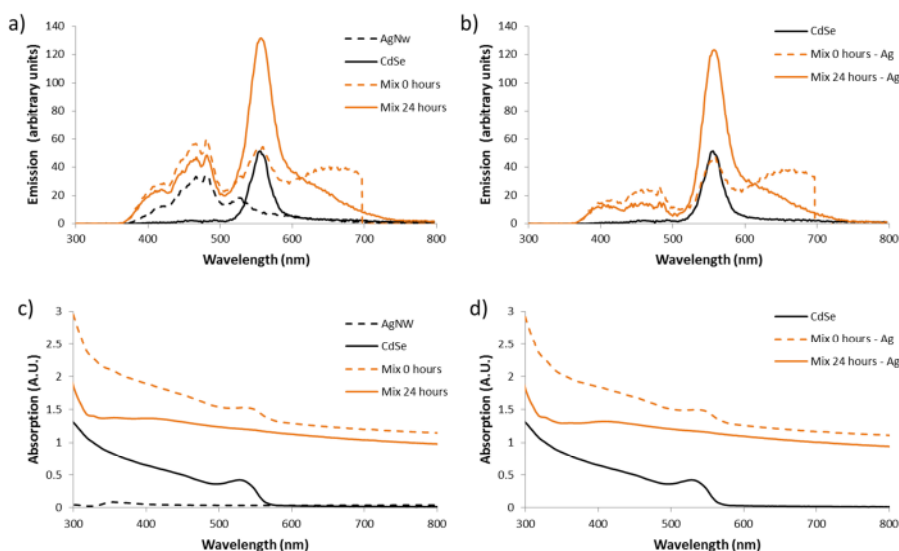


Figure 3.29: Emission (top) and absorption (bottom) spectra of NC/NW mixes. Right hand side shows silver subtracted from the results of the 0 hour and 24 hour mix.

The absorption spectra indicate that the silver nanowires have a relatively small impact on absorption. However, when CdSe NCs are mixed with the AgNWs, the total absorption is greater than the sum of its parts. This may be explained by the fact that the UV-Vis spectrometer used in this study did not have an integrating sphere and therefore scattering could not be taken in to account. Any scattering would reduce the amount of light reaching the detector therefore increasing the instrument's perception of absorption. Scattering would also account for the $1/\text{wavelength}$ shape of the response. For both peak spectra, one would assume that at wavelengths much greater the band gap, the absorption would be negligible and the spectra would therefore be transposed down to zero at these points, this is however not the case. It can also be seen that the absorption peak is reduced for the two mix batches, with the peak seemingly degrading with time also. A reduction in the absorption peak would lead to a reduction in device performance.

As evident in the TEM images, a ratio loading of 1:1 NCs to NWs left some parts of the Ag nanomesh uncovered by NCs. Increasing the coverage of NWs by NCs is therefore an obvious area to try and improve the cell's efficiency under visible light. To assess the viability of this, mixtures with a higher density of NCs were also produced, one with a 5:1 NC to NW ratio and one with a 10:1 ratio. All mixtures had the same quantity of AgNWs.

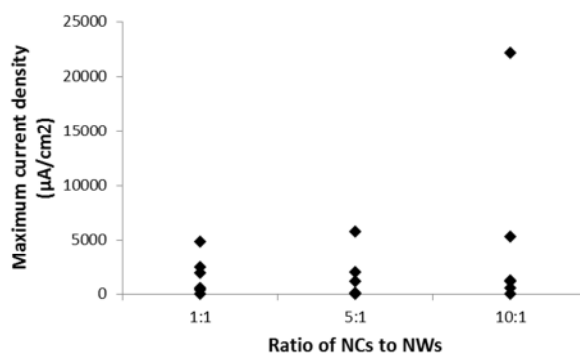


Figure 3.30: Maximum current density as a function of NC density.

As one would expect for the same quantity of silver used in each cell, the maximum current density doesn't seem to vary with NC density, apart from one, perhaps anomalous, result. This is shown in Figure 3.30.

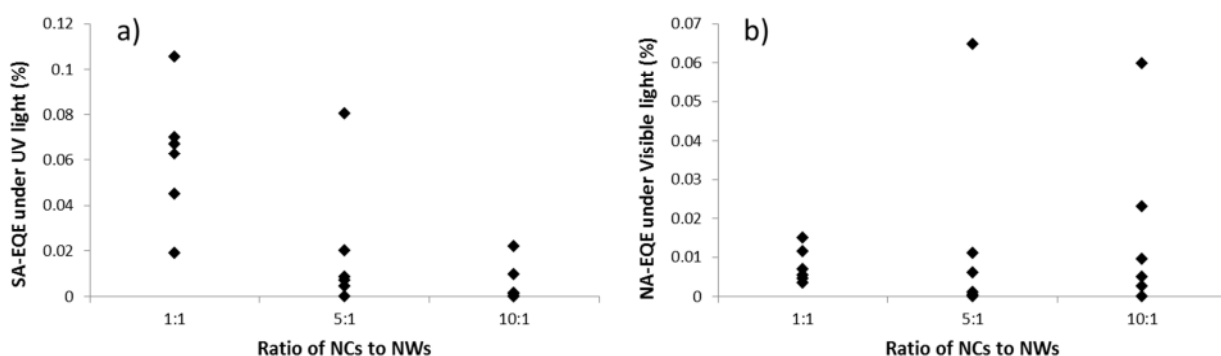


Figure 3.31: EQE performance of devices with a range of NC to NW ratios.

Figure 3.31 shows the EQE of each device fabricated as a function of the NC loading. As expected, the efficiency of cells under UV light tends to decrease as NC loading increases. Under the visible light, the results don't illustrate as clear a trend with most devices tending to have a NA-EQE of under 0.02 % regardless of NC loading. It can however be seen that an increase in NC loading seems to increase the possibility of a cell having a greater performance with one cell having a higher than 0.02 % efficiency in the 5:1 loading ratio and two cells having efficiencies higher than 0.02 % for the 10:1 loading ratio.

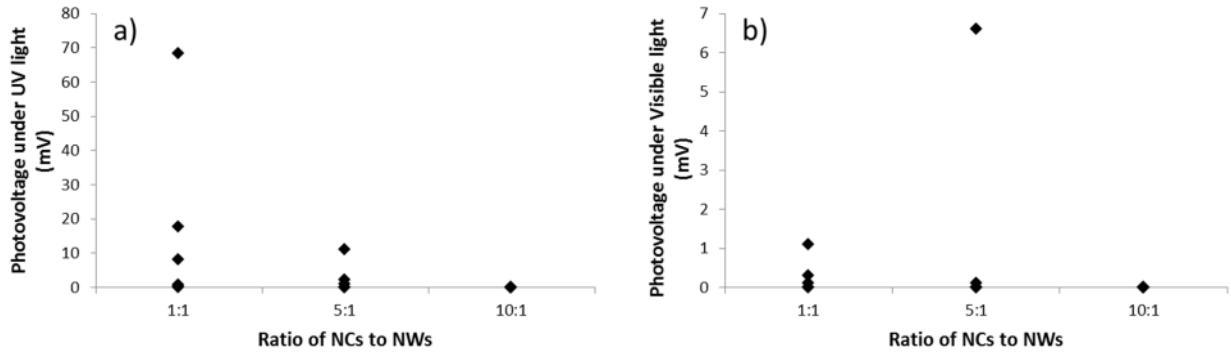


Figure 3.32: Photovoltage performance of devices with a range of NC to NW ratios.

As was the case for the EQE, the photovoltage of cells illuminated by UV light decreases with increasing NC density. This is shown in Figure 3.32. In fact, cells that had the highest NC density displayed no measurable photovoltage under any wavelength of illumination. A similar trend is true for the 5:1 ratio where only once cell shows a photovoltage under visible light. This photovoltage is however much greater than any of the cells that contained a 1:1 ratio.

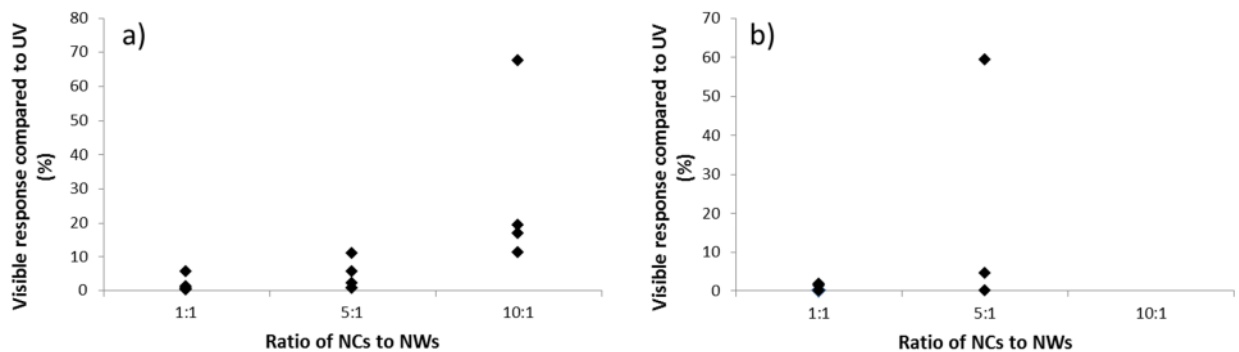


Figure 3.33: Ratio of response under visible light to response under UV light for both EQE (a) and photovoltage (b).

When comparing the visible response to the UV response, as shown in Figure 3.33, the EQE consideration is perhaps a more useful tool to identify any trend associated with NC loading. This is because the 10:1 ratio didn't produce any photovoltage under visible light and therefore can't be used. When considering the EQE, it can be seen that the visible response does become a more significant aspect of the cell's output as NC loading increases. However, if this comes at the cost of a decrease in output in the UV region, then it may not be the best optimisation method. As suggested when considering the TEM images, a linear increase in

NC density doesn't necessarily mean a linear increase in the number of NCs that adsorb on to the surface of the Ag nanomesh with agglomeration of NCs being a perhaps major issue that would cause a decrease in UV response but no increase in visible response. An optimisation method where NCs are attached preferentially to the Ag nanomesh as opposed to furthering contribute to a NC agglomeration will likely provide great improvements to the efficiencies produced by the device.

An advantage of this study is that it has allowed the experimentation of different NC loadings without the repeated use of toluene. It has been found that an increase in NC loading probably improves current output under visible light yet the photovoltage is affected detrimentally. It also indicates that the decrease in cell performance under UV light isn't just due to the negative effects of toluene but also due to the increased NC loading which will absorb photons of UV light therefore preventing them from exciting an electron in the TiO_2 . As the increase in efficiency under visible light doesn't seem to account for the decrease in efficiency under UV light, it is possible that photon absorption by NCs that aren't in proximity to a depletion region caused by the SB formation between Ag and TiO_2 is occurring. This may be due to a too high a concentration of NCs which may be blocking photons from the NCs that are in fact at the AgNW/ TiO_2 interface.

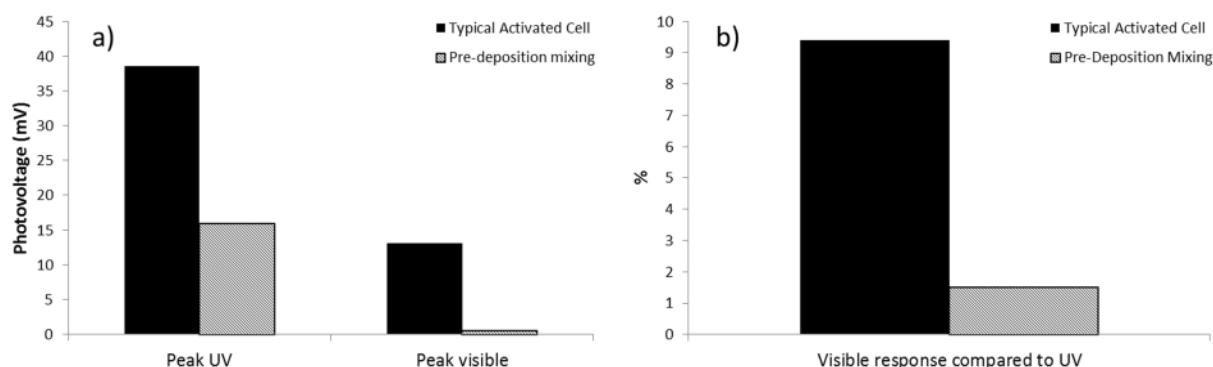


Figure 3.34: Comparison of typical photovoltages produced through both deposition types.

As well as comparing loading, it is also possible to compare against the standard deposition route. This was performed for a NC to NW mixing ratio of 1:1 which closely compares to the standard ratio of NCs to NWs. As shown in Figure 3.34, the typical deposition route shows a higher photovoltage under both UV light and visible light. Similarly for the EQE, illustrated in Figure 3.35, pre-deposition mixing typically results in a similar or worse efficiency.

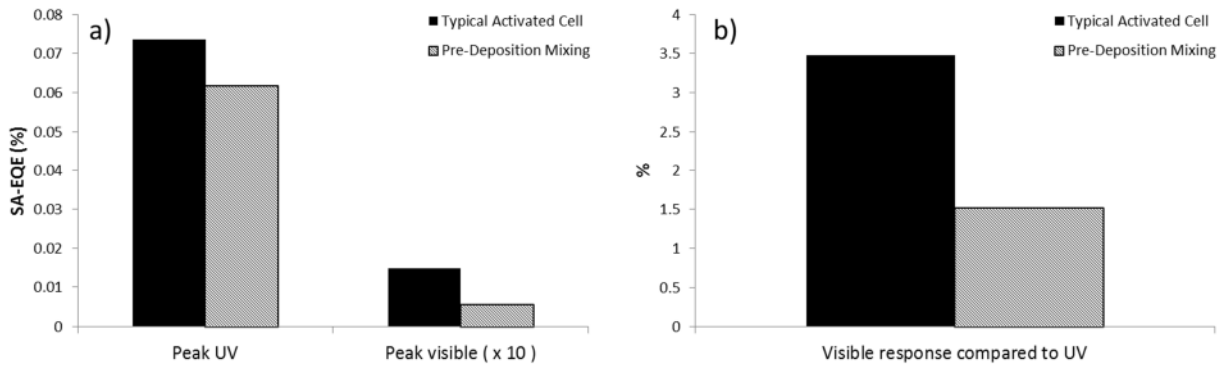


Figure 3.35: Comparison of typical EQEs produced through both deposition types.

This outcome could be attributed to the fact that mixing allows for NCs to adsorb on to both the top and bottom of NWs therefore possibly creating a buffer layer between the bulk TiO₂ and the silver nanomesh, this would reduce the effect of the SB therefore decreasing device performance. However, the maximum current density for pre-deposition mixing is in fact higher than the standard deposition method. This is shown in Figure 3.36. This lower performance can be attributed to the reduced peak in absorption observed in Figure 3.29 for mixed NCs.

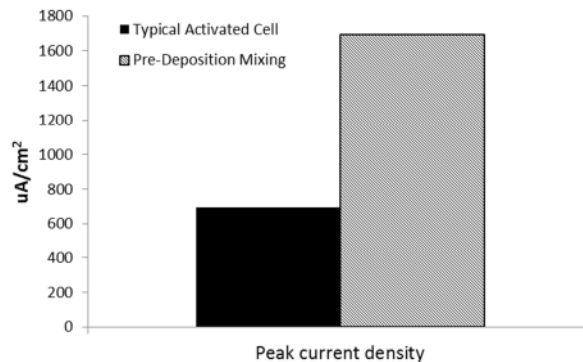


Figure 3.36: Difference in maximum current density between pre-deposition mixing and a typical activated cell.

Even though pre-deposition mixing has allowed a better understanding of the effect of increasing the NC density, it does not help in device optimisation with the standard deposition technique appearing to create a better standard of cells.

3.9 Pre-Fabrication Mixing

Silver nanowires can also be fabricated using a CuCl_2 salt mediated polyol process as according to Korte et al. [147]. These wires have an average diameter of 74 nm and length of 20 μm and are therefore similar to the standard nanowires purchased through Blue Nano. In-house fabrication allows for pre-fabrication mixing to be studied. Various methods have been devised to co-create nanostructures [148-152] however none have involved silver nanowires and semiconducting nanoparticles. It is postulated that through introducing NCs during the growth stage of the AgNWs, complete surface coverage of the nanowires by the nanocrystals will be promoted. This will be the case as long as the introduction of NCs doesn't interfere with the growth of NWs. After NC injection, the as synthesised wires are then separated by multi-pass filtration with acetone and then water before being re-dispersed into ethanol according to Jarrett et al. [153].

3.9.1 Results

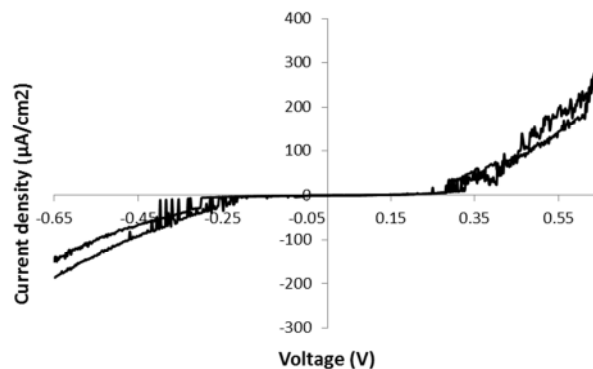


Figure 3.37: Typical IV curve for a cell after pre-fabrication mixture deposition.

Figure 3.37 shows that although displaying significant noise, a SB is formed. The maximum current densities however are relatively low. Further to the poor IV curves produced, as illustrated in Figures 3.38 and 3.39, the photovoltages and EQEs produced are also poor. Many device showed no sensible output and those that did had low values for EQE and photovoltage and also noisy curves.

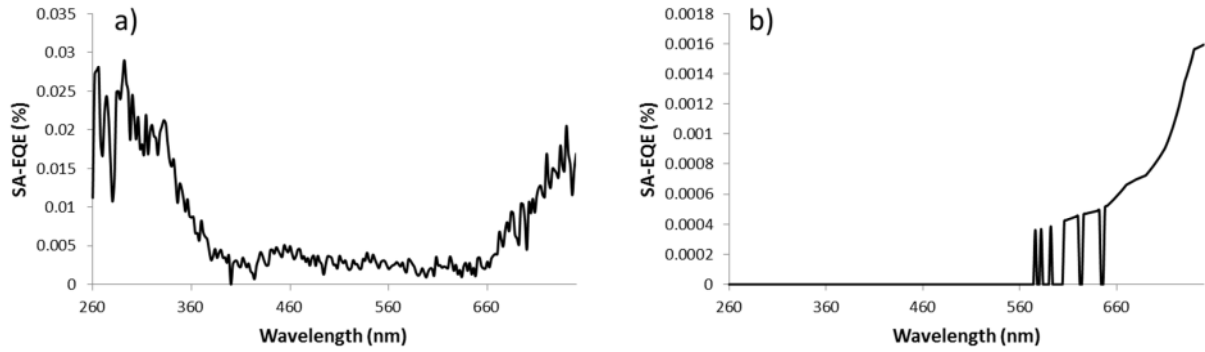


Figure 3.38: Illustration of the EQE as a function of wavelength of a working (a) and not-working (b) cell after pre-fabrication mixture deposition.

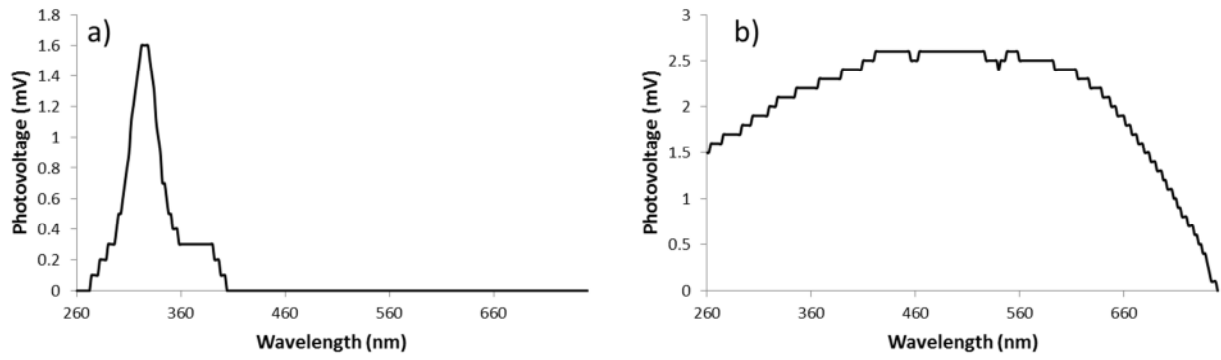


Figure 3.39: Illustration of the photovoltage as a function of wavelength of a working (a) and not-working (b) cell after pre-fabrication mixture deposition.

These poor results can be explained with the SEM images shown in Figure 3.40. While the silver nanowires shown look typical, the decorating crystals are significantly larger than desired. Large platelets are also visible on the right hand image of Figure 3.40. These platelets can't be attributed to any particular element by EDX analysis but as these platelets are not TiO_2 , they and the larger than usual NCs will be interfering with the desired device architecture formation. The NCs are in fact so large that the desired adsorption that is shown in parts of Figure 3.27 will be impossible to achieve. This growth in NC size is most likely due to an increased rate of Ostwald ripening brought about by the relatively high temperatures employed during NW growth. This pre-fabrication mixing method is therefore an unsuitable candidate for device optimisation.

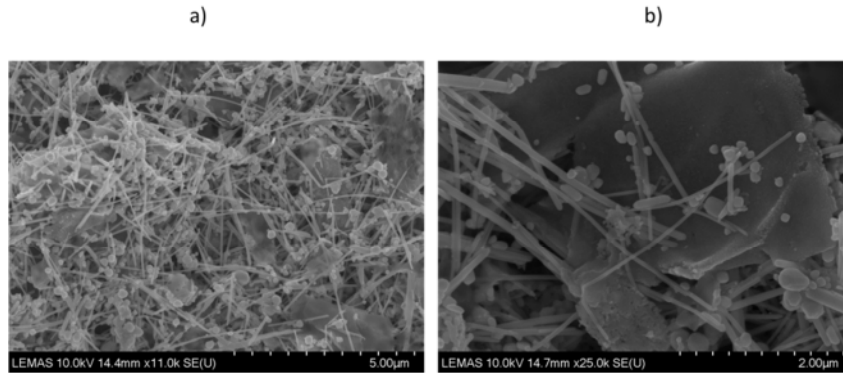


Figure 3.40: SEM images of cells fabricated using a pre-fabrication mixture of AgNW and CdSe NCs.

3.10 Ageing

Operational lifetime is a significant factor for any energy generating technology and is a pertinent issue for other third generation solar cells [154-157]. In terms of the developed, novel solar cell, TiO_2 is a robust material that is unlikely to degrade over time [158-160]. However, NCs can react with oxygen and moisture in the air [76, 161]. This NC ageing can be attributed to development of surface states upon the NCs which act as recombination centres, leading to degradation [160]. Silver also has known issues of oxidation and sulphidisation with time [161, 162].

Typical NC Schottky barrier solar cells are known to degrade in air within minutes [163]. Two main mechanisms have been postulated for this degradation. The first is through the loss of the typically labile passivating ligands with time. The use of more robust ligands has been shown to reduce degradation [163]. The second is at the NC-metal interface where it has been shown that metals can oxidise and also react with the NC ligands causing degradation. This degradation of the metal results in a degradation of the Schottky barrier, causing a reduction in the spatial extent of the depletion region and also introduces trap states at the interface that serves as recombination centres and also hinders electron transport [76, 161, 163]. This demonstrates the need for careful choice of ligands so that NCs are suitably passivated but the metal isn't degraded. However, it should also be noted that some oxidation has been shown to be beneficial as it has been found that the formation of NC oxides can play an integral step in increasing V_{oc} and EQE [74].

With respect to choice of metal contact, it has been found that using a metal with a deep work function such as Au or Ag rather than Al helps to prevent degradation through a significant improvement in stability in air. For example, the use of Ag contacts over Al has been found to result in no rapid catastrophic decay in air [161].

3.10.1 Results

In this section, the performance of primitive and activated cells are assessed over a variety of metrics. Figure 3.41 shows how the EQE under UV light changes over a period of two months. It can be seen that the performances of primitive cells stays relatively constant with perhaps a slight increase whereas the activated cell exhibits a sharp decrease with time up to a point of 25 days at which point, the EQE starts to gradually rise again. Over the period of measurement, the EQE of the primitive cell when illuminated by UV light showed a 35 % decrease. This decrease in the activated cell was 77 %.

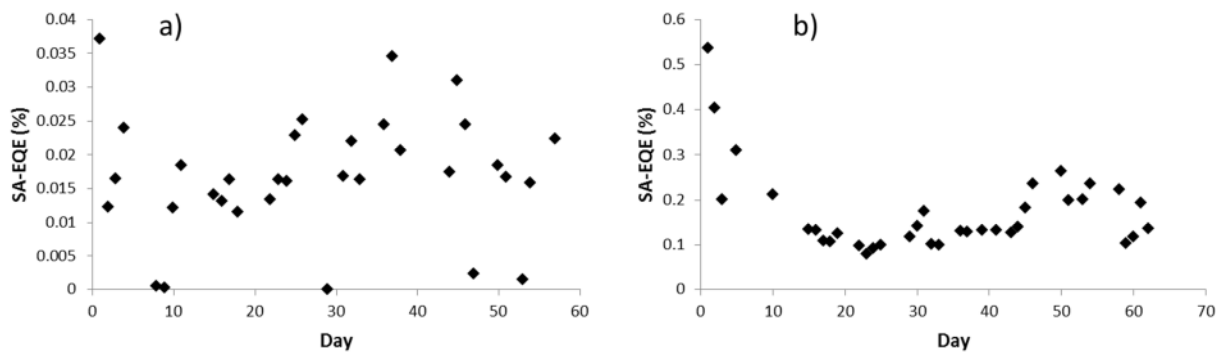


Figure 3.41: EQE under UV light of a typical primitive (a) and activated (b) cell.

When considering the photovoltage, the primitive and activated devices again show different trends. The primitive device shows a steady increase in photovoltage as the number of days increases whereas the activated device initially increases up to a maximum at 25 days before decreasing again. This is shown in Figure 3.42. All of the photovoltage plots for one activated device are shown in Figure 3.43, it can be seen that all curves follow the same shape but the amplitude of the response under UV light can vary considerably as time progresses.

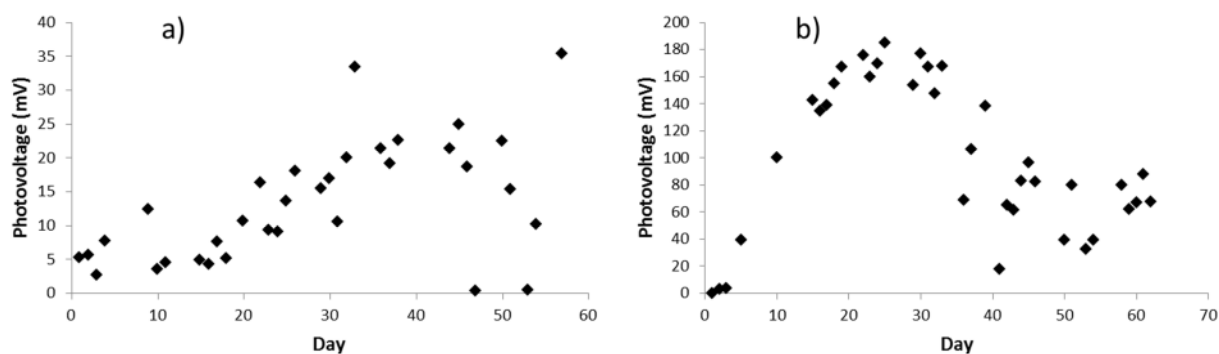


Figure 3.42: Photovoltage under UV light of a typical primitive (a) and activated (b) cell.

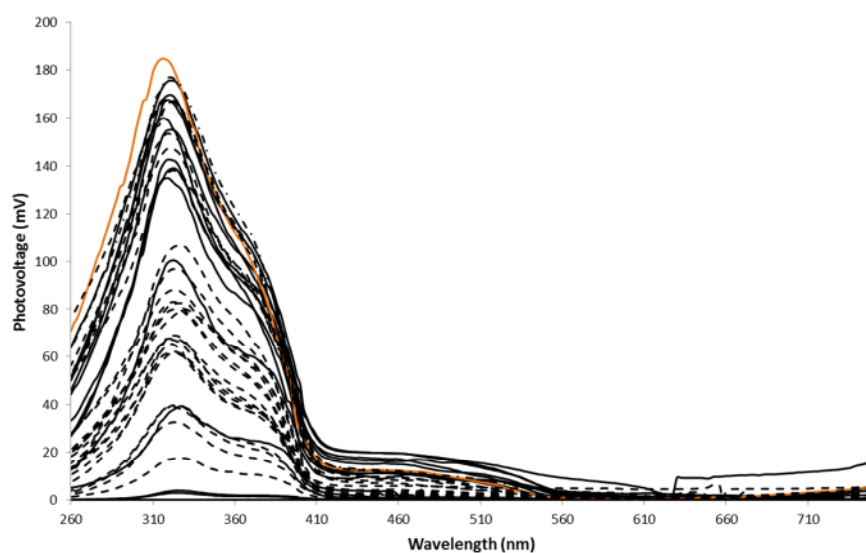


Figure 3.43: Photovoltage of an activated device for every day of measurement. Days less than the 25th day are solid black, the 25th day is orange and days after the 25th are dashed black.

For the activated device, it is also possible to examine the performance under visible light. Figure 3.44 shows how the NA-EQE and photovoltage changes over time. It can be seen that the photovoltage plot exhibits a similar trend to that shown in Figure 3.42. While not exactly similar, the EQE when illuminated with UV light and when illuminated with visible light both exhibit a downward trend. This shows that when considering the photovoltage, the ageing of the cell is affecting the charge generated in the TiO_2 and charge generated in the NCs in the same way and therefore this effect may be brought about through a change that will be common to both materials such as a change in the Ag nanomesh which accepts holes from both the TiO_2 and NCs. The EQE shows a similar ($\approx 75\%$) decrease under both types of illumination. However, the rate of change with respect to time is different. This suggests

that there is a detrimental effect happening upon both TiO_2 and NCs but that they are effected by the change at a different rate.

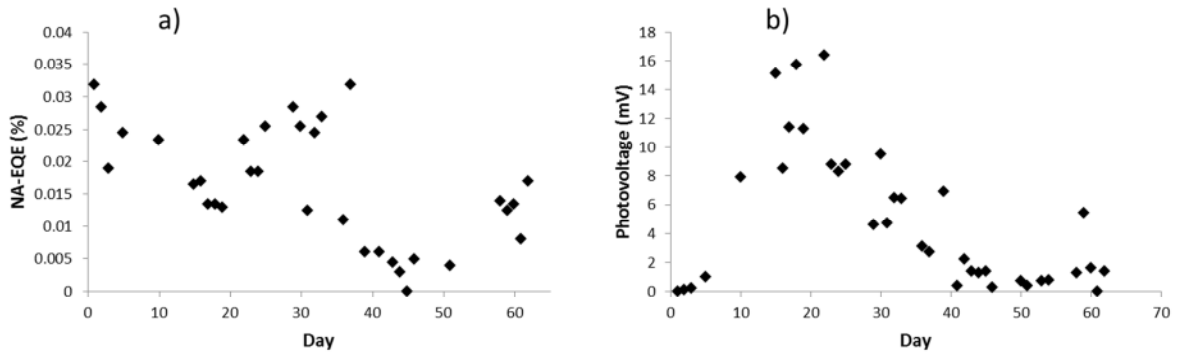


Figure 3.44: Photocurrent and photovoltage of a typical activated cell under visible light.

Similarly to the photovoltage and photocurrent, the maximum current density shows different trends for the primitive and activated cells. As shown in Figure 3.45, primitive cells display a decreasing maximum current density up to an age of around 25 days at which point, the maximum current density remains constant whereas, for activated cells, the maximum current density initially remains constant up to an age of around 30 days at which point it starts to increase.

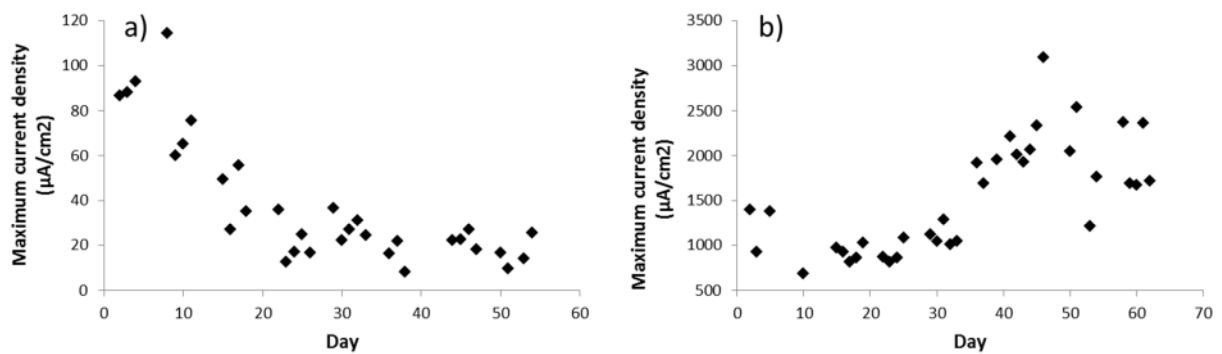


Figure 3.45: Maximum current density produced under generation of IV curves for a typical primitive (a) and activated (b) cell.

Through analysing each individual IV curve, the series resistance and leakage resistance can be determined. Figure 3.46 illustrates how series resistance changes over time for a typical

activated and primitive cell. It should be noted how the shape of these curves are very similar to those displayed in Figure 3.42.

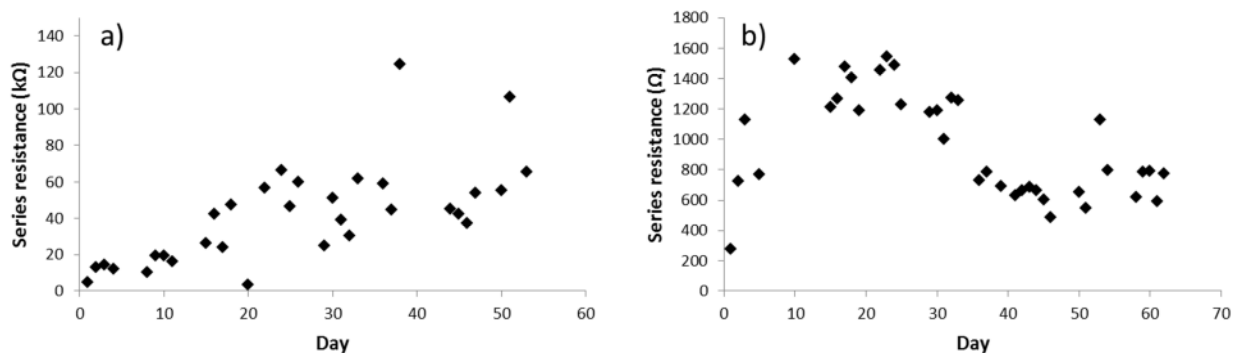


Figure 3.46: Series resistance of a typical primitive (a) and activated (b) cell.

The same curve shapes are also exhibited in Figure 3.47 which shows the leakage resistance as a function of time. It is therefore apparent that as the photovoltage, leakage resistance and series resistance all follow the same trend, they must be linked.

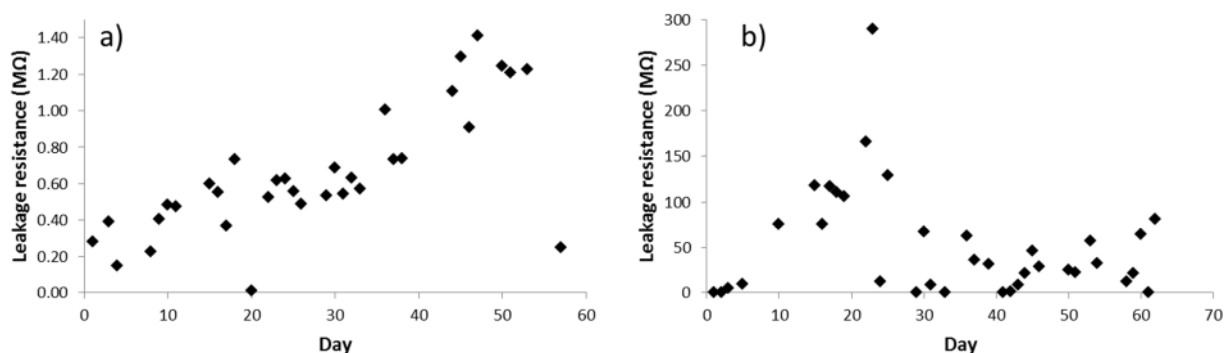


Figure 3.47: Leakage resistance of a typical primitive (a) and activated (b) cell.

Both resistances are affected by the physical properties of the cell material. These properties can change with age. When the leakage resistance increases, the EQE should increase in a similar fashion. The opposite is true for the series resistance where an increase in series resistance will lead to a decrease in EQE. The two resistances have the opposite effect on the EQE to each other and therefore when following the same trend as is illustrated, one will counteract the impact of the other. This therefore explains the relative flatness of the EQE curves when compared the resistance curves. It can be seen that the primitive device exhibits

a slight increase in EQE with time suggesting that the leakage resistance is having a more dominant effect. As opposed to following the shape of the resistance curves, the EQE of the activated device under UV light seems to show an inverse shape therefore indicating that the series resistance is the dominant mechanism in this instance.

It is however more difficult to explain the EQE of the activated device when illuminated by visible light which while displaying noise, shows a linearly downward trend with time that isn't shown in the resistance plots. This is perhaps because the series and leakage resistances that are obtained will be dominated by the properties of the bulk, primitive device and are therefore not applicable to charge movement between the NCs and Ag nanomesh.

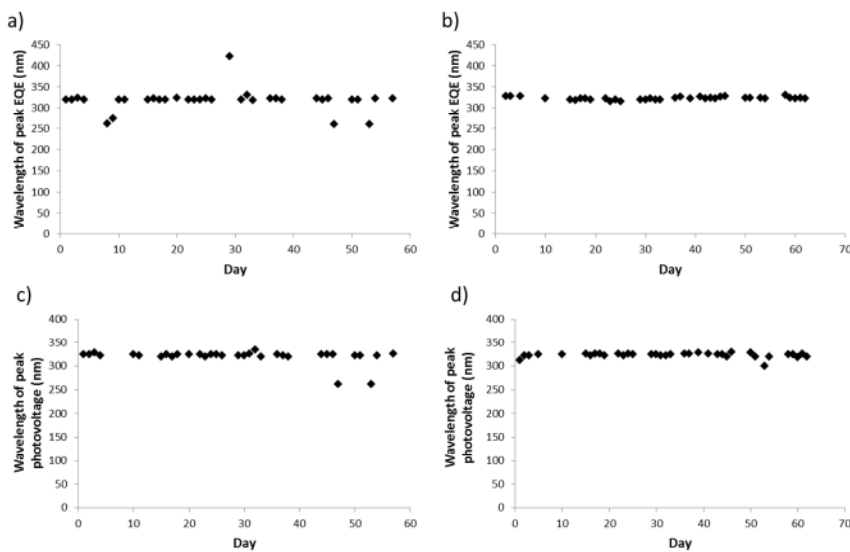


Figure 3.48: Position of peak UV EQE (top) and photovoltage (bottom) for primitive (left) and activated (right) cells.

Figure 3.48 shows the position of the peak response of the solar cells, both for the photovoltage and EQE. These positions are determined by the band gap of TiO_2 with these results therefore suggesting, as would be expected, that the band gap of TiO_2 is not changing with time. However, as shown in Figure 3.49, the position of the response of the nanocrystals does change with time. It could be logical to suspect that NCs would grow with time and with growth, a redshift in response towards the bulk band gap value would be observed. The opposite is in fact observed. A possible explanation for this phenomenon can be attributed to oxidation of NCs. Oxidation of the surface would lead to a semiconducting core that becomes smaller with time, this results in the observed blueshift.

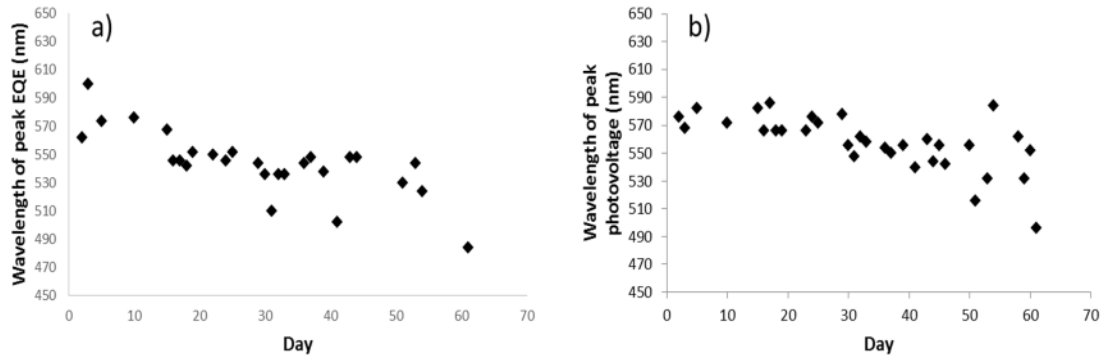


Figure 3.49: Wavelength of initial EQE (a) and photovoltage (b) response.

After electrical measurements over a period of two months, the devices were observed through SEM. Figure 3.50 shows a typical SEM image and EDX map of an aged primitive device. The cell appears no different from cells that are imaged immediately after fabrication. As discussed previously, one would expect oxidation and/or sulphidisation of the silver nanowires. EDX spectroscopy however shows no sulphur signal and that the oxygen map correlates very well to the titanium map, as is expected for the TiO_2 bulk surface. It may be however that the wires have oxidised to some extent but any oxygen response from the location of the wires will be negligible when compared to the oxygen response at the location of the TiO_2 .

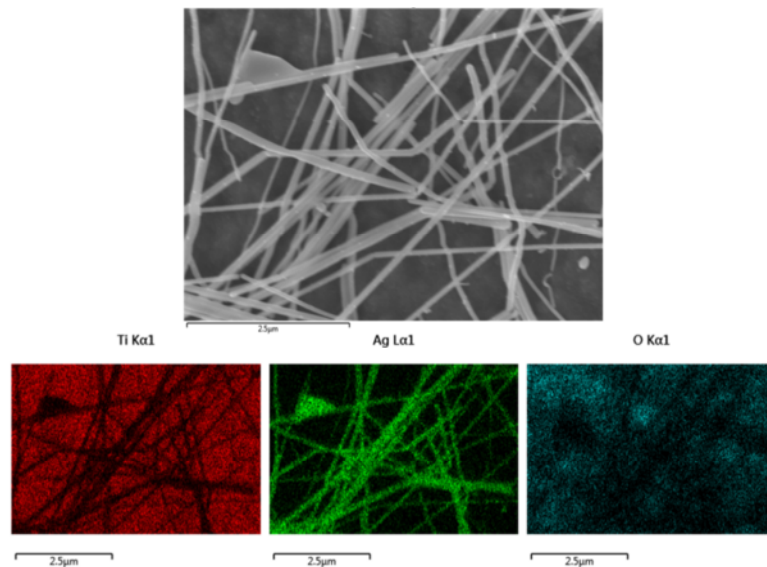


Figure 3.50: SEM and EDX of a typical primitive device after two months.

Next, activated devices were observed through SEM and as illustrated in Figure 3.51, a prevalent carbon film was visible through both forms of imaging. As this film is not observed in primitive devices, it must be concluded that its occurrence is due to the deposition of NCs, possibly due the presence of excess ligands that contaminate the NC solution.

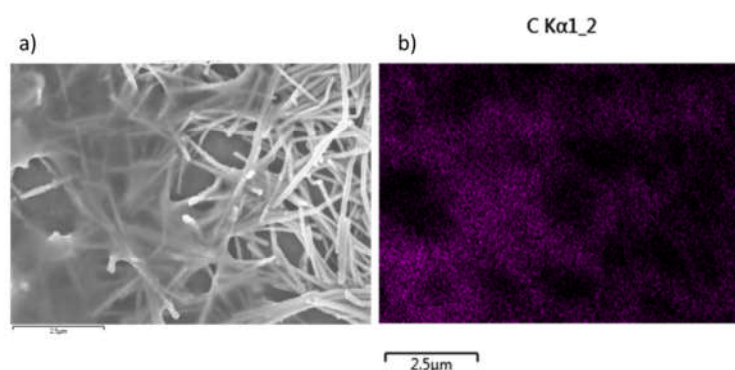


Figure 3.51: SEM (a) and carbon EDX mapping (b) of a typical activated device after two months.

Figure 3.52 shows a more in-depth EDX analysis of a typical 2-month old activated device. Again, the oxygen and titanium response is the inverse of the silver response which is as expected. A Te response is present from the CdTe NCs used for activation as well as the previously discussed carbon response. However, there is also a sulphur response which isn't present in EDX mapping for newly-fabricated activated cells, nor is it present in Figure 3.50. These results indicate that NC deposition is responsible for undesired cell alteration in two ways, first it promotes the coverage of a carbon film and secondly, it enables age-induced sulphidisation of the Ag nanomesh. One could suspect that this may be due to the previously discussed effect of ligands reacting with the metal contact. However, this can't be true as the COOH functionalised alkanes used in capping CdTe contain no sulphur. The sulphur is therefore most likely present through reaction with air. These carbon and sulphur processes may explain why the activated cell shows an enhanced degradation in EQE over the measurement period when compared with a primitive device.

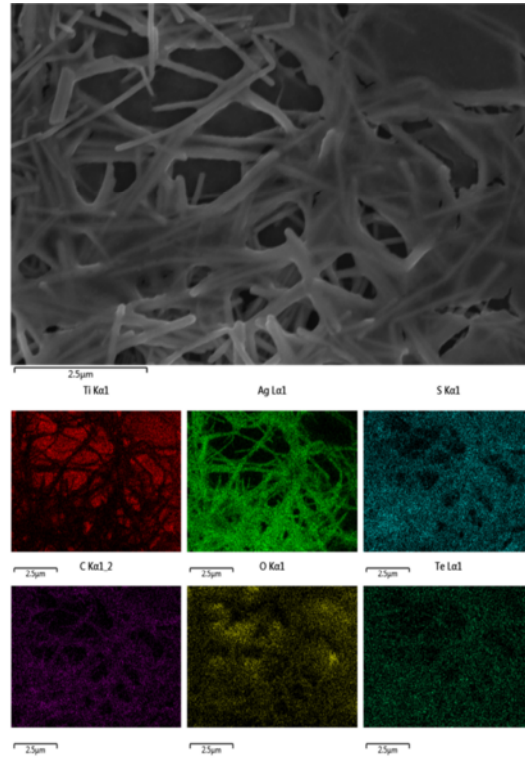


Figure 3.52: SEM and multi-element EDX mapping of a typical activated device after two months.

Despite showing significant degradation, the demonstrated primitive device performs favourably when compared to the typical NC Schottky barrier design which has been shown to suffer almost complete degradation in air within minutes or days [161, 163]. Even when using a silver contact, degradation still reduces NC-SB cell performance by 40 % in less than 100 hours [161]. A 35 % reduction over 60 days is significantly better. However, when activated, a 40% reduction in 5 days is observed. This therefore highlights the detrimental effect NCs have to the Schottky barrier cell. Indeed, when considering the performance of an activated device under visible light, the change in EQE may be attributed to a multitude of processes including: loss of ligands, oxidation due to ligands, change in NC shape, promotion of carbon film and sulphidisation of the Ag nanomesh.

Electrodes have been identified as the significant source of ageing, and once replaced, it is possible that a typical NC Schottky barrier cell will only show a minor degradation in performance [73]. Through replacing the electrodes, the EQE has been shown to decrease by 20 % over a period of 6 months [74]. This is a stark improvement over the previously discussed degradation which takes place over a period of hours. However, replacing the electrode may prove impractical for the proposed design, especially when decorated with NCs.

While silver has been shown to be better than Aluminium, it is still clearly a cause of degradation in the demonstrated cell design. The introduction of an intermediate material between the semiconductor and metal layers such as a thin LiF layer may prove beneficial. This has been shown to improve cell performance through increasing the leakage resistance and decreasing series resistance [161].

3.11 Conclusion

When considering device optimisation, there is a play-off between maximising the response under visible light and avoiding a short circuit. This is first observed when optimising the load of silver where 20 μL of the AgNw suspension at a concentration of 2.5 mg/ml was chosen to be the standard. This was despite the possibility of a higher loading leading to a greater performance and was selected to ensure that a short circuit is avoided.

Experimentation when considering the optimum loading of NCs was also found to affect the rectifying properties of the cell. The optimum NC loading was found to be dependent on the material considered. This may have been as a result of the different solvents used for each NC material as it was observed that the response under UV light was also affected by repeated depositions of NCs. Taking the whole suite of results in to account, it seems that where possible, water should be used as the solvent and chloroform avoided. It is also a possibility that a high volume of any liquid starts to have a detrimental effect and therefore solvent use should be kept to a minimum where possible.

Towards the end of this research, a paper by Law et al. came to the attention of the author [66]. It was suggested that if the NC layer is too thick, a 'dead region' of NCs will be created where if a photon is absorbed within this region, there is a much greater chance of recombination. The fraction of light absorbed in the dead region increases with decreasing wavelength and therefore higher energy photons are more likely to be absorbed within said region. As a result of this, any excitons produced through these high energy photon absorptions will be more prone to recombination. This could also explain the drop in EQE at lower wavelengths exhibited by the demonstrated cells at and also suggests that the NC loading is too high. A further study of NC loading but at significantly lower loads may therefore be beneficial.

Despite the possibility of creating incomplete nanomeshes, it was expected that shorter wires (those with a lower aspect ratio) would increase the available area for NCs to be in contact with both silver and TiO_2 , this would therefore increase the photocurrent produced by the device. It was found that short-wire cells in fact had a greater maximum current density produced from IV curve generation. This indicates that there was a greater surface area of

silver in contact with the TiO_2 with the short wires. One possible explanation for this is that long wires have a greater potential to rest on top of another wire therefore while maintaining the electrically conductive mesh, it does not contribute to increasing the Ag- TiO_2 interface area. Short-wire activated cells give a marginally worse relative photocurrent under visible light but the relative photovoltage is marginally better. Cells that functioned through a nanomesh consisting of bonded short wires were also found to have noisier results and nanomeshes fabricated from long wires were selected as standard. Filamentary structure was proposed to enhance contact area between NC and NW. However, results were negligible.

The deposition order of nanowires and nanocrystals was also investigated. Despite potential improvements through the ability to thermally remove native ligands, depositing NCs before the Ag nanomesh results in a worse device. Mixing of the two nanomaterials before deposition is also possible. This also allows investigation in to the optimum NC loading without solvent use being a contributing factor. Increased NC loading does lead to an increased EQE under visible light. However, despite the reduced influence of solvent, it is still found that increasing NC density decreases EQE under UV light. This may be attributed to NCs absorption of UV photons that would otherwise contribute to electrical output through charge separation at the TiO_2 and Ag boundary. Increased NC density also leads to a decrease in photovoltage under both visible and UV light. Compared to the standard deposition route, mixing of nanomaterials before deposition is found to result in worse performing solar cells, this may be due to NCs interfering with the contact between AgNWs and TiO_2 . Pre-fabrication mixing is unachievable as the high temperatures required destroy the NCs.

The performance of primitive and activated cells was investigated over time. It was found that NC decoration affected how the cells aged. The presence of NCs enhanced sulphidisation of AgNWs and also resulted in the formation of a carbonaceous film over the top of the cell. The response of the NCs is also found to blueshift with time. As the photovoltage of both primitive and activated cells are affected in similar ways, the change with time of the Ag nanomesh is most likely the significant contributing factor. However the change of EQE with time is dependent on whether the cell is primitive or activated and therefore is most likely determined by changes in the TiO_2 and NC material.

4 Device Optimisation by Nanocrystal Modification

4.1 Introduction

Due to their large surface area to volume ratio, the surface of NCs plays a prominent role in its properties. Surface modification and control is therefore a key way to manipulate the properties of NCs for a desired result. This chapter begins by introducing the effect that NC surface modification can have on cell performance before introducing and evaluating various modification techniques. Finally, it concludes.

To ensure that NCs stay suspended, well dispersed and don't agglomerate, it is necessary to utilise ligands in most NC applications. Ligands, as shown in Figure 4.1, are acids and other chained molecules that through either steric or electrostatic repulsion, prevent NC particles from coming in to contact with each other [164]. For a 5 nm NC there will typically be 296 atoms at the surface and 204 ligands, equating to a typical NC surface coverage of 69% [164]. When not present, it has been shown that degradation of NC solar cells is promoted due to the ready access of water and oxygen to the undefended NC surface [76]. This highlights the importance in considering ligands in any NC solar cell.

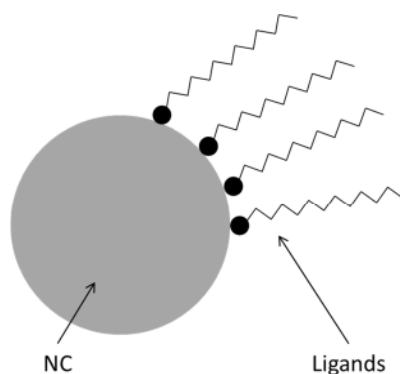


Figure 4.1: A nanocrystal encapsulated by ligands.

As well as preventing agglomeration, ligand use has other effects, some desired and some undesired. For example, solubility of the NCs is determined by the choice of ligand. Some Ligands are soluble only in polar medium whereas others are soluble only in non-polar solvents [165]. It has been noted previously that the solvent used during NC deposition can have a significant impact on cell performance. Through ligand exchange, the potential exists to disperse NCs in new solvents therefore removing the need for chloroform and instead creating the possibility to use the more beneficial water.

Since they are typically electrical insulators, combined with any polar electric fields that they create [166], ligands also have an influence on carrier transportation [167]. Other factors that are affected by ligands include luminescence, optical transparency, prevention of trap states caused by ageing [168] and surface adsorption rate [82].

The advantageous use of plasmon resonance in the nanomesh is also tuneable through ligand choice. The impact of plasmon resonance is a function of the distance of the impacted material from the noble metal which depending on separation, can either enhance or quench NC photoluminescence [169]. This separation can be dictated through choice of ligand and therefore presents an opportunity of optimisation. Further to plasmon optimisation, Förster resonance energy transfer (FRET) is another area that presents itself to be optimised through ligand use. The efficiency of energy transfer through FRET is inversely proportional to the distance to the power of six [170]. Any Reduction in NC separation through the use of a shorter chained ligand molecule will therefore greatly increase the impact of any FRET taking place.

Care should be taken when assessing if ligand replacement results in a closer packing of NCs as while this can cause a redshift in the optical absorption properties [171], this redshift may also be caused by a change in the dielectric environment around the NCs [172] or through Ostwald ripening if any heat has been applied.

A further potential for ligand utilisation is through linker assisted self-assembly. Here, a ligand will have two functional groups, one which strongly adheres to the NCs and the other that will enhance NC adsorption on to a surface. Thus a monolayer surface coverage is promoted [67]. This has been shown to influence the efficiency of interfacial electron transfer [173]. The correct choice of linker molecule can also be used to effectively passivate defects [174]. Such defects can reduce the SBH by up to 80% of the original level [139].

Table 4.1: Native ligands of the NCs used in this study.

Material	Solvent	Ligand
CdS	Toluene	Oleic acid
CdSe	Toluene	Hexadecylamine
CdTe	Water	COOH functionalised alkanes
CuInS ₂	Chloroform	Dodecanethiol

Table 4.1 lists the native ligands (NLs) that were incorporated on to the NCs used in this study and Figure 4.2 illustrates their molecular structure. It can be seen that each ligand used consists of a molecular chain that has a functional group (e.g. thiol, amine) attached to one end. This functional group is used to bind to either the NC or the surface that the NC is adhering to. Upon binding, the ligand is deprotonated [175]. Within this short list, there exists significant differences already. For example, thiol based ligands have been found to quench the fluorescence of CdSe NCs while amines at low concentrations enhance fluorescence [176]. It should be considered that while a decreased photoluminescence yield suggests a longer exciton lifetime, this doesn't necessarily directly relate to an increased cell quantum efficiency, other indirect recombination paths may also open up.

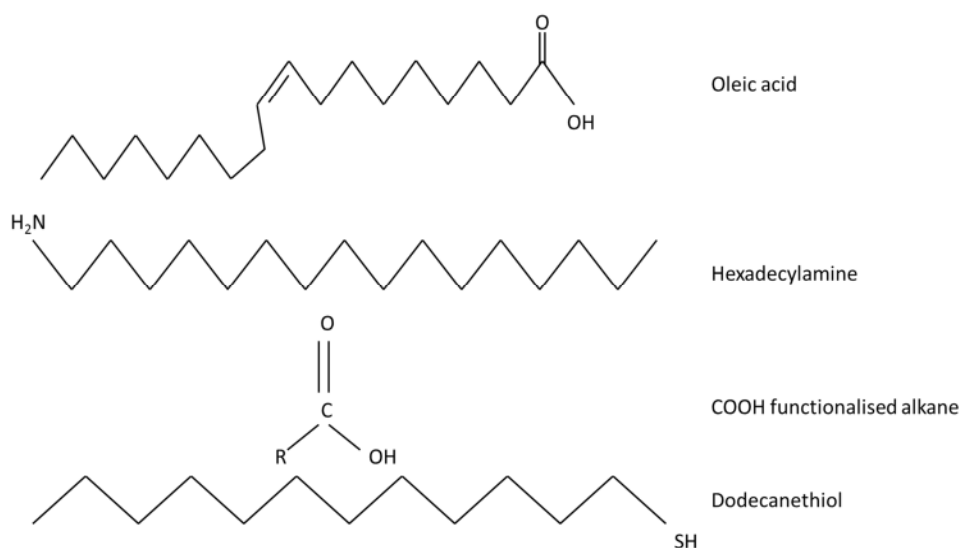


Figure 4.2: Molecular structure of the native ligands of the NCs used in this structure.

Ligand replacement therefore creates opportunities to use the ligand that is best suited for solar PV use. This would be a ligand that prevents agglomeration and crystal growth but has minimal electrical resistance and also has a high optical transparency. However, the choice of correct ligand will be a balancing act between all the previously mentioned properties. For example, while one type of ligand may facilitate a higher loading of NCs on to the desired surface, it may reduce the rate of electron injection in the system [177].

However, there can be issues with ligand replacement, typical problems include that replacement ligands can be toxic and/or corrosive, films of NCs can be difficult to perform ligand exchange upon due to diffusion limitations [178] or that the film can crack due to volume changes [179].

Another form of NC surface modification is through the use of core-shell NCs, as shown in Figure 4.3. Shells formed around semiconducting inorganic NCs are typically other inorganic semiconductors with a similar lattice constant but with a different band gap. A heterojunction therefore forms at the interface between the core and the shell.

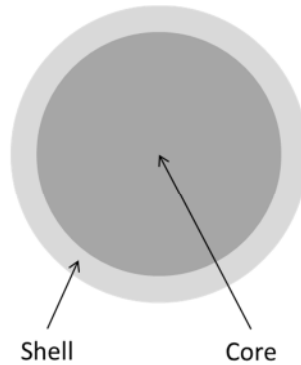


Figure 4.3: A nanocrystal comprising of a core encapsulated by a shell.

Shells are frequently utilised for band gap engineering to increase fluorescence of NCs in biomedical applications [180-182]. This incorporates a Type I shell as demonstrated in Figure 4.4 where electrons and holes are trapped within the core of the core-shell NC and recombination is therefore encouraged.

While type I structures encourage exciton radiative recombination, type II structures can be used to encourage charge separation. Type II structures reduce overlap between the electron and hole wave-functions, decreasing the rate of direct recombination and therefore potentially improving the efficiency of charge extraction for the solar cell. It has however been noted that since type II structures hold an increased chance that a charge carrier will be found in the shell region of the particle, there will be an increased chance of an unwanted interaction with surface trap states [183].

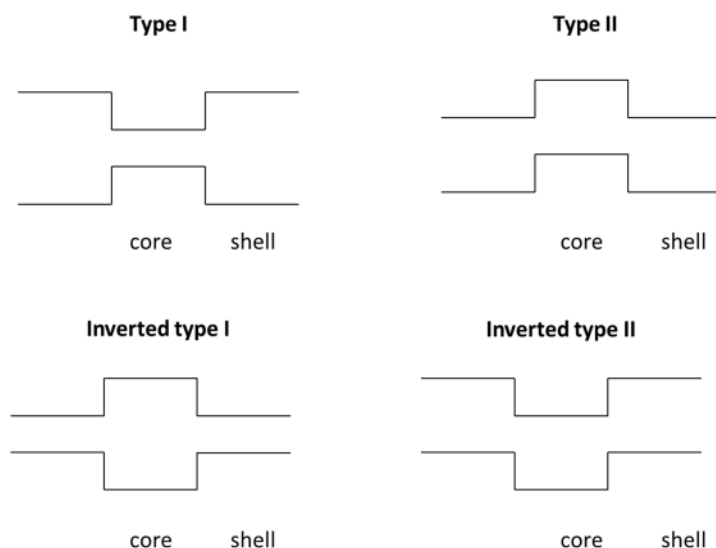


Figure 4.4: Band gap structures formed in core-shell NCs.

Care is needed when selecting core and shell coupling as lattice mismatch can cause strain which can change the core size resulting in a change in the conduction band and valence band levels [184]. This change in levels can be so significant that what was intended to be a type I structure may in practice be a type II and vice-versa [185].

Core-shell type NCs will still have ligands to prevent agglomeration and the two surface modifications are not mutually exclusive.

The simplest method to accomplish ligand removal is through thermal annealing. This involves raising the temperature above that of the decomposition temperature or boiling point of any ligand used. This is, as mentioned previously, unsuitable for this study as the AgNWs will be deformed, losing the use of the nanomesh as an electrode [186]. Furthermore, there is also some debate about the efficacy of this method [187]. However, it has been found that even moderate heating irrespective of whether the temperature is above the boiling point of the coating ligand or not can be beneficial, with Drndić et al. [172] finding that despite 350 °C and a 35 minute heating time being the optimum conditions, even heating at 110 °C for 5 minutes was shown to bring an improvement in photocurrent and this therefore may still be a viable avenue. Care must also be taken as annealing can lead to sintering of NCs and the generation of undesired carbonaceous species through partial ligand pyrolysis [188].

Ligands can be swapped through the relatively simple process of ligand exchange. Ligand exchange occurs where a NC with native ligands is exposed to an excess of new ligands and heat is applied. The NC will take up the new ligands if kinetically favourable [164]. Care

must be taken so as not to enter a ripening regime, causing NC growth through the application of excessive heat. Ligand exchange can also result in a reduced stability in air of NCs. The surface of some NCs including CdSe can also undergo adverse photooxidative reactions [189] leading to deterioration. After ligand exchange is complete, purification must be performed through precipitation and redispersion in an applicable solvent. However, some reports state that purification can inadvertently remove the newly applied ligands [168]. Care should also be taken to never allow precipitated particles to fully dry as drying causes irreversible agglomeration [186].

4.2 Application to Solar Cells

Many ligands have been found to improve the passivation of NC surfaces [190]. However, the process of selecting the right ligand through ligand exchange to optimise the properties of the selected NCs for PV use holds a much more significant impact. Zhang et al. [191] found that through converting the ligand used from oleic acid to octylamine, the photocurrent of their cell increased up to 100 times under a -1 V bias this can lead to a 600-fold increase in maximum power output. This exchange leads to a blue-shift of absorbance [191]. It is also found that annealing at 220 °C results in complete quenching of PL meaning rapid exciton dissociation. A temperature of 220 °C may be low enough so as to maintain the Ag nanomesh of the demonstrated device.

The replacement of oleic acid with pyridine has been reported to be straightforward with a resulting redshift of NC response and a more efficient hole transfer from the NC [192]. Replacing TOPO as a ligand with pyridine has also been found to increase performance, further to this, heating the now pyridine coated-NCs to the achievable temperature of 120 °C has proven to increase the EQE by a factor of 6 [193]. This increase was explained by the removal of both interfacial and excess pyridine which acts a non-radiative recombination site. Interfacial surfactants are known to hinder transfer of charges between components and therefore the removal of these ligands through heat facilitates greater charge transfer. Letherdale et al. also studied the replacement of TOPO with pyridine and observed a 10 times improvement in EQE for CdSe NCs [194]. However, care should be taken when choosing pyridine as a ligand as it is relatively labile and therefore detachment with time will put at risk the passivation of the NCs [163, 195].

Being a shorter chained molecule than oleic acid, Mercaptopropionic acid (MPA) holds potential as a NC ligand. MPA is a bifunctional linker with the first functional group (thiol) enabling tight binding to the NCs and the second functional group (carboxylate) offering preferential adsorption on to the TiO₂ [196]. This theoretically promotes a monolayer coverage [67]. Furthermore MPA can also be used to control the pH which provides a

potential method of controlling the quantity adsorbed on to the TiO_2 surface. A high pH causes TiO^- to become dominant at the surface therefore resulting in a Coulombic repulsion between the surface and NCs, thus hindering efficient absorption [83, 197]. It has been found that in NC- TiO_2 interactions, ranging the pH from 7 to 5 changes NC coverage from a poor coverage to agglomeration of NCs upon the surface. A pH of 6 was found to result in a monolayer coverage [83].

There also exists potential to replace organic ligands with an inorganic capping shell such as SiO_2 [198] or metal sulphides [199]. Said inorganic shells differ from the shells used in core-shell NCs in that they are for the same external purpose as organic ligands as opposed to affecting the band structure of the NC. Over organic ligands, they hold advantages in that they allow for an increase in electronic coupling between NC and the adhered to surface. Inorganic capping shells also allow for harsher processing conditions. However, these methods can entail the use of toxic chemical detergents [198]. Inorganic capping shells have been proven to lead to an increase in electronic coupling compared to organic connections which leads to increased exciton dissociation [199]. Tetrafluoroborate salts have also been shown to stabilise NCs with no observed aggregation or precipitation as well being stable in polar solvents [200, 201].

As well as ligand exchange, ligand removal holds various advantages and disadvantages. The most apparent of which is completely removing any electrical impedance to charge transfer. Complete ligand removal will however result in a loss of solubility. It is proposed that since the ligands will be deprotonated when attached to a NC film, if the pH at the interface between them is lowered to a certain value, the ligands should re-protonate and therefore detach from the NCs [175]. Strong acids such as HCl and H_2SO_4 can therefore be utilised to perform ligand removal.

The idea of type II structures is that the band alignment is such that it efficiently assists the charge separation of excitons. One such example of this is CdTe core with CdSe shell. This is the type II structure that is seen as one of the most suitable for PV [183, 184]. It is possible to grow these structures within normal lab conditions. The process is however convoluted and requires multiple steps and processes. It has been shown that exciton lifetime increases with shell thickness indicating that the core-shell structure is driving the charge separation process and “thus providing additional active pathways for non-radiative recombination which is competing with radiative luminescence” [202]. It has also been shown however that cells consisting of type II NCs can have undesirably low efficiencies and this is attributed to high non-radiative recombination losses that can occur extremely quickly when compared to radiative recombination in type II NCs [183].

It has been found that any shell layer on CdTe results in an improved efficiency when used in a QDSSC [202]. In QDSSCs, CdSe core with CdS shell NCs have been shown to have a higher I_{sc} , V_{oc} and EQE compared to core only CdSe NCs. This improvement is attributed to faster electron transport and a slower charge recombination for the core-shell system [203].

Shells can be grown on to core NC particles through successive ionic layer adsorption and reaction (SILAR) methods which can give good control over shell size. This procedure however requires argon flow conditions and high temperatures [204].

4.3 Results

Ligand modification was selected as the main focus for further study as shell growth is often incorporated in to NC synthesis [142] and therefore most methods are inapplicable to purchased NCs. However, CuInS₂ NCs were fabricated in-house and therefore a study of the shell effectiveness could also be performed.

Since each substance used as a ligand will have a unique boiling point, the use of thermogravimetric analysis (TGA) to determine ligand composition holds promise. Inorganic NCs will not be altered at the temperatures used and any weight loss within the TGA will be due to the ligands. This method however is wasteful and requires too large a sample mass for the scale of this study. Elemental (CHNS) analysis, another commonly utilised method, prevents the need to waste large quantities of sample. It can however create inconclusive results when elements appear in both the NC and ligand. For example, sulphur which is found in both CuInS₂ and in dodecanethiol. The previously used absorption and emission optical measurements as well as photoresponse measurements are the most suitable method of determining the relative performance of ligand exchange reactions.

4.3.1 Mercaptopropionic Acid

CdTe NCs capped with COOH functionalised alkanes and oleic acid-capped CdS NCs were treated to perform a ligand exchange resulting in MPA-capped NCs which are potentially better suited for PV application. These materials were selected owing to the fact that they were suspended in similar solvents and had similar native ligands as the reagents used in literature. Following the method of Chen et al., 1 ml of NCs at a concentration of 5 mg/ml were mixed with 1 ml of MPA and 1 ml of acetone in a vial. The solution was stirred continuously for 35 minutes. 7 ml ethanol was then added and the solution centrifuged at 4500 rpm for 10 minutes. The supernatant fluid was discarded and the resulting precipitate (MPA-capped NCs) was dispersed in 5 ml ethanol. 400 μ L of TMAOH in water was added to make the solution clear followed by 100 μ L of acetic acid which adjusted the pH to 6

[197]. The newly coated NCs were subsequently deposited on the primitive cell structure as per the standard procedure. The molecular structure of MPA is illustrated in Figure 4.5.

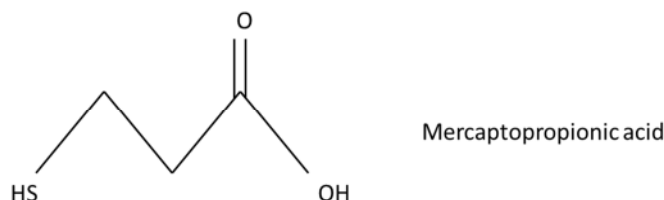


Figure 4.5: Molecular structure of mercaptopropionic acid.

The UV-Vis absorption graphs shown in Figure 4.6 display the spectra of both CdTe and CdS before and after ligand exchange. All plots show an absorption peak at wavelengths around the expected band gaps indicating that the ligand exchange process did indeed work and the resulting batch contains the same NC composition as compared to pre-processing. During the ligand exchange process, it is likely that some of the NCs are lost during purification. The concentration of the MPA-capped NCs is therefore unknown and it is therefore impossible to ascertain any information from the relative intensities of the signals because of this. It can be seen however that for CdTe that has undergone MPA ligand exchange, the response is somewhat blueshifted towards higher energies compared with CdTe NCs with native ligands. This relationship is reversed for the CdS NCs with MPA ligand exchange causing a redshift in response to lower energies. The disparity in results may be due to the respective molecular lengths of the native ligands. Oleic acid is longer than MPA whereas if the COOH functionalization is simply methanoic acid, the ligand exchange would lead to a longer chained ligand and thus a reduced packing fraction.

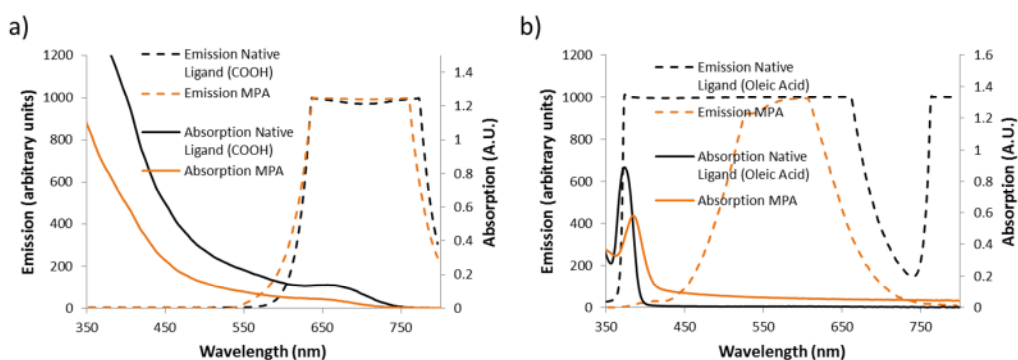


Figure 4.6: Absorption and emission spectra before and after ligand exchange with MPA, CdTe (a) and CdS (b).

Figure 4.7 displays IV curves for both primitive cells before NC deposition and the same cells once they've been activated by MPA coated NCs. It can be seen that the deposition causes a significant decrease in maximum current density. The solvent utilised for MPA-capped NCs is ethanol and as discussed previously, solvents can have a significant effect on the primitive cell. Ethanol was not considered in the study as none of the NCs with native ligands utilised ethanol as a solvent. However, the AgNW solution is suspended and deposited, in ethanol and because of this it is highly unlikely that ethanol will have a significantly detrimental effect upon the primitive cell.

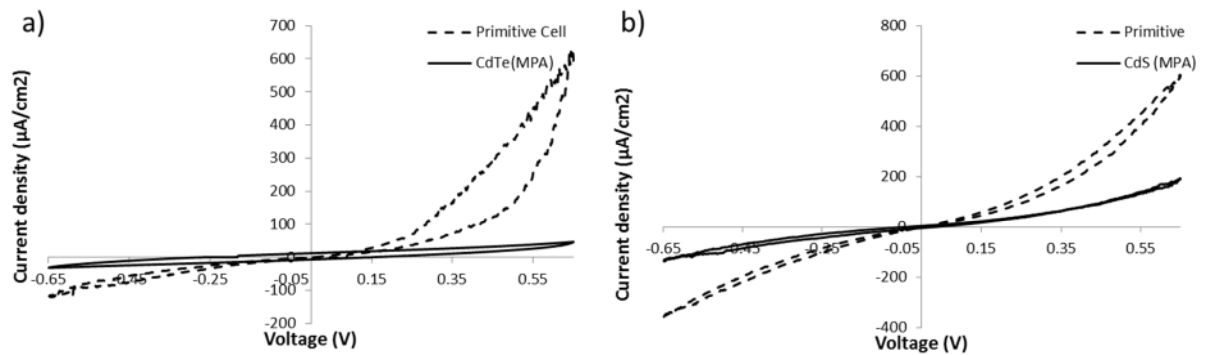


Figure 4.7: IV curves of cells before and after activation by MPA-capped CdTe (a) and CdS (b).

Figure 4.8 shows the SA-EQE and NA-EQE for cells both when primitive and after activation with MPA-capped NCs. It can be seen that the MPA-capped NCs display a significantly greater photocurrent than the primitive cells. A visible response is observed for both types of NCs which when compared with NCs capped with native ligands is significantly greater. As with native ligand-capped CdS NCs, due to a band gap of 390 nm, it is difficult to ascertain the response caused by the NCs over the response caused by the TiO_2 . There is a flattening of EQE indicative of NC response at roughly 385 nm. However, this is the same region that can be affected by plasmonic resonance attributed the Ag nanomesh.

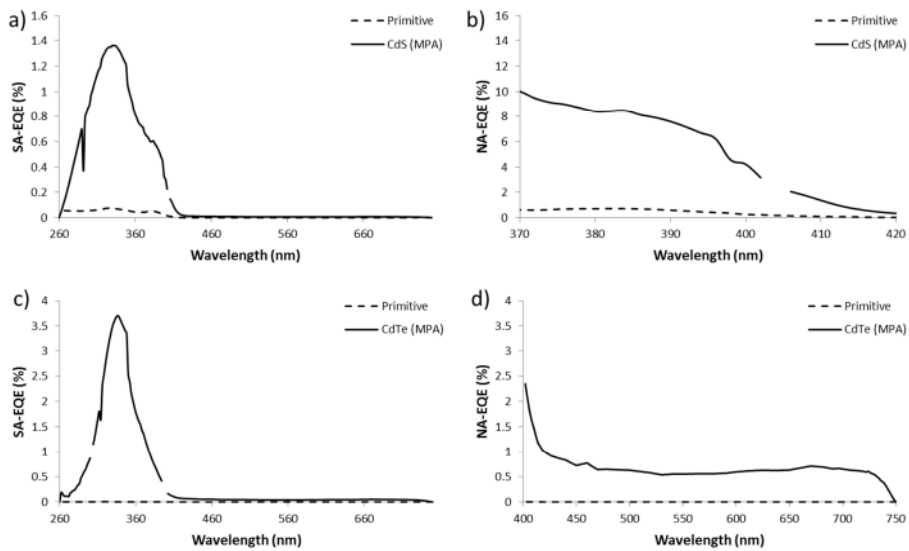


Figure 4.8: EQE plots of cells activated by MPA-capped CdS (a and b) and CdTe (c and d).

It is also however evident that as well as impacting on the visible response of these cells, the UV response is also significantly affected. The peak response for the CdS-activated NCs is improved by a factor ranging from 18 to 52 and for CdTe, a factor ranging from 130 to 800. As discussed previously, the process of ligand exchange has the potential to have significant impacts on the photovoltaic properties of NC-activated cells. However, in theory, this UV response of the activated cell should still be as a result of the interaction between the Ag nanomesh and TiO₂ bulk and therefore unaffected by the ligand associated with the NC.

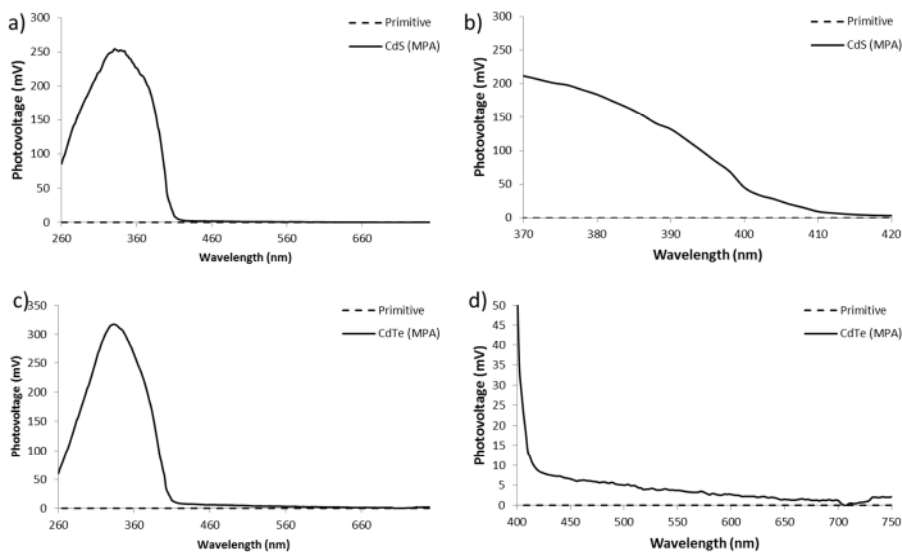


Figure 4.9: Photovoltage plots of cells activated by MPA-capped CdS (a and b) and CdTe (c and d).

Figure 4.9 displays photovoltage response of cells that have been activated with MPA-capped NCs. The same trend appears as with the photocurrent response, there is a sharp rise in performance in both visible and UV parts of the spectrum. In the UV region, the peak photovoltage increase ranged from a factor of 2 to a factor of 500. For both the photocurrent and photovoltage, the ligand exchange resulted in a redshift of the UV response. It should also be noted that the improvement in UV response when using MPA-capped NCs is the opposite of the effect when using NL-capped CdS NCs which utilise chloroform as the solvent. This indicates that some of the improvement in response may be attributed to the change in solvent.

Capping NCs in MPA evidently results in a large improvement in performance. However, as discussed, the significant rise in response under UV light is unexpected. Comparing the ratio of the EQE of a typical NL-capped CdTe-activated cell under visible light and under UV light with the ratio of a typical MPA-capped CdTe-activated cell actually shows a decrease in performance with the ratio being reduced by half. When considering the photovoltage, the Vis/UV ratio for a typical MPA-capped CdTe-activated cell is also worse, again being roughly half of a standard native ligand-capped CdTe-activated cell. Due to the difficulty in discerning the response due to the NC and the response due to the TiO₂, it is not possible to determine the Vis/UV ratio of CdS-activated cells.

It therefore becomes apparent that as opposed to increasing the relative responsivity of a cell under visible light, the relative performance is in fact worse and the overall device improvement may be in fact due to an alternative factor.

When considering the IQE, this overall device improvement is even more stark. Figure 4.10 shows that MPA-capped CdTe NCs produce cells with a very high NA-IQE. Furthermore, at some wavelengths, the NA-IQE reaches values greater than 100 %. It also should be noted that the wavelengths of light that yield these high values of IQE correlate well with the peak of the solar spectrum.

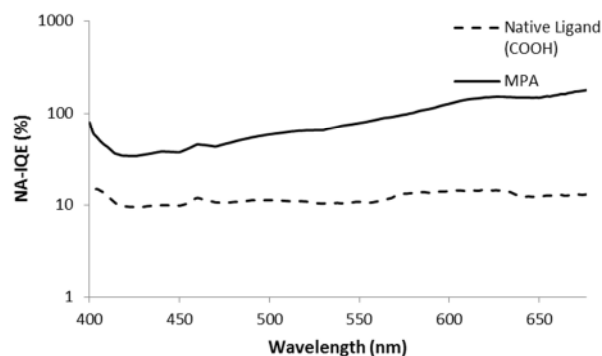


Figure 4.10: IQE plot of a typical MPA-capped and native ligand-capped CdTe-activated cell.

A NA-IQE greater than 100 % suggests that more NCs are functional than just those that are in contact with both the TiO₂ and Ag nanomesh. Possible reasons for this include a ballistic transport mechanism where hot electrons originating from NCs adhered to other parts of a nanowire are transported through the nanowires and into the TiO₂. Alternatively, holes or energy could transfer from adjacent NCs to NCs in contact with both nanowires and TiO₂, exciton diffusion is an example of this [205].

Further to an observed NA-IQE greater than 100 %, it can also be seen that the IQE decreases at shorter wavelengths. This may be due to the undesired back reaction of electrons transferring from NCs in to the Ag nanomesh becoming more prevalent when electrons are in excited states within the NC.

4.3.2 Inorganic Metal Sulphide Shell

As discussed by Zhang et al., NCs can be connected inorganically. This should create a ‘connected but still confined’ particle arrangement which increases electrical conductivity [199]. A dilute (NH₄)₂S methanol solution was made to a concentration of 4 mM, cells that were previously activated by CdS and CdTe were then soaked in the solution for 30 seconds. Again, these materials were chosen due to the similarity of the native ligands to those that were considered by Zhang et al. 30 seconds is deemed sufficient time to form the metal sulphide shell that will promote bonding to form a larger NC film assembly while still maintaining quantum confinement. The cells were then soaked in methanol for 30 s to remove any excess (NH₄)₂S and replaced organic ligand residues. This method can only be performed post NC deposition as after ligand removal, the NCs will no longer be able to be suspended in any polar or nonpolar solvents [199].

As the metal sulphide shell encapsulation is a post-deposition treatment, pre-deposition optical characterisation is not possible. The post-deposition treatment does however enable

like for like comparison in that the same activated cell can be observed before and after treatment therefore negating the influence of intrinsic cell variability in the results. This ligand replacement method was performed on CdS-activated and CdTe-activated cells, typical IV curves of which are shown in Figure 4.11.

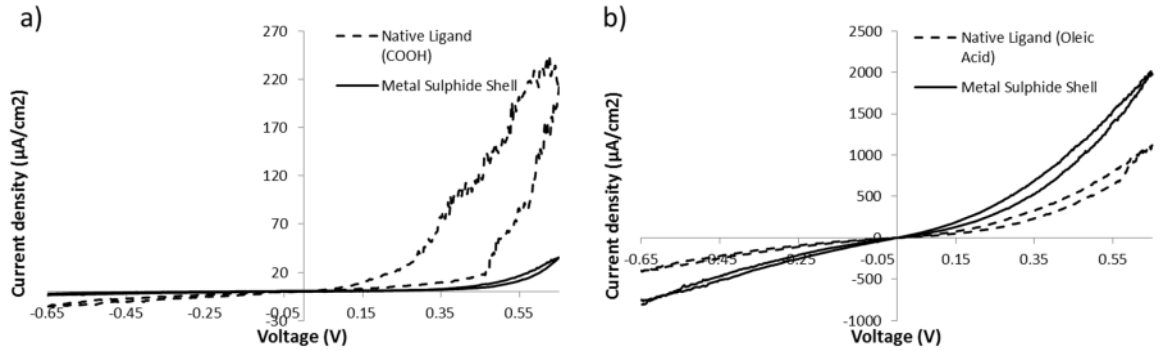


Figure 4.11: IV curves for CdTe (a) and CdS (b) before and after metal sulphide shell treatment.

It was observed that the effects of the treatment show no correlation with an equal number of cells showing an improvement and a worsening of the maximum current for each type of NC. The quality and ideality of the IV curves also show no trend with ligand exchange treatment.

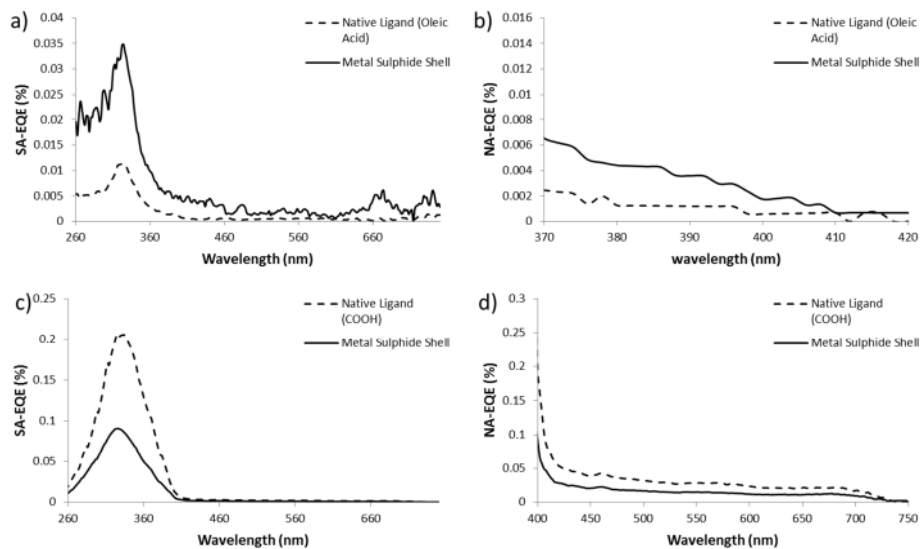


Figure 4.12: EQE plots for CdS (a and b) and CdTe (c and d) activated cells before and after metal sulphide shell treatment.

As with the IV curves, the EQE response, illustrated in Figure 4.12, also shows no discernible trend. Both the UV and visible response seems to be randomly affected. This is also true for the photovoltage, as shown in Figure 4.13.

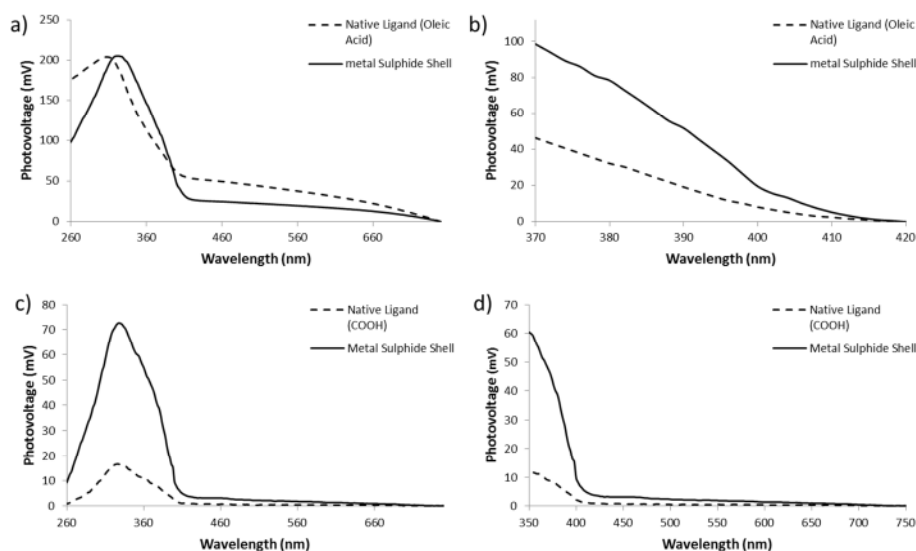


Figure 4.13: Photovoltage plots for CdS (a and b) and CdTe (c and d) activated cells before and after metal sulphide shell treatment.

Despite showing no overall obvious trend such as that seen with MPA-capped NCs, when considering the average Vis/UV ratio, cells that were treated to contain metal sulphide shell CdTe NCs have better values than the average Vis/UV ratio for cells decorated with native ligand-capped CdTe NCs. In fact, the ratio more than doubles for the EQE and the photovoltage ratio is increased by a factor of 1.5.

4.3.3 Acidic Ligand Removal

As discussed previously, ligand removal is another method to improve the electrical properties of the deposited NCs. Sulphuric acid was used to strip CdTe NCs of their native ligands. This was performed both pre-NC deposition and post-NC deposition. For pre-NC deposition treatment, 1 ml of 0.5 mg/ml NL-CdTe was mixed with a solution of 1 M H_2SO_4 that was diluted in water to a pH of 4. The mixture was left overnight until there was a visible change within the vial. With the ligands removed, the NCs are no longer able to be suspended and the NCs are precipitated, eventually sedimenting at the bottom of the vial. The mixture is then centrifuged for 20 minutes at 4500 rpm and the supernatant removed. The ligand-stripped NCs are then deposited on to a primitive cell structure. For the post-NC deposition treatment, CdTe-activated cells are left in sulphuric acid with a pH of 4 overnight

and then rinsed with water. This enables comparison of the cells before and after treatment [175].

Acidic treatment of the CdTe NCs resulted in the particles dropping out of suspension. This therefore made optical measurements of the ligand stripped-NCs before deposition unachievable since the NCs would not stay in suspension in a cuvette for sufficient a time to perform the spectroscopy runs. To apply the ligand stripped-NCs to the cells, the particles were scraped by a small pipette tip and spread on to the cell. This method is not ideal however as while it is impossible to determine the exact quantity of NCs deposited, the value will be higher than the previously determined optimum value due to the practical limits of the technique. There is also the probability that through application, the Ag nanomesh will be disrupted and parts made isolated from the continuous mesh therefore degrading performance. To compound this, the deposition doesn't result in an even coating which can lead to the NCs being relatively far from the top contact electrode which when combined with a broken nanomesh, could result in the deposited NCs being unable to make an impact.

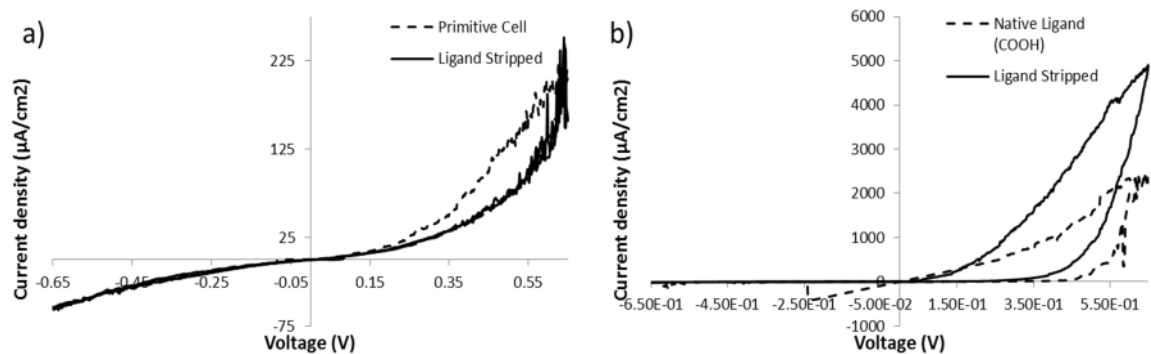


Figure 4.14: IV curves for CdTe-activated cells that have undergone acidic ligand stripping both pre-deposition (a) and post deposition (b).

Figure 4.14 displays typical IV curves of both pre and post-deposition treated NCs. It can be seen that for the pre-deposition treated NCs, there is no change in shape of curve or size of response. This is different to most of the other IV curves where some change in IV response is always observed and may be due to the fact that no solvent was used during deposition. The fact that there is no reduction in maximum current therefore indicates that the Ag nanomesh isn't damaged during NC deposition. For post-deposition treated NCs, the peak observed current density always improves after ligand stripping with the improvement ranging from a factor of 2 to a factor of 100.

The EQE as a function of wavelength for cells that have undergone acidic ligand stripping is displayed in Figure 4.15. For activated cells that have undergone post-deposition treatment, there is a slight raise in the UV response and a significant raise in the visible response. For pre-deposition treated cells, the improvement in the UV was more stark, increasing by factors ranging from 1.4 to 8. The cells however produced no response in the visible suggesting that the NCs are not performing as expected. It is also of note that all cells that were post-treated, underwent a blueshift in UV response whereas all cells that were pre-treated underwent a redshift in UV response.

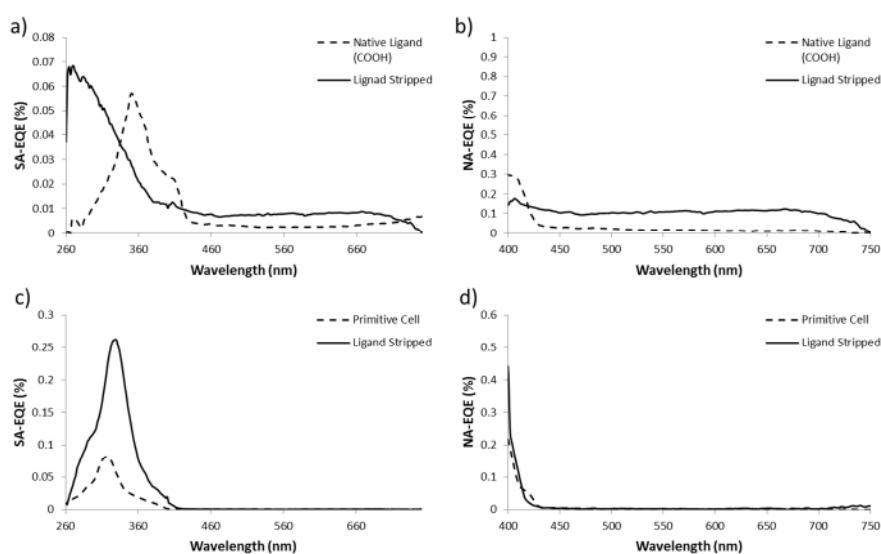


Figure 4.15: EQE plots for Post-deposition treatment (a and b) and pre-deposition treatment (c and d) of CdTe-activated cells.

Figure 4.16 displays typical photovoltage scans for cells activated with acid treated NCs. In a reverse to the photocurrent response, cells that underwent post-deposition treatment performed worse, both in the UV and in the visible, than before they were treated. The visible response is especially affected, being completely removed from the cells when the NCs contained native ligands. For NCs that were pre-treated with H_2SO_4 , when applied to activate a cell, half of the cells displayed a visible response. Further to this, all of the cells exhibited a higher response in the UV. Similar to the results of the photocurrent measurements, cells that were activated with pre-treated NCs underwent a redshift in the UV response. However, unlike photocurrent measurements, cells that were post-treated showed no trend in UV response shift with some response moving to higher wavelengths and some to lower.

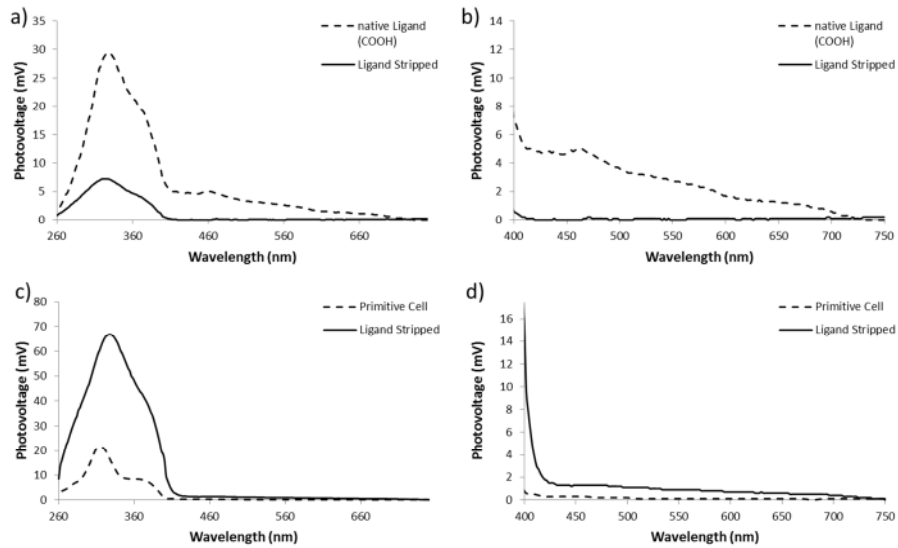


Figure 4.16: Photovoltage plots for Post-deposition treatment (a and b) and pre-deposition treatment (c and d) of CdTe-activated cells.

For cells that underwent post-deposition treatment, it was deemed unnecessary to remove the cells from the PCB with all cells that were removed from the PCB for treatment performing worse than those remaining on the PCB. This therefore indicated that the Ag nanomesh is unharmed when submerged in H_2SO_4 and more damage is done through the handling of the solar cell that is necessary to remove it from the PCB.

Further to pre-deposition ligand stripping resulting in no visible EQE, the photovoltage Vis/UV ratio was also determined to be worse than that of a standard native ligand capped-CdTe activated cell with a decrease by roughly a factor of 5. However, despite post-deposition ligand stripping resulting in no visible photovoltage, the EQE Vis/UV ratio improved by a similar factor. It is unclear why these two methods would have such different results.

4.3.4 Octylamine

Following the method of Zhang et al., this straightforward ligand exchange involved precipitating 1 ml of CdTe NCs at a concentration of 0.5 mg/ml with methanol, drying and then dispersion in an excess of octylamine. The solution is then heated for 16 hours at 70 °C. The now octylamine-capped NCs are then precipitated in N,N-dimethylformamide before being redispersed in chloroform [191]. The newly coated NCs were subsequently deposited on to the primitive cell structure. The molecular structure of octylamine is illustrated in Figure 4.17.



Figure 4.17: Molecular structure of octylamine.

Figure 4.18 shows the optical measurements for CdTe NCs before and after ligand exchange. It can be seen that the exchange causes a stark reduction in both the emission and absorption intensities. This is most likely due to NCs being lost during the ligand exchange procedure. The absorption values are roughly 10 times smaller for the octylamine-capped NCs. As absorption units are a logarithmic scale, this is a large decrease in the amount of light that is absorbed by the NCs. One way to account for this would be to deposit a greater amount of the suspension on to a cell therefore comparing an equal amount of NCs. However, as this leads to the requirement of unrealistic quantities, this method can't be achieved and it was therefore decided that the standard amount of suspension should be deposited therefore assessing the effectiveness of the overall ligand exchange method, including both the effect of the newly capped NCs and the wastage of the ligand exchange process.

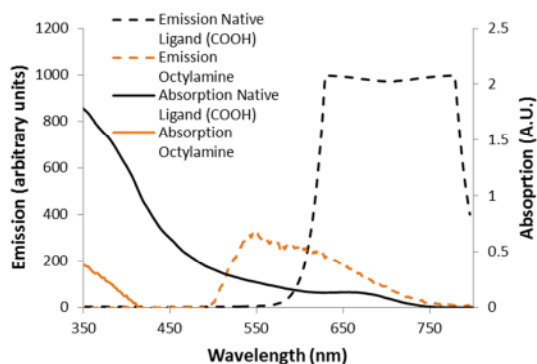


Figure 4.18: Absorption and emission spectra before and after ligand exchange with octylamine.

As suggested in the literature, to improve the short circuit current, the octylamine-capped NCs were also subjected to heat treatment. After measuring the electrical characteristics of the activated cell, the devices were placed in an oven and heated at 220 °C for one hour. After annealing, the devices were characterised again.

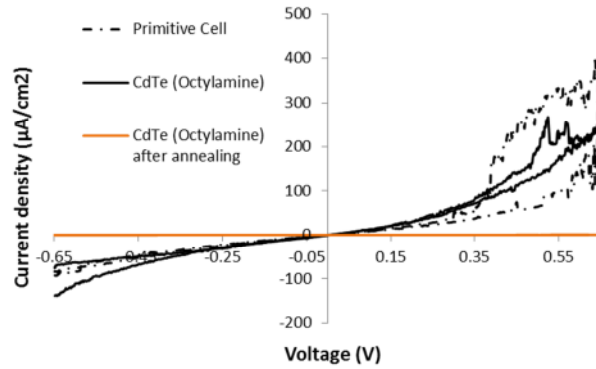


Figure 4.19: IV characteristics of a typical cell when primitive, activated by octylamine-capped CdTe and after annealing.

Figure 4.19 shows that there is relatively little difference between the IV profiles of the primitive and activated cell, apart from a slight reduction in the maximum current density as would be expected for the use of chloroform as the solvent. It can be seen however that annealing drastically decreases the maximum current density and therefore does not have the desired effect. This may be due to the annealing temperature being so high that the Ag nanomesh is destroyed in the process.

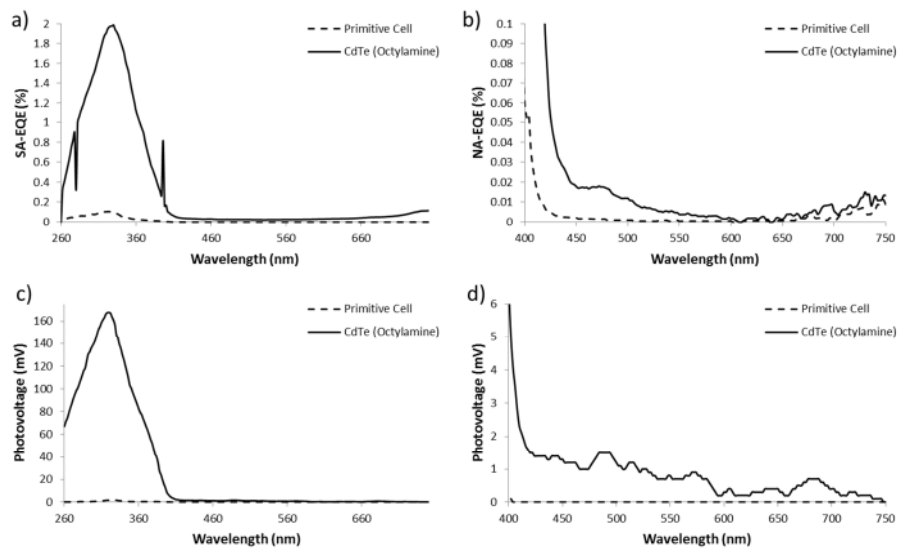


Figure 4.20: EQE (a and b) and photovoltage (c and d) plots of cells activated by octylamine-capped NCs.

Typical EQE and photovoltage plots for before and after octylamine-capped NC deposition are shown in Figure 4.20. It can be seen that activation does work with cells producing both a photocurrent and photovoltage in visible light. This response is however very small when

compared to the response under UV light with a typical ratio being 0.4 % for the EQE and 1.1 % for the photovoltage. When compared to a typical CdTe-decorated cell, these values are roughly 2.5 and 2 times worse respectively. Again, it is seen that ligand modification is having more effects than the one that is desired. Octylamine deposition is resulting in activity under UV light that is far greater than that observed for the primitive cell.

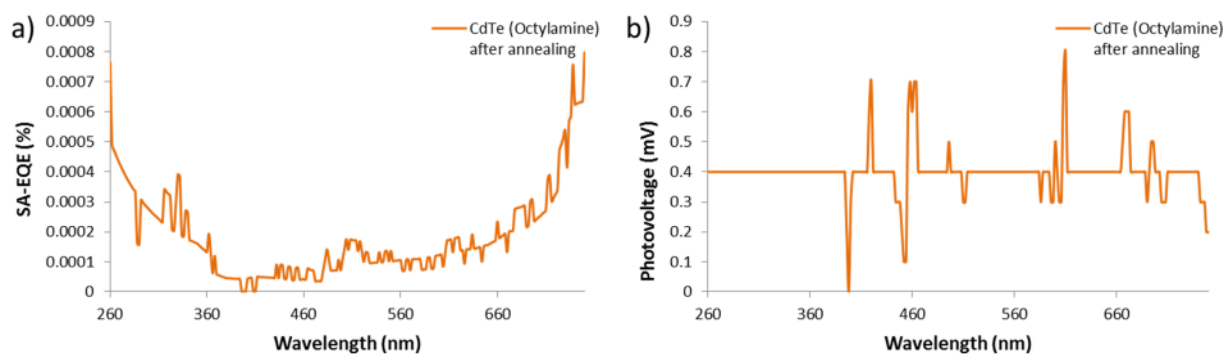


Figure 4.21: EQE (a) and photovoltage (b) plots of a typical octylamine-capped NC-activated cell after annealing.

As suggested by Figure 4.19, annealing the devices completely destroy any photovoltaic performance, this is evidenced by the EQE and photovoltage plots shown in Figure 4.21.

It can therefore be seen that using octylamine as a capping agent can result in cells that are active under visible light although when compared to cells that have been activated by CdTe NCs that are still with their native ligands, the relative performance under visible light to the performance under UV light is worse. Contrary to what was found by Zhang et al., annealing the device destroys the cell as opposed to improving the short-circuit current [191]. This is most likely due to heat damaging the Ag nanomesh.

4.3.5 Pyridine

CdTe NCs capped with COOH functionalised alkanes were subject to ligand exchange to create pyridine coated NCs. To perform this, following the method of Huynh et al., 1 ml of the original native ligand solution at a concentration of 0.5 mg/ml was dried in air, 5 ml of pyridine was then added and the solution was stirred for one hour. The NCs were then precipitated in 10 ml of hexane as pyridine-coated NCs are insoluble in hexanes. The solution was then left to dry and the procedure repeated 5 times. Finally, the NCs were redispersed in 1 ml of pyridine for future use. This procedure has been shown to replace more than 95 % of the native ligands with pyridine [193]. The newly coated NCs were

subsequently deposited on the primitive cell structure. The molecular structure of pyridine is illustrated in Figure 4.22.

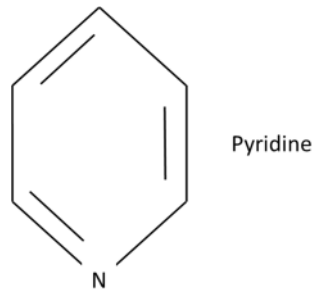


Figure 4.22: Molecular structure of pyridine.

Figure 4.23 shows the optical properties of CdTe NCs before and after ligand exchange. There appears to be no change in the effective band gap in the material with both the emission and absorption responses occurring at the same wavelength. The absorption peak is however significantly reduced after the ligand exchange treatment. It can also be seen that in both the absorption and emission spectra for the pyridine-capped NCs there is a feature at around 425 nm. This is of yet, unexplained.

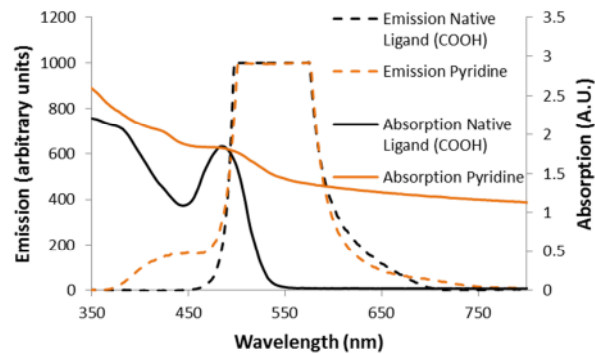


Figure 4.23: Absorption and emission spectra before and after ligand exchange with pyridine.

Likewise to the cells decorated with octylamine-capped NCs, cells decorated by pyridine-capped NCs have been shown to improve in performance upon annealing [193]. Upon activation and measurement, cells were placed in an oven and heated to 120 °C for three hours. After annealing, the devices were characterised again.

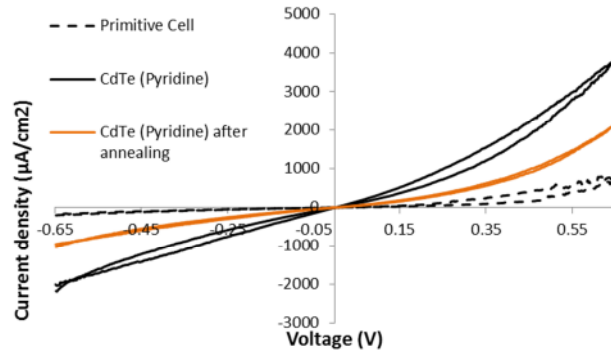


Figure 4.24: IV characteristics of a typical cell when primitive, when activated by pyridine-capped CdTe and after annealing.

As shown in Figure 4.24, the maximum current density is improved slightly upon pyridine-capped CdTe deposition and this is most likely due to the use of pyridine as a solvent. However, annealing had the effect of reducing the maximum current density.

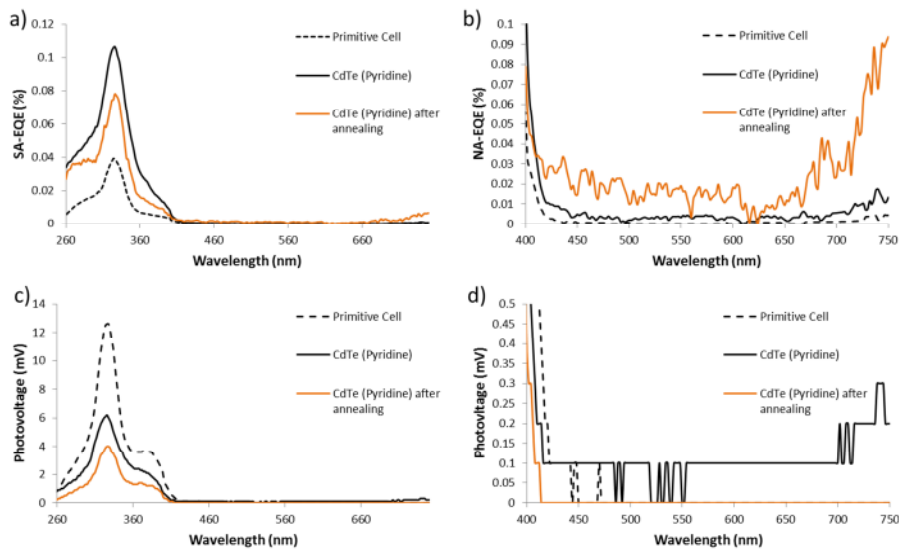


Figure 4.25: EQE (a and b) and photovoltage (c and d) plots of a typical cell when primitive, activated by pyridine-capped CdTe and after annealing.

Figure 4.25 shows that activation by pyridine-capped CdTe NCs does produce a response under visible light. However, this response is very small and only just distinguishable from background noise. Under UV light, annealing degrades both the EQE and the photovoltage. Under visible light, no photovoltage is detectable and the EQE response has a significant increase in noise. As with the octylamine-capped NCs, the ligand exchange reaction doesn't seem to increase the performance of NCs under visible light with a typical EQE Vis/UV

ratio of 0.4 % being more than twice as poor as when using native ligand-capped CdTe NCs. When using pyridine, the photovoltage Vis/UV ratio is slightly increased.

It can therefore be concluded that while ligand replacement is successful, there is no benefit in performing the procedure with no discernible improvement in cell performance. Contrary to Huynh et al., annealing also had no positive effect to cell performance [193]. Again this is most likely due to the use of the Ag nanomesh and while 120 °C has been shown to be a suitable temperature, 3 hours is 9 times longer than the typical annealing time and this length of time perhaps allows a great enough energy for partial destruction of the continuity of the nanomesh.

4.3.6 Core-Shell Nanocrystals

CuInS₂ NCs were synthesised as according to Booth et al. [142]. Upon quenching, some NCs were removed and diluted in chloroform as appropriate. The remaining NCs underwent further processing, again, as according to Booth et al. [142] to grow a ZnS shell around the core. This results in a Type I band alignment which is postulated to promote radiative recombination and therefore decrease photovoltaic performance. Ideally, a Type II structure would also be studied. However, due to lack of equipment and time constraints, no other band alignment formation could be fabricated.

Figure 4.26 shows the UV-Vis absorption and PLS emission spectra of NCs both with and without a ZnS shell. It can be seen that the emission peak is very wide, covering over 300 nm, indicating that the solution of CuInS₂ is polydisperse with a large size distribution. From Figure 4.26, it is also apparent that the addition of a shell creates a blueshift in NC response which is to be expected [142].

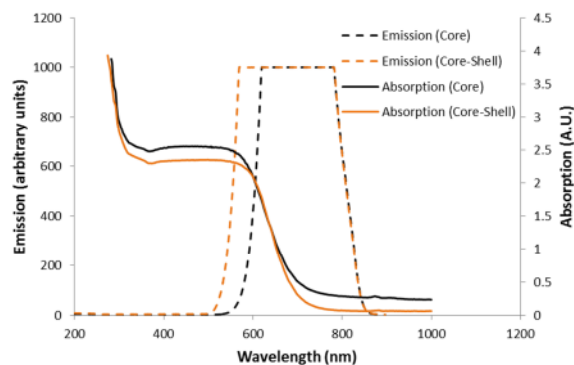


Figure 4.26: Absorption and emission spectra of CuInS₂ NCs with and without a ZnS shell.

The EQE and photovoltage response of cells activated by CuInS₂ NCs with and without a ZnS shell are shown below. However, as displayed in Figure 4.27, many of the photoresponse measurements displayed significant noise and could therefore not be used when determining the efficacy of these NCs.

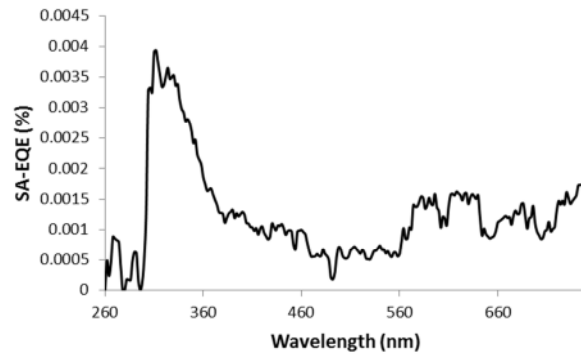


Figure 4.27: Example of a noisy photocurrent response when utilising CuInS₂ NCs that had a ZnS shell.

For both types of cells, those activated with NCs containing a ZnS shell and those containing core-only NCs, the EQE performance, as displayed in Figure 4.28, was similarly poor. NC deposition led to a sharp decrease in UV performance. Visible performance, if any, was unable to be discerned from signal noise.

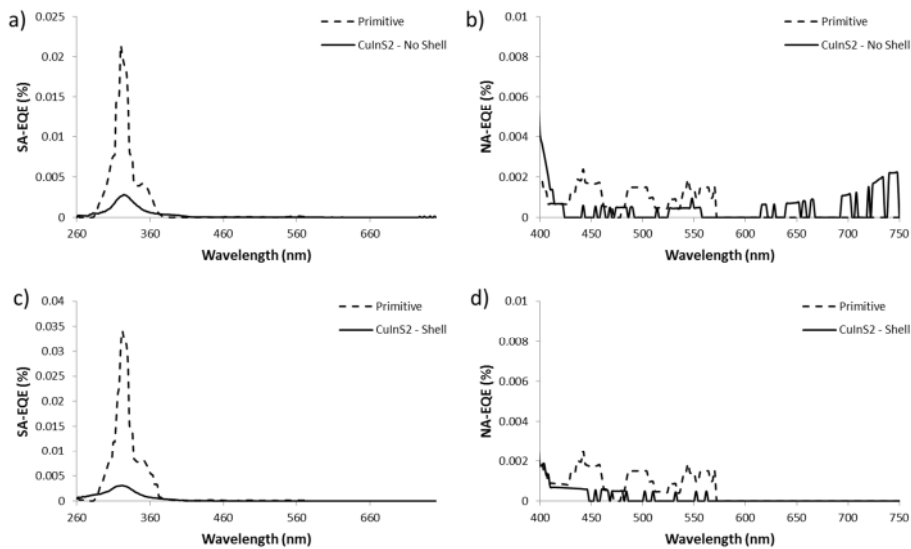


Figure 4.28: EQE plots for core-only (a and b) and ZnS-shell (c and d) CuInS₂-activated cells.

For the photovoltage, only a small amount of the cells made were responsive in the visible. This was similarly true for when using each set of NCs. The UV response seems unaffected by NC deposition while the visible response, when occurring is small. It can be seen in Figure 4.29 that the cells which utilised ZnS coated NCs had a possible blue shift in response which agrees with the optical measurements discussed previously.

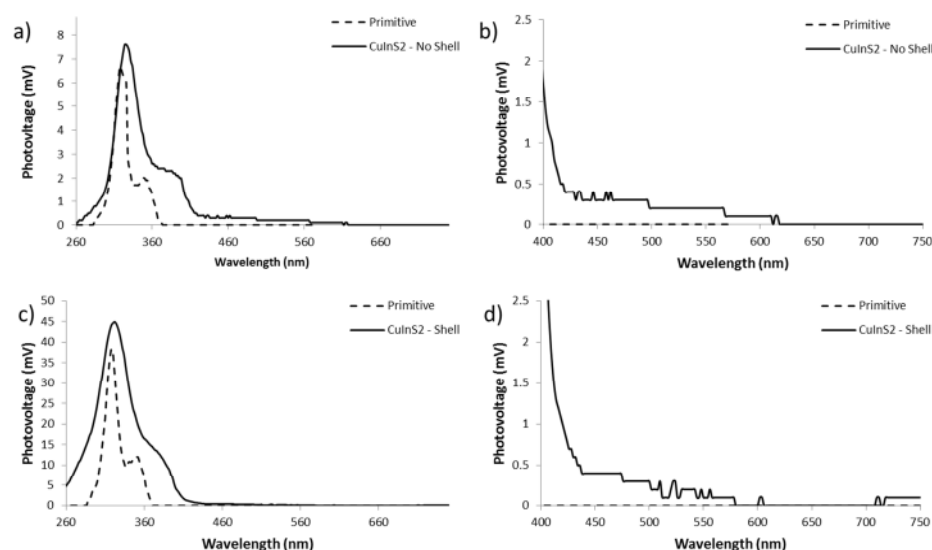


Figure 4.29: Photovoltage plots for core-only (a and b) and ZnS-shell (c and d) CuInS₂-activated cells.

Regardless of whether a shell is utilised or not, the photoresponses of these cells are poor, making the task of determining the potential of a core-shell NC-activated solar cell an impossible one. The poor performance of these cells can be attributed to at least one of two things. First, the NC core material could be a poor choice. Second, the solvent used could be having a significant detrimental effect. Since CuInS₂ cells have been shown to work in a variety of solar applications [206-208] and the optical results as displayed in Figure 4.26 show optically functional NCs, it leads one to the conclusion that the performance issues are in part due to the chloroform solvent which further highlights the importance of the solvent used.

Figure 4.30 compares the performance of all of the methods studied. Due to the poor results, CuInS₂ with a ZnS shell was omitted. As ligand modification is expected to improve the electronic properties of the cell, one would expect an increase in the EQE Vis/UV ratio compared to when using native ligands. However, it can be seen that only two methods achieved this and one of those methods resulted in zero photovoltage under visible light. Use of the metal sulphide shell resulted in an improvement in the Vis/UV ratio for both

photovoltage and EQE. It must also be remembered that, while a useful metric for determining the efficacy of ligand modification, overall cell performance is the most important variable. The greatest cell performance was found when using MPA-capped NCs.

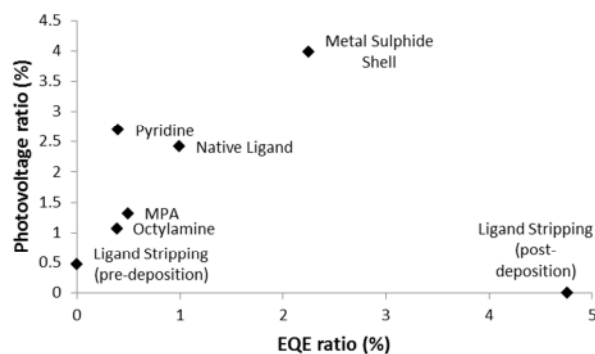


Figure 4.30: Comparison of the average effectiveness of ligand exchange techniques.

4.3.7 Acid Treatment

It is apparent that many of the ligand treatments have yielded limited results. However, one of the methods that have produced the most promising results improves the effectiveness of the cell under UV light just as much as under visible light. This therefore suggests that the treatment is having some effect other than improving the electrical properties of the NCs. The IV curves shown in Figure 4.7 indicate that the leakage resistance increases substantially which would in turn improve the photovoltage and EQE. Possible reasons for this increase in leakage resistance are that the chemicals used are affecting surface chemistry at the TiO_2 / Ag nanomesh interface thus increasing Schottky barrier height or that the chemicals are deactivating defect sites within the TiO_2 .

This method, namely the use of MPA as a ligand utilises a strong acid in the process. It is therefore possible that it is the use of acid that is improving the performance of the whole cell. It has been postulated that the pH induced protonation on the TiO_2 surface can result in a lowering of the conduction band of the TiO_2 [67]. This would result in an increase in EQE but decrease in V_{oc} . Furthermore, as discussed previously, oxidation of NCs has been shown to increase carrier mobility through the passivation of surface trap states. It has been shown that acid treatment enhances said oxidation [178]. These trap states may also affect carriers generated in TiO_2 under UV illumination. Removal of these states may therefore enhance the performance of the cell under all wavelengths of light.

To assess the effectiveness of acid treatment on the overall performance of the cell, primitive cells were fabricated, tested and then deposited in a bath of MPA for five minutes. After the five minutes, the cells were allowed to dry before further testing. After characterisation of the primitive device, native ligand-capped CdTe NCs were then used to activate the cells before further characterisation.

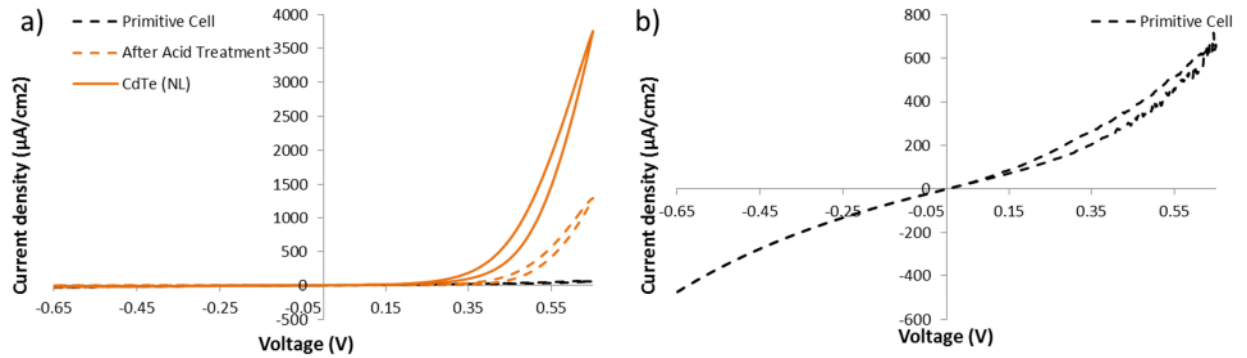


Figure 4.31: IV characteristics of a typical primitive cell before acid treatment, after acid treatment and after decoration with CdTe.

As shown in Figure 4.31, acid treatment shows a drastic increase in the maximum current density of a primitive cell with a typical factor improvement of around 100. It can also be seen that after acid treatment, the curve is closer to the ideal shape with less reverse bias leakage and also less noise. Decoration further increases the magnitude of the current density. The stark increase in maximum current suggests that the acid treatment is affecting the Ag-TiO₂ interface.

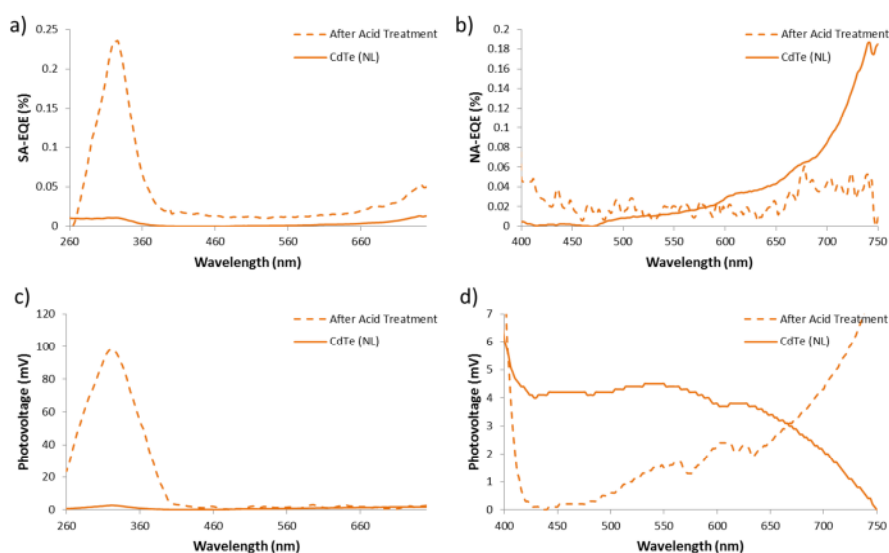


Figure 4.32: EQE (a and b) and photovoltage (c and d) plots of a typical acid-treated cell before and after CdTe NC deposition.

Figure 4.32 shows that contrary to what is observed in Figure 4.31, CdTe deposition degrades the performance of the cell. This is unusual because, as noted previously, the use of water as a solvent typically improves cell performance regardless of NC use. Under visible light, NC activation possibly produces a photovoltage. However, considering that the photovoltage for the acid-treated primitive cell and the EQE for the activated cell both display unexpected responses, it is not clear as to how much this visible response should be regarded. This type of mixed result set is typical for all cells that underwent this experiment where one result, current or voltage shows a desired response but the other results prove unreliable.

4.4 Conclusion

Native ligands can reduce electron transfer efficiency by a factor of 10 [167]. However without the use of ligands, it is difficult to control the morphology and dispersion of NCs. It is therefore advantageous to accomplish integration of semiconductor NCs in to PV cells through ligand modification. Various ligand exchange techniques were investigated and it was found that the replacement of native ligands with a metal sulphide shell was found to give the greatest enhancement of the visible response.

Some ligand modification techniques led to great increases of cell performance under UV light. Acidic environments was postulated to be a possible cause of this increase. However, despite improved IV characteristics, the treatment created significant noise in photoresponse

plots so that primitive devices suggested a response under visible light. This is most likely not the case and renders the recorded results for activated devices unreliable.

Throughout experimentation, difficulty in comparison was encountered due to the intrinsic variability between cells. Further work needs to consider how to get the improvement of the both Vis/UV ratios such as those seen when capping NCs with a metal sulphide shell while simultaneously achieving the overall cell improvement observed when using MPA-capped NCs.

Alternative optimisation techniques include sintering with CdCl_2 vapours, a technique that is used frequently in thin film CdTe cells [78]. This removes energetic barriers at grain boundaries thus improving carrier transport. Optical density is also increased, this would increase the amount of photons absorbed near the AgNW/ TiO_2 interface [209].

Further work on low-temperature annealing is also an area for further device improvement. It has been found that annealing typical NC Schottky barrier solar cells in a vacuum at temperatures ranging from 110 °C to 150 °C results in a significant improvement in EQE but no improvement in V_{oc} . Furthermore, it has been found that annealing in air at similar temperatures showed more pronounced gains with improvements in IQE, EQE and V_{oc} . The EQE improvements due to vacuum annealing is most likely due to ligand pyrolysis whereas the overall cell improvement during annealing in air can be attributed to the modification of trap states brought about due to the formation of NC oxides [74].

For a typical NC Schottky barrier solar cell, creating a rough metal-semiconductor interface allowed an increased absorbance while maintaining a high charge separation efficiency. This created a near 100-fold EQE improvement [73]. While this technique is not applicable to the demonstrated device, it highlights the fact that there is still significant potential for single, simple adjustments to greatly improve device performance. Furthermore, in-Situ decoration techniques such as chemical bath deposition and SILAR could be investigated, these have been shown to perform better than colloidal NC deposition for QDSSCs [210].

The performance of the demonstrated device, despite efforts to optimise it is still poor. It is therefore pertinent to, as well as continued engineering research, consider alternative and parallel methods to reduce the carbon intensity and increase the electrical output of solar PV. The following chapters will consider the broader aspects of carbon intensity reduction and develop techniques that are applicable not only to the demonstrated device but to all solar PV technologies. These methods will ensure that regardless of technology, progress towards achieving the triple objective of cost reduction, efficiency increase and lowering of carbon intensity is made.

5 Life Cycle Analysis

5.1 Introduction

Carbon reduction is the main driver for renewable energy development, especially in economically developed areas such as the EU. These areas have higher emissions and would benefit from more efficient solar energy technologies that also have lower levels of embodied carbon. It is therefore vital to be able to accurately calculate the true embodied carbon of any energy technology and use this to inform and influence policy.

This chapter will aim to accurately capture the emissions associated with PV technologies and assess how these values are linked to current UK policy. To achieve this, an introduction to life cycle assessment is given before discussing its application to both the demonstrated device and a standard silicon device. A life cycle analysis is then performed before applying the results to assess current UK policy. A conclusion is then made.

Lifecycle assessment methods are intended to capture the resource inputs and environmental impacts at every stage in the lifecycle of a process or product, in this case electricity production from solar PV. It is a flawed assumption to presume that renewable energy technologies are zero carbon as they rely on existing fossil fuel infrastructure for material extraction, fabrication, assembly, delivery and so forth. Without conducting a lifecycle analysis of the full supply chain impacts of energy technologies, only the direct emissions from combustion will be captured, leading to an underestimate of their impact. Lifecycle assessment is the dominant method for quantifying the environmental impacts generated throughout a product's lifecycle.

A review of lifecycle emissions of energy technologies by the International Panel on Climate Change (IPCC) [211] indicates the potential lifecycle emissions of renewable electricity generation technologies in comparison to conventional fossil fuels, as shown in Table 5.1. While this perspective attaches emissions to renewable electricity technologies, they are still overwhelmingly more favourable than producing energy from fossil fuels.

Table 5.1: Aggregated LCA results (gCO₂e/kWh) from electricity generation technologies [211].

	Energy Source										
	Bio-power	Solar PV	Solar CSP	Geothermal	Hydropower	Ocean	Wind	Nuclear	Natural gas	Oil	Coal
Minimum	-633	5	17	6	6	2	2	1	290	510	675
Maximum	75	217	89	79	43	23	81	220	930	1170	1689
CCS											
Minimum	-1368								65		98
CCS											
Maximum	-594								245		396

It is however difficult to compare the results of each technology in this report due to methodological diversity, differing data sources and technological characteristics assumed across the studies. For example, both process-based and economic input-output methods are used for life cycle analysis, when bottom-up product specific inventories are not available they are compiled from different life cycle databases and processes deemed significant to be included in an inventory are subjective. Some studies adopt a cradle-to-gate perspective where decommissioning activities are excluded, others include these but make different assumptions on recycling and disposal options. Published standards for LCA (ISO14040 and PAS 2050) provide guidelines, but no consistent method is defined. A methodology that reduces discrepancies between comparable studies is therefore desirable.

Hybrid LCA methods provide an opportunity to overcome elements of error inherent in traditional LCA methods. Supply chains associated with energy technologies are numerous and complex. Additionally, their global nature means pressures are dispersed, creating a large and distant web of suppliers and a near-infinite number of possible production layers. Conventional LCA methods have had to set a system boundary since it is near impossible to collect process-specific data for such a large number of possible supply chain paths. As a result, some upstream activities are excluded from the analysis leading to significant truncation errors. It has been estimated that up to 50 % of the impacts can be ‘lost’ [212, 213]. This underestimation is compensated for by using economy-wide data in the form of input-output analysis. However, while the input-output method characterises a complete ‘boundary-less’ system, it is constrained by aggregated sector representation. In the context of energy technologies, electricity is represented as one economic sector, not distinguishing between specific technologies.

Published in the late 1970s [214] but becoming more applied in the last decade, is the emergence of a new breed of hybrid methods to overcome the limitations of boundary truncation errors while maintaining product specificity. Conceptually hybrid methods combining process-analysis and input-output analysis have been relatively well documented [215-220]. These began as a ‘tiered hybrid analysis’ where additional upstream emissions missed from process-based inventories were added using input-output analysis. This later developed to a completely integrated hybrid LCA where a process database is embedded in an input-output table and all interactions between individual processes and economic sectors or industries are modelled in a consistent framework.

In theory, a fully integrated hybrid LCA is favoured. However due to computational complexity, applications are sparse [215]. To our knowledge Wiedmann et al. [221] were the first to apply an integrated multi-regional hybrid LCA using the case study of supply chain emissions of wind power generation in the UK. Acquaye [222] applied the same model to an emissions assessment of biodiesel adding additional estimates for emissions originating from land use change. The same model is applied in this chapter.

This methodology allows for a more comprehensive environmental evaluation of the use of renewable energy generation technologies and their corresponding policy incentives. A brief description of the method is given here and the reader is referred to Wiedmann et al. [221] for a detailed technical description. The technical characteristics and data sources for this application are described in detail below. Figure 5.1 illustrates the methodological framework employed to conduct the LCA.

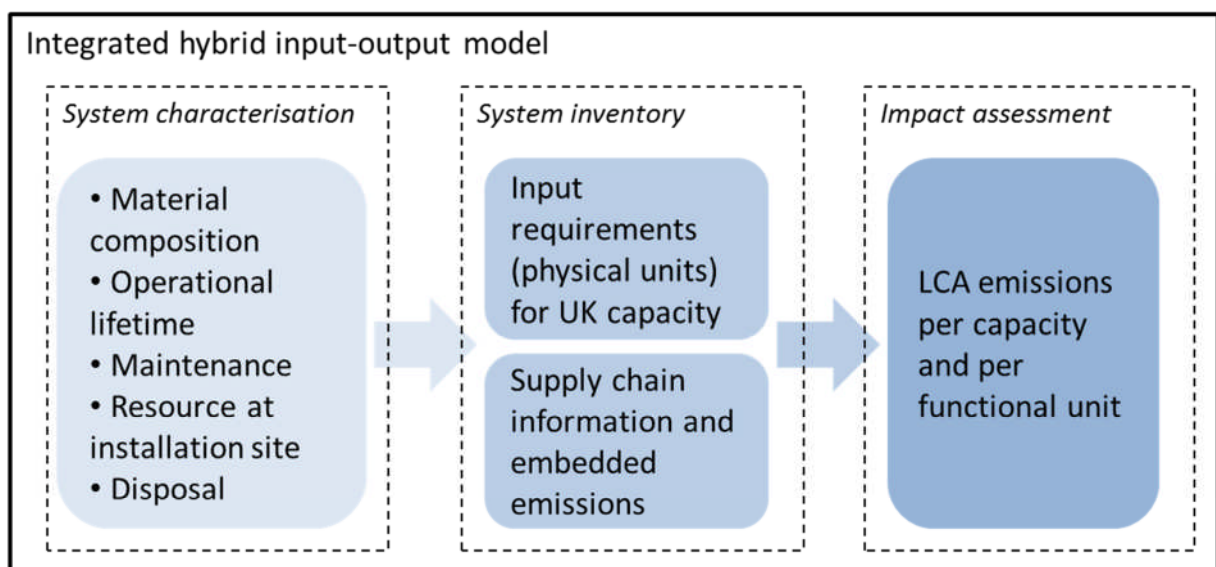


Figure 5.1: Methodological framework of lifecycle analysis.

A total requirements matrix links an $m \times m$ process matrix describing the inputs of goods to processes in physical units (A_{gp}) to an $n \times n$ input-output technology matrix derived from financial transactions between economic sectors ($I - A_{ss}^*$). This is done via an $n \times m$ upstream matrix (C_u) and an $m \times n$ downstream matrix (c_d). Commodity flows from the input-output sectors cut-off from the process inputs matrix complete the upstream component, and physical goods produced by specific processes used in the background economy (the input-output system) complete the downstream component. The trade interactions of all processes and products globally are integrated into a two-region UK-centric model. The total requirement matrix H can be written as equation (5.1):

$$H = \begin{bmatrix} -A_{gp} & -C_d \\ -C_u & I - A_{ss}^* \end{bmatrix} \quad (5.1)$$

Negative numbers indicate inputs to processes and positive numbers indicate outputs of a process. The process matrix is populated by a 3931*3931 matrix from ecoinvent v.2.1 (2009) data and a two region supply and use table representing 224 economic sectors. Using a multi-region model extends the national boundary to account for international trade. Only sectors in the input-output table deemed to have been cut-off in the process matrix are retained upstream. It has been assumed that the electricity generated is used by the transmission sector.

Greenhouse gas emissions are calculated by pre-multiplying H with direct emissions data and post-multiplying by demand for the good in question (electricity from micro-renewables), represented by equation (5.2):

$$q = [B \ B^*] \times H \times [y] \quad (5.2)$$

B and B^* are vectors representing greenhouse gas emissions from each process and the emissions intensity of each economic sector respectively. For example, electricity generated by the micro-generation installation will have zero emissions (unlike combustion of fossil fuels). However, emissions will be associated with resource inputs such as silicon production. y is a vector specifying the level of demand for the process or sector of interest. Direct emissions are re-proportioned to the final good (micro-generation electricity) via the interactions represented in the integrated matrix. Results can be separated from the process and input-output model and therefore process only results can be compared to those employing the hybrid method.

5.2 Application of LCA to the Demonstrated Device

Life cycle analysis has for a long time been widely regarded as the most important environmental management tool developed and it is therefore pertinent to apply this methodology to the cell demonstrated in the previous chapters [223]. However, despite claims that LCA is necessary for assessing developments in nanotechnology, very few papers have actually managed to achieve the task [224]. The reason behind this is that LCAs can only be performed for products and processes that are already shaped and close to market introduction [224].

It has been acknowledged that the environmental and health implications of using nanomaterials has not been delineated fully [225] and that current automated LCA approaches would give potentially misleading results for nano-based applications [226]. The same is true for the Wiedmann model. Emissions databases rely on historical data collected predominantly from mature industries and there is a dearth of relevant data regarding the fate, transport and toxicity of novel substances such as nanomaterials [226]. The need for extensive data promotes retrospective risk analysis, this means that existing LCA practices are ill-suited to support early research or R&D LCAs with significant barriers existing relating to data availability, rapid technology change, and isolation of environmental from technical research [226].

Persistent data gaps exist in the estimation of energy requirements in nanomaterial production due to the scarcity of production process information, especially as some of the material fabrication processes used aren't up to full production scale yet [227]. Issues with the use of lab data include that the energy used in lab syntheses doesn't scale up isometrically with the final product of mass and that there are no allocated rules defined for direct energy inputs. As laboratory instruments aren't completely dedicated to the synthesis of a single product during their own life cycles, when accounted for, this will result in an overestimation of the energy consumed for the process [228]. Further unknowns include use-phase product performance, end-of-life disposal pathways and life cycle material release [226]. Emissions associated with transport are also difficult to ascertain when there is no established supply chain [228]. Furthermore to issues in production process data, regarding NC photovoltaics, further unknowns exist in prototype cells. These include parameters such as lifetime [229], efficiency [228] encapsulation [230], active area size, and end of life treatment [227].

On a per unit mass basis, nanomaterials in fact typically require a higher energy input due to the extra energy needed to mechanically reduce the particle size or for a gas-phase fabrication process requiring high energy consumption for synthesis [231]. The reduced

mass use however theoretically results in lower carbon intensities. Any LCA of current NC PV devices can only, at best, provide snapshots under R&D conditions [231] and any attempt to accomplish NC PV LCAs is only compounded by the fact that uncertainty in LCA GHG emission estimates is already large for photovoltaic technologies [229].

A recent review of the current state of the LCA of PV technologies decided that novel, third generation solar cells are too new to be considered [232]. It acknowledges that even in 2014 there are still very few studies of second generation PV technologies, let alone third generation. Commercial production of thin film CdTe only started in 2004 [230] and data has therefore not had time to disseminate. There have been some attempts to perform LCAs on more established third generation solar cells such as DSSCs. However, the lack of data required to perform the studies has been acknowledged as a problem [226, 229]. Those LCAs that have been performed on novel technologies are typically accomplished through extrapolation of laboratory-scale process data and then extrapolation based on literature which, as discussed, is not entirely accurate [227].

No data exists for the energy intensity of the fabrication processes involved in the demonstrated device therefore data collection is impossible and LCA is therefore bound to fail. Possible prospective LCA strategies to consider the energy embodied in prototypal devices have been proposed. These include developing structured scenarios within LCA models, consideration of experience curves from analogous industries to identify potential future improvements in efficiency, thermodynamic process modelling, uncertainty bounding analyses to provide upper and lower limits to environmental impact and dimensional analysis to explore scaling effects [226]. It has however been acknowledged that such an anticipatory approach requires a synergy of social, environmental and technical knowledge that is beyond current capabilities [226].

LCA is a detailed method that requires a large amount of data availability and a high level of certainty that does not exist for nanomaterials [224]. It is therefore concluded that comprehensive LCA studies on nanomaterial-containing products cannot be carried out until more is known about the environmental impacts of the materials [224]. Preliminary conclusions are likely to change and are in need of routine updates. With the proposed device still very much in a prototype stage, it is impractical to assign an environmental value yet [225].

It is however practical to utilise the Wiedmann model in assessing the environmental impact of bulk silicon PV technology thus providing three benefits. Firstly, it will establish the application of an integrated hybrid LCA approach to solar PV creating a platform to enable the analysis of all types of PV technology when relevant data does become available.

Secondly it will help to determine the most carbon intensive aspects of the use of present-day solar PV, helping to identify the areas which may benefit from further application of nanotechnology. Thirdly, though application of the model on the most commonly used PV technology, it enables analysis of the LCA results with respect to governmental policies and national targets.

5.3 Application of LCA to Silicon Photovoltaics

Monocrystalline cells are considered most representative of the type of panels which will be predominantly used in the UK in the coming years [233] and since solar PV installations have little variation between designs [234], a typical monocrystalline silicon installation is therefore considered as the case study. The case study installation consists of 22.1 m² of laminated panels sized 125 cm² which are each made up of 72 single crystalline silicon solar cells and has a total capacity of 3 kWp.

Data has been collected for the case study of solar PV systems for material composition, technology manufacture, transportation energy consumption and waste generation within the manufacturing process. Assumptions have also been made for the processes of materials extraction and production, as well as the installation based upon consensus within the literature and ecoinvent database v.2.1 (2009). It is assumed that all components are produced from newly extracted materials and don't contain any recycled content. The impact of all materials and products used in the infrastructure has been included. It is acknowledged that in reality, the technologies considered may contain some recycled content which would bring down the overall life cycle impact of the product however due to uncertainty in the proportions, a worst-case scenario of no recycled materials has been assumed. Where specific transportation distances were not available distances have been assumed. After connection to the grid, the transmission and distribution of the electricity have not been taken into account. This is usually not technology dependant and therefore not necessary for this study. Disposal of the technology has also not been considered in this study.

5.3.1 Material Composition

Figure 5.2 shows the composition of materials used in a single silicon PV crystalline panel. Solar glass makes up the majority of the material within the panel, with aluminium and steel contributing 25% of the remaining materials. Electronics and silicone make up only 1% each.

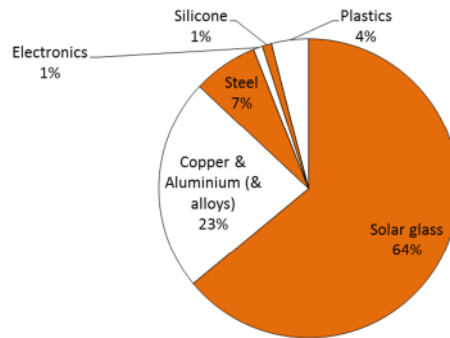


Figure 5.2: Material composition by mass of the considered solar PV single crystalline panel.

5.3.2 Operational Lifetime

Manufacturers offer a warranty for a system for 25 years. However, the International Energy Agency (IEA) solar PV LCA guidelines (2009) and published academic literature [235] suggest that the modules are more likely to degrade in efficiency as opposed to meeting a “fixed catastrophic failure point” and will therefore operate for longer than 25 years. A 30 years lifetime with an age related level of efficiency degradation has therefore been assumed for this study.

The core maintenance necessity for solar PV installations is the replacement of inverters which convert the DC current generated by the panels into grid compatible AC current. Theecoinvent database states that the average lifespan of an inverter is 12.5 years but there is variation due to factors such as differences in durability [236]. To account for inverter lifespan variation, an average use of 2.4 inverters is assumed over an installation’s lifetime. Aside from occasional cleaning of the modules (which has negligible impact), it is assumed that no other maintenance is required since solar PV panels have no moving parts.

5.3.3 Results

Process and integrated hybrid LCAs are performed and for the sake of comparison of the two methods, both lifecycle results are presented in Figure 5.3. It can be seen that adoption of the integrated hybrid method, to overcome truncation error, results in an emission increase of 20 % of the process method results. Wafer construction contributes 50 % of emissions using the process analysis, and its share reduces slightly to 47 % when using the hybrid method. Installation is the second highest contributor at 15 % and 17 % respectively. An improvement in efficiency in these two areas is therefore most likely to make a significant reduction in the embodied emissions associated with solar PV installations. With regards to installation, for example, an installation scheme where local areas or roads receive

installations at the same time may have a significant carbon reduction potential. The high contribution of wafer construction to the total embodied emissions of solar PV reinforces the need for an alternative to silicon technology and reduced material usage. This result consolidates the need to pursue other cell architectures and materials such as the demonstrated device where no silicon is used and no wafer processing is required.

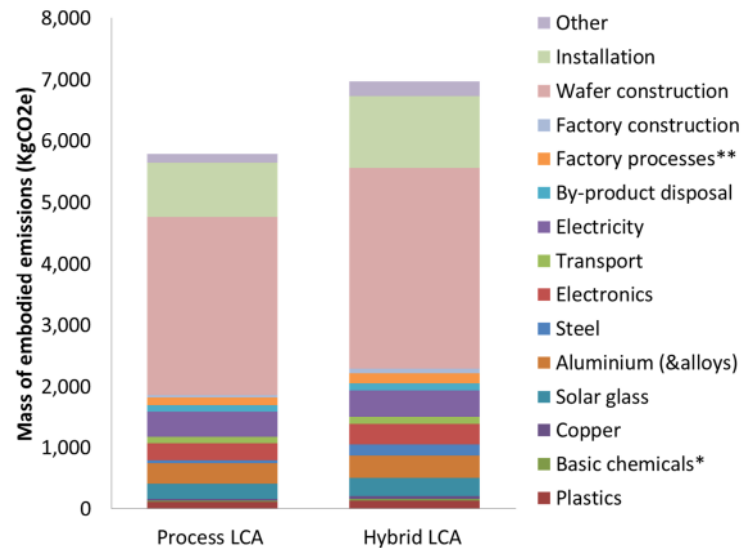


Figure 5.3: Emission results from single silicon solar PV installation (3kWp) comparing process-based and hybrid-based results.

As mentioned previously, a few LCA studies have been performed on second generation, thin film cells and overall, current literature seems in agreement that thin film CdTe has a much better environmental impact than commercial Si technologies [230, 237, 238]. This is mainly attributed to the fact that the micron-scale thick CdTe active layer requires considerably less material than monocrystalline Silicon cells [237]. Those few studies have also concluded that further to their lower energy requirements and despite their reduced efficiency, thin film technologies including CdTe also show better values for energy payback time (EPBT) and avoided emissions than established silicon technologies [227]. The greatest use of primary energy in second generation thin film cells is due to electricity demand during active layer film deposition, accounting for over half of the energy consumption [230]. This electrical film deposition technique won't be used in the demonstrated cell and therefore, if similar efficiencies are achieved (11 – 17 %), this suggests that the demonstrated cell will have even better EPBT values. Even if those efficiencies are too ambitious, the reduced processing inputs imply that lower efficiencies may still lead to an improvement in EPBT over Silicon cells.

5.3.4 Application to Policy

The remainder of the analysis will focus on the results of the integrated hybrid method. Using an integrated approach over a pure process or input-output approach has shown to yield truer results in terms of the detail of physical flows combined with system completeness. However, this does not escape uncertainties associated with data sources and model assumptions. Examples of uncertainty in the hybrid model relate to the process inventory, the manipulation of input-output tables and the conversion between monetary and physical data when integrating the two datasets. When comparing with other studies, the capacity in terms of power output, disposal and recycling assumptions, and the location of production and operation of generation technologies will lead to different results.

Carbon budgets have been devised to ensure the UK is on track to meet its legislative 80 % greenhouse gas emission reduction target by 2050 from 1990 levels [239]. Reasonable evidence exists that electricity generation will have to be at 50 gCO₂e/kWh by 2030 in order to meet these targets. The UK's electricity intensity in 2015 stands at 462 gCO₂e/kWh [240] and as opposed to a decrease, has climbed recently due to an increase in the proportion of coal in electricity generation. Of the 340 TWh of electricity generated in 2015, 19 % is from renewable sources (64.7 TWh) [3]. The Committee on Climate Change suggests that 30 – 40 GW of additional low carbon supply is needed to meet the decarbonisation target by 2030 [241].

Feed-in tariffs (FiTs) are one of a package of policies aiming to drive innovation in low carbon technologies and stimulate growth by providing price certainty in the market. Feed-in tariffs are available for a range of renewable electricity generating technologies up to a 5 MW rating and are the main incentive for the installation of micro-generation technologies. The scheme was designed to provide three financial benefits: money for each unit of electricity generated, money for energy that isn't used and is therefore exported back to the grid and money saved from reduced energy bills.

Although predicted to have the greatest technical potential, due to its initial high price, solar PV was also anticipated to have negligible penetration with waste and wind being predicted to be the most utilised sub 5 MW technology [242]. However, contrary to these predictions and most likely due to its rapid decrease in cost, since their introduction in April 2010 FiTs have caused a revolution in uptake of solar photovoltaics, resulting in significant growth in installations to the current installed capacity of over 5.4 GW by the end of July 2015 (rising from under 1 MW of capacity before its introduction) [3]. Solar PV makes up over 98% of the total renewable technology installations that have been registered under FiTs [243].

FiTs forms part of a policy framework to decarbonise the UK energy system. However, the evidence used to inform the policy was predominantly related to costs, capacity and deployment, not contribution to meeting decarbonisation targets. When calculating the UK's electricity intensity it is important to recognise and monitor the embedded emissions of such technologies to ensure that their full impact is taken into account. FiTs do not discriminate between different generation technologies or installation sites, despite the fact that the lifecycle emissions in their production could vary significantly. For example, where technologies are deployed in locations with a poor renewable resource the carbon intensity per kilowatt hour generated increases due to the fact that their lifecycle emissions are fixed. The implications of this have not been considered in discussions related to the possibility of achieving an electricity emissions target of 50 gCO₂e/kWh.

It has also been claimed by DECC that FiTs “will support over 750,000 small scale low carbon electricity installations and will have saved 7 million tonnes of carbon dioxide” [244]. However, there has been no justification of these figures and any methodology used in this calculation has yet to be found by the author. There is a major concern that past analyses of the lifecycle emissions of micro-generation technologies provide a significant underestimate of emissions.

The amount of CO₂e that is saved through the utilisation of a solar PV installation depends on how much of a reduction in national grid use is made and also how carbon intensive the grid is.

The carbon savings for each installation used can be calculated as shown in equation (5.3):

$$\text{Carbon savings} = \left(\sum_{t=1}^{30} O_i G(t) D(t) \right) - E \quad (5.3)$$

Where O_i is the initial annual output of the panel, $G(t)$ is the grid carbon intensity, $D(t)$ is the degradation factor of the panel and E is the embodied emissions of the panel.

PV output is dependent on insolation. Levels of horizontal irradiation in the UK range from 750 kWh/m²/year in northern Scotland to 1100 kWh/m²/year in southern England. Different levels have therefore been considered over this range to reflect the variation in UK conditions. It is important however to remember that factors such as zenith angle and azimuthal angle must also be taken in to account when determining the output of a solar PV installation.

As well as the level of irradiation, the output is also dependent on the performance of the panels. For this study, the installation was assumed to have an efficiency of 14.4 % and a performance ratio of 0.75.

The initial electricity output is given by equation (5.4):

$$O_i = A \cdot \eta \cdot R_p \cdot L \cdot I_j \quad (5.4)$$

Where O_i = initial electricity output (kWh), A = area of the panel (m^2), η = panel efficiency (%), R_p = performance ratio, L = panel lifetime (30 years), I_j = annual irradiance at installation site (kWh/m^2).

Table 5.2 details the calculated initial system generation under the considered levels of annual irradiance.

Table 5.2: Expected electricity generation for different annual irradiance values.

Annual Irradiance, I_j (kWh/m^2)	Initial Annual Output (kWh)
700	1,557
800	1,780
900	2,002
1000	2,224
1100	2,447

Degradation due to aging of the system was also considered [20, 23]. Degradation of the panel results in a linear reduction in performance over its useful lifetime. Despite system degradation being identified as an important area of assessment for PV LCA, it is often neglected in studies. The degradation factor effectively reduces the average performance over the system lifetime of 30 years by 20 %.

DECC holds monthly figures for the feed-in tariff scheme and as it has been found that the vast majority of installations are solar PV [245], for the purpose of this research, it is approximated that all installations taken up through the feed in tariff are solar PV.

Both the amount and timing of the installations will have a clear impact on the size of the carbon reduction achieved. Using historical data for the number of installations, it is possible to extrapolate forward to predict the number of installations completed between now and 2020. For this study, two scenarios were created: Scenario A follows the rate of installations that have occurred in the recent past and continues that trend, Scenario B extrapolates from where installations stood at time of calculation to DECC's prediction of having 750,000 installations by 2020 [244]. These two scenarios are shown in Figure 5.4.

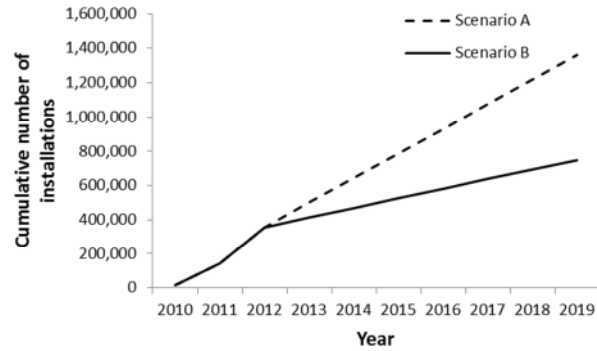


Figure 5.4: Considered scenarios for rate of scheme uptake.

As well as the need to predict the uptake of the scheme, it is also necessary to predict the carbon intensity of the national grid between now and 2050. Five scenarios have been considered: scenarios 1, 3 and 5 are targets for the national grid to reach an intensity of 200 gCO₂/kWh, 100 gCO₂/kWh and 50 gCO₂/kWh by 2030 respectively. These numbers arise from the uncertainty created by the electricity market reform [246]; Scenario 2 extrapolates from a Defra produced grid intensity projection that is used to “inform government decisions” [247] and scenario 4 extrapolates from the most recent projection made by the National Grid [248]. These 5 scenarios are shown in Figure 5.5 and listed in Table 5.3.

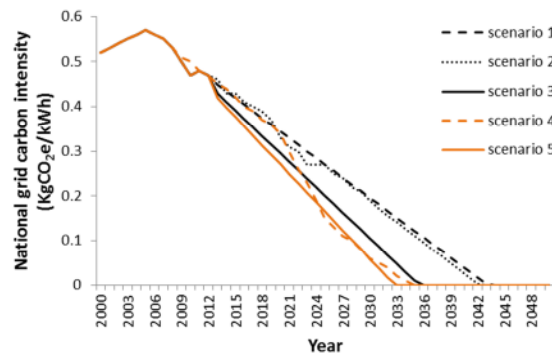


Figure 5.5: Considered scenarios for rate of decrease of grid carbon intensity.

Table 5.3: Description of grid decarbonisation scenarios used.

Grid Decarbonisation Scenario	Description
1	Target for the national grid to reach an intensity of 200 gCO ₂ /kWh, by 2030 respectively
2	Extrapolation from a Defra produced grid intensity projection that is used to “inform government decisions”
3	Target for the national grid to reach an intensity of 100 gCO ₂ /kWh, by 2030 respectively
4	Extrapolation from the most recent projection made by the National Grid
5	Target for the national grid to reach an intensity of 50gCO ₂ /kWh, by 2030 respectively

Incorporating the five levels of irradiance considered, 5 scenarios for grid decarbonisation and 2 scenarios for scheme uptake, there are therefore 50 different scenarios considered for the potential carbon saving created by the feed-in tariff scheme as shown in Figure 5.6.

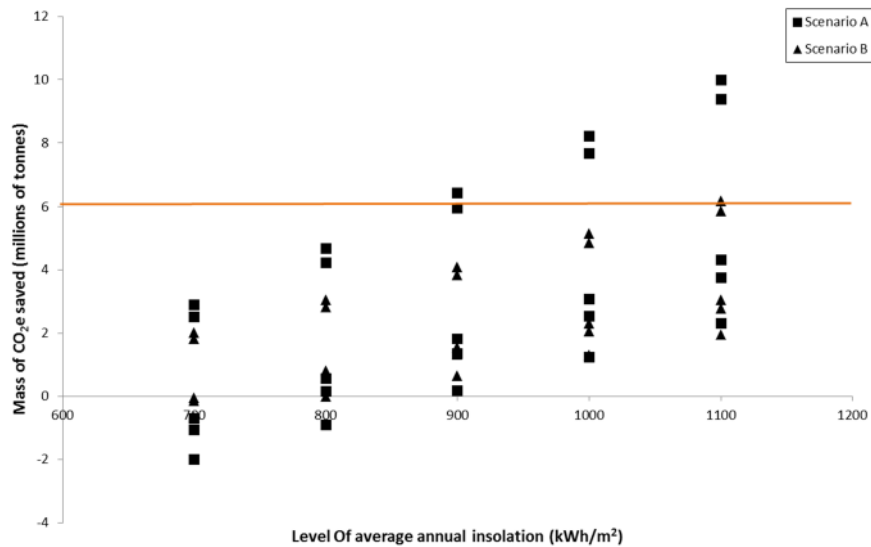


Figure 5.6: Quantity of carbon dioxide saved under each scenario. Horizontal line indicated DECC's prediction.

Figure 5.6 shows that under nearly every scenario, the carbon savings are less than the prediction made by DECC. This has most probably occurred due to a lack of consideration of the embodied emissions in each installation. It can be seen that under some scenarios, the scheme has a negative effect, this arises under levels of low insolation and also highly

optimistic grid decarbonisation scenarios. If the grid has low levels of pollution, it will be impractical to construct and install solar PV panels when a low carbon source is already available to be used. However, these scenarios that have yielded negative results are extremely improbable. For example, the most recent projection made by the National Grid has predicted a carbon free grid by 2035 which therefore negates the use of any micro-solar PV from this date onwards. This situation is of course highly improbable. These results however highlight the need to integrate policies and targets when calculating carbon reduction. FiTs will have a much stronger impact when used in conjunction with a slowly decarbonising grid whereas if the grid was to rapidly decarbonise, this may negate the usefulness of the feed-in tariff scheme.

A final outcome of the results to note is that none of the points that fall within scenario B (750,000 installations by 2020) reach the target of 7 million tonnes of CO₂ saved. This yet again suggests that DECC have failed to appreciate the true cost of the emission embodied in solar PV manufacture and installation. As introduced in Chapter 1, the consequences of these over assumptions of carbon savings may be severe. If scientific consensus agrees on a carbon reduction target then it is necessary to achieve that target. Inaccuracies in carbon reduction assessment may lead to a belief that enough has been done to prevent the deleterious effects of climate change when in reality there is still vital progress necessary to be made.

5.3.5 Carbon intensity of solar PV

The carbon intensity at different rates of irradiation is given in Figure 5.7. As is expected, the higher the irradiance received, the lower the carbon intensity. The value of the carbon intensity decreases from over 160 gCO₂/kWh in areas with the worst irradiance in the UK to around two thirds of that value in areas with the best irradiance in the UK.

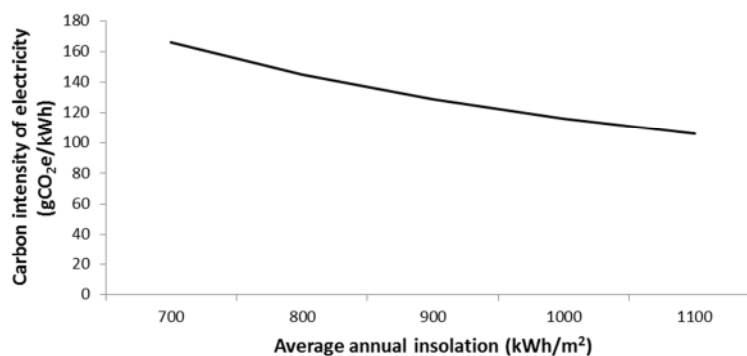


Figure 5.7: Carbon intensity of solar PV for different levels of levels of average annual irradiance.

These values can be used for comparison with the values quoted within the IPCC Special Report, shown in Table 5.1, where it can be seen that under all levels of insolation, the carbon intensity found through the conducted hybrid life cycle assessment fall between the minimum and maximum values for solar PV. Considering hybrid LCA is designed to avoid truncation errors, one would expect the values to be higher than most other conducted LCAs, especially those based upon the process method. The upper limit value of 217 gCO₂e/KWh that is quoted in Table 5.1 therefore seems overly conservative. The calculated carbon intensities also show that the governmental target of 50 gCO₂e/KWh is a very optimistic target, with solar PV microgeneration systems being two to three times as carbon intensive as the national target. This highlights that while PV is a viable, immediate improvement upon the fossil fuels currently used in the national energy mix, the technology is currently still too immature and requires too high an energy input. Even placed within the best locations within the UK, solar PV does not achieve the reduction in carbon intensity required. Alternative PV technologies with lower embodied emissions and higher efficiencies are therefore required.

5.3.6 Carbon payback time

Carbon payback period represents the time period of energy generation that must take place to offset the losses incurred in the installation period (i.e. the lifecycle emissions). Renewable energy sources offset their embedded CO₂e by replacing electricity generation from a carbon intensive source (e.g. fossil fuels). The number of years required to offset the embedded carbon of a technology at a specific site is given when equation (5.5) is satisfied:

$$[E_{CO_2} - \sum_{t=1}^t I_t a_t] < 0 \quad (5.5)$$

Where E_{CO_2} = Embedded CO₂e of the PV system (kg CO₂e), t = year after installation, I_t = intensity of the UK electricity grid in the t^{th} year (kgCO₂e/kWh), a_t = annual generation at the installation site for the t^{th} year.

Note that the annual generation for solar PV has been calculated to reflect panel efficiency degradation with time and under all scenarios, the grid is predicted to become less carbon intensive with time. This therefore creates a system of diminishing returns where the installations in their first year of operation will have the greatest contribution and subsequent years will show a decreased contribution.

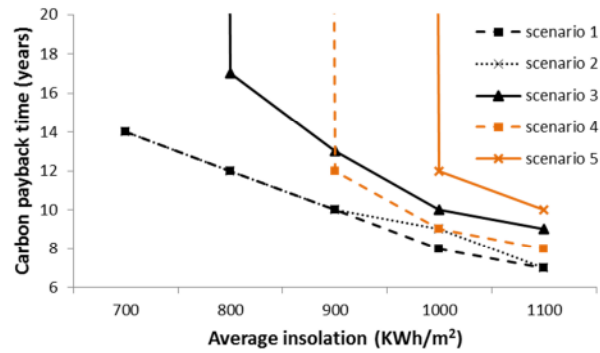


Figure 5.8: Carbon payback time under different levels of annual irradiance and grid decarbonisation scenarios.

Figure 5.8 shows how the carbon payback time of solar PV varies under different levels of insolation for each grid decarbonisation scenario. This assumes that the installation occurs in 2015. Any points not shown indicate that the installation does not achieve carbon payback. As discussed previously this is probably somewhat unrealistic and is a result of the overly optimistic grid decarbonisation scenarios. For example, scenario 4 predicts rapid decarbonisation resulting in a carbon free grid in 2035, leaving just 20 years for any solar PV installation to payback its embodied carbon.

5.4 Conclusion

Technologies such as solar PV could be thought of as infrastructure technologies which enable the capture of renewable resources. Their impacts are generated through their production, installation and maintenance rather than in their operation. It is therefore essential to account for these when assessing the carbon intensity of electricity generation to offer an accurate comparison with fossil fuel alternatives. It is also necessary to develop an accurate and robust LCA methodology that captures the entire emissions of a supply chain and avoids truncation errors. Here the integrated LCA methodology is, to the author's knowledge, proposed for use on solar PV for the first time.

There is no standardised prospective LCA technique yet and until such a one exists, it is impractical to ascertain the embodied GHG emissions of any novel solar cell, particularly one that utilises nanotechnology. It has become apparent that other studies have failed to include environmental impact with the release of novel PV technologies [249] and it would be false to quote any value for the demonstrated cell [250]. However, through a thorough and rigorous LCA of silicon PV, insights can be made in to the weaknesses of the incumbent technology and oversights of governmental policy pertaining to emissions reduction all the while establishing the framework for novel PV LCA once the data is available.

Through application of the integrated hybrid LCA, this work highlights the need for an alternative to silicon solar cells through recognition of the significant impact that silicon wafer production has on the carbon intensity. Low material usage and low cost deposition processes should enable a lower total value for embodied emissions. The demonstrated cell architecture may provide a pathway for this process.

The LCA also highlights the need for a better understanding of the carbon embodied in solar PV through highlighting policy flaws of the U.K. government. The renewable energy roadmap published by DECC states that, “Support for solar PV should deliver genuine carbon reductions that help meet the UK’s target of 15% renewable energy from final consumption by 2020 and in supporting the decarbonisation of our economy in the longer term – ensuring that all the carbon impacts of solar PV deployment are fully understood” [5]. However, results from this study differ greatly from these values and an increased accessibility to the methods used by DECC is necessary. The lifecycle emissions of solar PV provide a significant challenge to meeting electricity generation carbon intensity targets of 50g CO₂e/kWh by 2030. A complete re-assessment of the target should be undertaken based upon the full lifecycle impacts of renewable energy technologies. Alongside this there must be a comprehensive accounting system that considers the impacts of policies to discourage perverse technology choices that do not offer the required carbon savings. When establishing objectives and predictions for the carbon savings enabled through policy mechanisms, DECC must ensure that values are based upon thorough analysis and understanding. Their methodology should also be published freely and transparently for assessment.

Further to overly optimistic values for the carbon saving potential of silicon PV, current FiTs policy does not discriminate on the basis of the renewable resource at an installation site. To achieve a lower carbon intensity of electricity however would require prioritisation of more favourable sites. Criteria to ensure technologies are only deployed in favourable sites would incentivise appropriate use and move the UK closer to reaching a decarbonised electricity system.

Further consideration should also be given to the role of policy mechanisms for influencing supply chain decisions such as the material composition of products or their manufacturing locations. As the electricity intensity of different nations begins to change, the supply chain of technologies will become crucial in determining which scenario of electricity carbon intensity will apply. Solar PV is a global market with high levels of production in China, where electricity generation is heavily dependent on coal. Aims should therefore be made to either decarbonise the Chinese national grid or where possible, utilise a different, less carbon intensive supply chain. An attempt to reduce the carbon intensity of solar PV through reducing the carbon intensity of the Chinese national grid is presented in Chapter 7.

6 Methodology for the Assessment of PV Capacity Over a City Region Using Low-Resolution LiDAR Data

6.1 Introduction

It was seen in Chapter 5 that for a given insolation and size, the carbon savings of a single PV installation could be estimated. Arbitrarily selected insolation levels incident upon a single installation of a single size is still a somewhat hypothetical situation and real-world application of the methodology requires real-world values. To have a fully accurate assessment of the reduction in carbon emissions achieved through solar energy, the electrical output must be calculated through knowledge of the insolation incident upon all potential installations. Furthermore, knowledge of insolation values for all buildings in an area allows for prioritisation of installation sites. Selecting sites with the highest levels of insolation will allow for the highest levels of carbon savings.

Installing highly distributed PV within city environments, such as on building rooftops and facades, locates electricity generation close to electricity end use, reducing the requirement for modifications to the electricity distribution network and minimizing transmission losses. Roof mounted PV also avoids the cost and competition for land, and the possible social and environmental impacts associated with large arrays of ground mounted panels [251]. An accurate assessment of the potential roof-mounted PV capacity in city regions is an essential component for establishing regional and national carbon reduction policies and informing investment decisions [252]. However, such assessments are not straightforward because of the range in size, orientation, pitch, and geometric complexity typically found in roof profiles.

This chapter starts by introducing the need to be able to calculate the zenith and azimuthal angle of each building considered, a methodology for the assessment of solar insolation over a city region is then developed and the city of Leeds used as a case study. The methodology is then validated before the results of which are then directly linked with the embodied carbon values previously calculated to determine the carbon saving potential of solar energy deployment over a range of insolation values and installation sizes as would be the case for a city region. A conclusion is then made.

6.2 Background

Previously reported methods to calculate the potential PV capacity over a city region include image analysis of geometrically-corrected high-resolution aerial photography [253, 254], statistical approaches based on correlations between building class, population, and roof profile [255-257], and roof profile reconstruction from light detection and ranging (LiDAR) point clouds [258-269]. Methods that utilise LiDAR data usually employ an error-minimising plane-fitting algorithm that divides each roof into an arbitrary set of planes, which are referred to as roof segments. While such methods report high accuracy for large geometrically simple roofs, such as warehouses, they invariably require high-resolution LiDAR data to achieve accurate results for small buildings, such as residential properties, with inherently more complex roof profiles. This need for high resolution data often arises from the use of data driven methods such as Hough transform, random sample consensus (RANSAC), or region growing based techniques [266-268]. The presence of trees, chimneys, aerials, and dormer windows can further reduce accuracy, compounded by errors in LiDAR location referencing, noise, and ranging artefacts.

This chapter presents a methodology for the accurate reconstruction of roof profiles using low-resolution LiDAR data combined with building footprint datasets and knowledge of common roof profiles, recognising that using low-resolution LiDAR data alone is unlikely to generate accurate results. Compared to high-resolution LiDAR data, low-resolution data has greater coverage and is available at lower cost, making the methodology scalable to the regional and national level. A catalogue of common roof profiles is required, which is here localised for the UK. It is anticipated that application to other nations would require only a minor modification to the catalogue.

6.3 Methodology

The methodology is motivated by the need to accurately assess PV capacity over large regions of the built environment. The algorithms utilise low-resolution (2 m for the applied case study) LiDAR data, building footprint data, and knowledge of common roof profiles. LiDAR technology provides distance data and can be used to generate a grid of points over a region with each point containing (x, y, z) information which can be manipulated from a .csv file. Building footprint data comes in the form of a shapefile which can be manipulated by a GIS software package and provides the location and floor-plan shape of each building in a region as well as their areas. Other information, such as knowledge of building types and their frequency over the region is not used because such data is not routinely available and is rarely provided in a common format. For each building, a set of planar roof segments are

generated, allowing the presentation of segment orientation and pitch histograms in addition to cumulative capacity curves.

A visual inspection of aerial photographs confirms that large rooftops, from a variety of commercial and civic buildings, are usually geometrically simple but exhibit a wide variety of profile forms. This is in contrast to small rooftops, from residential properties, which can be geometrically complex but conform to a small catalogue of profile forms. This motivates the division of rooftops into *small* and *large* based on building footprint area. The determination of what constitutes as small and large buildings will be location specific and can be determined based on cultural and architectural factors. The two divisions are then processed using different algorithms.

6.3.1 Small Buildings

Most roof profiles for UK residential properties can be classified as *gabled*, *hipped*, or *flat*. A gabled profile consists of two flat segments intersecting along the roof ridge, while a hipped roof profile consist of four segments intersecting at 45° to the building sides when viewed from above, as illustrated in Figure 6.1. In all cases, every segment has the same pitch. These basic roof profiles can be adorned by chimneys, dormer windows, attached garages, porches, and extensions. A single rooftop can be shared by a number of properties. Terrace properties usually share a roof with a gabled profile, while semi-detached properties often share a roof with a hipped profile.

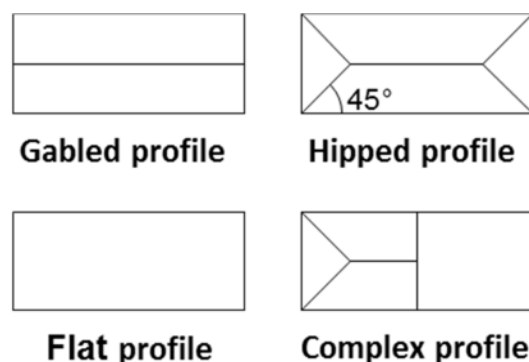


Figure 6.1: Illustration of roof profile catalogue when viewed from above. Depiction of a complex profile is an example.

Each small building is considered in turn. LiDAR points that lie within the building footprint polygon are extracted from the LiDAR point grid. This subset of LiDAR points is then rotated to both determine the orientation of the roof and prepare LiDAR point position data for roof profile classification. The centre point is defined as the point midway between the

minimum and maximum LiDAR point positions in the x and y directions, where z is defined as elevation. The LiDAR points are rotated about the centre point in order to minimise the range of LiDAR point positions in the y direction, and the rotation angle is recorded as the roof orientation. This procedure identifies the minor axis, and it is assumed that the major axis lies perpendicular to this.

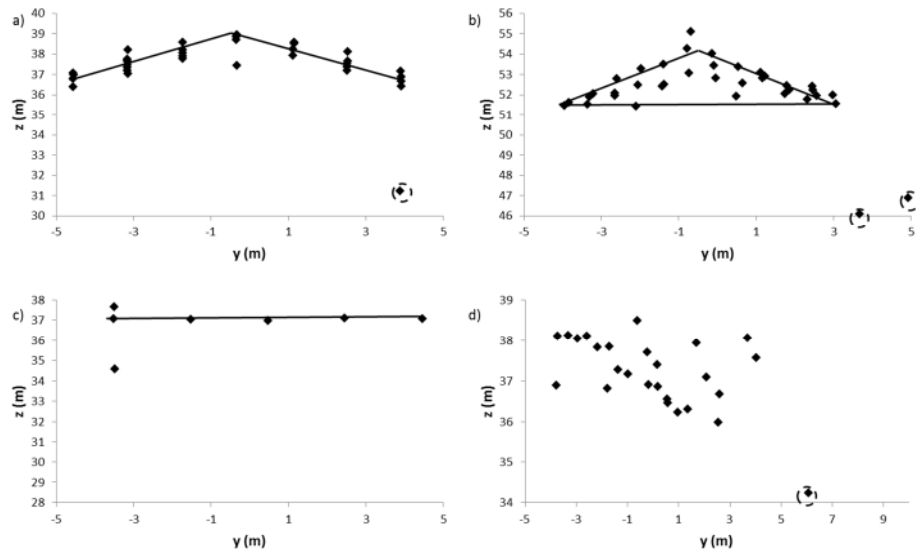


Figure 6.2: Sets of typical LiDAR points to illustrate each of the roof profile classes: a) gabled, b) hipped, c) flat, and d) complex. Points are viewed along the major axis. Grey lines provide a guide to the profile. Grey circles identify LiDAR points that are dismissed.

Each rooftop is then classified as either: *gabled*, *hipped*, *flat*, *complex*, or *unclassified*, as illustrated in Figure 6.1. The method and use of this categorisation is discussed later. Figure 6.2 plots sets of LiDAR points when viewed along the major axis of example buildings, illustrating each of the different roof profile classes. The roof edges are provided as a guide. LiDAR points with an elevation lower than 4 m below the maximum elevation are dismissed. Such points are either associated with porches or similar, or result from location referencing errors in the LiDAR point cloud. If the number of LiDAR points is less than 10 then the algorithm proves inaccurate, so the rooftop is classed as *unclassified*. Further consideration is not required because such small buildings, owing to their small area are less appropriate for PV. The division into *gabled* or *hipped* uses linear regression to calculate best fit planes for assumed gabled and hipped profiles. The planes are the superposition of the roof segments rotated by 0° , 90° , 180° , or 270° as appropriate. The plane with the strongest correlation (highest Pearson product-moment correlation coefficient) to the LiDAR points determines the classification of the roof profile and the corresponding pitch of the roof. If

the correlation is less than 0.4, then the roof is classed as *complex*. If the pitch of the roof is less than 15° , then the roof is classed as *flat*. Employing this algorithm produces an appraisal of roof profiles and pitches across a wide study area more efficiently than other more complex statistical methods [270]. The roof profile classification algorithm is summarised below. Once a class has been established, the algorithm ends and the next building is considered.

1. Dismiss LiDAR points that are more than 4 m below the maximum elevation
2. Class as *unclassified* if there are fewer than 10 LiDAR points
3. Calculate the correlation to a best fit line assuming a gabled profile
4. Calculate the correlation to a best fit line assuming a hipped profile
5. Class as *complex* if the maximum correlation is less than 0.4
6. Class as *flat* if the pitch of the best correlation is less than 15°
7. Class as *gabled* or *hipped* as associated by the maximum correlation

The roof profile class then determines the area and orientation of roof space available for PV installation. For rooftops classed as *gabled*, the roof is split into two segments along a line parallel to the major axis that passes through the centre point. The resource potential of the two segments are subsequently considered separately. For rooftops classed as *hipped*, the roof is split in to four segments, and all segments are considered separately. Rooftops classed as *flat* have one available segment, with PV assumed to be supported by an angle mounting with 15° pitch facing due south. Rooftops classed as *unclassified* contribute zero PV capacity. For rooftops classed as *complex*, there is no guarantee that the calculated orientation or pitch will correspond to a large roof segment. It is likely that there will be multiple roof segments at various angles, so complex buildings are considered to be inappropriate for PV installation. For all segments, an area reduction factor takes in to account obstructions to PV installation including aerials, chimneys, dormer windows and shading of the installation through artefacts such as vegetation and other buildings [256, 257, 271].

6.3.2 Large Buildings

Large buildings exhibit a diverse range of roof profiles, so the catalogue based approach utilised for small buildings is not effective. However, geometric features on large building rooftops are generally larger than the spatial resolution of the LiDAR data, so a more direct

approach can be taken to roof segmentation. The algorithm used here is similar to that used by ESRI ArcGIS [272].

Each large building is analysed in turn. The LiDAR points located within the building footprint polygon are then considered sequentially. Neighbouring LiDAR points are identified as those points that lie within a distance $(0.25 + 2^{0.5})d$ from the processed LiDAR point, where d is the spacing between LiDAR points. The LiDAR points are generally equally spaced within an orthogonal square grid, but are not always well orientated in the north-south east-west directions. By adding a buffer region to account for this, the equation ensures that all 9 nearest neighbours are found. For example, if the spacing between LiDAR points was 2 m, all points within a circle of radius 3.3 m will be found. This set of 9 local LiDAR points constitutes a 3×3 square array from which a roof segment pitch and orientation are calculated. If the set contains fewer than 9 points, then the processed LiDAR point must be close to the building boundary and is deemed unsuitable for PV installation.

A roof segment of area d^2 is associated with each LiDAR point. The best-fit plane to the set of 9 local LiDAR points is calculated using a least squares algorithm, providing dx , dy , and dz . The orientation of the segment is then calculated using equation (6.1),

$$orientation = \frac{360}{2\pi} \text{atan}_{4q} \left(\frac{dz}{dy}, -\frac{dz}{dx} \right) \quad (6.1)$$

where atan_{4q} is the 4-quadrant inverse tangent, and pitch is calculated using equation (6.2),

$$pitch = \frac{360}{2\pi} \text{atan} \left(\sqrt{\left(\frac{dz}{dy}\right)^2 + \left(\frac{dz}{dx}\right)^2} \right) \quad (6.2)$$

Some roof segments are distorted by location referencing errors in the LiDAR point cloud, or by roof furniture such as heating, ventilation, and air conditioning (HVAC) systems. Such segments are identified as having a pitch greater than 60° . These segments are dismissed, being either erroneous or unsuitable for PV installation. The large building algorithm can be extended by grouping adjacent segments when they have similar orientation and slope [273]. This would lead to improved efficiency when further analysing the roof segments but does not improve accuracy.

6.4 Application to the City Region of Leeds

The potential PV generation capacity was assessed over the city region of Leeds (UK) in order to demonstrate and validate the methodology. Leeds is a large city located in the north of England hosting a variety of domestic, commercial, and civic buildings of different ages and styles. The boundary of the region considered is identified in Figure 6.3, which covers

an area of 204 km² and includes 60,000 small buildings, which for the purpose of this case study are defined as having a footprint less than 200 m², and 15,000 large buildings. The population within this boundary is approximately 750,000 representing 1.2% of the UK population in 2011. Low-resolution LiDAR data was obtained from Landmap [274] with a grid resolution of 2 m and an elevation error margin of 0.15 m. There are 48×10^6 LiDAR points within the boundary. Building footprint data was obtained from Digimap [275]. The LiDAR points lying within each building footprint were filtered using a GIS-based system with output datasets in a text-based format. This resulted in a total of 5×10^6 LiDAR points under consideration. The total rooftop area available in the assessed region is 5.0×10^6 m² on small buildings and 11.3×10^6 m² on large buildings. Subsequent analysis was performed using MATLAB [276] running on a desktop computer. The assessment took 24 minutes, averaging 0.01 seconds for a building. To take into account shading and other roof uses, an area reduction factor of 0.9 was applied, following previous literature appropriate for Europe [277].

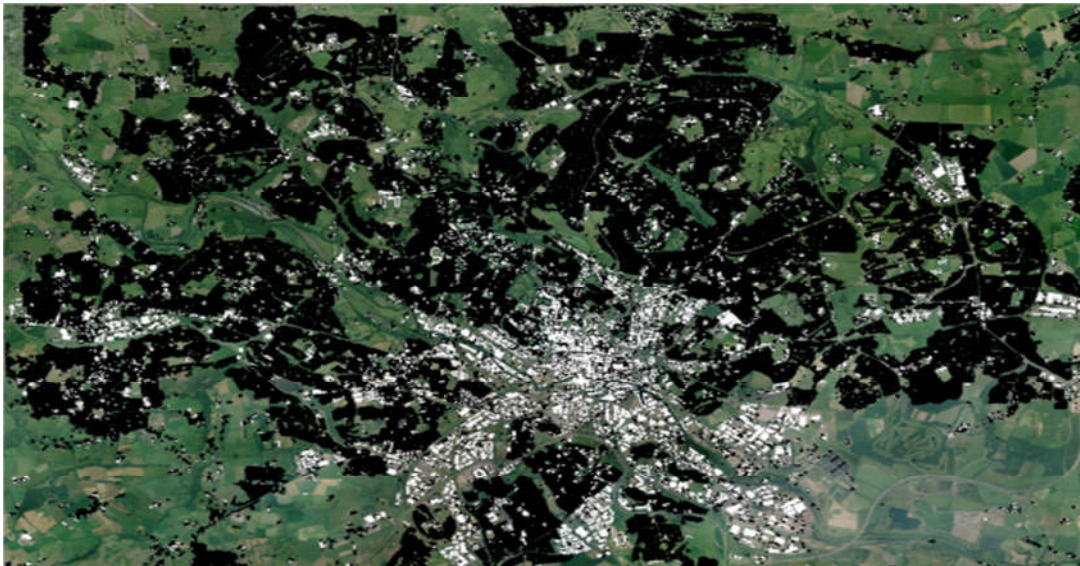


Figure 6.3: Boundary of the City of Leeds used in this assessment. Geometrically-corrected aerial photograph overlaid with small and large buildings filled in black and white respectively. Credit for photography: UKMap © The GeoInformation Group 2006; OS MasterMap [Shape geospatial data] EDINA Digimap Ordnance Survey Service 2013.

6.4.1 Roof Profile Assessment

Figure 6.4 shows frequency histograms for the orientation and pitch of roof segments weighted by the segment area. Small and large buildings are considered both separately and within combined plots. With reference to Figure 6.4(a), the pitch of rooftops on small

buildings peaks at 30° with the vast majority of small buildings having pitches within 10° of this value. A small peak at 15° occurs because flat roofs are assigned an angle of 15° for mounting PV. Figure 6.4(b) indicates that there are two common pitches for large buildings, one at 0° for flat roofs, and one at 9° which corresponds to the common 2:12 design accommodating efficient water run-off. Above 40° the frequency drops sharply for small buildings, but Figure 6.4(b) exhibits a long tail which is consistent with the more varied range of rooftop designs and features seen in larger buildings.

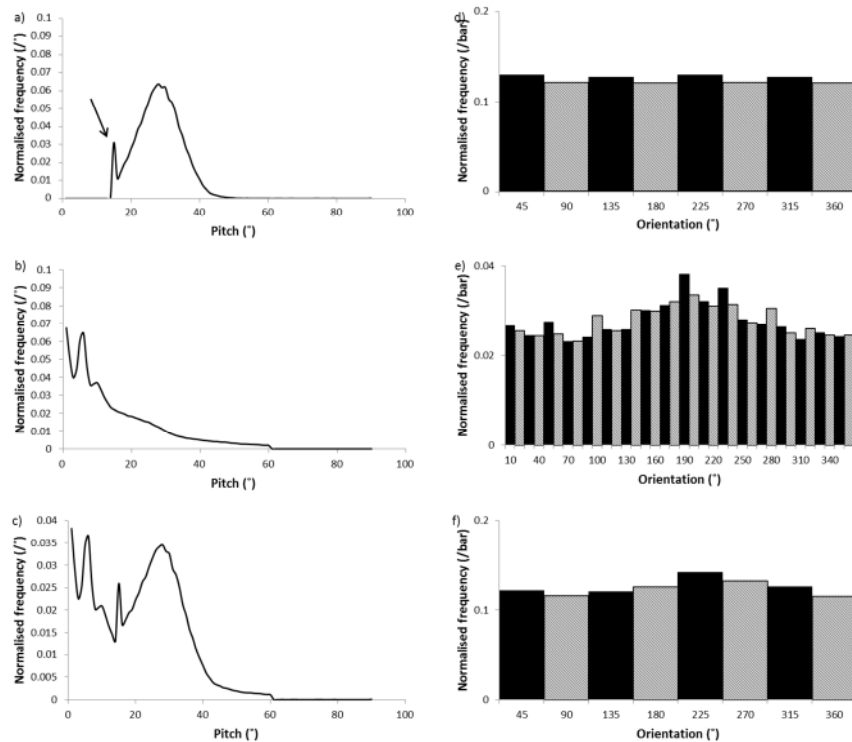


Figure 6.4: Area weighted histograms of roof segments for a) pitch of small buildings, b) pitch of large buildings, c) pitch of all buildings, d) orientation of small buildings, e) orientation of large buildings, and f) orientation of all buildings. Roof pitches are plotted as angles relative to the horizontal. Orientations are plotted as angles relative to north in a clockwise direction. The arrow in figure a) indicates the effect of assuming all flat roofs are given an artificial incline of 15° .

With reference to Figure 6.4(d), there is no clear preference for the orientation of small buildings. A 180° rotational symmetry is observed. This is because every roof segment has an associated opposite segment on the same rooftop, resulting from the geometrically symmetric nature of the roof profile classes. However, Figure 6.4(e) reveals that large buildings do have a preference for southerly orientation, making them particularly well suited for PV installation. This does not appear to be influenced by the orientation of roads

or rivers, or the landscape topography of the region. Note that the algorithm used to establish the orientation of small buildings results in some angular quantisation inherent from the orthogonal nature of the LiDAR point cloud and small size of the buildings. Hence, a minimum bin size of 45° is necessary in Figures 6.4(d) and 6.4(f) to generate accurate histograms. For the same reason, small building orientation has a maximum error of $\pm 22.5^\circ$ becoming smaller with larger rooftops. However, this has little impact on the annual output because insolation is relatively insensitive to orientation changes less than 22.5° . Furthermore, for regional calculations where many rooftops are considered collectively these random errors will tend to cancel.

The cumulative annual output of the city region of Leeds was calculated using the online PVGIS tool provided by the European Commission Joint Research Centre [278, 279]. The variables were set as latitude of $53^\circ 48' 4''$ north, longitude of $1^\circ 32' 54''$ west, CMSAF database, with an assumed system efficiency of 15%. The optimal pitch for the installation of PV at this location is 39° . A matrix of generation output data was calculated based on PVGIS with a 6° resolution in pitch and a 10° resolution in orientation. A performance factor was then assigned to each roof segment based on orientation and pitch, using linear interpolation between the tabulated values. Figure 6.5 shows specific annual yield and cumulative annual output plotted against the fraction of the total rooftop area available for PV. Small and large buildings were considered separately and combined. A performance factor is not included in the calculation of the specific annual yield. The most optimally angled roof segments are considered first, so the specific annual yield decreases and the cumulative annual output curve exhibits a decreasing gradient as less optimal segments contribute less to the total generation. Small buildings exhibit a higher specific annual yield because their pitch is generally closer to the optimal value.

The changes in gradient of the output curves are less accentuated than might be expected given that a vertical north-facing roof segment provides an annual output approximately 25% of that from an optimally angled panel [278, 279]. The output curves do reach this reduced gradient when the fraction of area is equal to one. However, the number of roof segments with extremely poor orientation and pitch is negligible and not visible on the output curves. In the case of small buildings, the output curves are dominated by rooftops with a pitch of approximately 30° . In this case, the annual output from a north facing segment is approximately 60% of that from a south facing segment.

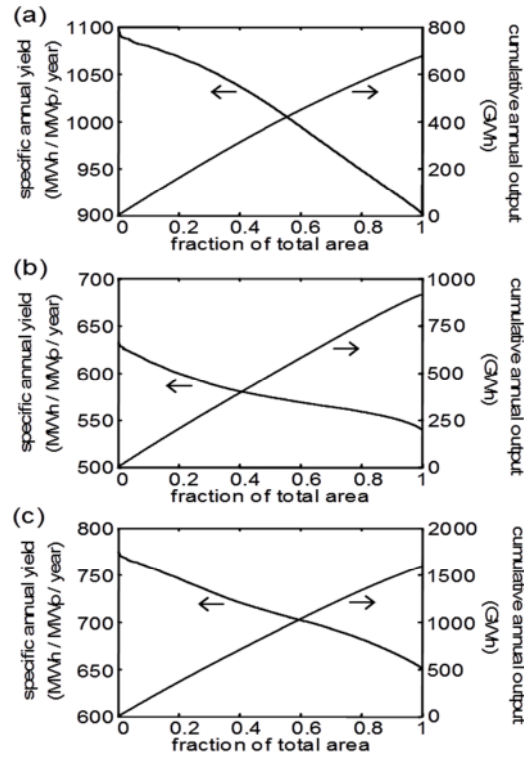


Figure 6.5: Plots of specific annual yield and cumulative annual output as a function of fraction of total area for a) small buildings, b) large buildings, and c) all buildings. The most optimally angled roof segments are considered first.

6.4.2 Validation

The small building roof profile classification algorithm was validated using a random sample of 242 buildings from the city region of Leeds. Each building was classified using both the algorithm described here and visually using geometrically-corrected aerial photographs. Table 6.1 shows the coincidence of this comparison. The random selection gave a fair representation of the ratio of the frequency of the different building types confirming that it is indeed a reliable sample.

Table 6.1: Comparison between classification from algorithm and validation from aerial photography. The units are number of buildings.

		Validation by Aerial Photography					
		Gabled	Hipped	Flat	Complex	Unclassified	
Classification Using Algorithm	Gabled	74	7	0	1	0	82
	Hipped	18	111	2	3	0	134
	Flat	0	0	3	2	0	5
	Complex	5	6	0	5	0	16
	Unclassified	0	0	0	0	5	5
		97	124	5	11	5	242

Table 6.1 highlights the success of the algorithm at identifying hipped rooftops yet 18% of gabled rooftops were incorrectly classified as hipped. This is most likely brought about due to the significant effect that noise can have on low-resolution data. The algorithm is poor at identifying all complex rooftops. However, complex rooftops occur infrequently so this has a minimal impact on cumulative PV output calculations. Loss of accuracy in identifying roof structure may have arisen from the elevation error margin of the LiDAR data or from the previously mentioned angular quantisation issues in determining the orientation. The overall success rate, using low-resolution LiDAR data, is 81%.

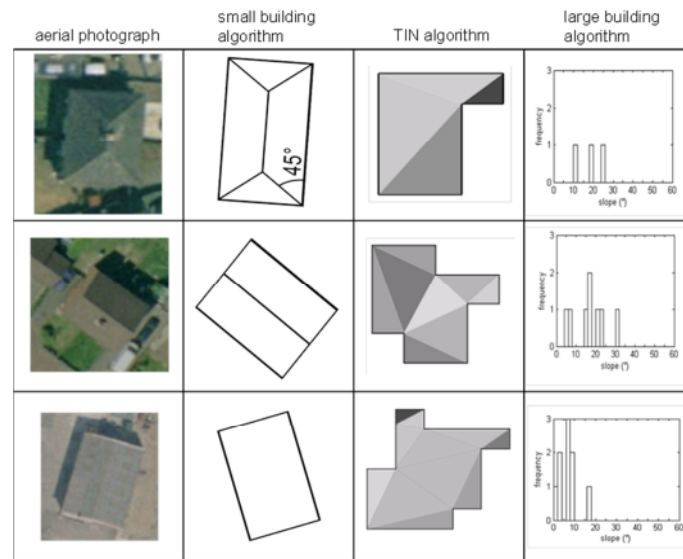


Figure 6.6: Comparison of the small building algorithm output, the TIN algorithm output, and the large building algorithm output, for examples of respectively small building hipped, gabled, and flat roof profiles. Credit for photography: UKMap © The GeoInformation Group 2006; OS MasterMap.

It is informative to consider the performance of alternative algorithms, which were originally designed for use with higher resolution LiDAR datasets, now implemented with low resolution data. Triangular irregular networks (TINs) are often generated from LiDAR point clouds as part of an algorithm to generate roof profiles [269]. Figure 6.6 provides a comparison of the small building algorithm output against aerial photographs, TIN profiles, and the large building algorithm output, all utilising the same low-resolution data. The TIN roof profiles provide a poor rooftop representation. Using the large building algorithm, a histogram of the pitches of generated segments is shown. The number of different pitches and their values are unrealistic.

6.5 Combination with Life Cycle Analysis

With a more accurate assessment of installation sizes and insolation values for these installations established, it is possible to determine more accurate values for the amount of carbon dioxide equivalent saved through installing roof mounted PV systems such as those encouraged through the feed-in tariff scheme. Here only small buildings are considered as the large buildings that were assessed for the roof top characterisation were broken down in to segments of 4 m², an unrealistic size for actual PV installations. Furthermore, large building installations are likely too large to qualify for FiTs.

LCA of an installation for each small building is accomplished through applying the formula as described in equation (5.3) but with inputting rooftop-specific values for the insolation

and the area. This will affect both the initial output and the embodied energy of the installation. For the sake of this study, embodied energy has been assumed to scale linearly with size. Due to the different processes involved and steps such as installation not likely scaling in such a manner, there will be some error associated with this. However, LCA database values are only given for the standard installation size of 22.1 m² and thus the performance of an LCA on every installation size is deemed impractical.

When each individual rooftop is considered, insolation values vary over the more realistic range of 292 KWh/m² to 1080 KWh/m² and the areas of the installations range from 13 to 90 m². The total carbon dioxide equivalent saving possible for widespread micro-PV deployment over the city region of Leeds ranges from 48 million tonnes for the most ambitious grid decarbonisation scenario to 82 million tonnes for the least ambitious scenario. It should be remembered that large buildings were not considered and that the total carbon dioxide equivalent saving possible will in fact be greater than this.

Despite considering fewer buildings than in section 5.3.4, the value for the quantity of CO₂e saved is in fact bigger. This can be attributed to the lack of staging in this study where all installations are assumed to be completed in 2015 and therefore providing an alternative source of energy to a more carbon intensive grid. If Leeds City Council were to implement a roll-out scheme over a period of years, the true carbon savings analysis could easily be performed.

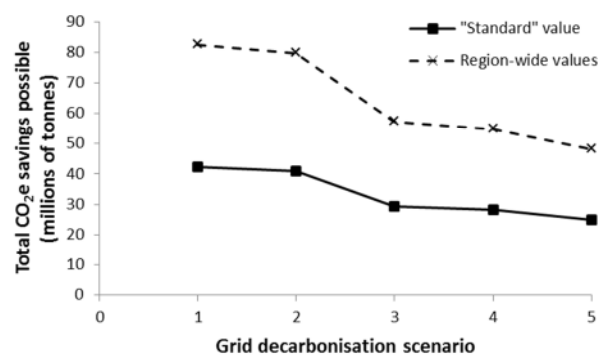


Figure 6.7: Difference in the potential CO₂e savings for PV installation over the region of the City of Leeds.

If instead of using the values derived from this methodology, the values estimated for area and insolation as used in Chapter 5 were instead applied to the same considered building stock, the total quantity of CO₂e saved is found to now range from 25 million tonnes for the most ambitious grid decarbonisation scenario to 42 million tonnes for the least ambitious

scenario. Therefore applying the methodology developed in this chapter has increased the calculated savings by 94 %. This is illustrated in Figure 6.7. These large discrepancies in carbon calculations have the potential to have a major impact when scaled up to the national and international level and, as discussed previously, when used in assessment of progress towards legal emissions reduction targets.

6.6 Conclusion

A computationally efficient methodology for roof profile classification is presented, for the purpose of regional PV capacity assessment, using widely available low-resolution LiDAR datasets. The results of such a PV capacity assessment can be used to enable a more accurate large-scale LCA of PV utilisation.

In this methodology, small and large buildings are considered separately. The roof segmentation algorithm for small buildings assigns a roof profile to each building from a catalogue of common profiles after identifying LiDAR points within the building footprint. Large buildings offer a more diverse range of roof profiles but geometric features are generally large, so a direct approach is taken to segmentation where each LiDAR point contributes a separate segment. The methodology was demonstrated by application to the city region of Leeds, UK, with 75,000 buildings. Validation by comparison to aerial photography indicates that the assignment of an appropriate roof profile to a small building is correct in 81% of cases. The small building algorithm also compares well against other methods that typically require higher resolution data such as TIN roof profiles. The methodology is readily scalable for county or national assessment of potential PV capacity. It is anticipated that application to other nations would require only a minor modification to the roof profile catalogue.

Through knowledge of the size of each rooftop and the individual insolation upon them, the quantity of CO₂e saved through PV installation can be calculated. This method will enable a more accurate assessment than using single values for rooftop size and insolation for a large amount of buildings over a region. It was calculated that using building-specific values increases the calculated value for quantity of CO₂e saved by 94%.

Further to this, an accurate dataset of roof-mounted PV capacity over city regions can assist strategic planning for carbon reduction by, for example, the identification and prioritisation of optimal locations for cost effective PV installations or assessment of the impact of regional policy change. With data values for every building in a city region, the dataset could be coupled with an interactive mapping tool to inform residents of individual building PV capacity.

7 Inter-Provincial Clean Development Mechanism

7.1 Introduction

Chapter 6 touched upon the ability to selectively choose the best location for solar PV installation. This would be the location with highest levels of insolation thus allowing the greatest amount of electricity to be produced and therefore increasing the quantity of CO₂e saved. As shown in equation 5.3, as well as increasing the electrical output, the other way to increase the quantity of CO₂e saved through PV utilisation is through reducing the amount of energy embodied in a PV installation. Chapter 5 highlighted the global nature of the solar PV supply chain. Silicon cell manufacture is dominated by Chinese production and as the majority of embodied emissions of solar PV use are attributed to this stage, efforts should be made to curb these emissions thus increasing the carbon saving potential of worldwide solar PV installations.

Such achievements in emissions reductions will arise through policy implementation and these policy issues must be addressed on a national, continental and international scale. China is a key example of an opportunity for large-scale policy implementation. Compared with other countries at the same latitude, China has a similar solar energy resource to the US and much better than Japan and Europe, combining this with its booming economy, rapidly growing population and its over-dependence on coal, highlights china as a place in critical need of increased, effective wide-spread solar energy deployment.

A key driver in renewable energy development globally is the clean development mechanism. To become more applicable to individual countries or political bodies, such as China, this policy mechanism is analysed and through a case-study of solar energy in China, an alternative/supplementary nationwide mechanism is proposed and the outcomes predicted and analysed.

This chapter starts by reviewing China and its current policies for renewable energy development. It will then provide an overview of the global CDM and discusses the implementation of an inter-provincial CDM in China before utilising PV as a technology to provide a case study for the mechanism's implementation and finally, concludes.

7.2 Background on China

In terms of climate change mitigation and the implementation of solar PV and other renewable technologies, China has a more significant role than most. It not only has the largest population in the world, but has also seen rapid economic growth in recent years

resulting in a dramatic increase in energy demand. Coal accounts for over 75% of its primary energy mix [280], a factor that has contributed to China becoming the largest CO₂ emitter in the world [281]. Since 2003, more than half of the increase in global CO₂ emissions can be attributed to China [282]. Although Chinese per capita CO₂ emissions reached the same level as the OECD average of around 7.5 tons in 2011 [283], the emission inequalities between urban and rural residents is over three-fold [284].

China aims to achieve 11.4% of its primary energy supply by non-fossil fuels by the end of 2015. However, current implementation of renewable energy development is largely relying on top-down policy and heavy governmental subsidies. There is no effective market orientated mechanism to accelerate the growth. The clean development mechanism (CDM) is an international tool that has made great progress in terms of emission trading since its inception in 2001, although there are criticisms about its effectiveness [285]. It has received very little attention on the national scale however and despite its use having significant potential. It also possesses the ability to run alongside other incentives and schemes while also being market-orientated and therefore minimising governmental costs.

This chapter aims to introduce the concept of an inter-provincial clean development mechanism (IP-CDM) and assess its potential implementation and effectiveness through a case study of the solar photovoltaics sector.

China's first clear indication of its dedication to renewable energy came through its 11th 5-year plan (2006-2010) where it moved away from an attitude of 'growth at any cost' towards a more balanced and sustainable growth pattern [286]. Included in the plan was an aim to reduce energy consumption per unit of gross domestic product (GDP) by 20% during the five years. Other policies that have influenced renewable and sustainable growth in China include: the 2006 Renewable Energy Development Law, the 2007 Mid-Long Term Development Plan, the 2009 Renewable Energy Law Amendment, the Strong and Smart grid plan, Feed-in tariffs and the solar roofs program [287].

The Renewable Energy Development Law in particular provided great strides in the implementation of renewable energy, stipulating that the electricity grid companies must buy all connected renewable energy [288] and that the expense of this shall be shared in the selling price [289]. The Mid-Long Term Development Plan can be seen as a supplementary policy to the Renewable Energy Development Law and tries to create a roadmap for the development and planning of renewable energy. This is mainly done by setting up policies in the five areas of: establishing a sustainable and stable market demand, improving the market environment, setting renewable power tariff and cost-sharing policies, increasing fiscal input

and tax incentives and accelerating technology improvement and industrial development [290].

There are several specific strategies that have been devised to help accelerate China's sustainable development, including reducing emissions, actively controlling the population, developing carbon sinks, adjusting the economic structure and speeding up the development of clean energy [291]. Unfortunately, reviews have found that so far, these approaches haven't had the desired effect [292]. Problems include the fact that a lot of subsidies have only been symbolic in nature, leading to a lack of tangible effect and that China's method of supporting renewable energy technologies through taxation has been too weak [293]. There have also been many issues with the current sustainable development policies including key issues about grid connection, tariff setting and cost distribution [294]. Issues have also been found with tenders, such as where state-owned companies can afford to lose money on a bid in the short-term, so long as they can control the resource for longer-term profit [292]. This has created a situation where more effort is going into creating a monopoly and controlling the resource than in actually implementing the energy efficient technologies. China also needs to consider the cost effectiveness of each policy strategy [9]. Zhang et al. [293] conclude that there is a lack of coordination and consistency in policy, a weak and incomplete encouragement system, no innovation in regional policy, an incomplete financing system for renewable energy projects and inadequate investment in the technical research and development for renewable energy.

With vast differences in availability of renewable resources and socio-economic diversity between Chinese provinces, regional policy is an area that should be given more attention [295]. To date, measures have not been accurately tailored to account for the diversity of local conditions [293, 296, 297] despite research finding that regions are in need of different incentives [287, 298].

7.3 An Overview of the Clean Development Mechanism

The global CDM is one of the mechanisms defined by the Kyoto Protocol that enables parties to effectively reduce their overall emissions cost by implementing measures in less developed countries [299]. This is based on the fact that regardless of where the carbon reduction takes place, the benefit to the atmosphere is the same.

The global CDM has two objectives: 1) to assist developing countries in achieving sustainable development and 2) to assist the developed countries in achieving their emissions limits. This second objective is achieved by using Certified Emissions Reductions (CERs). CERs, otherwise known as carbon credits, can be purchased from the party that is

hosting the reduction. These credits are awarded by assessing how much of a reduction in emissions the project has achieved when compared to a baseline scenario. The baseline emissions are the emissions that are predicted to have occurred if the project had not been implemented. The number of credits awarded is therefore proportional to the difference between the baseline emissions and the new lowered emissions that have resulted from the implemented project. These carbon credits can be traded, sold and used by developed countries as a means to help meet their emissions targets (EU, Kyoto or other) in a more cost effective way.

Through the formation of the CDM, a structure was defined to enable the participating parties to interact with each other and the mechanism as effectively as possible. One important aspect of this structure is the introduction of national CDM boards for every participating nation. Their purpose is to review CDM project activities within 8 aspects: (1) Participation qualification, (2) Project design document approval, (3) Baseline methodology and emission reductions auditing, (4) CER monitoring, (5) Terms relating to funding and technology transfer, (6) Defining accreditation period, (7) Project monitoring, and (8) Calculation of sustainable development effectiveness. In the case of China, this board consists of members from the National Development and Reform Commission (NDRC), the Ministry of Science and Technology (MOST), the Ministry of Foreign Affairs (MFA) and other national ministries [300]. In particular, the NDRC is the designated CDM national authority and has the roles of interacting with the CDM board and accepting project applications.

The last aspect listed under the national board responsibilities is to ensure sustainable development effectiveness and indeed, the first aim of the CDM as described in the Kyoto Protocol is to assist in sustainable development. Every project should therefore be able to guarantee that it is truly sustainable. A sustainable project was first defined by the UN as one that “meets the needs of the present without compromising the ability of future generations to meet their own needs” [301]. To measure if a project is truly sustainable is not as straightforward as it may first appear and many methods have been proposed to measure the true sustainability of CDM projects (e.g. [302-304]).

CDM projects can fall in to the following categories: demand-side energy efficiency; afforestation & reforestation; transport; HFCs, PFCs, SF₆ and N₂O reduction; renewable energy technology; CH₄ reduction and cement & coal mine/bed CH₄ recovery; supply-side energy efficiency and fuel switching. The most common project by far (69% of all CDM projects) is the implementation of renewable energy [305].

If the CDM was used to implement a renewable energy technology or to increase energy efficiency, this would result in a decrease in the amount of fossil fuel sources that would be required to be combusted. A decrease in fossil fuel combustion would lead to the co-benefits of a reduction in the emissions of other pollutants and the improvement of local air quality. Another benefit of the CDM is that as well as allowing developed countries to invest in emission reductions at the lowest price globally, it provides an instrument that enables the growth of sustainability in developing regions. For example, it has been found that the CDM can be used as a way to promote development in remote Chinese provinces and allows project developers in these provinces to enhance the profitability of project implementation [306].

The CDM's benefits are therefore potentially triple: it can reduce the rate of anthropogenic climate change, improve the development of poorer regions and through the potential reduction in fossil fuel combustion, it can improve local air quality, leading to co-benefits.

The CDM however has had its issues, especially in its implementation. The first issue is additionality. This is the need to prove the project would have happened anyway without the extra finance provided by the CDM. This issue has been raised frequently in scientific literature and political discourse [307-309]. Additionality is especially problematic in a country where sometimes wide-spread corruption can still be found. Many CDM projects are not "additional", which means that many projects registered under the CDM would have been built anyway, but allow industrialised countries to emit more. It is estimated that 75% of all approved CDM projects were already up and running at the time they were approved [310].

Second, the amount of carbon credits awarded to a project is also a contentious issue. The amount of credits awarded should be proportional to its effectiveness in reducing carbon emissions from a baseline scenario where the project was not put in place. Therefore accurate calculations of what the emissions were originally and what they will be after are vital for the accurate distribution of credits. However, an accurate, exhaustive and reliable database of carbon emissions is unavailable. Accurate carbon measurement may help with the issue of firms looking to take advantage of the scheme by raising their emissions before the implementation of a project and therefore getting more credits after the project's implementation.

Third, it has also been noted that the current global CDM process is quite complex, which may leave some private companies feeling overwhelmed, deterring them from investing.

Fourth, infrastructure issues also exist. There is no advantage in a sustainable development project if it can't be utilised. In China's case, transmission and grid reliability are a common

problem. For example, in July 2009 about 30% of China's wind capacity was not connected to the grid and was at that time not utilised.

Fifth, many CDM projects do not entail technology diffusion. For example, half of all the new hydropower capacity that is being built in China is in the CDM pipeline and while hydropower is a low carbon technology, it is a technology that China is more advanced in than many developed countries [311].

Last, a potential failing of the CDM is that its effective scope is limited to a few sectors and more financial and technological support is needed from developed countries to tackle the emissions from coal-dominated power industries in developing countries such as China and India. The CDM has also been found to be ineffective in reducing emissions from diffuse sources, such as in the transportation and household sectors [311].

While there are numerous issues with the CDM, it is still a vital and valuable tool and one that can, "despite its limitations, contribute to reducing economic inequality and uneven development in China" [306]. The CDM is therefore a mechanism that could be considered on a national level for China.

7.4 The Establishment of an Inter-Provincial Clean Development Mechanism in China

Based on long-term plans and international legislation, the Chinese central government sets national level targets that must be achieved. These targets usually encompass four areas: economic development, social development, resource and environmental concerns and administration. They can be broken down by central government to the provincial level where the provincial governors' performances are assessed through their ability to meet these targets. Central government must therefore develop incentives and schemes to ensure that these targets are achievable. Through this unique, central structure an opportunity to create innovative and effective policy mechanisms arises. According to China's National Climate Change Program, energy efficiency and renewable energy supplies are its top priorities in climate change mitigation [290]. As discussed previously, if China is to achieve its ambitious carbon intensity reduction plans, it will need a strong and complete policy and economic set. An inter-provincial clean development mechanism (IP-CDM) is therefore suggested as a mechanism to help achieve this and has the potential to excel within the centrally focussed governmental system of China. The IP-CDM would work in a similar way to the global CDM but on a national scale, more developed provinces would be able to buy carbon credits for the construction of sustainable developments in less developed provinces.

It must be stressed that this IP-CDM is in no ways intended to be the successor to the CDM but to run parallel to it and any successor. The credits gained in this scheme are not exchangeable with CDM credits as when the IP-CDM is utilised, the mechanism would still be China developing independently and not through a lesser developed country. The IP-CDM aims to use the foundations and lessons learned from the global CDM to attain further sustainability in China and beyond. With this in mind, while the potential successor to the global CDM may have some elements of a sectoral or inter-sectoral approach, this is not necessary for the IP-CDM. Considering, as will be seen, each province already has an emission reduction target, it would not be suitable to set sectoral emission baselines as well. Therefore, a project-by-project approach with an ex-post crediting system will be more beneficial. This style of mechanism can also create the opportunity for the central government to add further incentives for IP-CDM projects that are more heavily focussed on the nation's long term holistic climate change mitigation approach.

There are of course no divisions of provinces into annexes in China and therefore no clear analogy of what the 'Annex 1' (developed) provinces should be. However, there is no final need for the definition of these provinces as investment can be made or projects created in any province. It will be the provinces with the strictest emission reduction targets, worst natural resources and highest cost of labour that will be most obliged to use the mechanism and as will be seen, these are the provinces that are the richest in the country.

The 12th Five-Year Guideline of the People's Republic of China has been made for the years 2011-2015 inclusive including a national target of a 17% reduction in the carbon intensity (carbon dioxide equivalent (CO₂e) emissions per GDP) by 2015 [286]. It can be expected that as global concern about climate change intensifies, the national and provincial targets that will be set through further five-year plans will only become more stringent and ambitious.

As part of the 12th Five-Year Guideline, China's State Council set each province individual targets as shown in Table 7.1:

Table 7.1: Carbon intensity reduction targets of each province [312].

Carbon Intensity Reduction Target (%)	Provinces
19.5	Guangdong
19	Tianjin, Shanghai, Jiangsu, Zhejiang
18	Beijing, Hebei, Liaoning, Shandong
17.5	Fujian, Sichuan
17	Shanxi, Jilin, Anhui, Jiangxi, Henan, Hubei, Hunan, Chongqing, Shaanxi
16.5	Yunnan
16	Inner Mongolia, Heilongjiang, Guangxi, Guizhou, Gansu, Ningxia
11	Hainan, Xinjiang
10	Xizang

Nine of the ten richest provinces per capita in China have targets stricter than the national average of 17% and the top five richest provinces per capita (Tianjin, Shanghai, Beijing, Jiangsu and Zhejiang in descending order) plus Guangdong have the six strictest targets [312].

For the more developed provinces, labour costs can play an important role in meeting these targets. If these costs are high, it may deter the provincial government from investing in meeting these targets. A project is going to be much more feasible and attractive if the labour costs are significantly lower and minimum wage in the less developed provinces can be less than half those in the provinces with the highest GDP per capita [313].

To accompany this, in a review that took place towards the end of 2011, half of these ten richest provinces have an energy saving situation classed as either “grim” or “very serious”, indicating that these provinces are struggling to find solutions to meet the targets that the state council has set for them [314]. This closely mirrors the global CDM situation where developed regions are looking to lower their emissions and are in need of help to do so.

The IP-CDM would therefore help richer provinces meet their carbon intensity reduction targets by reducing GHG emissions while simultaneously increasing cleaner production of the poorer provinces and at the same time allowing their GDP to grow. And despite a few

issues that have been discussed, in the context of providing sustainable development, the global CDM is widely seen as a success [315, 316], indicating that an inter-provincial CDM model could make a noticeable impact.

7.5 IP-CDM Implementation Procedure

It has been found that inconsistencies between international rules and China's policies have prohibited China's central government from achieving the full potential of the CDM [306]. Therefore with the IP-CDM, China has an opportunity to create a self-suiting system that works within its unique structure to achieve maximum results.

As discussed in the previous section, China has an already established governmental structure to interact with the global CDM and this shows that a solid platform and robust system for management and decision making is already in place. It has been shown that regulation, policy and institutional arrangement have managed to rapidly promote international CDM activities since 2005 [316]. Therefore, it could be very easily replicated on the provincial level to great effect. The national CDM board could also oversee issues related to the IP-CDM, such as the auditing and monitoring of credits and individual provincial authorities could be created for each province. This provincial authority could consist of members of each Provincial Development and Reform Commission (PDRC). These would take the roles for the IP-CDM that are filled by members of the NDRC for the national CDM authority in the global CDM. These provincial authorities will then interact with each other and parties that are participating in the IP-CDM. Through this, instant and effective implementation can be achieved and the deployment of the IP-CDM can generate immediate impacts.

The Chinese State Council has already ordered a trial run of two provinces and five cities to set up carbon markets [299]. These trial carbon markets started in 2014 [317] and were the first steps in the government's massive undertaking of trying to establish a national emission trading system after 2016 [318]. As well as these official trial projects, over 100 emission trading schemes have also been established. The proposed IP-CDM therefore slots right in to this cap-and-trade style scheme and has the potential to be a major influence in the future Chinese national emission trading system. If this is the case, the timing of the implementation of the trading scheme, the issuance of credits and the introduction of new provincial emission targets, as provided by the five-year plans, should all be aligned and coordinated to achieve maximum cohesion.

7.6 Tackling the Flaws

As discussed previously, the global CDM is of course by no means perfect. However, for many issues, the previous program's difficulties simply give the IP-CDM the benefit of hindsight and the opportunity to improve on the original mechanism.

A seamless introduction of the IP-CDM will be extremely important to achieve as great an impact as possible. In this regard, it is important to stress again that the IP-CDM will be designed to run parallel to the global CDM and the two shall not interact. The credit allocation and auditing processes should be independent between the two. This ensures that issues, such as whom to allocate credits to will be avoided. Any international investment would fall under the realms of the global CDM. For more complex decisions, one route should be chosen outright from the start. For example, if an international company with plants in multiple locations is buying credits from a sustainable development project completed in a lesser developed province of China, they can choose who buys the credits, i.e. a factory in the richer province in China or a factory in Europe. Wherever the factory that buys the credits is based, that is who gets the credit for reducing emissions. If the plant is in China then the IP-CDM can be used, otherwise it would go through the route of the global CDM.

It could also be thought that the implementation of an IP-CDM may hinder international CDM projects with assessors possibly suggesting that funding is available for the proposed project through the IP-CDM instead. However, the provincial carbon intensity targets were put in place in 2012 and it was stipulated by the global CDM executive board that CDM decisions should not take into account any national policies that give comparative advantage to less emissions intensive technologies or fuels, provided that the law came into effect after 2001 (the E- policy) [319]. This allows for the dual existence of the CDM and IP-CDM and also allows China to continue adopting and implementing stringent emission intensity cuts and ambitious policies. This E- policy could be combined with other experiences of additionality issues [320] and a stringent and easy-to-regulate assessment method can be drawn up and applied.

The execution of the IP-CDM could also be seen as an ideal time to create a comprehensive and reliable national carbon emissions database. Current Chinese emission inventories have significant uncertainties [321]. If accurate emissions databases are available, the search for a loophole in emissions accounting will be identified more easily. This database would also be of significant use to ecological researchers looking to complete life cycle assessment studies of processes in China, which is an area that has already received a lot of academic attention

(e.g. [322]). The hybrid LCA methodology demonstrated in Chapter 5 could be used here to further increase accuracy.

The complexity of the CDM application and implementation procedures were found to be a hindrance and off-putting to some investors. The process should therefore be streamlined and a guide based on past experience should be produced. This guide should be concise but comprehensively cover areas on identifying, analysing and developing projects, as well as on how to obtain project financing [323]. This streamlining and guide would also lower costs and increase interest in the mechanism.

Due to the likely placement of projects within the poorer, western provinces, the IP-CDM will not solve the issues of rising energy demand in the large fast-growing coastal cities. This is a separate issue that must be considered but with electricity demand growth happening nationwide, the mechanism has the potential to provide some relief. Other issues that the IP-CDM unfortunately doesn't cover include the limited scope of its effectiveness and the lack of technology diffusion.

7.7 Potential Impact of the IP-CDM

If implemented efficiently and effectively, the IP-CDM can have significant results. Drawing parallels with the global CDM, the magnitude of the impact can be predicted. Assessing the total amount of annual CERs currently registered [324], the percentage of baseline emissions from annex I countries that this is equivalent to can be calculated to be roughly 7% [325]. Due to increased implementation speeds and an already developed understanding, it would therefore be practical to assume that the IP-CDM has the potential to account for an 8% decrease of participating provinces' emissions.

Although an absolute definition of which provinces are the 'Annex 1' provinces has not been made, it is more likely that the richer the province, the more it will make use of the IP-CDM. Therefore, for the sake of this calculation, it was empirically decided to split the provinces so that those having over 30,000 RMB per capita will be the ones investing in the IP-CDM, with the aim of reducing their emissions (i.e. similar to the annex 1 countries) and those provinces with a GDP below 30,000 RMB per capita, being those where the projects will be implemented. If these 18 provinces that were above the cut-off point in terms of GDP per capita were to have their baseline emissions [297] reduced by 8% due to IP-CDM projects, this would lead to a reduction of 459 million tonnes of CO₂e per year, with a total investment of 10.96 billion RMB (at an exchange rate of 1 euro = 7.9427 Yuan).

Another potential policy that could be employed to meet the national carbon intensity targets is through the use of a bubble policy, as was employed by the United States Environmental

Protection Agency in 1979 [326]. This policy draws an imaginary bubble around plants and allows a certain amount of carbon dioxide equivalent to be contained within that ‘bubble’. This means that emissions in one area can be increased provided that a decrease of emissions in another area compensates for it. Such an approach can simultaneously stimulate innovation and reduce the cost of emissions regulation [326].

The IP-CDM could be used in conjunction with this method where IP-CDM credits could be bought to increase the size of the ‘bubble’. The purchase of credits would then become more attractive for plant owners when buying credits is cheaper than the cost of reducing on-site emissions. This of course creates a similar approach to emission reduction as the cap and trade system, but does have subtle differences. For example, the purchase of credits isn’t just the purchase of permission to emit more carbon dioxide than allocated, but it is also paying for sustainable development and the development of lesser developed regions. These subtleties could create a system that is more attractive than the original cap-and-trade system and the true benefits of the coupling of these mechanisms should be further investigated.

7.8 A Case Study of Solar Photovoltaics

To further investigate the possible impact of the IP-CDM, its potential to interact with the most common type of CDM - renewable energy will now be considered. For this purpose, solar photovoltaics was chosen as a case study.

Solar PV is one of the burgeoning renewable energy technologies that can be used in climate change mitigation and is therefore used as one of the projects for the global CDM. Studies have predicted that PV generation will have a global generation share of 10% in 2030 and 20% by 2040. By the end of the century, renewable energy will account for over 80% of the energy mix and solar power is predicted to account for over 60% of that renewable energy supply [327]. It has also been suggested that PV will be cost competitive in China by 2030 [328].

China has an excellent solar resource with all of the country having at least an “average” solar resource rating and many provinces having a “very abundant” or “most abundant” solar resource. This is illustrated in Table 7.2.

Table 7.2: Solar resource map of China [329].

Zone	Annual Solar Radiation (kWh/m ²)	Share of the Nation Total (%)	Area
Most Abundant	≥ 1,750	17.4	Tibet, South Xinjiang, Qinghai, Gansu, West Inner Mongolia
Very Abundant	1,400 - 1,750	42.7	North Xinjiang, Northeast China, East Inner Mongolia, Huabei, North Jiangsu, Huangtu Plateau, East Qinghai, Gansu, West Sichuan, Hengduan Mountain, Fujian, South Guangdong, Hainan
Abundant	1,050 - 1,400	36.3	Hill areas in Southeast, Hanshui river basin, West Guangxi
Average	< 1,050	3.6	Sichuan, Guizhou

Beyond this, desertified land accounts for about a quarter of China's land area which is ideal for solar PV installation, especially large scale PV. In theory, 1% of this desertified land could be used to install 2,500 GWp of solar PV, which would be enough to supply the 2007 electrical output of China [328].

The implementation of solar PV is facing three barriers: technological, financial and practical. Currently the cost per kilowatt hour cannot compete with traditional sources of energy such as coal. Thus, a significant increase in the efficiency of PV technology is needed. Naturally, this is dependent on the amount of money devoted to solar PV research and the stimulus given to research and development. All new technologies follow a learning curve and require investment and initial use. Investment by enterprise is therefore necessary and this creates a financial barrier, where initial investment may be slow as short term rewards will be marginal if any. Practically, solar PV needs a supporting infrastructure and it also needs experts in the whole supply chain of the sector from production through to installation and maintenance. These three barriers need policy support to be lowered and then overcome.

China is starting to wake up to the potential of solar energy. However, the domestic solar PV sector still has some way to go before catching up with the national development of wind power, which is much more widely used. At the end of 2014, wind power in the People's Republic of China accounted for 114 GW of electricity generating capacity [329] already surpassing the 100 GW by 2020 target for installed wind power capacity that was set in 2005 [330]. Whereas for solar PV, China's cumulative capacity of photovoltaics reached 11.8 GW in 2014. In May 2011, the National People's Congress (NPC) set 5 GW as an official minimum PV target for 2015, with a longer-term target of 20–30 GW by 2020 [331].

This stark difference between wind and solar deployment is often attributed to the fact that wind energy is a more mature low carbon technology and therefore its cost is closer to grid parity than the less established solar PV technology [294]. There is currently a lack of R&D in solar PV and incentives are needed for its development. If implemented correctly, it would increase the speed that solar PV reaches wholesale grid parity.

In China, there is also an issue of location. The areas with the best natural resource for solar PV are also the least developed and far away from the richer east coastal regions. These western regions have less impetus to install solar PV and focus on sustainability as other factors, such as infrastructure development and improving the finances of the regions, are given priority.

China is the world's largest producer of solar PV cells, but currently 98% of these cells are exported to the international PV market [332]. This puts the PV manufacturing sector at the mercy of global economics. Due to this large reliance on exportation, it was heavily influenced by the 2008 financial crisis. Products couldn't be sold and some solar cell producers became bankrupt. This highlights the need for a domestic market if the solar cell manufacturing business is to be assured of stability and growth.

It has been shown that "good energy policies can effectively decrease the cost of power generation" [294]. With regard to solar PV flourishing in China, the country needs both strong policy and substantial programs. Already for wind, the cost of installation has been reduced, the localization of wind power manufacture has been stimulated and company investment has been driven up due to effective policies. This has led to a great reduction in wind power's grid price. The IP-CDM could be an ideal mechanism to create an increase in the deployment of solar PV.

7.8.1 The mutual benefits of solar PV and the inter-provincial CDM

Before solar PV's interaction with the IP-CDM can be assessed, an initial assessment should be conducted in order to ensure that it is a suitable technology. This covers two areas: it must first be assessed if solar PV is truly sustainable and then the issue of additionality should be considered.

Referring back to the issue of ensuring that each project is sustainable as discussed in section 7.3, it can be seen that Solar PV is a textbook example of a truly sustainable development. The project design document (PDD) of two randomly selected case studies of internationally funded CDM solar PV projects based in China (namely "CDM Project 4919: Ningxia Hongsipu 50MWp PV (photovoltaic) Power No.1 Plant Project" [333] and "CDM Project

4981 : CECIC Shizuishan Grid-connected Solar PV Power Generation Phase I” [334]) give the following justifications of sustainability:

- Utilizing solar energy to generate no GHG emissions electricity, reducing greenhouse gas emissions and other pollutants compared with fuel-fired power plant
- Diversifying power sources and making use of more clean energy
- Accelerating development of engineering and technology of large-scale grid-connected photovoltaic power plant; Stimulating the growth of the solar power industry in China
- Create employment opportunities during the construction and operation period of the project

These justifications clearly agree with the UN’s aims of sustainability and vitally, these reasons can clearly be replicated for any solar PV project. Thus, in the use of this technology in the IP-CDM, no issues of sustainability will be expected to be encountered.

As well as sustainability, additionality must also be proved. The previously mentioned approved PDDs that were studied yield similar results when assessing the financial situation of the respective projects. The first project claims that during the compilation of the Feasibility Study Report (FSR), the economic analysis showed that the internal rate of return of the proposed project is lower than the benchmark of 8%. The project therefore lacks initial financial attractiveness but with assistance from the CDM, the financial condition of the proposed project will be well improved. The other studied project has similar figures claiming that the CDM funding increases the project internal rate of return from 6.59% to 7.71%, which is still lower than the additionality benchmark of 8% but certainly more attractive. Without the CDM, solar PV is not financially attractive and therefore additionality is proved, meaning that with this technology, there will be none of the deception or misuse of the system that the global CDM struggled to control.

As solar PV is both sustainable and additional, it can be used as a project in the IP-CDM. This would therefore increase the rate of development of solar PV on top of the previously mentioned benefits of meeting emission targets, improving air quality and creating developments in less developed regions. Global CDM programs have accounted for nearly 2.5 GW – more than three quarters - of China’s total installed solar capacity [305]. This not only highlights the importance and effectiveness of a CDM style mechanism, but also shows the success that a well-organised and accessible policy can achieve.

With the IP-CDM, China not only has the opportunity to reduce its emissions but also the opportunity to take advantage of a fantastic natural resource with six of China’s ten poorest regions having access to a solar resource classed as “most abundant” or “very abundant”

[280, 328]. Therefore, an IP-CDM seems an ideal solution to a situation where there are developed regions needing to reduce their carbon intensity and poorer regions with abundant potential that may not have the funds to direct away from more immediate issues. Furthermore, the IP-CDM could also help grow the domestic share of the market for solar cell production.

Recently the Chinese solar industry has been struggling with overcapacity and trade disputes. This has mainly been due to what could be considered reckless expansion of the sector which resulted in a production capacity that is greater than total global demand. This led to a massive reduction in the sale prices of exported solar panels leading to the USA and EU - China's two main export markets - launching investigations in to dumping. Both the USA and the EU case ended with punitive tariffs ranging from 30 to 250 % being imposed on the importation of solar cells.

With the slowing of exports due to the global financial crisis and the anti-dumping cases, the PV sector in China is facing difficulties, especially medium and small-sized PV enterprises, many of whom are in a critical state due to their limited competitiveness. To aid the sector, China is attempting to design policies that will expand the Chinese solar market and reduce the gap between supply and demand. If these efforts fail, it could be disastrous, not least because the Chinese solar industry employs one million people but also because state-owned banks have lent billions of dollars in loans to the sector. The IP-CDM could therefore help with this aid, increasing domestic demand for solar PV cells and reducing the PV sector's reliance on an uncontrollable and unpredictable export market.

The IP-CDM can also be used as a means to overcome the previously mentioned barriers that are currently blocking the wide-spread use of solar PV. Creating more projects and installations will help the technology's path along the learning curve, while increasing solar PV company revenue that can be directed to further research and development. Increased deployment will also help with infrastructure development and will establish a skilled workforce that will provide technical know-how and experience.

This new policy will therefore help distribute wealth and develop poorer regions while stimulating the invigoration of solar PV deployment in China, providing the support needed to enable it to echo the success of the wind energy sector. The IP-CDM if implemented correctly could be the foundation stone of China's PV evolution.

7.8.2 Combination with Life Cycle Analysis

As well as growth of the domestic PV sector, the effect of the IP-CDM on PV exports can also be considered. A lower national grid carbon intensity will lead to less emissions

embodied within a PV installation. Not all of the emissions of an installation will be due to electricity use in China. However, according to Figure 4.3, the emissions of a PV system not accounted for in transport and installation amounts to 81% of its total. If half of this value is attributed to CO₂e emissions through electricity use from the national grid and the implementation of the IP-CDM reduced grid intensity by a quarter, this would save 700 Kg CO₂e per standard installation which when applied to the case study from Chapter 5 amounts to 162,000 tonnes CO₂e and when applied to the quantity of installations predicted by DECC for PV installations introduced through FiTs as discussed in Chapter 4, amounts to 530,000 tonnes CO₂e.

While some of these values have been chosen arbitrarily, it highlights the need for synergy between policy mechanisms and the need for a true appreciation of the emissions associated in renewable energy supply chains.

7.9 Conclusion

The IP-CDM is a mechanism that has the potential to achieve a quadruple benefit of air quality improvement, sustainable development of poorer regions, reduction of the rate of anthropogenic climate change and increase in the rate of development of domestic renewable energy sectors.

A recent report investigating the use of the global CDM for renewable energy development in China has identified that the “CDM is an indispensable incentive and a visible choice to promote renewable energy deployment in China, not only because the international carbon market has redirected to renewable energy and Chinese renewable energy is booming, but also because additional finance from CDM has supported Chinese renewable energy development” [316]. Investment in renewable energy has been proven to increase R&D, reduce costs and reduce the time that it takes for these technologies reach grid parity [9]. An IP-CDM could therefore be an ideal mechanism to achieve this.

There have been issues with the original, global CDM that will need to be addressed with any implementation of the IP-CDM. However, with experience and hindsight, a much more solid and effective mechanism can be created. Also for the IP-CDM to be as stable as possible, the emission reduction targets of the upcoming five-year plans should be published as early as is practical. It must also be considered how the IP-CDM should interact with any other policy mechanisms, especially the proposed nation-wide trading scheme.

This proposal does have its limitations and the mechanism of course will not single-handedly reduce the emissions of China to an acceptable amount and it is not designed to. It is designed to assist and provide a route for provinces to achieve their targets so that through

a concerted and dedicated effort, the worst effects of climate change can be avoided. How the mechanism will work within the governmental structure and alongside other policies needs to be further addressed, preferably by an organisation with experience and working knowledge of the system. An issue that remains is how the use of provincial CDM boards would work within a central government structure. This proposal is still very much theoretical and the complexities of its introduction in to the real world will need to be ironed out. Any implementation will of course have teething issues and it is vital that any major potential stumbling block that could cause a failure of the mechanism's introduction is spotted in advance and prevented.

This research should be furthered through the undertaking of a full socioeconomic analysis of the true impact that the IP-CDM would have in China. The use of the mechanism in other emerging economies could also be considered. The implementation of the IP-CDM should also be considered further, possibly in co-operation with the currently established national CDM board and PDRCs.

To summarise, a market-orientated policy mechanism is proposed, which can work alongside other policies and requires little government spending. It allows the country as a whole to continue its sustainable development, helps provinces meet their carbon intensity reduction targets, distributes wealth to the poorer regions and develops the Chinese renewable energy sector. Furthermore, through the decarbonisation of the Chinese grid and therefore lowering of embodied emissions in silicon cell manufacture, this mechanism has the ability to create a worldwide effect reducing the embodied emissions of the vast majority of global PV installations. The UK has just exempted certain participating Chinese manufacturers from the payment of anti-dumping duties [5] and it is therefore likely that to meet the GHG emissions reductions that the UK has agreed to, carbon savings made through solar PV use will be significantly determined through grid decarbonisation policies made in China.

8 Conclusion

8.1 Summary

The solar cell market is currently dominated by first generation cells. Silicon is a reliable and mature technology but the improvement potential is limited and barriers exist for further developments. These barriers include the high energy intensity of silicon processing which leads to both high costs and a high life cycle emissions. Furthermore, the efficiency of silicon solar technology is already close to reaching the Shockley-Queisser limit thus inhibiting the possibility of any significant further efficiency improvements. The main aim of this thesis is to address the three issues of cost, carbon intensity and efficiency, primarily through the introduction of a novel cell architecture.

Many novel (third generation) solar cell designs incorporate nanomaterials. Nanomaterials provide a means to reduce material usage and utilise less energy intensive processing techniques, such as solution processing, thus creating avenues through which to reduce cost and lower life cycle emissions. Furthermore, the opportunity exists to utilise quantum phenomena such as multiple exciton generation and quantum size confinement which creates the potential to increase the efficiency of nanomaterial-based solar cells above the Shockley-Queisser limit.

Existing solar cell technologies that incorporate nanomaterials as the active light absorbing layer can be broadly classed as either Schottky barrier solar cells, depleted heterojunction solar cells or quantum dot sensitized solar cells. NC-SB solar cells can be simple, robust, low cost and low carbon devices. However, they all currently follow the same architecture where a colloidal NC film is deposited on to an ITO substrate with metal contacts then evaporated on to the back of the device, the SB thus being formed at the interface between the NCs and the metal contacts.

This thesis proposes a novel solar cell where the SB is formed between the metal contact and a bulk semiconductor substrate. NC semiconductors are then used to decorate and activate the device. The device therefore operates over three interfaces. Charge separation of all excitons is created due to the depletion region created through the SB formed between the bulk TiO_2 and the metal contact. NCs are in contact with both the metal and TiO_2 with photogenerated electrons travelling through the bulk semiconductor in to the titanium substrate and holes travelling in to the metal contact. Excitons can also be generated and separated in the TiO_2 . As charge generation, charge separation and transport are carried out by different components, it becomes possible to study each component individually.

Furthermore, the metal contact and the ITO are replaced by an Ag nanomesh which operates as both the TCE and metal for SB formation. To the author's knowledge, AgNWs have never previously been used as the metal contact in a SB solar cell. AgNWs hold promise as a TCE due to their abundance, flexibility, relative cheapness and high performance.

This architecture holds advantages over typical NC-SB cell designs in that it reduces the need to percolate charge through a NC film and the role of crystal defects in NCs, which can have a detrimental impact on SB formation, is reduced.

To fabricate the device, a titanium chip is mechanically polished before undergoing electropolishing treatment. The chip is then heated in air to form a top oxide layer. Silver nanowires are then deposited on top and annealed. This forms a primitive cell that through exciton generation in the bulk TiO_2 generates electricity under illumination with UV light. NCs can then be drop cast on top of the device. This forms an activated cell which can generate electricity under both visible and UV light. Electropolishing is the rate determining step and also requires the use of hazardous materials. It has however been found to be necessary for successful device fabrication

Each step of fabrication was characterised and optimised in chapter 2 and the functionality of the device then demonstrated. IV, photovoltage and EQE curves were used to demonstrate the electrical characteristics of the device and to provide quantitative results. Four types of NCs were used to activate the device and the architecture performed as expected with decorated devices illustrating an electrical response at wavelengths that correlated with the optical responses of the NCs. The highest electrical output is attributed to excitons generated under UV light in the TiO_2 . Despite contribution to existing knowledge in the field of solar PV being achieved through successful device demonstration, the efficiencies created were still low.

Chapter 3 considered various methods that could be used to optimise the demonstrated device thus improving efficiency and reducing carbon intensity. This included the amount of nanomaterials to deposit and the order in which to deposit the nanomaterials. Through this work, it was found that the solvent used for nanomaterial deposition had a significant impact on cell performance and that water should be used preferentially over chloroform. Control over the morphology of the nanomesh was also considered. However, as with the previous studies, no significant increase in efficiency was achieved.

Observations as to how the cell performs over a period of two months were also made. It was found that primitive and activated devices aged differently indicating that NCs were responsible for certain specific aspects of the ageing, such as sulphidisation of the silver

nanomesh and the formation of a carbonaceous layer on the top of the cell. The visible response of activated cells was found to blueshift with time. The ageing of the device is comparable to that of other NC-SB cells.

Ligands were identified as having the potential to have a major influence in NC solar cell performance. Native ligands can be electrically insulating and reduce charge mobility whereas some other ligands could potentially offer improvements in device through controlling NC adsorption and spacing. Several ligand exchange methodologies were therefore considered in Chapter 4. It was found that as well as performance under visible light, upon some ligand exchanges, UV performance increased significantly. When accounting for unintended change in cell characteristics due to the exchange, ligand exchange was not found to significantly improve the performance of the activating NCs. Alternative optimisation techniques should therefore be considered.

No method was found to significantly increase device performance and thus until methods for improvement are found, despite offering a platform for a potentially low-cost, high efficiency cell, poor performance renders the cell unsuitable for general use. The purpose of solar PV is to reduce carbon emissions. However, low electrical output will lead to only a small amount of carbon emissions being saved.

In Chapter 5, the life cycle emissions associated with the demonstrated device were attempted to be determined. However, due to the retrospective nature of LCA, this objective was deemed unachievable. It was decided to apply an integrated hybrid LCA methodology to the market leading silicon technology. To the author's knowledge, this is the first time that such a methodology was applied to solar PV. This provides the three benefits of establishing the application of the methodology to solar PV thus allowing the application to NC-SB cells when the retrospective data exists, determining the most carbon intensive aspects of the use of present day solar technology and enabling analysis of LCA results with respect to present governmental policies and national targets.

The results of the hybrid LCA when applied to silicon solar cells highlights the need for an alternative; silicon cell fabrication is too carbon intensive. Low cost deposition processes and low material usage will greatly reduce the levels of embodied carbon and thus if good levels of efficiencies are realised, the demonstrated cell architecture may help in reducing the carbon intensity of solar PV.

It was found that the UK government greatly over-allocates the emission savings associated with solar PV which could lead to disastrous effects if this has occurred in all technology assessments as carbon reduction targets would then be falsely believed to have been met.

Due to their long lifetime, the carbon intensity of a solar PV installation is found to be greatly dependent on how the grid decarbonises with time. This is an issue that has received relatively little attention. Such as the fear of locking-in emissions with the potential commercial production of shale gas, solar PV with high values of embodied carbon should not be installed if fast grid decarbonisation is a true possibility.

Knowledge of real-world values for insolation upon buildings in a large region enables knowledge of the best locations to install solar PV. This will enable higher electrical output and thus a lower carbon intensity. Furthermore, more accurate values for the carbon saving potential of large-scale solar PV use can be determined.

LCAs are often performed for a single size installation and for a single insolation value. This is unrealistic and can lead to false estimates for the carbon saving potential of solar PV. Chapter 6 demonstrates a methodology for the assessment of solar insolation over a city region. This method utilises data that is often freely available and can analyse 75,000 buildings in 24 minutes on a desktop PC. The method is readily scalable for county or national assessment and applications to other nations would require only a minor modification to the roof profile catalogue.

When the building sizes and insolation values for all small buildings were applied to the results of the silicon PV LCA as performed in Chapter 5, it was calculated that using building-specific values increases the calculated value for quantity of CO₂e saved by 94%. This further highlights that if the realisation of emissions reduction targets is to have any true significance, there is a necessity for truly accurate accounting of abatement efforts.

Further to reducing carbon intensity through optimal installation location, reducing the emissions associated with cell fabrication was identified as a key opportunity. China was acknowledged as the main producer of solar PV and thus reducing the emissions of the Chinese grid was identified as a possibility for reducing the carbon intensity of solar PV.

A nationwide mechanism based on the CDM was proposed and theorised. The inter-provincial clean development mechanism would be a market-orientated policy mechanism that could work alongside other policies and would require little government spending. It was found that the implementation of the IP-CDM would achieved the a quadruple benefit of air quality improvement, sustainable development of poorer regions, reduction of the rate of anthropogenic climate change and increase in the rate of development of domestic renewable energy sectors.

If 40 % of the embodied carbon in solar PV is attributed to CO₂e emissions through electricity use from the Chinese national grid and the implementation of the IP-CDM reduced grid intensity by a quarter, this would save 700 Kg CO₂e for ever typical UK

installation. When applied to the quantity of installations predicted by DECC for PV installations achieved through the introduction of FiTs as discussed in Chapter 5, this amounts to 530,000 tonnes CO₂e.

Policy must be made to implement wide-spread PV deployment but it must also be made with full knowledge of the true carbon savings associated with this deployment through selection of the correct technology, knowledge of the electrical output (through solar input) and also knowledge of the true levels of carbon savings. The last few chapters have provided novel methodologies and mechanisms that can have immediate applications to the whole PV community. Furthermore, when the demonstrated device matures and exhibits suitable attributes for real-world applications, all chapters can be combined to enable accomplishment of reducing PV cost, increasing PV efficiency and reducing PV carbon intensity.

8.2 Future Work

There is need for solar cells with materials better suited than silicon, producing as clean energy as possible that with an output that is optimised through accurate placement. This thesis has presented demonstration of a device that attempts to achieve this through alternative material use, demonstration of a methodology that enables accurate understanding of the emissions associated with fabrication, proposal of a policy that reduces emissions associated with fabrication and development and demonstration of a methodology that enables large-scale solar resource assessment, highlighting the locations most suitable for placement of the demonstrated device.

Further work is needed to improve device performance. However, the device is still very much in prototypal stage and therefore significant room for improvement remains. Improvements can be made in overall device performance and, through use of ligand manipulation, response of the NCs to illumination with visible light can also be improved. The high NA-IQE of devices activated with MPA-capped CdTe NCs indicates that increasing the light absorbed by the device through increasing the areal density of functional NCs is the most promising route for optimisation. Routes for doing so include further optimisation of NC/NW geometry or through the use of porous TiO₂. Selection of a NC material that causes minimum degradation due to ageing is also an avenue of further research.

Due to the non-existence of data pertaining to emissions embodied in the fabrication process of the demonstrated device, no life cycle analysis could be performed. If data becomes available later, the hybrid LCA approach could be used to perform an analysis on the device

and a full comparison with silicon PV could be made. If, in the near-future, the ecoinvent database is expanded to include a range of installation sizes, these values could be combined with an expanded version of the developed solar resource assessment methodology to determine both electrical output and carbon savings of solar PV installations throughout the UK. This combined with further efforts to improve the efficiency of the demonstrated device will further enhance attempts to address the issues of cost, embodied carbon and efficiency that are associated with the incumbent silicon technology.

So it goes.

9 References

1. IPCC, *CLIMATE CHANGE 2014 SYNTHESIS REPORT*, R.K. Pachauri and L.A. Meyer, Editors. 2014, IPCC: Geneva, Switzerland.
2. Bates, L., *2013 UK Greenhouse Gas Emission, Final Figures*, DECC, Editor 2015.
3. Waters, L., J. Prime, and J. Hemingway, *Digest of United Kingdom Energy Statistics*, DECC, Editor 2015.
4. Pucker, G., E. Serra, and Y. Jestin, *Silicon Quantum Dots for Photovoltaics: A Review*.
5. DECC, *UK Renewable Energy Roadmap Update 2013*, 2013.
6. Burger, B., et al., *Photovoltaics Report*, 2014, Fraunhofer: Freiburg.
7. Spertino, F., P.D. Leo, and V. Cocina, *Which are the constraints to the photovoltaic grid-parity in the main European markets?* Solar Energy, 2014. **105**: p. 390-400.
8. Zhai, P. and E.D. Williams, *Dynamic Hybrid Life Cycle Assessment of Energy and Carbon of Multicrystalline Silicon Photovoltaic Systems*. Environmental Science & Technology, 2010. **44**(20): p. 7950-7955.
9. Zhang, D., et al., *Economical assessment of large-scale photovoltaic power development in China*. Energy, 2012. **40**(1): p. 370-375.
10. Shockley, W. and H.J. Queisser, *Detailed Balance Limit of Efficiency of p-n Junction Solar Cells*. Journal of Applied Physics, 1961. **32**(3): p. 510-519.
11. Service, R.F., *Can the Upstarts Top Silicon?* Science, 2008. **319**(5864): p. 718-720.
12. Xufeng, W., et al., *Design of GaAs Solar Cells Operating Close to the Shockley–Queisser Limit*. Photovoltaics, IEEE Journal of, 2013. **3**(2): p. 737-744.
13. Jäger-Waldau, A., *PV status report 2014*2014: EU JRC.
14. Chopra, K.L., P.D. Paulson, and V. Dutta, *Thin-film solar cells: an overview*. Progress in Photovoltaics: Research and Applications, 2004. **12**(2-3): p. 69-92.
15. Bagnall, D.M. and M. Boreland, *Photovoltaic technologies*. Energy Policy, 2008. **36**(12): p. 4390-4396.
16. Compagni, A., et al. *CRITICAL ISSUES AND RESEARCH NEEDS FOR CdTe-BASED SOLAR CELLS AD Compagni, JR Sites2, RW Birkmire3, CS Ferekides4, and AL Fahrenbruch5*University of Toledo, Dept. of Physics, Toledo, Ohio 43606 2Colorado State University, Dept. of Physics, Fort Collins, Colorado 80523. in *Photovoltaics for the 21st Century: Proceedings of the International Symposium*. 1999. The Electrochemical Society.

17. Noufi, R. and K. Zweibel. *High-efficiency CdTe and CIGS thin-film solar cells: highlights and challenges*. in *Photovoltaic Energy Conversion, Conference Record of the 2006 IEEE 4th World Conference on*. 2006. IEEE.
18. Lewis, N.S., *Toward Cost-Effective Solar Energy Use*. Science, 2007. **315**(5813): p. 798-801.
19. Henry, C.H., *Limiting efficiencies of ideal single and multiple energy gap terrestrial solar cells*. Journal of Applied Physics, 1980. **51**(8): p. 4494-4500.
20. Gratzel, M., *Photoelectrochemical cells*. Nature, 2001. **414**(6861): p. 338-344.
21. Ross, R.T. and A.J. Nozik, *Efficiency of hot - carrier solar energy converters*. Journal of Applied Physics, 1982. **53**(5): p. 3813-3818.
22. Goetzberger, A. and W. Greube, *Solar energy conversion with fluorescent collectors*. Applied physics, 1977. **14**(2): p. 123-139.
23. Brabec, C.J. and S.N. Sariciftci, *Recent developments in conjugated polymer based plastic solar cells* 2001: Springer.
24. Nozik, A.J., *Quantum dot solar cells*. Physica E: Low-dimensional Systems and Nanostructures, 2002. **14**(1-2): p. 115-120.
25. Jestin, Y., *1.26 - Down-Shifting of the Incident Light for Photovoltaic Applications*, in *Comprehensive Renewable Energy*, S. Editor-in-Chief: Ali, Editor 2012, Elsevier: Oxford. p. 563-585.
26. Richards, B.S., *Luminescent layers for enhanced silicon solar cell performance: Down-conversion*. Solar Energy Materials and Solar Cells, 2006. **90**(9): p. 1189-1207.
27. Klampaftis, E., et al., *Enhancing the performance of solar cells via luminescent down-shifting of the incident spectrum: A review*. Solar Energy Materials and Solar Cells, 2009. **93**(8): p. 1182-1194.
28. Tsakalakos, L., *1.23 - Application of Micro- and Nanotechnology in Photovoltaics*, in *Comprehensive Renewable Energy*, S. Editor-in-Chief: Ali, Editor 2012, Elsevier: Oxford. p. 515-531.
29. van Sark, W.G.J.H.M., et al., *Enhancing solar cell efficiency by using spectral converters*. Solar Energy Materials and Solar Cells, 2005. **87**(1-4): p. 395-409.
30. Strümpel, C., et al., *Modifying the solar spectrum to enhance silicon solar cell efficiency-An overview of available materials*. Solar Energy Materials and Solar Cells, 2007. **91**(4): p. 238-249.
31. Shao, Q., et al., *Intermediate-band solar cells based on quantum dot supracrystals*. Applied Physics Letters, 2007. **91**(16): p. 163503-3.
32. Cuadra, L., A. Martí, and A. Luque, *Present status of intermediate band solar cell research*. Thin Solid Films, 2004. **451-452**(0): p. 593-599.

33. Wang, W., A.S. Lin, and J.D. Phillips, *Intermediate-band photovoltaic solar cell based on ZnTe:O*. Applied Physics Letters, 2009. **95**(1): p. 011103-3.
34. Brown, A.S. and M.A. Green, *Impurity photovoltaic effect: Fundamental energy conversion efficiency limits*. Journal of Applied Physics, 2002. **92**(3): p. 1329-1336.
35. Canovas, E., et al., *Optimum nitride concentration in multiband III-N-V alloys for high efficiency ideal solar cells*. Applied Physics Letters, 2008. **93**(17): p. 174109-3.
36. Kechiantz, A.M., L.M. Kocharyan, and H.M. Kechiyants, *Band alignment and conversion efficiency in Si/Ge type-II quantum dot intermediate band solar cells*. Nanotechnology, 2007. **18**(40): p. 405401.
37. Marti, A., L. Cuadra, and A. Luque, *Partial filling of a quantum dot intermediate band for solar cells*. Electron Devices, IEEE Transactions on, 2001. **48**(10): p. 2394-2399.
38. Popescu, V., et al., *Theoretical and experimental examination of the intermediate-band concept for strain-balanced (In,Ga)As/Ga(As,P) quantum dot solar cells*. Physical Review B, 2008. **78**(20): p. 205321.
39. Luque, A., et al., *Operation of the intermediate band solar cell under nonideal space charge region conditions and half filling of the intermediate band*. Journal of Applied Physics, 2006. **99**(9): p. 094503-9.
40. Luque, A. and A. Martí, *Increasing the Efficiency of Ideal Solar Cells by Photon Induced Transitions at Intermediate Levels*. Physical Review Letters, 1997. **78**(26): p. 5014-5017.
41. Bremner, S.P., M.Y. Levy, and C.B. Honsberg, *Limiting efficiency of an intermediate band solar cell under a terrestrial spectrum*. Applied Physics Letters, 2008. **92**(17): p. 171110-3.
42. Martí, A. and G.L. Araújo, *Limiting efficiencies for photovoltaic energy conversion in multigap systems*. Solar Energy Materials and Solar Cells, 1996. **43**(2): p. 203-222.
43. Würfel, P., *Solar energy conversion with hot electrons from impact ionisation*. Solar Energy Materials and Solar Cells, 1997. **46**(1): p. 43-52.
44. Tisdale, W.A., et al., *Hot-Electron Transfer from Semiconductor Nanocrystals*. Science, 2010. **328**(5985): p. 1543-1547.
45. Nozik, A.J., *Spectroscopy and hot electron relaxation dynamics in semiconductor quantum wells and quantum dots*. Annual Review of Physical Chemistry, 2001. **52**: p. 193-231.
46. Landsberg, P.T., H. Nussbaumer, and G. Willeke, *Band - band impact ionization and solar cell efficiency*. Journal of Applied Physics, 1993. **74**(2): p. 1451-1452.

47. Schaller, R.D. and V.I. Klimov, *High Efficiency Carrier Multiplication in PbSe Nanocrystals: Implications for Solar Energy Conversion*. Physical Review Letters, 2004. **92**(18): p. 186601.
48. Semonin, O.E., et al., *Peak External Photocurrent Quantum Efficiency Exceeding 100% via MEG in a Quantum Dot Solar Cell*. Science, 2011. **334**(6062): p. 1530-1533.
49. Haes, A.J., et al., *A Nanoscale Optical Biosensor: The Long Range Distance Dependence of the Localized Surface Plasmon Resonance of Noble Metal Nanoparticles*. The Journal of Physical Chemistry B, 2003. **108**(1): p. 109-116.
50. van de Groep, J., P. Spinelli, and A. Polman, *Transparent conducting silver nanowire networks*. Nano Letters, 2012. **12**(6): p. 3138-3144.
51. Hutter, E. and J.H. Fendler, *Exploitation of localized surface plasmon resonance*. Advanced Materials, 2004. **16**(19): p. 1685-1706.
52. Kang, M.-G., et al., *Efficiency Enhancement of Organic Solar Cells Using Transparent Plasmonic Ag Nanowire Electrodes*. Advanced Materials, 2010. **22**(39): p. 4378-4383.
53. Fthenakis, V., *Sustainability of photovoltaics: The case for thin-film solar cells*. Renewable and Sustainable Energy Reviews, 2009. **13**(9): p. 2746-2750.
54. Hu, L., et al., *Scalable Coating and Properties of Transparent, Flexible, Silver Nanowire Electrodes*. ACS Nano, 2010. **4**(5): p. 2955-2963.
55. Lee, J.-Y., et al., *Semitransparent organic photovoltaic cells with laminated top electrode*. Nano Letters, 2010. **10**(4): p. 1276-1279.
56. Chung, C.H., et al., *Silver Nanowire Composite Window Layers for Fully Solution - Deposited Thin - Film Photovoltaic Devices*. Advanced Materials, 2012. **24**(40): p. 5499-5504.
57. Yu, Z., et al., *Silver Nanowire - Polymer Composite Electrodes for Efficient Polymer Solar Cells*. Advanced Materials, 2011. **23**(38): p. 4453-4457.
58. Sun, Y., et al., *Polyol synthesis of uniform silver nanowires: a plausible growth mechanism and the supporting evidence*. Nano Letters, 2003. **3**(7): p. 955-960.
59. Jarrett, R., et al. *Plasmonic Properties of Random Silver Nanowire Meshes Deposited onto Crystalline Silicon Solar Cells*. in *EU PVSEC*. 2014. Amsterdam.
60. Garnett, E.C., et al., *Self-limited plasmonic welding of silver nanowire junctions*. Nature materials, 2012. **11**(3): p. 241-249.
61. Sachse, C., et al., *Transparent, dip-coated silver nanowire electrodes for small molecule organic solar cells*. Organic Electronics, 2013. **14**(1): p. 143-148.

62. Könenkamp, R., *Inorganic Extended-Junction devices*, in *Nanostructured and Photoelectrochemical Systems for Solar Photon Conversion*. p. 393-452.
63. Chang, J.A., et al., *High-Performance Nanostructured Inorganic–Organic Heterojunction Solar Cells*. *Nano Letters*, 2010. **10**(7): p. 2609-2612.
64. Maiolo, J.R., H.A. Atwater, and N.S. Lewis, *Macroporous Silicon as a Model for Silicon Wire Array Solar Cells*. *The Journal of Physical Chemistry C*, 2008. **112**(15): p. 6194-6201.
65. Sargent, E.H., *Colloidal quantum dot solar cells*. *Nat Photon*, 2012. **6**(3): p. 133-135.
66. Law, M., et al., *Determining the Internal Quantum Efficiency of PbSe Nanocrystal Solar Cells with the Aid of an Optical Model*. *Nano Letters*, 2008. **8**(11): p. 3904-3910.
67. Emin, S., et al., *Colloidal quantum dot solar cells*. *Solar Energy*, 2011. **85**(6): p. 1264-1282.
68. Ma, W., et al., *Photovoltaic Devices Employing Ternary PbS_xSe_{1-x} Nanocrystals*. *Nano Letters*, 2009. **9**(4): p. 1699-1703.
69. Selinsky, R.S., et al., *Quantum dot nanoscale heterostructures for solar energy conversion*. *Chemical Society Reviews*, 2013. **42**(7): p. 2963-2985.
70. Hodes, G., *Comparison of Dye- and Semiconductor-Sensitized Porous Nanocrystalline Liquid Junction Solar Cells*. *The Journal of Physical Chemistry C*, 2008. **112**(46): p. 17778-17787.
71. Bang, J.H. and P.V. Kamat, *Quantum Dot Sensitized Solar Cells. A Tale of Two Semiconductor Nanocrystals: CdSe and CdTe*. *ACS Nano*, 2009. **3**(6): p. 1467-1476.
72. Clifford, J.P., et al., *Schottky barriers to colloidal quantum dot films*. *Applied Physics Letters*, 2007. **91**(25): p. 253117.
73. Klem, E.J.D., et al., *Efficient solution-processed infrared photovoltaic cells: Planarized all-inorganic bulk heterojunction devices via inter-quantum-dot bridging during growth from solution*. *Applied Physics Letters*, 2007. **90**(18): p. 183113.
74. Klem, E.J.D., et al., *Solution Processed Photovoltaic Devices with 2% Infrared Monochromatic Power Conversion Efficiency: Performance Optimization and Oxide Formation*. *Advanced Materials*, 2008. **20**(18): p. 3433-3439.
75. Luther, J.M., et al., *Schottky Solar Cells Based on Colloidal Nanocrystal Films*. *Nano Letters*, 2008. **8**(10): p. 3488-3492.
76. Debnath, R., et al., *Ambient-Processed Colloidal Quantum Dot Solar Cells via Individual Pre-Encapsulation of Nanoparticles*. *Journal of the American Chemical Society*, 2010. **132**(17): p. 5952-5953.

77. Liu, C.-Y. and U.R. Kortshagen, *A silicon nanocrystal Schottky junction solar cell produced from colloidal silicon nanocrystals*. *Nanoscale research letters*, 2010. **5**(8): p. 1253-1256.
78. Olson, J.D., et al., *CdTe Schottky diodes from colloidal nanocrystals*. *Applied Physics Letters*, 2010. **96**(24): p. 242103.
79. McFarland, E.W. and J. Tang, *A photovoltaic device structure based on internal electron emission*. *Nature*, 2003. **421**(6923): p. 616-618.
80. Mubeen, S., et al., *An autonomous photosynthetic device in which all charge carriers derive from surface plasmons*. *Nature nanotechnology*, 2013.
81. Hossein-Babaei, F., M.M. Lajvardi, and F.A. Boroumand, *Large area Ag-TiO₂ UV radiation sensor fabricated on a thermally oxidized titanium chip*. *Sensors and Actuators A: Physical*, 2012. **173**(1): p. 116-121.
82. Pernik, D.R., et al., *Tracking the Adsorption and Electron Injection Rates of CdSe Quantum Dots on TiO₂: Linked versus Direct Attachment*. *The Journal of Physical Chemistry C*, 2011. **115**(27): p. 13511-13519.
83. Tang, J., et al., *Self-assembly of CdSe/CdS quantum dots by hydrogen bonding on Au surfaces for photoreception*. *Chem. Commun.*, 2003(18): p. 2278-2279.
84. Bisquert, J., et al., *A review of recent results on electrochemical determination of the density of electronic states of nanostructured metal-oxide semiconductors and organic hole conductors*. *Inorganica Chimica Acta*, 2008. **361**(3): p. 684-698.
85. Tian, J. and G. Cao, *Semiconductor quantum dot-sensitized solar cells*. *Nano Reviews*, 2013. **4**: p. 10.3402/nano.v4i0.22578.
86. Calvin, S., et al., *Comparison of extended X-ray absorption fine structure and Scherrer analysis of X-ray diffraction as methods for determining mean sizes of polydisperse nanoparticles*. *Applied Physics Letters*, 2005. **87**(23): p. 233102.
87. Singh, A.K., *Advanced x-ray techniques in research and industry*2005: IOS Press.
88. Haight, R., F.M. Ross, and J.B. Hannon, *Handbook of Instrumentation and Techniques for Semiconductor Nanostructure Characterization*. Vol. 1. 2012: World Scientific.
89. Joy, D.C., A.D. Romig Jr, and J. Goldstein, *Principles of analytical electron microscopy*1986: Springer.
90. Tajima, K., et al., *Electropolishing of CP Titanium and Its Alloys in an Alcoholic Solution-based Electrolyte*. *Dental Materials Journal*, 2008. **27**(2): p. 258-265.
91. Kuhn, A., *The electropolishing of titanium and its alloys*. *Metal Finishing*, 2004. **102**(6): p. 80-86.

92. Osadchuk, R., W.P. Koster, and J.F. Kahles, *Recommended techniques For Polishing Titanium for metallographic Examination*. Metal Progress, 1953. **64**(4): p. 129-131.
93. Böhme, O., A. Bán, and H. Wendt, *Untersuchungen zum elektropolieren von titan*. Galvanotechnik, 1999. **90**(5): p. 1287-1297.
94. Piotrowski, O., C. Madore, and D. Landolt, *The Mechanism of Electropolishing of Titanium in Methanol - Sulfuric Acid Electrolytes*. Journal of The Electrochemical Society, 1998. **145**(7): p. 2362-2369.
95. Landolt, D., *Fundamental aspects of electropolishing*. Electrochimica Acta, 1987. **32**(1): p. 1-11.
96. Poullou, M., et al., *Titanium wave-like surface microstructure for multiple reflections in solar cell substrates prepared by an all-solution process*. Scripta Materialia, 2010. **62**(6): p. 411-414.
97. Fushimi, K. and H. Habazaki, *Anodic dissolution of titanium in NaCl-containing ethylene glycol*. Electrochimica Acta, 2008. **53**(8): p. 3371-3376.
98. Gunawarman, A., et al., *Fracture characteristics and microstructural factors in single and duplex annealed Ti-4.5Al-3V-2Mo-2Fe*. Materials Science and Engineering: A, 2001. **308**(1-2): p. 216-224.
99. Gale, W.F. and T.C. Totemeier, *Smithells metals reference book 2003*: Butterworth-Heinemann.
100. Lindquist, S.E., A. Lindgren, and Z. Yan - Ning, *On the Origin of the Bandshifts in the Action Spectra of Polycrystalline TiO₂ Electrodes Prepared by Thermal Oxidation of Titanium*. Journal of The Electrochemical Society, 1985. **132**(3): p. 623-631.
101. Tang, J., et al., *Electrochemical fabrication of large-area Au/TiO₂ junctions*. Electrochemistry Communications, 2003. **5**(6): p. 497-501.
102. Ting, C.-C., S.-Y. Chen, and D.-M. Liu, *Preferential growth of thin rutile TiO₂ films upon thermal oxidation of sputtered Ti films*. Thin Solid Films, 2002. **402**(1-2): p. 290-295.
103. Ting, C.C., S.Y. Chen, and D.M. Liu, *Structural evolution and optical properties of TiO₂ thin films prepared by thermal oxidation of sputtered Ti films*. Journal of Applied Physics, 2000. **88**(8): p. 4628-4633.
104. Jamesh, M., T.S.N. Sankara Narayanan, and P.K. Chu, *Thermal oxidation of titanium: Evaluation of corrosion resistance as a function of cooling rate*. Materials Chemistry and Physics, 2013. **138**(2-3): p. 565-572.
105. Jones, E. and O. Untracht, *JEWELRY CONCEPTS AND TECHNOLOGY*. 1987.
106. Siva Rama Krishna, D., Y.L. Brama, and Y. Sun, *Thick rutile layer on titanium for tribological applications*. Tribology International, 2007. **40**(2): p. 329-334.

107. Velten, D., et al., *Preparation of TiO₂ layers on cp-Ti and Ti6Al4V by thermal and anodic oxidation and by sol-gel coating techniques and their characterization*. Journal of Biomedical Materials Research, 2002. **59**(1): p. 18-28.
108. Wen, M., et al., *Thermal oxidation behaviour of bulk titanium with nanocrystalline surface layer*. Corrosion Science, 2012. **59**(0): p. 352-359.
109. Gemelli, E. and N. Camargo, *Oxidation kinetics of commercially pure titanium*. Matéria (Rio de Janeiro), 2007. **12**(3): p. 525-531.
110. Capek, D., et al., *Long-time anodisation of titanium in sulphuric acid*. Surface and Coatings Technology, 2008. **202**(8): p. 1379-1384.
111. Masahashi, N., et al., *Enhanced photocatalytic activity of rutile TiO₂ prepared by anodic oxidation in a high concentration sulfuric acid electrolyte*. Applied Catalysis B: Environmental, 2009. **90**(1): p. 255-261.
112. Von Fraunhofer, J.A., *Basic metal finishing*. 1976.
113. Diamanti, M.V., B. Del Curto, and M. Pedferri, *Interference colors of thin oxide layers on titanium*. Color Research & Application, 2008. **33**(3): p. 221-228.
114. Jaeggi, C., et al., *Film formation and characterization of anodic oxides on titanium for biomedical applications*. Surface and Interface Analysis, 2006. **38**(4): p. 182-185.
115. Menard, R.C., *Optical Measurement of Oxide Thickness on Titanium*. JOSA, 1962. **52**(4): p. 427-431.
116. Hossein-Babaei, F., S. Abbaszadeh, and M.S. Esfahani, *Gas sensitive porous silver-rutile high-temperature Schottky diode on thermally oxidized titanium*. Sensors Journal, IEEE, 2009. **9**(3): p. 237-243.
117. Lee, J.-Y., et al., *Solution-Processed Metal Nanowire Mesh Transparent Electrodes*. Nano Letters, 2008. **8**(2): p. 689-692.
118. Jarrett, R., et al., *Calculating the Criticality of Transparent Conductive Electrodes Used for Thin Film and Third Generation Solar Cells*, in *Photovoltaic Specialist Conference (PVSC)2014*, IEEE: Denver, Colorado, USA. p. 1436-1441.
119. De, S., et al., *Transparent, flexible, and highly conductive thin films based on polymer- nanotube composites*. ACS Nano, 2009. **3**(3): p. 714-720.
120. Geng, H.-Z., et al., *Effect of acid treatment on carbon nanotube-based flexible transparent conducting films*. Journal of the American Chemical Society, 2007. **129**(25): p. 7758-7759.
121. Barnes, T.M., et al., *Optical characterization of highly conductive single-wall carbon-nanotube transparent electrodes*. Physical Review B, 2007. **75**(23): p. 235410.
122. Contreras, M.A., et al., *Replacement of Transparent Conductive Oxides by Single-Wall Carbon Nanotubes in Cu(In,Ga)Se₂-Based*

- Solar Cells*. The Journal of Physical Chemistry C, 2007. **111**(38): p. 14045-14048.
123. Fanchini, G., H.E. Unalan, and M. Chhowalla, *Modification of transparent and conducting single wall carbon nanotube thin films via bromine functionalization*. Applied Physics Letters, 2007. **90**(9): p. 092114.
 124. Zhou, Y., et al., *Investigation on polymer anode design for flexible polymer solar cells*. Applied Physics Letters, 2008. **92**(23): p. 233308.
 125. Vollmer, A., et al., *Electronic and structural properties of graphene-based transparent and conductive thin film electrodes*. Applied Physics A, 2009. **94**(1): p. 1-4.
 126. Haacke, G., *New figure of merit for transparent conductors*. Journal of Applied Physics, 1976. **47**(9): p. 4086-4089.
 127. De, S., et al., *Silver Nanowire Networks as Flexible, Transparent, Conducting Films: Extremely High DC to Optical Conductivity Ratios*. ACS Nano, 2009. **3**(7): p. 1767-1774.
 128. Wang, X., L. Zhi, and K. Müllen, *Transparent, Conductive Graphene Electrodes for Dye-Sensitized Solar Cells*. Nano Letters, 2008. **8**(1): p. 323-327.
 129. Geng, H.-Z., et al., *Absorption spectroscopy of surfactant-dispersed carbon nanotube film: Modulation of electronic structures*. Chemical Physics Letters, 2008. **455**(4-6): p. 275-278.
 130. Gaynor, W., J.-Y. Lee, and P. Peumans, *Fully Solution-Processed Inverted Polymer Solar Cells with Laminated Nanowire Electrodes*. ACS Nano, 2010. **4**(1): p. 30-34.
 131. Derkacs, D., et al., *Improved performance of amorphous silicon solar cells via scattering from surface plasmon polaritons in nearby metallic nanoparticles*. Applied Physics Letters, 2006. **89**(9): p. 093103.
 132. Pillai, S., et al., *Surface plasmon enhanced silicon solar cells*. Journal of Applied Physics, 2007. **101**(9): p. 093105.
 133. Langley, D.P., et al., *Silver nanowire networks: Physical properties and potential integration in solar cells*. Solar Energy Materials and Solar Cells, 2014. **125**(0): p. 318-324.
 134. Kaempgen, M., G.S. Duesberg, and S. Roth, *Transparent carbon nanotube coatings*. Applied Surface Science, 2005. **252**(2): p. 425-429.
 135. Ferrer-Anglada, N., et al., *Synthesis and characterization of carbon nanotube-conducting polymer thin films*. Diamond and Related Materials, 2004. **13**(2): p. 256-260.
 136. DeLongchamp, D.M., et al., *Variations in Semiconducting Polymer Microstructure and Hole Mobility with Spin-Coating Speed*. Chemistry of Materials, 2005. **17**(23): p. 5610-5612.

137. Shah, M., et al., *Investigation of the electrical properties of a surface-type Al/NiPc/Ag Schottky diode using I–V and C–V characteristics*. Physica B: Condensed Matter, 2010. **405**(4): p. 1188-1192.
138. Smit, G.D.J., S. Rogge, and T.M. Klapwijk, *Scaling of nano-Schottky-diodes*. Applied Physics Letters, 2002. **81**(20): p. 3852-3854.
139. Marri, I. and S. Ossicini, *Oxygen vacancy effects on the Schottky barrier height at the Au/TiO₂(110) interface: A first principle study*. Solid State Communications, 2008. **147**(5–6): p. 205-207.
140. Könenkamp, R. and I. Rieck, *Electrical properties of Schottky diodes on nano-porous TiO₂ films*. Materials Science and Engineering: B, 2000. **69–70**(0): p. 519-521.
141. Veres, Á., et al., *Silver and gold modified plasmonic TiO₂ hybrid films for photocatalytic decomposition of ethanol under visible light*. Catalysis Today, 2012. **181**(1): p. 156-162.
142. Booth, M., et al., *Determining the Concentration of CuInS₂ Quantum Dots from the Size-Dependent Molar Extinction Coefficient*. Chemistry of Materials, 2012. **24**(11): p. 2064-2070.
143. Zweibel, K., *Thin film PV manufacturing: Materials costs and their optimization*. Solar Energy Materials and Solar Cells, 2000. **63**(4): p. 375-386.
144. Leatherdale, C.A., et al., *On the Absorption Cross Section of CdSe Nanocrystal Quantum Dots*. The Journal of Physical Chemistry B, 2002. **106**(31): p. 7619-7622.
145. Yu, W.W., et al., *Experimental Determination of the Extinction Coefficient of CdTe, CdSe, and CdS Nanocrystals*. Chemistry of Materials, 2003. **15**(14): p. 2854-2860.
146. Kochuveedu, S.T., et al., *Surface-Plasmon-Enhanced Band Emission of ZnO Nanoflowers Decorated with Au Nanoparticles*. Chemistry – A European Journal, 2012. **18**(24): p. 7467-7472.
147. Korte, K.E., S.E. Skrabalak, and Y. Xia, *Rapid synthesis of silver nanowires through a CuCl-or CuCl₂-mediated polyol process*. J. Mater. Chem., 2008. **18**(4): p. 437-441.
148. Karunakaran, C., V. Rajeswari, and P. Gomathisankar, *Antibacterial and photocatalytic activities of sonochemically prepared ZnO and Ag–ZnO*. Journal of Alloys and Compounds, 2010. **508**(2): p. 587-591.
149. Lee, M.-K. and H.-F. Tu, *Au–ZnO and Pt–ZnO Films Prepared by Electrodeposition as Photocatalysts*. Journal of The Electrochemical Society, 2008. **155**(12): p. D758-D762.
150. Pawinrat, P., O. Mekasuwandumrong, and J. Panpranot, *Synthesis of Au–ZnO and Pt–ZnO nanocomposites by one-step flame spray pyrolysis and its application for photocatalytic degradation of dyes*. Catalysis Communications, 2009. **10**(10): p. 1380-1385.
151. Ruiz Peralta, M.D.L., U. Pal, and R.S. Zeferino, *Photoluminescence (PL) Quenching and Enhanced Photocatalytic Activity of Au-*

- Decorated ZnO Nanorods Fabricated through Microwave-Assisted Chemical Synthesis.* ACS Applied Materials & Interfaces, 2012. **4**(9): p. 4807-4816.
152. Zheng, Y., et al., *Photocatalytic Activity of Ag/ZnO Heterostructure Nanocatalyst: Correlation between Structure and Property.* The Journal of Physical Chemistry C, 2008. **112**(29): p. 10773-10777.
 153. Jarrett, R. and R. Crook. *The Separation of Silver Nanowires from Solution Using a Novel Filtration Technique, a Comparative Study.* in PVSAT-9. 2013. Swansea, UK.
 154. Gledhill, S.E., B. Scott, and B.A. Gregg, *Organic and nano-structured composite photovoltaics: An overview.* Journal of Materials Research, 2005. **20**(12): p. 3167-3179.
 155. Grätzel, M., *Dye-sensitized solar cells.* Journal of Photochemistry and Photobiology C: Photochemistry Reviews, 2003. **4**(2): p. 145-153.
 156. Norrman, K., et al., *Degradation Patterns in Water and Oxygen of an Inverted Polymer Solar Cell.* Journal of the American Chemical Society, 2010. **132**(47): p. 16883-16892.
 157. Zaban, A., et al., *Photosensitization of Nanoporous TiO₂ Electrodes with InP Quantum Dots.* Langmuir, 1998. **14**(12): p. 3153-3156.
 158. Nazeeruddin, M.K., et al., *Conversion of light to electricity by cis-X₂bis(2,2'-bipyridyl-4,4'-dicarboxylate)ruthenium(II) charge-transfer sensitizers (X = Cl-, Br-, I-, CN-, and SCN-) on nanocrystalline titanium dioxide electrodes.* Journal of the American Chemical Society, 1993. **115**(14): p. 6382-6390.
 159. O'regan, B. and M. Grätzel, *A low-cost, high-efficiency solar cell based on dye-sensitized colloidal TiO₂ films.* Nature, 1991. **353**(6346): p. 737-740.
 160. Shalom, M., et al., *Core/CdS Quantum Dot/Shell Mesoporous Solar Cells with Improved Stability and Efficiency Using an Amorphous TiO₂ Coating.* The Journal of Physical Chemistry C, 2009. **113**(9): p. 3895-3898.
 161. Tang, J., et al., *Schottky Quantum Dot Solar Cells Stable in Air under Solar Illumination.* Advanced Materials, 2010. **22**(12): p. 1398-1402.
 162. Liu, C.-H. and X. Yu, *Silver nanowire-based transparent, flexible, and conductive thin film.* Nanoscale Res. Lett, 2011. **6**(1): p. 75.
 163. Koleilat, G.I., et al., *Efficient, Stable Infrared Photovoltaics Based on Solution-Cast Colloidal Quantum Dots.* ACS Nano, 2008. **2**(5): p. 833-840.
 164. von Holt, B., et al., *Ligand exchange of CdSe nanocrystals probed by optical spectroscopy in the visible and mid-IR.* Journal of Materials Chemistry, 2008. **18**(23): p. 2728-2732.
 165. Hines, M.A. and G.D. Scholes, *Colloidal PbS nanocrystals with size - tunable near - infrared emission: observation of post - synthesis*

- self - narrowing of the particle size distribution*. *Advanced Materials*, 2003. **15**(21): p. 1844-1849.
166. Wu, M., et al., *Electron Transfer and Fluorescence Quenching of Nanoparticle Assemblies*. *The Journal of Physical Chemistry C*, 2010. **114**(13): p. 5751-5759.
167. Milliron, D.J., et al., *Electroactive Surfactant Designed to Mediate Electron Transfer Between CdSe Nanocrystals and Organic Semiconductors*. *Advanced Materials*, 2003. **15**(1): p. 58-61.
168. Kalyuzhny, G. and R.W. Murray, *Ligand Effects on Optical Properties of CdSe Nanocrystals*. *The Journal of Physical Chemistry B*, 2005. **109**(15): p. 7012-7021.
169. Kulakovich, O., et al., *Enhanced Luminescence of CdSe Quantum Dots on Gold Colloids*. *Nano Letters*, 2002. **2**(12): p. 1449-1452.
170. Harris, D.C., *Quantitative Chemical Analysis* 2007: W. H. Freeman.
171. P. Gaponik, N., D. V. Talapin, and A. L. Rogach, *A light-emitting device based on a CdTe nanocrystal/polyaniline composite*. *Physical Chemistry Chemical Physics*, 1999. **1**(8): p. 1787-1789.
172. Drndić, M., et al., *Transport properties of annealed CdSe colloidal nanocrystal solids*. *Journal of Applied Physics*, 2002. **92**(12): p. 7498-7503.
173. Dibbell, R.S. and D.F. Watson, *Distance-Dependent Electron Transfer in Tethered Assemblies of CdS Quantum Dots and TiO₂ Nanoparticles*. *The Journal of Physical Chemistry C*, 2009. **113**(8): p. 3139-3149.
174. Ip, A.H., et al., *Hybrid passivated colloidal quantum dot solids*. *Nat Nano*, 2012. **7**(9): p. 577-582.
175. Aldana, J., et al., *Size-Dependent Dissociation pH of Thiolate Ligands from Cadmium Chalcogenide Nanocrystals*. *Journal of the American Chemical Society*, 2005. **127**(8): p. 2496-2504.
176. Ling, D., M.J. Hackett, and T. Hyeon, *Surface ligands in synthesis, modification, assembly and biomedical applications of nanoparticles*. *Nano Today*, 2014. **9**(4): p. 457-477.
177. Hines, D.A. and P.V. Kamat, *Quantum Dot Surface Chemistry: Ligand Effects and Electron Transfer Reactions*. *The Journal of Physical Chemistry C*, 2013. **117**(27): p. 14418-14426.
178. Zarghami, M.H., et al., *p-Type PbSe and PbS Quantum Dot Solids Prepared with Short-Chain Acids and Diacids*. *ACS Nano*, 2010. **4**(4): p. 2475-2485.
179. Luther, J.M., et al., *Structural, Optical, and Electrical Properties of Self-Assembled Films of PbSe Nanocrystals Treated with 1,2-Ethanedithiol*. *ACS Nano*, 2008. **2**(2): p. 271-280.

180. Chen, Y., et al., *Core/Shell Structured Hollow Mesoporous Nanocapsules: A Potential Platform for Simultaneous Cell Imaging and Anticancer Drug Delivery*. ACS Nano, 2010. **4**(10): p. 6001-6013.
181. Michalet, X., et al., *Quantum Dots for Live Cells, in Vivo Imaging, and Diagnostics*. Science, 2005. **307**(5709): p. 538-544.
182. Zimmer, J.P., et al., *Size Series of Small Indium Arsenide-Zinc Selenide Core-Shell Nanocrystals and Their Application to In Vivo Imaging*. Journal of the American Chemical Society, 2006. **128**(8): p. 2526-2527.
183. McElroy, N., et al., *Comparison of solar cells sensitised by CdTe/CdSe and CdSe/CdTe core/shell colloidal quantum dots with and without a CdS outer layer*. Thin Solid Films, 2014. **560**(0): p. 65-70.
184. Mélinon, P., et al., *Engineered inorganic core/shell nanoparticles*. Physics Reports, 2014. **543**(3): p. 163-197.
185. Balet, L.P., et al., *Inverted Core/Shell Nanocrystals Continuously Tunable between Type-I and Type-II Localization Regimes*. Nano Letters, 2004. **4**(8): p. 1485-1488.
186. Webber, D.H. and R.L. Brutchey, *Ligand Exchange on Colloidal CdSe Nanocrystals Using Thermally Labile tert-Butylthiol for Improved Photocurrent in Nanocrystal Films*. Journal of the American Chemical Society, 2012. **134**(2): p. 1085-1092.
187. Hillhouse, H.W. and M.C. Beard, *Solar cells from colloidal nanocrystals: Fundamentals, materials, devices, and economics*. Current Opinion in Colloid & Interface Science, 2009. **14**(4): p. 245-259.
188. Kovalenko, M.V., et al., *Expanding the Chemical Versatility of Colloidal Nanocrystals Capped with Molecular Metal Chalcogenide Ligands*. Journal of the American Chemical Society, 2010. **132**(29): p. 10085-10092.
189. Hines, D.A., M.A. Becker, and P.V. Kamat, *Photoinduced Surface Oxidation and Its Effect on the Exciton Dynamics of CdSe Quantum Dots*. The Journal of Physical Chemistry C, 2012. **116**(24): p. 13452-13457.
190. Karakoti, A.S., et al., *Surface functionalization of quantum dots for biological applications*. Advances in Colloid and Interface Science, 2015. **215**(0): p. 28-45.
191. Zhang, S., et al., *Enhanced infrared photovoltaic efficiency in PbS nanocrystal/semiconducting polymer composites: 600-fold increase in maximum power output via control of the ligand barrier*. Applied Physics Letters, 2005. **87**(23): p. 233101.
192. Trotzky, S., et al., *Ligand removal from soluble CdTe nanocrystals evidenced by time-resolved photoluminescence spectroscopy*. Journal of Physics D: Applied Physics, 2008. **41**(10): p. 102004.

193. Huynh, W.U., et al., *Controlling the Morphology of Nanocrystal-Polymer Composites for Solar Cells*. *Advanced Functional Materials*, 2003. **13**(1): p. 73-79.
194. Leatherdale, C.A., et al., *Photoconductivity in CdSe quantum dot solids*. *Physical Review B*, 2000. **62**(4): p. 2669-2680.
195. Popp, B.V. and S.S. Stahl, *Mechanism of Pd(OAc)₂/Pyridine Catalyst Reoxidation by O₂: Influence of Labile Monodentate Ligands and Identification of a Biomimetic Mechanism for O₂ Activation*. *Chemistry – A European Journal*, 2009. **15**(12): p. 2915-2922.
196. Lee, H.J., et al., *Anchoring cadmium chalcogenide quantum dots (QDs) onto stable oxide semiconductors for QD sensitized solar cells*. *BULLETIN-KOREAN CHEMICAL SOCIETY*, 2007. **28**(6): p. 953.
197. Chen, J., et al., *Directly assembled CdSe quantum dots on TiO₂ in aqueous solution by adjusting pH value for quantum dot sensitized solar cells*. *Electrochemistry Communications*, 2009. **11**(12): p. 2265-2267.
198. Ziegler, J., et al., *Silica - Coated InP/ZnS Nanocrystals as Converter Material in White LEDs*. *Advanced Materials*, 2008. **20**(21): p. 4068-4073.
199. Zhang, H., et al., *Surfactant Ligand Removal and Rational Fabrication of Inorganically Connected Quantum Dots*. *Nano Letters*, 2011. **11**(12): p. 5356-5361.
200. Dong, A., et al., *A Generalized Ligand-Exchange Strategy Enabling Sequential Surface Functionalization of Colloidal Nanocrystals*. *Journal of the American Chemical Society*, 2011. **133**(4): p. 998-1006.
201. Rosen, E.L., et al., *Exceptionally Mild Reactive Stripping of Native Ligands from Nanocrystal Surfaces by Using Meerwein's Salt*. *Angewandte Chemie International Edition*, 2012. **51**(3): p. 684-689.
202. Patil, P., C. Laltlanzuala, and S. Datta, *Sensitized solar cell from type-II CdTe/CdSe core/shell nanocrystals synthesized without seed purification at low temperature*. *Journal of Alloys and Compounds*, 2014. **607**(0): p. 230-237.
203. Yu, X.-Y., et al., *High performance and reduced charge recombination of CdSe/CdS quantum dot-sensitized solar cells*. *Journal of Materials Chemistry*, 2012. **22**(24): p. 12058-12063.
204. Li, J.J., et al., *Large-Scale Synthesis of Nearly Monodisperse CdSe/CdS Core/Shell Nanocrystals Using Air-Stable Reagents via Successive Ion Layer Adsorption and Reaction*. *Journal of the American Chemical Society*, 2003. **125**(41): p. 12567-12575.
205. Akselrod, G.M., et al., *Subdiffusive Exciton Transport in Quantum Dot Solids*. *Nano Letters*, 2014. **14**(6): p. 3556-3562.
206. Klenk, R., et al., *Solar cells based on CuInS₂—an overview*. *Thin Solid Films*, 2005. **480–481**(0): p. 509-514.

207. Santra, P.K., et al., *CuInS₂-Sensitized Quantum Dot Solar Cell. Electrophoretic Deposition, Excited-State Dynamics, and Photovoltaic Performance*. The Journal of Physical Chemistry Letters, 2013. **4**(5): p. 722-729.
208. Weil, B.D., S.T. Connor, and Y. Cui, *CuInS₂ Solar Cells by Air-Stable Ink Rolling*. Journal of the American Chemical Society, 2010. **132**(19): p. 6642-6643.
209. Chakrabarti, R., et al., *Photoconductivity of CdTe films*. Thin Solid Films, 1996. **288**(1–2): p. 32-35.
210. Kouhnavard, M., et al., *A review of semiconductor materials as sensitizers for quantum dot-sensitized solar cells*. Renewable and Sustainable Energy Reviews, 2014. **37**: p. 397-407.
211. Edenhofer, O., R.P. Madruga, and Y. Sokona, *Renewable Energy Sources and Climate Change Mitigation: Special Report of the Intergovernmental Panel on Climate Change*, 2012, IPCC: New York.
212. Arvesen, A., R.M. Bright, and E. Hertwich, *Considering only first-order effects? How simplifications lead to unrealistic technology optimism in climate change mitigation*. Energy Policy, 2011. **39**: p. 7448 - 7454.
213. Lenzen, M. and G. Treloar, *Differential Convergence of Life-Cycle Inventories toward Upstream Production Layers: Implications for Life-Cycle Assessment*. Journal of Industrial Ecology, 2003. **6**(3 - 4): p. 137 - 160.
214. Bullard, C.W., P.S. Penner, and D.A. Pilati, *Net Energy Analysis: Handbook for Combining Process and Input-Output Analysis*. Resources and Energy, 1978. **1**: p. 267 - 313.
215. Suh, S. and G. Huppes, *Methods for Life Cycle Inventory of a product*. Journal of Cleaner Production, 2005. **13**: p. 687 - 697.
216. Suh, S., *Functions, commodities and environmental impacts in an ecological-economic model*. Ecological Economics, 2004. **48**: p. 451 - 467.
217. Crawford, R.H., *Life cycle energy and greenhouse emissions analysis of wind turbines and the effect of size on energy yield*. Renewable and Sustainable Energy Reviews, 2009. **13**(9): p. 2653-2660.
218. Lenzen, M. and R.H. Crawford, *The Path Exchange Method for Hybrid LCA*. Environmental Science and Technology, 2009. **43**: p. 8251 - 8256.
219. Heijungs, R., et al., *Toward an Information Tool for Integrated Product Policy: Requirements for Data and Computation*. Journal of Industrial Ecology, 2006. **10**(3): p. 147 - 158.
220. Joshi, S., *Product Environmental Life-Cycle Assessment Using Input-Output Techniques*. Journal of Industrial Ecology, 1999. **3**(2 - 3): p. 95 - 120.

221. Wiedmann, T.O., et al., *Application of Hybrid Life Cycle Approaches to Emerging Energy Technologies - The Case of Wind Power in the UK*. Environmental Science and Technology, 2011. **45**: p. 5900-5907.
222. Acquaye, A.A., et al., *Identification of 'Carbon Hot-Spots' and Quantification of GHG Intensities in the Biodiesel Supply Chain Using Hybrid LCA and Structural Path Analysis*. Environmental Science and Technology, 2011. **45**: p. 2471 - 2478.
223. Schaltegger, S., *Economics of life cycle assessment: Inefficiency of the present approach*. Business Strategy and the Environment, 1997. **6**(1): p. 1-8.
224. Fleischer, T. and A. Grunwald, *Making nanotechnology developments sustainable. A role for technology assessment?* Journal of Cleaner Production, 2008. **16**(8): p. 889-898.
225. Fthenakis, V., et al. *Nanomaterials in PV manufacture: Some life cycle environmental-and health-considerations*. in *Photovoltaic Specialists Conference (PVSC), 2009 34th IEEE*. 2009. IEEE.
226. Wender, B.A., et al., *Illustrating anticipatory life cycle assessment for emerging photovoltaic technologies*. Environmental science & technology, 2014. **48**(18): p. 10531-10538.
227. Parisi, M.L., A. Sinicropi, and R. Basosi, *Life cycle assessment of Grätzel-type cell production for non conventional photovoltaics from novel organic dyes*. Int J Heat Tecchnol, 2011. **29**(2): p. 161-169.
228. Parisi, M.L., S. Maranghi, and R. Basosi, *The evolution of the dye sensitized solar cells from Grätzel prototype to up-scaled solar applications: A life cycle assessment approach*. Renewable and Sustainable Energy Reviews, 2014. **39**: p. 124-138.
229. de Wild-Scholten, M., A. Veltkamp, and E.S. Energy. *Environmental life cycle analysis of dye sensitized solar devices; status and outlook*. in *22nd European Photovoltaic Solar Energy Conference, Milan, Italy*. 2007.
230. Fthenakis, V.M., H.C. Kim, and E. Alsema, *Emissions from photovoltaic life cycles*. Environmental science & technology, 2008. **42**(6): p. 2168-2174.
231. Kim, H.C. and V. Fthenakis, *Life cycle energy and climate change implications of nanotechnologies*. Journal of Industrial Ecology, 2013. **17**(4): p. 528-541.
232. Gerbinet, S., S. Belboom, and A. Léonard, *Life Cycle Analysis (LCA) of photovoltaic panels: A review*. Renewable and Sustainable Energy Reviews, 2014. **38**: p. 747-753.
233. Cucchiella, F. and I. D'Adamo, *Estimation of the energetic and environmental impacts of a roof-mounted building-integrated photovoltaic systems*. Renewable and Sustainable Energy Reviews, 2012. **16**(7): p. 5245-5259.

234. Hsu, D.D., et al., *Life Cycle Greenhouse Gas Emissions of Crystalline Silicon Photovoltaic Electricity Generation*. Journal of Industrial Ecology, 2012. **16**: p. S122-S135.
235. Skoczek, A., T. Sample, and E.D. Dunlop, *The results of performance measurements of field-aged crystalline silicon photovoltaic modules*. Progress in Photovoltaics: Research and Applications, 2009. **17**(4): p. 227-240.
236. Krein, P.T. and R.S. Balog. *Cost-Effective Hundred-Year Life for Single-Phase Inverters and Rectifiers in Solar and LED Lighting Applications Based on Minimum Capacitance Requirements and a Ripple Power Port*. in *Applied Power Electronics Conference and Exposition, 2009. APEC 2009. Twenty-Fourth Annual IEEE*. 2009.
237. Ito, M., K. Komoto, and K. Kurokawa, *Life-cycle analyses of very-large scale PV systems using six types of PV modules*. Current Applied Physics, 2010. **10**(2): p. S271-S273.
238. Kim, H., et al., *Life cycle assessment of cadmium telluride photovoltaic (CdTe PV) systems*. Solar Energy, 2014. **103**: p. 78-88.
239. Committee on Climate Change, *Meeting Carbon Budgets - Third Progress Report to Parliament*, 2011: London. p. 139.
240. DEFRA, *2015 Guidelines to Defra / DECC's GHG Conversion Factors for Company Reporting: Methodology Paper for Emission Factors*, D.f. Environment, Editor 2015: London.
241. Committee on Climate Change, *The Fourth Carbon Budget – Reducing emissions through the 2020's*, 2010: London. p. 25.
242. Steward, A. and B. Madden, *Design of Feed-in Tariffs for Sub-5MW Electricity in Great Britain*, 2009, Element Energy: London.
243. *Central Feed-in Tariff register, Monthly central Feed-IN Tariff register statistics*, D.o.E.a.C, Editor 2015.
244. DECC, *Feed-in Tariffs: Government's Response to the Summer 2009 Consultation*, 2010.
245. Central Feed-In Tariff Register, *Monthly central Feed-In Tariff register statistics*, D.o.E.a.C. Change, Editor 2012.
246. Dixon, R., *Electricity Market Reform – ensuring electricity security of supply and promoting investment in low-carbon generation [January 2013 update]: Impact Assessment*, 2013.
247. Market Transformation Programme, *BNXS01: Carbon Dioxide Emission Factors for the UK Energy Use Version 4.2*, 2010.
248. Hawkes, A., *Pathways to 2050 - Key Results: MARKAL Model Review and Scenarios for DECC's 4th Carbon Budget Evidence Base*, AEA, Editor 2011, DECC: London.
249. Gavankar, S., S. Suh, and A. Keller, *Life cycle assessment at nanoscale: review and recommendations*. The International Journal of Life Cycle Assessment, 2012. **17**(3): p. 295-303.

250. Miseljic, M. and S. Olsen, *Life-cycle assessment of engineered nanomaterials: a literature review of assessment status*. Journal of Nanoparticle Research, 2014. **16**(6): p. 1-33.
251. Chiabrando, R., E. Fabrizio, and G. Garnero, *The territorial and landscape impacts of photovoltaic systems: Definition of impacts and assessment of the glare risk*. Renewable and Sustainable Energy Reviews, 2009. **13**(9): p. 2441-2451.
252. Hay, J.E. and K.J. Hanson, *Evaluating the solar resource: a review of problems resulting from temporal, spatial and angular variations*. Solar Energy, 1985. **34**(2): p. 151-161.
253. Bergamasco, L. and P. Asinari, *Scalable methodology for the photovoltaic solar energy potential assessment based on available roof surface area: Further improvements by ortho-image analysis and application to Turin (Italy)*. Solar Energy, 2011. **85**(11): p. 2741-2756.
254. Kabir, M.H., W. Endlicher, and J. Jägermeyr, *Calculation of bright roof-tops for solar PV applications in Dhaka Megacity, Bangladesh*. Renewable Energy, 2010. **35**(8): p. 1760-1764.
255. Brito, M.C., et al., *Photovoltaic potential in a Lisbon suburb using LiDAR data*. Solar Energy, 2012. **86**(1): p. 283-288.
256. Izquierdo, S., M. Rodrigues, and N. Fueyo, *A method for estimating the geographical distribution of the available roof surface area for large-scale photovoltaic energy-potential evaluations*. Solar Energy, 2008. **82**(10): p. 929-939.
257. Wiginton, L.K., H.T. Nguyen, and J.M. Pearce, *Quantifying rooftop solar photovoltaic potential for regional renewable energy policy*. Computers, Environment and Urban Systems, 2010. **34**(4): p. 345-357.
258. Awwad, T.M., et al., *An improved segmentation approach for planar surfaces from unstructured 3D point clouds*. The Photogrammetric Record, 2010. **25**(129): p. 5-23.
259. Gooding, J., et al., *Solar City Indicator: A methodology to predict city level PV installed capacity by combining physical capacity and socio-economic factors*. Solar Energy, 2013. **95**: p. 325-335.
260. Gorte, B., *Segmentation of TIN-structured surface models*. International Archives of Photogrammetry Remote Sensing and Spatial Information Sciences, 2002. **34**(4): p. 465-469.
261. Jochem, A., et al., *Automatic Roof Plane Detection and Analysis in Airborne Lidar Point Clouds for Solar Potential Assessment*. Sensors, 2009. **9**(7): p. 5241-5262.
262. Kassner, R., et al., *Analysis of the solar potential of roofs by using official lidar data*. International Archives of Photogrammetry, Remote Sensing and Spatial Information Sciences, 2008. **37**: p. 399-403.
263. Kodysh, J.B., et al., *Methodology for estimating solar potential on multiple building rooftops for photovoltaic systems*. Sustainable Cities and Society, 2013(0).

264. Lukač, N. and B. Žalik, *GPU-based roofs' solar potential estimation using LiDAR data*. Computers & Geosciences, 2013. **52**(0): p. 34-41.
265. Nguyen, H.T., et al., *The Application of LiDAR to Assessment of Rooftop Solar Photovoltaic Deployment Potential in a Municipal District Unit*. Sensors, 2012. **12**(4): p. 4534-4558.
266. Nguyen, V., et al. *A comparison of line extraction algorithms using 2D laser rangefinder for indoor mobile robotics*. in *IEEE/RSJ International Conference*. 2005. IEEE.
267. Overby, J., et al., *Automatic 3D building reconstruction from airborne laser scanning and cadastral data using Hough transform*. International Archives of Photogrammetry and Remote Sensing, 2004. **35**(B3): p. 296-301.
268. Rottensteiner, F., et al., *Automated delineation of roof planes from lidar data*. International archives of the photogrammetry, remote sensing and spatial information sciences, 2005. **36**(3/W19): p. 221-226.
269. Vosselman, G. and S. Dijkman, *3D building model reconstruction from point clouds and ground plans*. International Archives of Photogrammetry Remote Sensing and Spatial Information Sciences, 2001. **34**(3/W4): p. 37-44.
270. Maas, H.-G., *Closed solutions for the determination of parametric building models from invariant moments of airborne laserscanner data*. transformation, 1999. **2**: p. 20.
271. Pillai, I.R. and R. Banerjee, *Methodology for estimation of potential for solar water heating in a target area*. Solar Energy, 2007. **81**(2): p. 162-172.
272. Burrough, P.A. and R.A. McDonnell, *Principles of geographical Information Systems*1998: Oxford University Press.
273. Rottensteiner, F. and C. Briese, *Automatic generation of building models from LIDAR data and the integration of aerial images*. International Archives of the Photogrammetry, Remote Sensing and Spatial Information Sciences of the ISPRS, 2003. **34**(3/W13): p. 174-180.
274. *Cities Revealed* © The GeoInformation Group, 2008.
275. *OS MasterMap [Shape geospatial data], Updated: December 2011, Ordnance Survey (GB), Using: EDINA Digimap Ordnance Survey Service, <<http://edina.ac.uk/digimap>>, Downloaded: February 2013*
276. MATLAB, R2012a. The Mathworks Inc., Natick, Massachusetts.
277. Lehmann, H. and S. Peter, *Assessment of roof & façade potentials for solar use in Europe*. Institute for sustainable solutions and innovations (ISUSI): Aachen, Germany, 2003.
278. Huld, T., R. Müller, and A. Gambardella, *A new solar radiation database for estimating PV performance in Europe and Africa*. Solar Energy, 2012. **86**(6): p. 1803-1815.

279. Šúri, M., et al., *Potential of solar electricity generation in the European Union member states and candidate countries*. Solar Energy, 2007. **81**(10): p. 1295-1305.
280. NBS, *Energy, China Statistical Yearbook 2010*, China Statistics Press: Beijing, China.
281. Guan, D., et al., *Journey to world top emitter: An analysis of the driving forces of China's recent CO₂ emissions surge*. Geophysical Research Letters, 2009. **36**(4): p. L04709.
282. Steckel, J.C., et al., *From carbonization to decarbonization?—Past trends and future scenarios for China's CO₂ emissions*. Energy Policy, 2011. **39**(6): p. 3443-3455.
283. Olivier, J.G., G. Janssesn-Maenhout, and J.A.H.W. Peters, *Trends in Global CO₂ emissions - 2012 report*, 2012, Joint Research Centre,.
284. Feng, K., K. Hubacek, and D. Guan, *Lifestyles, technology and CO₂ emissions in China: A regional comparative analysis*. Ecological Economics, 2009. **69**(1): p. 145-154.
285. Subbarao, S. and B. Lloyd, *Can the Clean Development Mechanism (CDM) deliver?* Energy Policy, 2011. **39**(3): p. 1600-1611.
286. Geng, Y., et al., *Towards a national circular economy indicator system in China: an evaluation and critical analysis*. Journal of Cleaner Production, 2012. **23**(1): p. 216-224.
287. Rigter, J. and G. Vidican, *Cost and optimal feed-in tariff for small scale photovoltaic systems in China*. Energy Policy, 2010. **38**(11): p. 6989-7000.
288. Chen, Q., et al., *Preliminary exploration on low-carbon technology roadmap of China's power sector*. Energy, 2011. **36**(3): p. 1500-1512.
289. Schuman, S. and A. Lin, *China's Renewable Energy Law and its impact on renewable power in China: Progress, challenges and recommendations for improving implementation*. Energy Policy, 2012. **51**(0): p. 89-109.
290. NDRC, *China's National Climate Change Programme*, 2007, National Development and Reform Commission,.
291. Liu, L.q., C.x. Liu, and Z.y. Sun, *A survey of China's low-carbon application practice - Opportunity goes with challenge*. Renewable and Sustainable Energy Reviews, 2011. **15**: p. 2895-2903.
292. Ma, L., et al., *Integrated energy strategy for the sustainable development of China*. Energy, 2011. **36**(2): p. 1143-1154.
293. Zhang, P., et al., *Opportunities and challenges for renewable energy policy in China*. Renewable and Sustainable Energy Reviews, 2009. **13**(2): p. 439-449.
294. Wang, Q., *Effective policies for renewable energy—the example of China's wind power—lessons for China's photovoltaic power*. Renewable and Sustainable Energy Reviews, 2010. **14**(2): p. 702-712.

295. Feng, K., et al., *Analyzing drivers of regional carbon dioxide emissions for China*. Journal of Industrial Ecology, 2012. **16**(4): p. 600-611.
296. Lindner, S., et al., *CO2 emissions from China's power sector at the provincial level: Consumption versus production perspectives*. Renewable and Sustainable Energy Reviews, 2013. **19**: p. 164-172.
297. Liu, Z., et al., *Uncovering China's greenhouse gas emission from regional and sectoral perspectives*. Energy, 2012. **45**(1): p. 1059-1068.
298. Guan, D. and K. Hubacek, *China can offer domestic emission cap-and-trade in post 2012*. Environmental Science & Technology, 2010. **44**(14): p. 5327-5327.
299. Han, G., et al., *China's Carbon Emission Trading: An overview of Current Development*, 2012, Forum for Reforms, Entrepreneurship and Sustainability.
300. NDRC, *Measures for the Operation and Management of CDM Projects*, 2005, Department of Climate Change: China.
301. Brundtland, G.H., *Report of the World Commission on Environment and Development: Our Common Future*, 1987, United Nations: Oslo, Norway.
302. Dyer, G., M. McKay, and M. Mira, *From Clean Development to Strategic Sustainable Development: A strategic approach to the Clean Development Mechanism*, 2007.
303. Heuberger, R., et al., *CDM Projects under the Kyoto Protocol: A Methodology for Sustainability Assessment – Experiences from South Africa and Uruguay*. Environment, Development and Sustainability, 2007. **9**(1): p. 33-48.
304. Thorne, S. and S. Raubenheimer. *Sustainable Development appraisal of Clean Development Mechanism projects - experiences from the SouthSouthNorth project*. in *Forum for Economics and Environment*. 2002. Prague, Czech Republic.
305. UNEP Risoe, *Overview of the CDM pipeline*, 2012, United Nations Environment Programme: Risoe, Denmark.
306. Bayer, P., J. Urpelainen, and J. Wallace, *Who uses the Clean Development Mechanism? An empirical analysis of projects in Chinese provinces*. Global Environmental Change, 2013(0).
307. Greiner, S. and A. Michaelowa, *Defining Investment Additionality for CDM projects—practical approaches*. Energy Policy, 2003. **31**(10): p. 1007-1015.
308. Yunna, W. and C. Quanzhi, *The demonstration of additionality in small-scale hydropower CDM project*. Renewable Energy, 2011. **36**(10): p. 2663-2666.
309. Zhang, J. and C. Wang, *Co-benefits and additionality of the clean development mechanism: An empirical analysis*. Journal of Environmental Economics and Management, 2011. **62**(2): p. 140-154.

310. Bullock, S., M. Childs, and T. Picken, *A Dangerous Distraction - Why offsetting is failing the climate and people: the evidence*, 2009, Friends of the Earth,.
311. Vöhringer, F., et al., *Reinforcing the EU dialogue with developing countries on climate change mitigation*. 2010.
312. NBS, *National Accounts, China Statistical Yearbook 2007*, China Statistics Press: Beijing, China.
313. Fair Wage Network. *Minimum wage adjustments of Chinese provinces / municipalities*. 2011 30/01/2013]; Available from: <http://fair-wage.com/en/fair-wage-observatory/new-legal-provisions/101-2011-minimum-wage-adjustments-of-chinese-provincesmunicipalities-.html>.
314. NDRC. *Regional energy-saving goal in the first half of 2011the completion of a barometer*. 2011 30/01/2013]; Available from: http://www.ndrc.gov.cn/xwfb/t20110729_426427.htm.
315. Nautiyal, H. and Varun, *Progress in renewable energy under clean development mechanism in India*. Renewable and Sustainable Energy Reviews, 2012. **16**(5): p. 2913-2919.
316. Wang, Q. and Y. Chen, *Barriers and opportunities of using the clean development mechanism to advance renewable energy development in China*. Renewable and Sustainable Energy Reviews, 2010. **14**(7): p. 1989-1998.
317. Bing, X., et al., *Global reverse supply chain redesign for household plastic waste under the emission trading scheme*. Journal of Cleaner Production, 2015. **103**: p. 28-39.
318. Lo, A.Y. and X. Yu, *Climate for Business: Opportunities for Financial Institutions and Sustainable Development in the Chinese Carbon Market*. Sustainable Development, 2015: p. n/a-n/a.
319. Baker & McKenzie. *Type E- policies*. CDM Rulebook: Clean Development mechanism, Rules, Practice & Procedures 30/01/2013]; Available from: <http://cdmrulebook.org/4963>.
320. Schneider, L., *Assessing the additionality of CDM projects: practical experiences and lessons learned*. Climate policy, 2011. **9**(3): p. 242-254.
321. Guan, D., et al., *The gigatonne gap in China's carbon dioxide inventories*. Nature Climate Change, 2012. **2**(9): p. 672-675.
322. Gong, X., et al., *Research and development of Chinese LCA database and LCA software*. Rare Metals, 2006. **25**(6, Supplement 2): p. 101-104.
323. Nygard, J., et al., *Clean Development Mechanism In China: Taking a Proactive and Sustainable Approach*, 2004, The World Bank, Ministry of Science and technology, The Deutsche Gesellschaft für Technische Zusammenarbeit, German Technical Cooperation Unit (GTZ), Federal Ministry of Economic Cooperation and Development, Swiss State Secretariat for Economic Affairs: Washington D.C.

324. UNFCCC, *Issued CERs/tCERs as at 31 December 2012*, 2012, United Nations Framework Convention on Climate Change: <http://cdm.unfccc.int/Registry/index.html>.
325. UNFCCC, *Greenhouse Gas Emissions Data for 1990 - 2003: key GHG Data*, 2005, United Nations Framework Convention on Climate Change: Bonn, Germany.
326. EPA, *"Bubble" Policy Added to EPA's Cleanup Strategy*, 1979, United States Environmental Protection Agency.
327. Jaeger-Waldau, A., *Overview of the Global PV industry*, 2012, European Commission Joint Research Centre.
328. Li, J., et al., *China Solar PV Report*, 2007, China Environmental Science Press.
329. Fried, L., et al., *Global Wind Report: Annual market update 2014*, 2015, Global Wind Energy Council: Brussels, Belgium.
330. Liao, C., et al., *Wind power development and policies in China*. Renewable Energy, 2010. **35**(9): p. 1879-1886.
331. Masson, G., S. Orlandi, and M. Rekingier, *Global Market Outlook For Photovoltaics 2014 - 2018*, 2014, European Photovoltaic Industry Association: Brussels, Belgium.
332. Li, J. and L. Ma, *Background Paper: Chinese Renewables Status Report*, 2009, Renewable Energy Policy Network for the 21st Century.
333. Zhe, S., *Project 4919 : Ningxia Hongsipu 50MWp PV (photovoltaic) Power No.1 Plant Project*, 2011, UNFCCC: Yinchuan, China.
334. Jie, T., *Project 4981 : CECIC Shizuishan Grid-connected Solar PV Power Generation Phase I project*, 2011, UNFCCC: Shizuishan, China.